

**Assessment of Partitioning Tracers for Estimation of  
DNAPL Source Zone Architecture**

A dissertation  
submitted by  
Rhiannon E. Ervin

In partial fulfillment of the requirements  
for the degree of

Doctor of Philosophy

in

*Civil and Environmental Engineering*

Tufts University

May, 2012

Advisor: Dr. C. Andrew Ramsburg

## **ABSTRACT**

It is estimated that 15,000 to 25,000 sites across the United States are impacted by dense nonaqueous phase liquid (DNAPL) contamination. The difficulties in cleaning up and closing out these sites have prompted many to consider the potential benefits of partial removal of the source mass. Mathematical models developed to assess these benefits often employ metrics of the spatial distribution of DNAPL mass within the source. This spatial distribution is termed the DNAPL architecture. Interestingly, there are currently no field methods available for characterization of the DNAPL architecture. Thus, the overall objective of this research was to develop a framework for assessing the local-scale DNAPL architecture using partitioning tracers in push-pull tests. The central hypothesis of the research is that differences in the mass transfer kinetics between high and low saturation areas will permit estimation the mass fraction of DNAPL present in pools (i.e., pool fraction). This hypothesis was tested using laboratory experiments and mathematical modeling. Liquid-liquid-equilibrium experiments and subsequent thermodynamic modeling were employed to assess the phase behavior of partitioning of three representative alcohol tracers (1-pentanol, 1-hexanol, and 2-octanol) with a model DNAPL (trichloroethene), and determine the range of concentrations over which partitioning may be assumed linear. Results from 1-D column experiments and 2-D aquifer cell experiments indicate that tracer transport in systems comprised of TCE-DNAPL can be described with linear driving force models that employ mass transfer coefficients developed for the dissolution of pure-component DNAPLs. Push-pull tests conducted in

heterogeneous source zones created within 2-D aquifer cells indicate that partitioning tracers can describe DNAPL architecture, but not the pool fraction metric. Tests in these heterogeneous source zones also indicate that differences in push-pull test breakthrough curves are not dominated by mass transfer kinetics between high and low saturation areas. Instead, simulations conducted in several, simplified source zones suggest push-pull tracer tests are strongly affected by the amount of the vertical domain that contains DNAPL and the distance from the well to the DNAPL mass. Results of this research indicate that push-pull tests may be useful within a larger characterization framework to help resolve local-scale architecture, thereby improving predictions of contaminant plume response to various level of treatment within the source. It is recommended that future work focus on 3-D simulations to explore the influence of radially distributed DNAPL on the ability of the push-pull test to estimate the vertical extent of the DNAPL and distance from the well to the DNAPL mass.

## **DEDICATION**

I would like to dedicate this work to my mom, Deena Barber, who instilled in me the value of education, told me everyday how smart I was, constantly encouraged me in everything I attempted, taught me the importance of hard work, and showed me the value of being passionate about your career. I would not be where I am today without her continual love and support.

## **Acknowledgements**

I would like to gratefully acknowledge my committee members, Dr. Linda Abriola (Tufts University), Dr. Kurt Pennell (Tufts University), Dr. Grant Garven (Tufts University), Dr. John Christ (U.S. Air Force Academy) and Dr. C. Andrew Ramsburg (Tufts University), for their time and guidance which has helped me to continually make progress on this research. Additionally, I would like to acknowledge the ER-1612 project team for their many intellectual contributions. Thanks to Doug Walker for helping me with the 2-D aquifer cell experiments and for teaching me how to perform the light transmission analysis. I would also like to thank my fellow IMPES group members who frequently offered helpful suggestions and aided me in sampling during the long aquifer cell experiments. Thank you to Dr. Nicole Berge (University of South Carolina) who not only taught me many of the experimental procedures used herein, but also the attention to detail required to conduct quality laboratory research. Additional thanks to Dr. Linda Abriola and Dr. John Christ for helping develop transport models necessary to complete this work. I most especially want to thank Mr. Ali Boroumand (Tufts University) who developed and wrote the transport models used herein. Without the knowledge, patience and dedication of Mr. Boroumand, precise modeling of each transport experiment would not have been possible. Lastly, I would like to thank my advisor, Dr. C. Andrew Ramsburg who has continually supported and encouraged me on both an academic and personal level throughout my graduate career. Dr. Ramsburg has contributed greatly to the significant results and findings discussed herein.

Portions of Chapters 4 and 5 are published in the Journal of Contaminant Hydrology and can be found using the following citation: Ervin, R.E., Boroumand, A.B., Abriola, L.M. and C.A. Ramsburg. 2011. Kinetic limitation on tracer partitioning in ganglia dominated source zones. Journal of Contaminant Hydrology, 126:195-207.

Funding for this research was received from the Strategic Environmental Research & Development Program under Project ER-1612. The content of this dissertation does not necessarily represent the views of the agency and has not been subject to agency review. Partial funding for conference travel was provided by the Graduate Student Travel Fund and by the School of Engineering at Tufts University.

## TABLE OF CONTENTS

<b>ABSTRACT</b>	<b>IX</b>
<b>DEDICATION</b>	<b>XI</b>
<b>ACKNOWLEDGEMENTS</b>	<b>XII</b>
<b>TABLE OF CONTENTS</b>	<b>XIV</b>
<b>LIST OF FIGURES</b>	<b>XX</b>
<b>LIST OF SYMBOLS</b>	<b>XXVII</b>
<b>EXECUTIVE SUMMARY</b>	<b>XXXI</b>
<b>CHAPTER 1: BACKGROUND</b>	<b>1</b>
<b>1.1 Chlorinated Solvents</b>	<b>1</b>
1.1.1- Chemical Properties	1
1.1.2 - Uses: Past and Present	4
1.1.3 - Infiltration and Entrapment	6
<b>1.2 Influence of Source Zone Architecture on Contaminant Mass Flux</b>	<b>9</b>
1.2.1 - Integral Pump Test	13
1.2.2 - Multi-Level Sampler	13
1.2.3 - Passive Flux Meter	15
1.2.4 - Flow Bypassing	16
1.2.5 - Partial Mass Removal	17
<b>1.3 Source Zone Architecture Metrics</b>	<b>21</b>
1.3.1 - Temporal Moments	21
1.3.2 - Spatial Moments	23
1.3.4 - Ganglia-to-Pool Ratio	25
1.3.5 - Pool Fraction	26
<b>1.4 Source Zone Characterization</b>	<b>26</b>
1.4.1 - Soil Coring	27
1.4.2 - Partitioning Interwell Tracer Test	27
1.4.3 - Push-Pull Test	31
<b>1.5 Tracer DNAPL Interactions</b>	<b>32</b>
1.5.1 - Liquid-Liquid Equilibrium	32
1.5.2 - Surface Interactions	40
1.5.3 - Tracer Mass Transport in Porous Media	44
1.5.3.1 - Mass Transport Models in Regions of Entrapped DNAPL Saturation	44
1.5.3.2 - Mass Transport Models in Pool Dominated or Heterogeneous DNAPL Saturations	47
1.5.4 - Mass Transfer Coefficient Correlations	53
1.5.4.1 - Ganglia Dissolution Correlations	53
1.5.4.2 - Pool Dissolution Correlations	56

## **CHAPTER 2: OBJECTIVES AND HYPOTHESES \_\_\_\_\_ 68**

*Objective 1: Measure the liquid-liquid-equilibrium of each 1-pentanol, 1-hexanol, and 2-octanol (three representative tracers) in a TCE-water system. \_\_\_\_\_ 71*

*Objective 2: Compare the measured liquid-liquid-equilibrium behavior of each alcohol to the behavior predicted using UNIFAC \_\_\_\_\_ 72*

*Objective 3: Explore the processes controlling partitioning tracer mass transport in columns containing uniform distributions of entrapped TCE-DNAPL \_\_\_\_\_ 73*

*Objective 4: Assess mass transfer kinetics in systems containing a single pool of TCE-DNAPL. \_\_\_\_\_ 74*

*Objective 5: Examine the influence of injection and extraction flow rates during a push-pull test conducted in heterogeneous DNAPL source zones. \_\_\_\_\_ 75*

*Objective 6: Explore the influence of DNAPL architectural features on push-pull test breakthrough curves. \_\_\_\_\_ 76*

## **CHAPTER 3 – MATERIALS AND METHODS \_\_\_\_\_ 78**

**3.1 – Materials \_\_\_\_\_ 78**

**3.2 - Analytical Methods \_\_\_\_\_ 81**

3.2.1 - Alcohol and TCE Concentrations - Gas Chromatography \_\_\_\_\_ 81

3.2.2 - Bromide and Chloride Concentrations - Ion Chromatography \_\_\_\_\_ 81

3.2.3 - DNAPL Water Content - Karl Fischer Titration \_\_\_\_\_ 82

3.2.4 - DNAPL Phase Density - Pycnometer \_\_\_\_\_ 82

3.2.5 - Interfacial Tension – Drop Shape Analyzer \_\_\_\_\_ 82

**3.3 - Experimental Methods \_\_\_\_\_ 83**

3.3.1 - Liquid-Liquid-Equilibrium \_\_\_\_\_ 83

3.3.2 - 1-D Column Experiments \_\_\_\_\_ 83

3.3.3 2-D Box Experiments – Pooled Source Zone \_\_\_\_\_ 85

3.3.4 - 2-D Box Experiments – Heterogeneous Source Zone \_\_\_\_\_ 88

3.3.5 - Light Transmission Imaging \_\_\_\_\_ 91

**3.4 - Mathematical Modeling \_\_\_\_\_ 92**

3.4.1 - Thermodynamic modeling of LLE \_\_\_\_\_ 92

3.4.2 - Partitioning Tracer Transport - Ganglia \_\_\_\_\_ 95

3.4.2.1 - Equilibrium \_\_\_\_\_ 96

3.4.2.2 - Linear Driving Force \_\_\_\_\_ 97

3.4.2.3 - Dual Diffusion \_\_\_\_\_ 98

3.4.2.4 - Dual Diffusion and Surface Partitioning \_\_\_\_\_ 99

3.4.3 - Partitioning Tracer Transport – Pooled Source Zone \_\_\_\_\_ 100

3.4.4 - Partitioning Tracer Transport - Heterogeneous DNAPL Distributions \_\_\_\_\_ 105

## **CHAPTER 4 – EQUILIBRIUM PARTITIONING AND INTERFACIAL ADSORPTION OF SELECTED ALCOHOLS IN SYSTEMS COMPRISING ALCOHOL, TCE-DNAPL AND WATER \_\_\_\_\_ 106**

**4.1 - Introduction \_\_\_\_\_ 106**

**4.2 - Results and Discussion \_\_\_\_\_ 107**

4.2.1 – Equilibrium Partitioning \_\_\_\_\_ 107

4.2.2 – UNIFAC Modeling \_\_\_\_\_ 113

4.2.3 - Fitting UNIFAC Parameters \_\_\_\_\_ 113

4.2.4 - Adsorption of the Selected Tracers at the TCE-DNAPL/Water Interface \_\_\_\_\_ 117

**4.3 - Conclusions \_\_\_\_\_ 120**

<b>CHAPTER 5 - PARTITIONING KINETICS OF TRACERS WITHIN TCE-DNAPL GANGLIA</b>	<b>122</b>
5.1 - Introduction	122
5.2 - Results and Discussion	123
5.2.1 – Nonequilibrium Mass Transfer Coefficients	123
5.2.2 - Slow flow mass transfer kinetics	131
5.3 - Conclusions	135
<b>CHAPTER 6 – PARTITIONING KINETICS ASSOCIATED WITH TCE-DNAPL POOLS</b>	<b>136</b>
6.1 - Introduction	136
6.2 – Experimental Design	137
6.2.1 Aquifer Cell Packing Structure and TCE-DNAPL Source Zone	137
6.2.2 – Tracer Test Design	142
6.3 – Results	144
6.3.1 Numerical Modeling of Effluent BTCs	150
6.3.2 Local Concentrations as Established from the Array of Sampling Ports	157
6.4 – Conclusions	192
<b>CHAPTER 7 – ASSESSMENT OF HETEROGENEOUS DNAPL ARCHITECTURE USING A PUSH-PULL TEST</b>	<b>194</b>
7.1 - Introduction	194
7.2 - Push-Pull Test Design	195
7.3 - Assessment of Low Pool Fraction Source Zone	197
7.4 - Assessment of Mid Pool Fraction Source Zone	210
7.5 - Assessment of High Pool Fraction Source Zone	221
7.6 – Pool Fraction Comparison	232
7.7 – Discussion	240
7.7.1 - Temporal Moments	240
7.7.2 - Equilibrium Push-Pull Model	245
7.7.3 – Comparison of Method of Moments and Analytical Solution for Interpretation of Push-pull Partitioning Tracer Tests	259
7.7.4 - Linear Driving Force Model	262
7.8 – Conclusions	281
<b>CHAPTER 8 – 2-D MODELING ASSESSMENT OF PUSH-PULL CAPABILITIES</b>	<b>283</b>
8.1 - Introduction	283
8.2 - Simulation Design	283
8.3 - Results	285
8.3.1 – Effect of Vertical Distribution on Push-Pull BTCs	285
8.3.2 – Effect of Horizontal Distribution on Push-Pull BTCs	291
8.4 - Discussion	296

8.4.1- <i>Development of Simplified Regressions</i>	296
8.4.2 – <i>Application of Simplified Regressions</i>	306
8.4.3 – <i>Estimation of Average Saturation</i>	316
8.5 <i>Conclusions</i>	319
<b>CHAPTER 9 – CONCLUSIONS AND RECOMMENDATIONS</b>	<b>321</b>
9.1 - <i>Conclusions</i>	321
9.2 – <i>Scientific and Engineering Contributions</i>	326
9.3 – <i>Recommendations</i>	327
<b>APPENDIX I</b>	<b>332</b>
<b>REFERENCES</b>	<b>344</b>

## List of Tables

<b>Table 1.1</b> Physical and Chemical properties of chlorinated ethenes.....	3
<b>Table 1.2</b> Principal advantages and disadvantages of integral pump tests, multi-level sampler, and passive flux meter.....	12
<b>Table 3.1</b> Physical properties of alcohol tracers and TCE.....	78
<b>Table 3.2</b> Locations of the local sampling ports shown in Figure 3.1.....	87
<b>Table 3.3</b> Locations of the local sampling ports shown in Figure 3.2.....	90
<b>Table 3.4</b> UNIFAC group interaction parameters ( $\alpha_{ij}$ ).....	94
<b>Table 4.1</b> Reported partition coefficients.....	112
<b>Table 4.2</b> Adjusted interaction parameters that visually allow the UNIFAC model to capture the 1-hexanol, water mutual solubility point.....	115
<b>Table 4.3</b> Isotherm parameters for tracers at a TCE-DNAPL-water interface...	119
<b>Table 5.1</b> Parameters related to column experiments and simulations.....	125
<b>Table 6.1</b> Relevant 2-D box parameters.....	140
<b>Table 6.2</b> Experimental Parameters for pooled TCE-NAPL in 2-D Box.....	143
<b>Table 6.3</b> Moment calculations for pooled box experiments.....	148
<b>Table 6.4</b> Sum of squared error between experimental effluent data and model predictions for each tracer in experiments 1-3.....	156
<b>Table 6.5</b> Sum of squared error between experimental data and model predictions at local sampling ports for experiment 1.....	162
<b>Table 6.6</b> Sum of squared error between experimental data and model predictions at local sampling ports for experiment 2.....	168
<b>Table 6.7</b> Sum of squared error between experimental data and model predictions at local sampling ports for experiment 3.....	176
<b>Table 6.8</b> Sum of squared error between 2-octanol experimental effluent data and model predictions shown in Figure 6.22.....	179
<b>Table 6.9</b> Sum of squared error of 2-octanol port data .....	185

<b>Table 7.1</b> Tracer test flow rates for mixed source zone experiments.....	195
<b>Table 7.2</b> Size and location of the 5 lenses and F-70 block .....	200
<b>Table 7.3</b> Low pool fraction box parameters.....	202
<b>Table 7.4</b> Size and location of the 5 lenses and F-70 block.....	212
<b>Table 7.5</b> Mid pool fraction box and corresponding tracer test parameters.....	214
<b>Table 7.6</b> Size and location of the 5 lenses and F-70.....	223
<b>Table 7.7</b> High pool fraction box and corresponding tracer test parameters.....	225
<b>Table 7.8</b> Method of moment estimations of overall TCE-DNAPL saturation and volume for the low pool fraction box.....	242
<b>Table 7.9</b> Method of moment estimations of overall TCE-DNAPL saturation and volume for the mid pool fraction box.....	243
<b>Table 7.10</b> Method of moment estimations of overall TCE-DNAPL saturation and volume for the high pool fraction box.....	244
<b>Table 7.11</b> Analytical solution estimations of dispersivity, overall TCE-DNAPL saturation and volume for the low pool fraction box.....	249
<b>Table 7.12</b> Analytical solution estimations of dispersivity, overall TCE-DNAPL saturation and volume for the mid pool fraction box.....	250
<b>Table 7.13</b> Analytical solution estimations of dispersivity, overall TCE-DNAPL saturation and volume for the high pool fraction box.....	251
<b>Table 7.14</b> Estimated average TCE-DNAPL saturation.....	256
<b>Table 7.15</b> Fitted dispersivities and squared residual from the least squares fitting of all nine push-pull bromide data sets.....	273
<b>Table 7.16</b> Sum of squared error between laboratory BTCs and 2-D linear driving force model predictions.....	274
<b>Table 8.1</b> Regression equations and corresponding $R^2$ values representing the dependence of the $C/C_0$ value of the second inflection.....	303
<b>Table 8.2</b> Estimated percent of the vertical domain containing TCE-DNAPL.....	312

## List of Figures

<b>Figure 1.1</b> Depiction of DNAPL release into the subsurface, modified from Keuper and Frind (1991).....	7
<b>Figure 1.2</b> Percent reduction in mass discharge due to Percent reduction in source zone mass.....	20
<b>Figure 1.3</b> Type one and Type two ternary phase diagrams.....	38
<b>Figure 1.4</b> A diagram of the conceptual model used by Liggieri et al. (1997) to discuss surface interactions.....	42
<b>Figure 1.5</b> The top picture (a) represents a more “real” system where the DNAPL is distributed in many regions of high saturation.....	48
<b>Figure 3.1</b> Sieve analysis for Ottawa Federal Fine.....	80
<b>Figure 3.2</b> Sieve analysis for F-70.....	80
<b>Figure 3.3</b> 2-D box setup used to conduct partitioning tracer experiments in Chapter 6.....	86
<b>Figure 3.4</b> 2-D box setup used to conduct push-pull experiments in heterogeneous source zones in Chapter 7.....	89
<b>Figure 4.1</b> Ternary phase diagrams at $22.0\pm 0.1^{\circ}\text{C}$ for 1-pentanol (a), 1-hexanol (b), and 2-octanol (c).....	108
<b>Figure 4.2</b> The distribution of 1-pentanol (a), 1-hexanol (b) and 2-octanol (c) between the DNAPL and aqueous phases.....	109
<b>Figure 4.3</b> Dilute regions for each 1-pentanol (a), 1-hexanol (b) and 2-octanol (c) partitioning between the DNAPL and aqueous phases.....	111
<b>Figure 4.4</b> The distribution of 1-pentanol (a), 1-hexanol (b) and 2-octanol (c) between the DNAPL and aqueous phases.....	116
<b>Figure 4.5</b> TCE-DNAPL-water interfacial tension at $22\pm 2^{\circ}\text{C}$ as a function of 1-pentanol (a), 1-hexanol (b), and 2-octanol (c) aqueous concentrations.....	118
<b>Figure 5.1</b> Breakthrough curves for bromide (a), 1-pentanol (b), 1-hexanol (c), and 2-octanol (d).....	124
<b>Figure 5.2</b> Breakthrough curves for bromide (a), 1-pentanol (b), 1-hexanol (c), and 2-octanol (d).....	129

<b>Figure 5.3</b> Breakthrough curve of 2-octanol for experiment conducted at 0.5 mL/min.....	133
<b>Figure 5.4</b> Limitation of the local equilibrium assumption for partitioning alcohols in zones of uniformly entrapped DNAPL.....	134
<b>Figure 6.1</b> Packing structure used to create the pooled source zone.....	139
<b>Figure 6.2</b> 2-D aquifer cell used to examine partitioning tracer transport in a pooled TCE-DNAPL source zone.....	141
<b>Figure 6.3</b> Effluent concentrations for 2-D box experiments 1 (panel a), 2 (panel b) and 3 (panel c).....	145
<b>Figure 6.4</b> Effluent concentrations for 2-D box experiments 1 (panel a), 2 (panel b) and 3 (panel c).....	146
<b>Figure 6.5</b> Concentration measurements shown on linear (a) and log (b) scales, taken from local the local port 2C.....	149
<b>Figure 6.6</b> Comparison of experiment 1 effluent data and model simulations using the Nambi and Powers (2003) mass transfer coefficient correlation.....	153
<b>Figure 6.7</b> Comparison of experiment 2 effluent data and model simulations using the Nambi and Powers (2003) mass transfer coefficient correlation.....	154
<b>Figure 6.8</b> Comparison of experiment 3 effluent and model simulations using the Nambi and Powers (2003) mass transfer coefficient correlation.....	155
<b>Figure 6.9</b> Comparison of column 1 port data from experiment 1 and model simulations using the Nambi and Powers (2003).....	158
<b>Figure 6.10</b> Comparison of column 2 port data from experiment 1 and model simulations using the Nambi and Powers (2003).....	159
<b>Figure 6.11</b> Comparison of column 3 port data from experiment 1 and model simulations using the Nambi and Powers (2003).....	160
<b>Figure 6.12</b> Comparison of column 4 port data from experiment 1 and model simulations using the Nambi and Powers (2003).....	161
<b>Figure 6.13</b> Comparison of column 1 port data from experiment 2 and model simulations using the Nambi and Powers (2003).....	164
<b>Figure 6.14</b> Comparison of column 2 port data from experiment 2 and model simulations using the Nambi and Powers (2003).....	165

<b>Figure 6.15</b> Comparison of column 3 port data from experiment 2 and model simulations using the Nambi and Powers (2003).....	166
<b>Figure 6.16</b> Comparison of column 4 port data from experiment 2 and model simulations using the Nambi and Powers (2003).....	167
<b>Figure 6.17</b> Flow field generated by the confined model immediately upon restarting flow after the flow interruption.....	170
<b>Figure 6.18</b> Comparison of column 1 port data from experiment 3 and model simulations using the Nambi and Powers (2003).....	172
<b>Figure 6.19</b> Comparison of column 2 port data from experiment 3 and model simulations using the Nambi and Powers (2003).....	173
<b>Figure 6.20</b> Comparison of column 3 port data from experiment 3 and model simulations using the Nambi and Powers (2003).....	174
<b>Figure 6.21</b> Comparison of column 4 port data from experiment 3 and model simulations using the Nambi and Powers (2003).....	175
<b>Figure 6.22</b> Results of mass transfer coefficient correlation sensitivity study for the experiment 1, 2-octanol effluent data set.....	178
<b>Figure 6.23</b> Results of mass transfer coefficient correlation sensitivity study for experiment 1, column 1, 2-octanol port samples.....	181
<b>Figure 6.24</b> Results of mass transfer coefficient correlation sensitivity study for experiment 1, column 2, 2-octanol port samples.....	182
<b>Figure 6.25</b> Results of mass transfer coefficient correlation sensitivity study for experiment 1, column 3, 2-octanol port samples.....	183
<b>Figure 6.26</b> Results of mass transfer coefficient correlation sensitivity study for experiment 1, column 3, 2-octanol port samples.....	184
<b>Figure 6.27</b> Results of mass transfer coefficient correlation sensitivity study for experiment 1, column 1, 2-octanol port samples.....	188
<b>Figure 6.28</b> Results of mass transfer coefficient correlation sensitivity study for experiment 1, column 2, 2-octanol port samples.....	189
<b>Figure 6.29</b> Results of mass transfer coefficient correlation sensitivity study for experiment 1, column 3, 2-octanol port samples.....	190

<b>Figure 6.30</b> Results of mass transfer coefficient correlation sensitivity study for experiment 1, column 2, 2-octanol port samples.....	191
<b>Figure 7.1</b> Packing structure of the low pool fraction box.....	199
<b>Figure 7.2</b> Low pool fraction TCE-DNAPL spill.....	201
<b>Figure 7.3</b> Low pool fraction fast-fast breakthrough curves.....	204
<b>Figure 7.4</b> Low pool fraction slow-fast breakthrough curves.....	205
<b>Figure 7.5</b> Low pool fraction fast-slow breakthrough curves.....	206
<b>Figure 7.6</b> Early time BTCs of low pool fraction bromide.....	208
<b>Figure 7.7</b> Comparison of low pool fraction bromide (a), 1-pentanol (b), 1-hexanol (c) and 2-octanol (d) BTC tails for each experiment.....	209
<b>Figure 7.8</b> Packing structure of the mid pool fraction box.....	211
<b>Figure 7.9</b> Mid pool fraction TCE-DNAPL spill.....	213
<b>Figure 7.10</b> Mid pool fraction fast-fast breakthrough curves.....	215
<b>Figure 7.11</b> Mid pool fraction slow-fast breakthrough curves.....	216
<b>Figure 7.12</b> Mid pool fraction fast-slow breakthrough curves.....	217
<b>Figure 7.13</b> Comparison of mid pool fraction bromide (a), 1-pentanol (b), 1-hexanol (c) and 2-octanol (d) BTCs for each experiment.....	219
<b>Figure 7.14</b> Comparison of mid pool fraction bromide (a), 1-pentanol (b), 1-hexanol (c) and 2-octanol (d) BTC tails for each experiment.....	220
<b>Figure 7.15</b> Packing structure of the high pool fraction box.....	222
<b>Figure 7.16</b> High pool fraction TCE-DNAPL spill.....	224
<b>Figure 7.17</b> High pool fraction fast-fast breakthrough curves.....	226
<b>Figure 7.18</b> High pool fraction slow-fast breakthrough curves.....	227
<b>Figure 7.19</b> High pool fraction fast-slow breakthrough curves.....	228
<b>Figure 7.20</b> Comparison of high pool fraction bromide (a), 1-pentanol (b), 1-hexanol (c) and 2-octanol (d) BTCs for each experiment.....	230

<b>Figure 7.21</b> Comparison of high pool fraction bromide (a), 1-pentanol (b), 1-hexanol (c) and 2-octanol (d) BTC tails for each experiment.....	231
<b>Figure 7.22</b> Comparison of fast-fast experiments across all three pool fractions. Figure includes bromide (a), 1-pentanol (b).....	233
<b>Figure 7.23</b> Comparison of fast-fast experiment tails across all three pool fractions. Figure includes bromide (a), 1-pentanol (b).....	234
<b>Figure 7.24</b> Comparison of slow-fast experiments across all three pool fractions. Figure includes bromide (a), 1-pentanol (b).....	235
<b>Figure 7.25</b> Comparison of fast-slow experiments across all three pool fractions. Figure includes bromide (a), 1-pentanol (b).....	236
<b>Figure 7.26</b> Comparison of slow-fast experiment tails across all three pool fractions. Figure includes bromide (a), 1-pentanol (b).....	237
<b>Figure 7.27</b> Comparison of fast-slow experiment tails across all three pool fractions. Figure includes bromide (a), 1-pentanol (b).....	238
<b>Figure 7.28</b> Equilibrium modeling of mid pool fraction fast-fast experiment. Displayed are bromide (a), 1-pentanol (b).....	247
<b>Figure 7.29</b> Equilibrium modeling of low pool fraction fast-fast experiment. Displayed are bromide (a), 1-pentanol (b).....	248
<b>Figure 7.30</b> Effect of increasing saturation on 2-octanol BTCs generated by the analytical solution.....	254
<b>Figure 7.31</b> 1-pentanol (panel a) and 1-hexanol (panel b) BTCs from the high pool fraction fast-slow test.....	257
<b>Figure 7.32</b> Bromide BTCs for the low pool fraction, fast-slow test (circles) and the high pool fraction, fast-fast test (triangles).....	261
<b>Figure 7.33</b> Comparison of linear driving force push-pull simulations to experimental data for the fast-fast test in the low pool fraction box.....	264
<b>Figure 7.34</b> Comparison of linear driving force push-pull simulations to experimental data for the slow-fast test in the low pool fraction box for.....	265
<b>Figure 7.35</b> Comparison of linear driving force push-pull simulations to experimental data for the fast-slow test in the low pool fraction box.....	266

<b>Figure 7.36</b> Comparison of linear driving force push-pull simulations to experimental data for the fast-fast test in the mid pool fraction box.....	267
<b>Figure 7.37</b> Comparison of linear driving force push-pull simulations to experimental data for the slow-fast test in the mid pool fraction box.....	268
<b>Figure 7.38</b> Comparison of linear driving force push-pull simulations to experimental data for the fast-slow test in the mid pool fraction box.....	269
<b>Figure 7.39</b> Comparison of linear driving force push-pull simulations to experimental data for the fast-fast test in the high pool fraction box.....	270
<b>Figure 7.40</b> Comparison of linear driving force push-pull simulations to experimental data for the slow-fast test in the high pool fraction box.....	271
<b>Figure 7.41</b> Comparison of linear driving force push-pull simulations to experimental data for the fast-slow test in the high pool fraction box.....	272
<b>Figure 7.42</b> Influence of simplifying assumptions inherent in the push-pull analytical solution.....	279
<b>Figure 7.43</b> Influence of simplifying assumptions inherent in the push-pull analytical solution.....	280
<b>Figure 8.1</b> Representations of the 40 source zones examined with the 2-D push-pull model.....	284
<b>Figure 8.2</b> 2-octanol BTCs resulting from push-pull tests conducted in realizations 24, 29, 30 and 31.....	286
<b>Figure 8.3</b> 2-octanol BTCs resulting from push-pull tests conducted in realizations 9, 10, 27, and 28.....	288
<b>Figure 8.4</b> 2-octanol BTCs resulting from push-pull tests conducted in realizations 3, 4, 5, and 6.....	290
<b>Figure 8.5</b> 2-octanol BTCs resulting from push-pull tests conducted in realizations 7, 8, and 21.....	292
<b>Figure 8.6</b> 2-octanol BTCs resulting from push-pull tests conducted in realizations 38, 39, and 40.....	294
<b>Figure 8.7</b> 2-octanol BTCs resulting from push-pull tests conducted in realizations 10 and 39.....	295
<b>Figure 8.8</b> Relationship between the $(V_{ext}/V_{inj})^*$ and $D_{front}$ .....	299

<b>Figure 8.9</b> Estimated vs. actual ( $V_{ext}/V_{inj}$ )* .....	299
<b>Figure 8.10</b> Relationship between %Z and the $C/C_0$ value of the first inflection point.....	301
<b>Figure 8.11</b> Predicted vs. actual $C/C_0$ value of second inflection point.....	304
<b>Figure 8.12</b> Estimations of TCE-DNAPL front using simulated (a) and measured (b) 2-octanol BTCs in the low pool fraction box.....	308
<b>Figure 8.13</b> Estimations of TCE-DNAPL front using simulated (a) and measured (b) 2-octanol BTCs in the mid pool fraction box.....	309
<b>Figure 8.14</b> Estimations of TCE-DNAPL front using simulated (a) and measured (b) 2-octanol BTCs in the high pool fraction box.....	310
<b>Figure 8.15</b> Source zone corresponding to the mid pool fraction.....	315
<b>Figure 8.16</b> 2-octanol BTC (triangles) from the mid pool fraction.....	318

## List of Symbols

$A$ – cross sectional area of 2-D aquifer cell [L <sup>2</sup> ]	$D_H$ – hydrodynamic dispersion coefficient [L <sup>2</sup> ·T <sup>-1</sup> ]
$A_{pool}$ – surface are of the pool [L <sup>2</sup> ]	$D_e$ – effective aqueous diffusion coefficient [L <sup>2</sup> ·T <sup>-1</sup> ]
$a_L$ – half saturation constant [M·L <sup>-3</sup> ]	$D_x$ – longitudinal dispersion coefficient [L <sup>2</sup> ·T <sup>-1</sup> ]
$\hat{a}$ - elliptical major semi-axis length [L]	$D_y$ – transverse dispersion coefficient [L <sup>2</sup> ·T <sup>-1</sup> ]
$\hat{b}$ - elliptical minor semi-axis length [L]	$D_z$ – vertical transverse dispersion coefficient [L <sup>2</sup> ·T <sup>-1</sup> ]
$b$ – radius of DNAPL droplet [L]	$f_i$ – fugacity of pure component i [-]
$C_{aq}$ – aqueous phase concentration [M·L <sup>-3</sup> ]	$\bar{f}_i$ - fugacity of component i in mixture [-]
$C_{aq}^{im}$ – immobile aqueous concentration [M·L <sup>-3</sup> ]	$f$ – fraction contaminated with NAPL [-]
$C_{aq}^m$ – mobile aqueous concentration [M·L <sup>-3</sup> ]	$F$ – fraction of tracer/NAPL interactions occurring at equilibrium [-]
$C_n$ – DNAPL phase concentration [M·L <sup>-3</sup> ]	$G^{ex}$ – excess Gibbs Energy [M·L <sup>2</sup> ·T <sup>-2</sup> ·Mol <sup>-1</sup> ]
$C_{int}$ – aqueous/DNAPL interfacial concentration [M·L <sup>-3</sup> ]	$h_1$ – hydraulic head on left-hand side of the 2-D box [L]
$C_s$ – aqueous solubility concentration [M·L <sup>-3</sup> ]	$h_2$ – hydraulic head on right-hand side of the 2-D box [L]
$d_M$ – medium grain diameter [L]	$H$ – packed height of 2-D box [L]
$d_{50}$ – median grain diameter [L]	$I_z$ – variation of NAPL mass about the center [M]
$D_{aq}$ – aqueous phase diffusion coefficient [L <sup>2</sup> ·T <sup>-1</sup> ]	$\hat{k}$ - lumped mass transfer coefficient [T <sup>-1</sup> ]
$D_{front}$ - distance between the injection/extraction well and the DNAPL front [L]	$k_f$ – mass transfer coefficient [L·T <sup>-1</sup> ]
$D_N$ – DNAPL phase diffusion coefficient [L <sup>2</sup> ·T <sup>-1</sup> ]	$k^*$ - local mass transfer coefficient [L·T <sup>-1</sup> ]
	$k_{rw}$ - relative permeability [L <sup>2</sup> ]

$K$ – hydraulic conductivity [ $L \cdot T^{-1}$ ]	$\underline{q}$ – darcy velocity [ $L \cdot T^{-1}$ ]
$K_p^{c_i}$ - concentration dependant tracer partition coefficient [ $L_{aq} \cdot L^{-1}_{DNAPL}$ ]	$\hat{q}_i$ – UNIQUAC surface area parameter for species i [-]
$L$ – characteristic length [L]	$\hat{r}_i$ – UNIQUAC/UNIFAC volume parameter for species i [-]
$L_{box}$ – length of the 2-D box [L]	$r_{pool}$ – radius of NAPL pool [L]
$l_x$ – length of NAPL pool in x direction [L]	$r_{spread}$ – spread of NAPL mass [-]
$l_y$ – length of NAPL pool in y direction [L]	$R$ – retardation factor [-]
$M$ – total NAPL mass of system [M]	$Re$ – Reynold’s Number [-]
$M_N$ – $N^{th}$ temporal moment [-]	$R_r$ - domain defined by the rectangular NAPL-water interfacial area [ $L^2$ ]
$M_n$ – $N^{th}$ temporal moment normalized by $0^{th}$ moment [-]	$R_e$ - domain defined by the elliptical NAPL-water interfacial area [ $L^2$ ]
$M_{ijk}$ – spatial moment [-]	$S$ – area of control plane [ $L^2$ ]
$\dot{m}$ - mass discharge [ $M \cdot T^{-1}$ ]	$S_{aq}$ – average aqueous phase saturation [-]
$n$ – porosity [-]	$S_n$ – average NAPL saturation [-]
$\underline{n}$ - vector normal to the control plane [-]	$\tilde{S}_n$ - point NAPL saturation [-]
$n_{vg}$ – Van Genuchten parameter [-]	$\hat{S}_n$ - trajectory average NAPL saturation along a streamtube [-]
$N_i$ – total number of moles [Mol]	$S_{n,c}$ – average NAPL saturation in contaminated domain [-]
$P_c^b$ - the capillary pressure at the base of the pool [ $M \cdot L^{-1} \cdot T^{-2}$ ]	$S_{nr}^{max}$ - maximum residual saturation [-]
$P_c^t$ - is the capillary pressure at the top of the pool [ $M \cdot L^{-1} \cdot T^{-2}$ ]	$S_s$ – specific storage [ $L^{-1}$ ]
$Pe$ – Peclet Number [-]	$Sh$ – Sherwood Number [-]
$Q$ – volumetric flow rate [ $L^3$ ]	$t$ – time [T]
$Q_k$ - UNIFAC surface parameter for functional group “k” [-]	$t_0$ – pulse injection time [T]
	$U_i$ – uniformity index [-]

$u_{mn}$  - measure of interaction energy between groups m and n  
[ $M \cdot L^2 \cdot T^{-2} \cdot mol^{-1}$ ]

$V_{ext}$  - extraction volume in push-pull test  
[ $L^3$ ]

$V_{inj}$  - injection volume in push-pull test  
[ $L^3$ ]

$(V_{ext}/V_{inj})^*$  - is the  $V_{ext}/V_{inj}$  value at which normalized concentration drops from 1.0 [-]

$x_i$  - mole fraction of component i [-]

$x_i^{aq}$  - mole fraction of component i in the aqueous phase [-]

$x_i^{aq,sol}$  - aqueous solubility mole fraction [-] of component i

$x_i^{NAPL}$  is the mole fraction of component i in the NAPL phase [-]

$x_{cm}$  - horizontal center of mass [-]

$\hat{x}$  - horizontal distance from center of mass [L]

%Z - percent of the vertical domain containing DNAPL [-]

$z$  - coordination number [-]

$\bar{z}$  - depth to center of mass [L]

$\alpha_L$  - longitudinal dispersivity [L]

$\alpha_T$  - transverse dispersivity [L]

$\alpha_V$  - vertical dispersivity [L]

$\alpha_{ij}$  - 2-D dispersivity for [L]

$\gamma$  - interfacial tension [ $M \cdot T^{-2}$ ]

$\hat{\gamma}_i$  - activity coefficient of component i [-]

$\gamma_m$  - mass transfer coefficient between the mobile and immobile domains [ $T^{-1}$ ]

$\Gamma$  - surface concentration [ $mol \cdot L^{-2}$ ]

$\Gamma_0$  - tracer equilibrium surface concentration [ $mol \cdot L^{-2}$ ]

$\Gamma_\infty$  - maximum tracer surface concentration [ $mol \cdot L^{-2}$ ]

$\Gamma_k$  - activity coefficient of group "k" in the mixture [-]

$\Gamma_k^{(i)}$  - residual contribution to the activity coefficient of group "k" in a pure fluid of species "i" molecules [-]

$\theta_n$  - volume fraction of DNAPL [-]

$\theta_{n,0}$  - initial volume fraction of DNAPL [-]

$\theta_{aq}$  - volume fraction of aqueous phase [-]

$\theta_a^m$  - volume of mobile aqueous phase by volume of the entire domain [-]

$\mu_{aq}$  - dynamic viscosity of the aqueous phase [ $M \cdot L^{-1} \cdot T^{-1}$ ]

$\phi$  - hydraulic head [L]

$\rho_b$  - soil bulk density [ $M \cdot L^{-3}$ ]

$\rho^n$  - NAPL density [ $M \cdot L^{-3}$ ]

$\tau_{ij}$  - UNIQUAC binary interaction parameter [-]

$\tau_{jk}$  - UNIQUAC binary interaction parameter [-]

$\tau_{ji}$  - UNIQUAC binary interaction parameter [-]

$v$  - pore water velocity [ $L \cdot T^{-1}$ ]

$\nu_k^{(i)}$  - the number of k groups present in species "i" [-]

$\phi_a^m$  - fraction of aqueous phase in the mobile domain [-]

$\hat{\phi}_i$  - volume fraction of species i [-]

$\omega$  - dimensionless mass transfer coefficient [-]

$\Omega$  - extent of domain [ $L^3$ ]

## EXECUTIVE SUMMARY

Sites across the United States, both privately and government owned are contaminated with solvents due to historical use in dry cleaning or degreasing operations. In 2003, the EPA estimated that anywhere from 15,000 to 25,000 sites in the United States are impacted by dense nonaqueous phase liquid (DNAPL) contamination (U.S. EPA, 2003). Additionally, though there have been significant advances in remediation technologies, there is disagreement as to whether these technologies are capable of remediating DNAPL sites within a reasonable time frame and at a reasonable cost (U.S. EPA, 2003). The physical and chemical properties of DNAPLs result in complex source zone architectures, which, due to low DNAPL solubility, can take decades or even centuries to dissolve. The use of Maximum Contaminant Levels (MCL) as the cleanup standard makes the remediation of DNAPL sites even more difficult, as this level of cleanup is an unrealistic expectation for many sites.

The difficulty of reaching site closure in the MCL framework has shifted focus toward understanding the relationship between DNAPL source zone architecture and downstream dissolved phase concentrations. This plume is often more hazardous than the source zone because of its mobility, making it the primary exposure pathway at most sites. Therefore, future remediation objectives may focus increasingly on reducing dissolved phase plume concentrations or plume mass discharge.

Since available treatments are unlikely to remove 100% of the source zone DNAPL mass, current focus is placed on understanding the benefits of partial

source zone cleanup. Available models can predict the effectiveness of partial source zone remediation using metrics that describe source zone architecture. However, currently no field methods exist for characterizing these metrics at specific sites. The work presented in this dissertation focuses on using push-pull partitioning tracer tests to characterize pool fraction, a metric that relates the amount of pooled DNAPL mass to the total DNAPL mass of a source zone.

Push-pull tracer tests are conducted by injecting a pulse of partitioning and non-partitioning tracers through a NAPL source zone, and then reversing the flow to pump the pulse back out of the same well. Tracers are selected that partition into the NAPL to different extents, and comparison of tracer breakthrough curves (BTCs) permits estimation of an overall NAPL saturation along the flow path of the tracer. To date, partitioning tracer tests have been used to determine overall NAPL saturation, but have not been used to estimate source zone architecture metrics.

The overall objective of this work is to explore the influence of nonlinear partitioning, non-equilibrium mass exchange and non-uniformity in DNAPL spatial distribution when employing alcohol tracer tests to characterize local-scale source zone architecture. The knowledge gained about these processes will then be used in an attempt to design a push-pull test for estimating pool fraction. To attain this overall objective, six specific objectives have been identified: 1) fully characterize, the liquid-liquid-equilibrium in a TCE-water system for three representative partitioning tracers (1-pentanol, 1-hexanol and 2-octanol); 2) assess ability of the UNIFAC thermodynamic model to predict the equilibrium behavior

of these systems; 3) determine the processes controlling partitioning tracer mass transport in systems comprising uniform saturations of entrapped TCE-DNAPL; 4) Characterize partitioning tracer transport in a 2-D domain containing a single, large TCE pool; 5) Examine the influence of injection and extraction flow rate during a push-pull tests conducted in heterogeneous source zones; 6) Explore the influence of DNAPL architectural features on push-pull test breakthrough curves.

Though linear partitioning is an assumption commonly employed to analyze partitioning tracer test results, the liquid-liquid-equilibrium studies conducted in this work demonstrate that equilibrium partitioning is nonlinear for all three alcohol tracers. Results however elucidate a range of dilute concentrations over which tracer partitioning may be approximated as linear. However, this linear range is different for all tracers and needs to be thoroughly understood before linear partitioning can be safely assumed.

UNIFAC is group contribution method that has been employed to estimate liquid-liquid equilibrium behavior in systems similar to the ternary systems examined herein; therefore the UNIFAC model was used to predict alcohol-water-TCE equilibrium behavior for each tracer. Results demonstrate that the thermodynamic model is able to predict the overall behavior. However, estimations of partition coefficients in the dilute range - range where the partitioning may be approximated as linear - are not accurate. Results of the thermodynamic modeling therefore suggest that these models may have utility when screening potential tracers, but experiment-based characterization is

necessary for accurate quantification of the partitioning behavior, particularly within the dilute/linear region where most tracers will be applied.

Upon complete characterization of the equilibrium system, efforts explored physical-chemical effects which may influence tracer transport in real systems. Here a series of 1-D column experiments were conducted to examine the dominant resistances to tracer mass transport in uniform saturations of TCE-DNAPL ganglia. Three resistances were interrogated using a numerical model appropriate to each resistance. The resistances were: resistance in an aqueous phase boundary layer surrounding the TCE-DNAPL droplet; resistance at the interface between the aqueous and DNAPL phases; resistance within the TCE-DNAPL droplet due to diffusion within the DNAPL. Comparison of model predictions and experimental BTCs demonstrates that diffusion through the hypothetical aqueous phase boundary layer controls the kinetics of tracer exchange between the aqueous phase and TCE-DNAPL. Additionally, tracer transport in these column experiments can be adequately described using a linear driving force model that incorporates an aqueous phase mass transfer coefficient correlation developed for NAPL ganglia dissolution.

Column experiments conducted herein represent one end member of source architecture - uniformly distributed TCE-DNAPL ganglia. The other end member is a source containing a single pool. Thus the kinetics of alcohol exchange between the aqueous phase and a single pool of TCE-DNAPL were examined in a series of 2-D aquifer cell experiments. Tracer BTCs were assessed at sampling ports within the domain and in the flux-averaged effluent. The intent

of these experiments was to test the ability of NAPL pool dissolution correlations to describe tracer transport in pool dominated systems. Results of these experiments determined that a linear driving force model using a mass transfer coefficient correlation developed for NAPL pool dissolution can predict both local scale and over all partitioning tracer transport.

The final laboratory experiments examined partitioning tracer transport in heterogeneous TCE-DNAPL source zones. Three push-pull tests were conducted in three source zones of low, mid and high pool fraction. Each of the three push-pull tests employed different flow rate combinations for both the injection and extraction. The purpose of these experiments was to determine if differences in transport time scales between pools and ganglia can be used to distinguish between pool dominated and ganglia dominated source zones. Results indicate that all three flow rate combination result in similar tracer BTCs; this implies that practitioners can use the economically advantageous fast flow rates in the field without loss of information. Additionally, while push-pull BTCs appear to be influenced by source zone architecture, they do not appear to be directly related to pool fraction. Modeling efforts determined that partitioning tracer transport in heterogeneous source zones can be predicted using a linear driving force model employing a mass transfer coefficient correlation developed from NAPL pool dissolution.

Lastly, the model developed to describe partitioning tracer transport in heterogeneous source zones was used to determine whether push-pull tests are able to distinguish between source zones of different vertical and horizontal

distributions. Push-pull tests were simulated in forty simplified source zones contrived to have distinct different vertical and/or horizontal distributions. Results indicate that push-pull tests may be able to distinguish differences in vertical DNAPL distribution. Additionally push-pull test BTCs may be useful for estimating the distance between the injection/extraction well and the DNAPL front. However, the tests appear to be unable to distinguish differences in horizontal DNAPL distribution.

The work presented in this dissertation has been able to characterize partitioning tracer behavior in a number of systems. LLE experiments were used to measure the non-linear partitioning behavior of three representative alcohol tracers, including linear partition coefficients and the concentration range for which these partition coefficients are valid. 1-D column experiments and 2-D box experiments were used to validate linear driving force models describing partitioning tracer transport in ganglia DNAPL, pooled DNAPL and heterogeneous DNAPL source zones. These models showed that mass transfer correlations developed from NAPL dissolution are useful for describing tracer transport through DNAPL source zones. Validation of these models allowed for the simulation of additional push-pull tests in source zones of different vertical and horizontal distributions. Simulations indicate that push-pull tests conducted in these simplified source zones are able to distinguish certain DNAPL architectural features and that further investigations is warranted in more complex systems.

# Assessment of Partitioning Tracers for Estimation of DNAPL Source Zone Architecture

## CHAPTER 1: BACKGROUND

### *1.1 Chlorinated Solvents*

#### *1.1.1- Chemical Properties*

Nonaqueous phase liquids (NAPLs) are hazardous organic liquids that are slightly soluble in water and form a visible separate phase in the subsurface (Mayer and Hassanizadeh, 2005). There are two categories of NAPLs, light (LNAPL) and dense (DNAPL). LNAPLs (e.g. gasoline, benzene and toluene) are less dense than the resident groundwater and therefore tend to reside near the water table; DNAPLs (e.g. chlorinated solvents such as PCE, TCE and TCA) are more dense than the resident groundwater and typically migrate downward through the saturated zone. A NAPL can be one pure chemical or can be a mixture of compounds with varying physical and chemical properties. The term NAPL refers to the phase comprising a contaminant or mixture of contaminants; the term is not interchangeable with the contaminant of concern.

Shown in Table 1 are some of the relevant physical and chemical properties of a set of chloroethenes - on group of chlorinated solvents. Of these TCE and PCE are common solvents used in dry cleaning operations in many industries. The solubility of these compounds is generally low (on the order of mg/L), which one key factor in why remediation of this TCE and PCE is difficult. Although these chlorinated ethenes have low solubilities, it should be recognized

that their solubilities are orders of magnitude higher than drinking water limits. TCE and PCE have solubilities of approximately 982 mg/L and 212 mg/L (at 20 °C) but both currently have an EPA maximum contaminant level of 5 ug/L. Note that in September of 2011, the EPA released its Final Health Assessment for TCE, characterizing it as a carcinogenic chemical due to its non-Hodgkin's Lymphoma and liver cancer risks. Consequently, if not remediated, NAPLs comprising chlorinated ethenes can exist in the subsurface for decades and contaminate large volumes of groundwater (Mayer and Hassanizadeh, 2005).

**Table 1.1.** Physical and Chemical properties of a selection of representative chlorinated ethenes.

Chlorinated Solvent	Abbreviation	Molecular Weight (g/mol)	Density (g/mL)	Dynamic Viscosity (cP)	Aqueous Solubility (wt%)	Water Solubility in Organic (wt%)
Perchloroethene	PCE	165.8	1.61 <sup>c,d</sup>	0.798 <sup>c,d</sup>	0.0212 <sup>a,e</sup>	0.0105 <sup>b,d</sup>
Trichloroethene	TCE	131.4	1.45 <sup>c,d</sup>	0.532 <sup>b,d</sup>	0.0984 <sup>a,e</sup>	0.032 <sup>b,d</sup>
1,1-Dichloroethene	1,1-DCE	97.0	1.17 <sup>b,d</sup>	0.358 <sup>a,d</sup>	0.255 <sup>a,e</sup>	0.035 <sup>b,d</sup>
cis-1,2-Dichloroethene	cis-DCE	97.0	1.28 <sup>a,f</sup>	0.411 <sup>a,g</sup>	0.667 <sup>a,e</sup>	0.055 <sup>b,e</sup>
trans-1,2-Dichloroethene	trans-DCE	97.0	1.26 <sup>a,f</sup>	0.411 <sup>a,g</sup>	0.472 <sup>a,e</sup>	0.055 <sup>b,e</sup>

<sup>a</sup>at 20 °C; <sup>b</sup>at 25 °C; <sup>c</sup>at 30 °C; <sup>d</sup>Riddick and Bunger (1970); <sup>e</sup>Horvath et al. (1999); <sup>f</sup>Morrison (2007); <sup>g</sup>NOAA (2012)

### *1.1.2 - Uses: Past and Present*

Chlorinated ethenes were extensively used in multiple industries. As a result of accidental spills, improper handling and improper disposal, these solvents are found in their DNAPL form at many industrial sites, waste disposal sites, and other locations of unknown use (Mayer and Hassanizadeh, 2005). All throughout the United States, sites both privately and government owned are contaminated with solvents previously used in dry cleaning or degreasing operations (Pankow and Cherry, 1996; EPA SCRD, 2001; Kavanaugh, 2003; NRC, 2005). Accurate characterization remains a substantial challenge to the effective remediation of DNAPL source zones (US EPA, 1993, 2004; NRC, 2005; Abriola et al., in press).

Chlorinated solvent production started in Germany in the 1800's and reached the United States around 1906. Their use in manufacturing became widespread during World War II and continued to increase for the next 30 years. Use of these solvents included, but was not limited to, electronics, instrument manufacturing, aerospace, dry cleaning, metal degreasing, photo processing, printing and paint removal. Because of their widespread use, chlorinated solvent disposal took many forms which resulted in both accidental and purposeful introduction into the subsurface from leaking tanks, leaking chemical distribution pipelines, spillage during transportation, landfill disposal, settling ponds, and storm drains (Pankow and Cherry, 1996).

Dry cleaning is one of the industries from which chlorinated solvent contamination is widespread. In urban areas and it has been estimated that 75%

of all dry cleaning facilities are contaminated (Schmidt et. al., 1999). Starting in the 1940's chlorinated solvents, primarily perchloroethene (PCE), became the predominant solvent used in dry cleaning operations (EPA SCRDR, 2001). Dry cleaning facilities routinely generate small quantities of hazardous waste. Before hazardous waste regulations were implemented, this waste was often disposed of in dumpsters or discharged into the sanitary sewer system via storm drains. Environmental legislation in the 1960s and 1970s led to the investigation of the hazards posed by drycleaner operations. The Resource Conservation and Recovery Act (RCRA) forced drycleaners to dispose of PCE as hazardous waste in the 1980s. However, in 1999, a State Coalition for the Remediation of Drycleaners (SCRDR) report currently estimates that of the approximately 22,300 active drycleaner facilities in the nation, 75% contain some level of contamination (Schmidt et al., 1999).

Due to environmental regulations and the development of alternate solvents, the use of solvents such as PCE and TCE has decreased over the past thirty years. For example, in 2006, the California Air Resources Board voted to phase out the use of PCE in drycleaning by 2023 (California EPA). However, these solvents are still used to some extent. According to the University of Massachusetts, Lowell, as of 2005 TCE is still being used in electronics connectors, metal working, adhesives, sealants, paints, textiles, and other industrial chemicals in Massachusetts. However, the use has decreased by 77% since 1990 (Toxics Use Reduction Institute, 2010).

### *1.1.3 - Infiltration and Entrapment*

In the subsurface, DNAPLs may exist as a separate liquid phase, dissolved in the groundwater, volatilized in the vapor phase of the vadose zone and/or associated with the porous media solid phase (Figure 1.1). Thus, there are many pathways for the contaminant to move through the subsurface.

Upon release, dense organic liquids generally migrate downward through the vadose zone, often reaching the groundwater table. The density and viscosity of the DNAPL will primarily determine if the compound moves directly downward, or spreads horizontally (Mayer and Hassanizadeh, 2005). If the DNAPL mass exceeds the displacement pressure at the water table, the DNAPL will penetrate into the groundwater and continue to move downward. As the DNAPL moves downward, capillary forces cause a trail of residual DNAPL to be left in its path (Pankow and Cherry, 1996). This downward migration will continue until the DNAPL is unable to overcome the capillary pressure; often this occurs on top of a layer lower permeability media. The capillary forces in the lower permeability media are higher than those in the surrounding media, which causes the DNAPL to spread out and pool on top of these layers. As the pool height increases, it may reach a point where the DNAPL pressure overcomes the capillary forces of the low permeability lens.

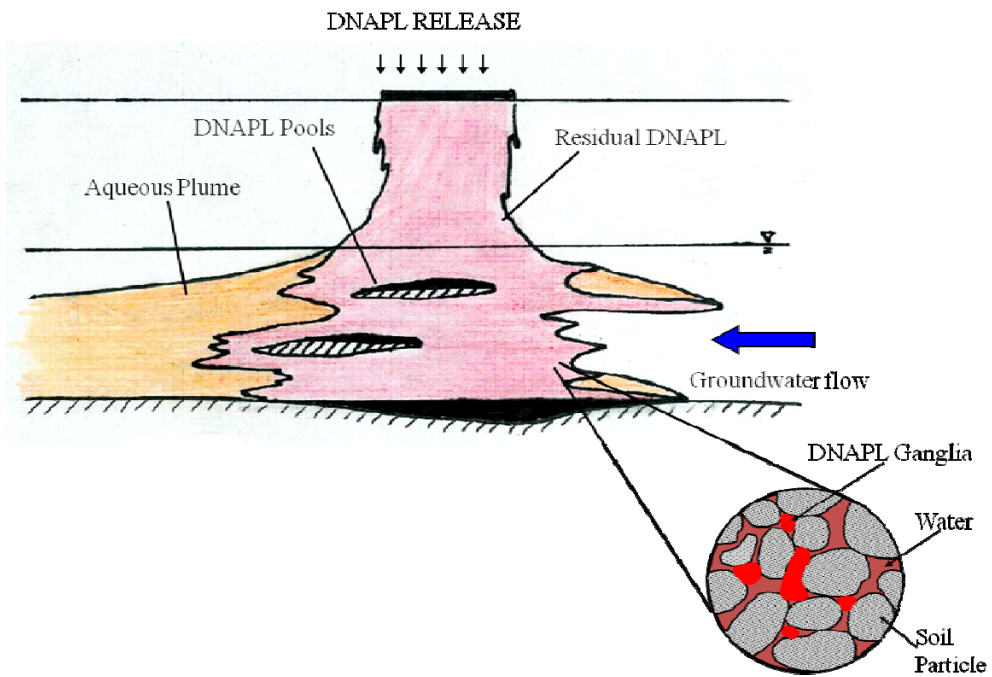


**Figure 1.1** Depiction of DNAPL release into the subsurface, modified from Keuper and Frind (1991).

The pool height at which this occurs can be estimated from a 1-D force balance:

$$H = \frac{P_c^b - P_c^t}{\Delta\rho g} \quad (1.1)$$

Here  $H$  is the pool height (L),  $P_c^b$  is the capillary pressure at the base of the pool ( $M \cdot L^{-1} \cdot T^{-2}$ ),  $P_c^t$  is the capillary pressure at the top of the pool ( $M \cdot L^{-1} \cdot T^{-2}$ ),  $\Delta\rho$  is the density difference between the DNAPL and water ( $M \cdot L^{-3}$ ), and  $g$  is the gravitational constant ( $L \cdot T^{-2}$ ) (Kueper et al., 1993). In addition to increasing pool height, the DNAPL may also spread to the edge of the low permeability lens, reach higher permeability media and continue its migration downward. This pattern will continue, often resulting in pools of DNAPL connected by “fingers” of residual saturation (Mayer and Hassanizadeh, 2005).

While the physical properties of the DNAPLs largely control their subsurface transport, the geology at the spill location also plays an important role. The subsurface in most locations is heterogeneous due to many factors such as the layering of lenses or the tightness of the media packing (Mayer and Hassanizadeh, 2005). A large amount of laboratory and field research has shown that the heterogeneity of the subsurface can impact DNAPL entrapment on a scale ranging from millimeters to meters (e.g. Poulsen and Kueper, 1992). The impact of this geological heterogeneity then is that one cannot integrate residual saturations over the whole volume to calculate the amount of DNAPL mass present (Mayer and Hassanizadeh, 2005).

## ***1.2 Influence of Source Zone Architecture on Contaminant Mass Flux***

The region that contains the DNAPL phase, including the solid phase that is associated with that DNAPL is termed the source zone. The spatial distribution of the DNAPL within the source zone (i.e. locations of low and high saturation zones) is referred to as the source zone architecture. As will be discussed in the following sections, this architecture has important implications on site cleanup.

As groundwater flows through the source zone, it slowly dissolves away components of the DNAPL and moves downstream, creating a plume of contamination. The groundwater plume is frequently the most hazardous aspect of a contamination event because it carries the contaminants from the source zone to possible receptors such as human water supply or sensitive environmental areas. Assessments of over thirty chlorinated solvent plumes at Superfund sites show that large plumes can be several kilometers long and contain anywhere from 0.5 to 70 drums of dissolved liquid solvent (Mackay and Cherry, 1989; Pankow and Cherry, 1996). One principal exposure pathway occurs when the plume reaches drinking water wells, often with dissolved concentrations well above the drinking water MCLs (e.g. Pankow and Cherry, 1996; U.S. EPA Clu-In, 2012). Another common exposure pathway is vapor intrusion (e.g. Little et al., 1992; U.S. EPA, 2002; Johnston and Gibson, 2011). Here, the groundwater migrates near or under a building and, because of contaminant volatility, vapors are emitted into the overlying buildings. The exposure pathway is then inhalation of the contaminant vapor. The plumes have also affected sensitive environmental areas

by discharging into surface water bodies, possibly exposing aquatic life (Pankow and Cherry, 1996; Lorah and Olsen, 1999; Conant et al., 2004).

Just as the source zone is made up of regions of varying saturation, the dissolved plume also has regions of high and low concentration. The variations in concentration are due to both the spatial distribution of the dissolving DNAPL phase and to non-uniform flow caused by heterogeneous porous media. This can be due to dilution effects, mass transfer limitations and/or mixed DNAPL effects (Mayer and Hassanizadeh, 2005). Reduction of dissolved concentrations below a certain level is a common remediation objective. However, the spatial variability of dissolved concentrations, potential of preferential flow paths and fluctuations in rate and direction of groundwater flow makes dissolved concentration a difficult metric to quantify (U.S. EPA, 2003). Therefore, it has been suggested that contaminant mass flux in the dissolved plume is a more appropriate measure for cleanup performance than total contaminant mass reduction or dissolved phase concentration (e.g. Rao et al., 2001; Rao and Jawitz, 2003).

There are multiple methods for measuring and defining mass flux, all of which involve measurement across a downstream plane. One common metric used to describe the amount of mass dissolving off a source zone is the source strength (Rao et al., 2002; US EPA, 2003; Stroo et al., 2003; IRTC, 2004; Falta et al., 2005; Goltz et al., 2007). The source strength is the mass discharge or the normalized mass discharge (normalized by cross sectional area of the plane of measurement) crossing a downstream transect and is useful for comparing

different sites. When calculated from measurements of dissolved phase concentration, mass discharge,  $\dot{m}$  [ $M \cdot T^{-1}$ ] is:

$$\dot{m} = \int \underline{q} C_{aq} \cdot \underline{n} dS \quad (1.2)$$

where  $\underline{q}$  is the Darcy velocity [ $L \cdot T^{-1}$ ],  $C_{aq}$  is the contaminant concentration [ $M \cdot L^{-3}$ ],  $\underline{n}$  is the vector normal to the plane and  $S$  is the area of a control plane [ $L^2$ ]. Normalizing the mass discharge by the cross sectional area of the control plane gives a spatially averaged mass flux. The size of this control plane over which the normalization is carried out is important. If the control plane is too large, the signal from an area of high flux may be greatly diluted by the large amount of low flux area surrounding it. This will cause the flux across the plane to appear to be low, and the hot spot will be missed. However, using too small of an averaging plane will require many measurements, which may be impractical.

A number of different techniques are used to measure the mass flux or mass discharge, including integral pump tests, multi-level samplers and passive flux meters (Borden et al., 1997; Schwartz et al., 1998; King et al., 1999; Bockelman et al., 2001; Einarson and Mackay, 2001; Hatfield et al., 2002, 2004; Annable et al., 2005). All of these methods incur uncertainty due to interpolation between sample points and averaging of sample points. Though water velocity varies spatially in many locations, it is frequently assumed to be uniform throughout a transect and the contaminant concentration is usually the only variable that is interpolated (Semprini et al., 1995; Borden et al., 1997; King et al., 1999; Kao and Wang, 2001). Table 1.2 provides a brief summary of these techniques, while further details are provided below.

**Table 1.2** Principal advantages and disadvantages of integral pump tests, multi-level sampler, and passive flux meter.

<b>Measurement Technique</b>	<b>Principal Advantages</b>	<b>Principal Disadvantages</b>
Integral Pump Test	<ul style="list-style-type: none"> <li>- Provides a direct measure of contaminant discharge</li> <li>- Allows for an overall estimate of concentrations that are not as strongly influenced by areas of high concentration</li> </ul>	<ul style="list-style-type: none"> <li>- The need for signal inversion may result in non-unique estimates of flux</li> <li>- Alters the flow field, which may results in inaccurate estimations of flux under natural gradient conditions</li> <li>- Produces large quantities of contaminated water</li> </ul>
Multi-Level Sampler	<ul style="list-style-type: none"> <li>- Provides a direct measure of concentration in spatially discrete intervals</li> <li>- Can be nested in plume transects for long term sampling</li> </ul>	<ul style="list-style-type: none"> <li>- Needs to be combined with flow field information to estimate mass flux</li> <li>- A sampling density of 6-7% of the transect area is necessary to produce an accurate estimate of the spatial distribution of the concentration</li> </ul>
Passive Flux Meter	<ul style="list-style-type: none"> <li>- Provides a direct measure of total mass and total flow to which the meter has been exposed over a given period of time</li> <li>- Can provide effective pre- and post- treatment assessments when sampling duration is kept constant</li> </ul>	<ul style="list-style-type: none"> <li>- A sampling density of 6-7% of the transect area is necessary to produce and accurate estimate of the spatial distribution of concentration</li> <li>- Measurements are temporal averages</li> <li>- Longer deployments maybe influenced by microbial growth.</li> </ul>

### *1.2.1 - Integral Pump Test*

Integral pump tests are conducted with one or more fully screened pumping wells that cross a plane in a plume. The wells are pumped at a constant rate for a short period of time while the change in contaminant concentration over is recorded. Mass discharge is then calculated from the contaminant concentrations and the pumping rate. This method allows the simultaneous quantification of contaminant mass fluxes and average contaminant concentrations at control planes (Bockelman et al., 2001). However, the estimate of mass flux requires the changing concentration signals be inverted with numerical or analytical solutions (Schwartz et al., 1998; Bayer-Raich et al., 2003a, 2003b and 2004). Results of these inversions are not always unique, meaning that, often, a set of possible mass flux spatial distributions in the plume is produced (Bauer et al., 2004). The integral pump test also allows for the determination of contaminant mass flux that is spatially averaged across the cross sectional area of the plume. Large amounts of water are removed from the subsurface and analyzed for contaminant concentrations. Therefore, that average mass flux calculations from integral pump tests are not dominated by one area with a large concentration signal (Jarsjo et al., 2005). However, it is expensive to treat the large amount water produced by the integral pump test.

### *1.2.2 - Multi-Level Sampler*

Multi-level samplers are another method that is used to estimate contaminant mass flux (Borden et al., 1997; King et al., 1999; Einarson and Mackay, 2001; Kavanaugh et al., 2011). These samplers tend to be smaller-scale

than integral pump tests and are nested in a plume transect for long term sampling. They give discrete spatial measurements of concentration. The concentration measurements can then be multiplied by flow measurements, usually spatially averaged flow, to estimate mass flux at specific locations. The flux estimates at each point are interpolated and integrated over the transect to estimate mass discharge and spatially-averaged mass flux. Results are highly dependent on the spatial scale, especially the vertical scale, of sampling (Guilbeault et al., 2005). Li et al. (2007) developed a method for estimating mass flux and quantifying the uncertainty in the measurements. They found that in control planes with disconnected hot spots, a minimum sampling density of 6-7% (using regular sampling patterns) is necessary to have an accurate model of uncertainty. Most sampling densities range between 1 and 4 % (Li et al., 2007). This is because high sampling density is often expensive due to installation and monitoring costs. Li and Abriola (2009) developed an algorithm to predict the best multi-level sampling locations and the minimum sample density necessary to predict mass discharge and uncertainty. This algorithm was numerically tested and produced a 50% reduction in necessary sampling density compared to regular sampling patterns (Li and Abriola, 2009). In a recent study at Ft. Lewis, Washington, multi-level samplers were used to help design a bioremediation strategy by giving information about the presence of vertical gradients and preferential flow paths. During bioremediation multi-level samplers provided critical information on the distribution of amendments, redox parameters and biological activity indicators (Kavanaugh et al., 2011).

### *1.2.3 - Passive Flux Meter*

The passive flux meter method employs a novel device within existing boreholes to estimate mass flux (Hatfield et al., 2002, 2004; Annable et al., 2005). These differ from the integral pump test and multi-level samplers in that they give a more direct measurement of smaller scale, time averaged mass flux. A passive flux meter consists of a sorbent, permeable medium that is emplaced in either a borehole or a sampling well. As contaminated water flows through the medium, tracers are released from the flux meter and the contaminant compounds sorb to the meter. After a certain period of time, the meter is removed from the subsurface. The average flow rate is calculated from the amount of tracer lost, and the contaminant mass flux from the amount of contamination adsorbed (Annable et al., 2005). This method of measuring flux gives a time-averaged mass flux at specific vertical and horizontal locations. To obtain a spatially averaged mass flux, there must be interpolation and integration between points. Again, a nonuniform flow field may make these estimates somewhat inaccurate. The advantage over multilevel samplers is that the passive flux meters also measure volumetric flow at the point of concentration measurements. This allows the flow at each measurement point to be known without needing to estimate the spatial variability of permeability and hydraulic conductivity. The passive flux meters installed at Ft. Lewis were able to capture the highly variable groundwater velocities, which allowed for better predictions of mass flux than technologies that used that assumed constant groundwater velocities (Kavanaugh et al., 2011). As with the multi-level sampler, Li et al. (2007) determined that a minimum

sampling density of 6-7% is necessary to have an accurate estimation of uncertainty. Brooks et al. (2008) compared the flux meter and the integral pump test, and determined that both methods had similar performance. The passive flux meter gave flux measurements as a function of depth, but covered a small horizontal distance. On the other hand, the integral pump test was able to cover a much larger volume, but did not give discrete measurements. Overall, Brooks et al. (2008) concluded that both methods provide critical site characterization data.

#### *1.2.4 - Flow Bypassing*

The geological heterogeneity of the subsurface, at both the pore scale and the macro-scale (layering and soil texture contrasts), cause preferential flow paths to exist (Schwille, 1988; Illangasakare et al., 1995; Kueper and Frind, 1991). When DNAPL is distributed as homogeneous ganglia, the large amount of contact between the DNAPL and the groundwater allows for more dissolution, and consequently, dissolved concentrations coming off these areas are often near aqueous solubility. Contrastingly, DNAPL pooled on top of lower permeability zones has less surface area contact with the flowing groundwater, and therefore, less dissolution (Johnson and Pankow, 1992). Some water will flow through the lower permeability region (due to both porous media type and DNAPL presence), but most of it will flow through areas of higher permeability, bypassing the lower permeability zone. This is why “older” source zones tend to be dominated by pooled DNAPL and low dissolved concentration signals with small areas of high concentration hot spots that correspond to these pool locations.

### *1.2.5 - Partial Mass Removal*

Because no one technology can remove 100% of the DNAPL mass, focus has shifted to evaluating synergies among remediation technologies and the benefits of partial DNAPL mass removal (Saenton and Illangasakare, 2007; Stroo et al., 2003; Christ et al., 2005). Potential benefits of removing a fraction of DNAPL mass in the source zone include decreasing risk by reducing dissolved concentrations reaching receptors, reducing the mobility of the DNAPL itself, shortening source lifetime, and enhancing natural attenuation (Sale and McWorter, 2001; Rao et al., 2002). Stroo et al. (2003) discuss the influence of source zone architecture on the reduction of down gradient mass flux. When the DNAPL is primarily distributed homogeneously, it may be necessary to remove up to 95% of the mass to start to see any reduction in dissolved concentrations. On the other hand, if the DNAPL is distributed heterogeneously with most of the mass in high permeability areas, much less mass needs to be removed to see a benefit in dissolved mass flux.

Even combining remediation strategies, no treatment has yet been found that can provide complete contaminant removal. Holzmer et al. (2000) treated a TCE-DNAPL source zone with surfactant flushing at Camp Lejeune, NC and found that up to 10% of the mass still remained in the low permeability layers. Jawitz et al. (2000) used co-solvent flushing at a PCE-DNAPL site in Jacksonville, FL, removing 35-38% of the DNAPL mass. Even though the amount of DNAPL mass removed was not large, dissolved phase contaminant concentrations were reduced by 92%. A number of remediation technologies

were employed at the Ft. Lewis Site in Washington State. In one location, Electrical Resistive Heating was able to achieve an 87% reduction in dissolved TCE concentrations (Beyke and Flemming, 2005). At two other locations on the Ft. Lewis Site, bioremediation was implemented. After two bioaugmentation injections in each location, total contaminant mass reduction was estimated as 26-49% in one location and 10-78% in the other (Kavanaugh et al., 2011). Typically however, achieving greater than a 2-log reduction in dissolved phase concentrations is needed to reach drinking water standards. Thus, a number of researchers agree that reducing plume concentrations below drinking water standards is unlikely (Sale and McWhorter, 2001; Soga et al., 2004; McGuire et al., 2006).

Since no current technology, or combination of technologies, can remove all of the DNAPL mass from the subsurface, it is necessary to quantify the benefits of partial mass removal (Stroo et al., 2003; Abriola, 2005; Christ et al., 2006). Stroo et al., (2003) demonstrate, using the chart shown in Figure 1.2, that mass removal typically removes the mass in high permeability areas. If the source zone is highly heterogeneous with most of the DNAPL in high permeability areas (upper left) a 75% reduction in source zone mass can decrease downgradient mass flux by about 90%; however, if the source zone is mostly homogeneous (lower right), a 75% reduction in source zone mass has hardly any impact on downgradient mass flux. Generally, most real sites have a more linear relationship (middle, red line in Figure 1.2) between mass flux reduction and source zone mass reduction than the two extremes presented in Figure 1.2 (Stroo

et al., 2003; Jawitz et al., 2005). However, it is still important to understand the site specific source zone architecture in order to evaluate the benefit of removing source zone mass.

What is not represented in Figure 1.2 is the time required for a given percent mass removal. Consider for example the case of the homogeneous source (green line in the lower right of Figure 1.2). This line may represent a uniform saturation of ganglia or a uniform distribution of pools having similar size, which would clean up much faster than the pooled source (blue line in the upper left of Figure 1.2) (Jawitz et al., 2005). Jawitz et al. (2005) concluded that as the heterogeneity in aquifer properties increases, less mass reduction is necessary to achieve a certain level of flux reduction; however, overall source longevity increases.

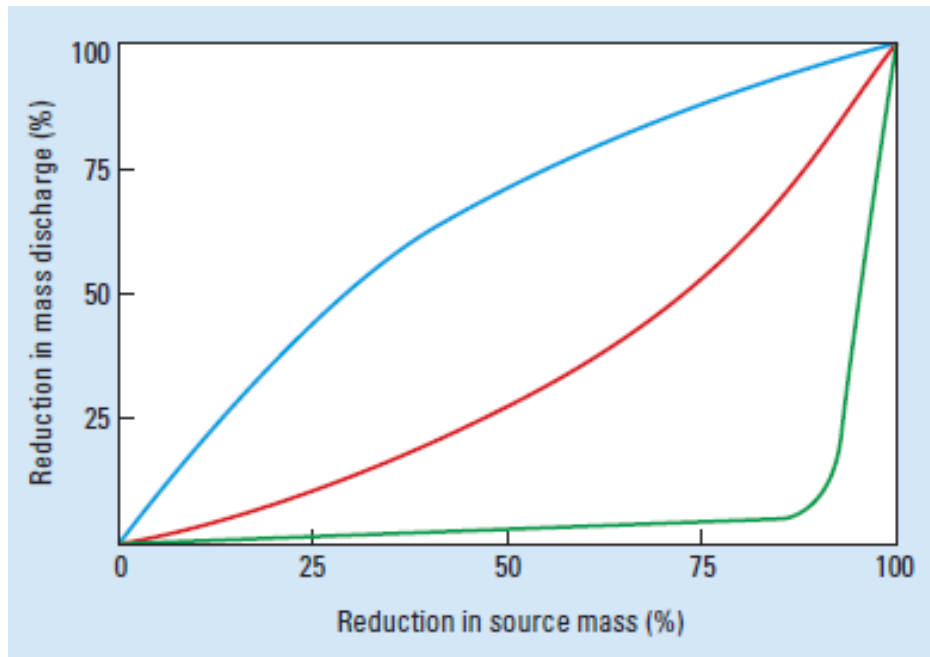


**Figure 1.2** Percent reduction in mass discharge due to Percent reduction in source zone mass for three different scenarios: a theoretical relationship in a highly heterogeneous aquifer with most of the DNAPL located in the higher permeability zones (upper left, blue); a theoretical relationship in a homogeneous aquifer (lower right, green); a field demonstration at Dover Air Force Base in Dover, Del. (middle, red). Figure taken from Stroo et al., 2003.

### *1.3 Source Zone Architecture Metrics*

Lemke et al. (2004b) state that the ability to predict risk reduction, when defined as reduction of dissolved contaminant concentrations or as reduction of contaminant mass flux across a downgradient plane, depends on the initial and evolving configurations of pools and entrapped DNAPL in the source zones. For aggressive source zone treatments to be effective, some knowledge of the amount and distribution of the DNAPL in the source zone is necessary (Christ et al. 2005). To characterize the exact architecture of a source zone requires an unreasonably high density of sampling points, which is difficult and expensive to carry out. In lieu of attempting to determine the exact spatial distribution, many research teams are considering metrics to describe important aspects of the source zone architecture. The most common metrics being considered are: temporal moments, spatial moments, reactive travel times and ganglia-to-pool ratio. The idea here is these metrics may be evaluated with less sampling than would otherwise be need to assess the spatial distribution of the DNAPL. However, it should be recognized that use of the source zone architecture metrics represents a compromise between the value of the information and the cost of obtaining the information.

#### *1.3.1 - Temporal Moments*

Temporal moments have been used by multiple researchers as a metric for describing source zone architecture (e.g. Jin et al., 1995; Saripalli et al., 1997; Annable et al. 1998b; Jawitz et al., 2003). This metric uses the moments of partitioning and nonpartitioning tracer breakthrough curves collected from

multiple extraction wells to describe the amount of mass in the source zone. The  $N^{\text{th}}$  temporal moment is calculated as

$$M_N = \int_0^{\infty} t^N C_{aq}(t) dt \quad (1.3)$$

where  $C_{aq}(t)$  is the concentration distribution over time or the breakthrough curve. Normalized moments,  $M_n$  are the  $N^{\text{th}}$  absolute moment normalized by the zeroth moment. By comparing the first normalized moments of the partitioning and nonpartitioning tracer, the retardation factor,  $R$ , can be calculated as

$$R = \frac{M_1^p - \frac{t_0}{2}}{M_1^{np} - \frac{t_0}{2}} \quad (1.4)$$

where  $t_0$  (pulse injection time) is used to correct each moment. This retardation value can then be used in the method of Jin et al. (1995) to calculate the average DNAPL saturation in the system.

Jawtisz et al. (2003) use an extended method of temporal moments (e.g. Valocchi, 1985) of partitioning tracers to characterize spatial distribution of DNAPLs using only one well location. This model uses an equilibrium stream tube approach where the subsurface is divided into two domains, one without DNAPL and one with a homogeneous NAPL saturation or a distribution of saturations described by the fraction  $f$ . This allows for the calculation of four spatial descriptions of DNAPL saturation: 1) Point saturation,  $\tilde{S}_n$ ; 2) Average saturation of the whole spatial domain,  $S_n$ ; 3) Average saturation for the contaminated fraction of the domain,  $S_{n,c} = S_n / f$ ; 4) Trajectory-averaged

saturation along a stream tube,  $\hat{S}_n$ .  $S_n$  can be estimated with the first temporal moment of partitioning tracer data (e.g., Jin et al., 1995). The homogeneous binary model can extend partitioning tracer analysis to second moments, which allows for the calculation of  $S_n$  and  $f$  (Jawitz et al., 1998). The addition of the third temporal moment allows for the calculation of the mean and variance of the trajectory-averaged stream tube saturation.

### 1.3.2 - Spatial Moments

Spatial moments can be employed to quantify the amount of DNAPL in a volume of subsurface when a high frequency sampling of an array containing a high density of spatially discrete samples can be obtained (e.g. Dekker and Abriola, 2000; Lemke et al. 2004a; Saenton and Illangasekare, 2007). A spatial moment  $M_{ijk}$  as defined by Kueper and Frind (1991a) and Essad and Hess (1993) is

$$M_{ijk} = \int_{-\infty}^{\infty} \int_{-\infty}^{\infty} \int_{-\infty}^{\infty} n \rho^n s_n(x, y, z) x^i y^j z^k dx dy dz \quad (1.5)$$

where  $n$  is the porosity,  $\rho^n$  is the DNAPL density [ $M \cdot L^{-3}$ ],  $x, y$ , and  $z$  represent the Cartesian coordinates and  $i, j$  and  $k$  are the respective moment orders. The horizontal center of mass is calculated

$$x_{cm} = \frac{1}{M} \int_{\Omega} x dm \quad (1.6)$$

where  $M$  is the total mass of the system,  $\Omega$  is the extent of the domain [ $L^3$ ],  $x$  is the horizontal coordinate [-] and  $dm$  is the increment of mass in the domain [-].

The variation of the mass about the center of mass is given by the second moment around the z-axis

$$I_z = \int_{\Omega} \hat{x}^2 dm \quad (1.7)$$

where  $\hat{x}$  is the distance from the horizontal center of mass [L]. The spread of the DNAPL mass is then calculated as

$$r_{spread} = \sqrt{\frac{I_z}{M}} \quad (1.8)$$

The depth of the center of mass is also important and is calculated as the first moment about the x-axis,

$$\bar{z} = \frac{1}{M} \int_{\Omega} z dm \quad (1.9)$$

The estimation of spatial moments in the field is difficult because it requires many sample points and has therefore rarely been used in field situations (Jawitz et al., 1998, 2000).

### *1.3.3 - Reactive Travel Times*

Jawitz et al. (2005) further expanded upon the concept of temporal moments to introduce the reactive travel time metric. As in Jawitz et al. (2003), the field is divided into a Lagrangian framework of non-interacting, stream tubes. Each stream tube may contain a different amount of DNAPL, which results in a spatial distribution of DNAPL saturations. Each stream tube is characterized by a single travel time which results as a combination of the flow field and the DNAPL saturation in each stream tube. The aquifer flow heterogeneities are then

characterized by a distribution of nonreactive travel times and the DNAPL spatial distribution heterogeneity is described by a distribution of reactive travel times. With this approach, the nonreactive and reactive travel times are calculated from nonreactive and reactive tracer tests, respectively (Jawitz et al., 2005). As in Jawitz et al. (2003) the reactive tracer partitioning is assumed to occur at equilibrium.

#### 1.3.4 - Ganglia-to-Pool Ratio

The ganglia-to-pool ratio (GTP) is a ratio of the amount of DNAPL mass in the source zone that is distributed as ganglia to that distributed as pools (Christ et al. 2005). The idea behind this metric is that ganglia and pools have different dissolution behavior and time scales of dissolution (Lemke et al., 2004b). Therefore the contaminant mass flux downgradient of the source zone will evolve differently as the source zone mass dissolves depending on the amount of ganglia and of pools in the source zone (Lemke et al., 2004b; Lemke and Abriola, 2006). The mathematical description of GTP is:

$$GTP = \frac{\sum \rho_n S_n \phi \Delta x \Delta y \Delta z \forall S_n < S_{nr}^{\max}}{\sum \rho_n S_n \phi \Delta x \Delta y \Delta z \forall S_n \geq S_{nr}^{\max}} \quad (1.10)$$

Here, pools are defined as regions of the source zone where the DNAPL saturation is above the maximum residual DNAPL saturation  $S_{nr}^{\max}$  [-], often chosen to be 15% (Lemke et al., 2004b). The maximum residual saturation depends on both the DNAPL and the medium (Parker and Lenhard, 1987).

### 1.3.5 - Pool Fraction

Pool fraction (PF) is similar to GTP in that it describes the source zone as a distribution of pools and ganglia. However, since pool fraction is normalized by total DNAPL mass, it is bounded between 0 and 1. In contrast, GTP is unbounded. For example, as the amount of ganglia increases and the amount of pooled DNAPL decreases (as is seen at the end of the life of any DNAPL source zone), GTP goes to infinity. PF in this case goes to zero. Pool fraction is defined as the amount of DNAPL mass distributed as pools, normalized by the total DNAPL mass. Mathematically, pool fraction is:

$$PF = \frac{\sum \rho_n S_n \phi \Delta x \Delta y \Delta z \forall S_n \geq S_{nr}^{\max}}{\sum \rho_n S_n \phi \Delta x \Delta y \Delta z \forall S_n} \quad (1.11)$$

### 1.4 Source Zone Characterization

To incorporate any of the source zone architecture metrics discussed above into a model to predict downstream mass flux, they need to be estimated at the sight of interest. DNAPL source zone mass is most commonly assessed by either taking soil cores at discrete locations and interpolating values between these measurements or by using partitioning tracer tests to get an estimation of overall source zone saturation. The advantages and drawbacks to each of these methods are discussed below.

#### *1.4.1 - Soil Coring*

The most common method used to assess DNAPL architecture in the source zone is soil coring (Meinardus et al., 2002). However, this method is expensive and only interrogates a set of small volumes. Many properties used to describe subsurface hydrology (e.g. hydraulic conductivity) have correlation lengths on the order of ten meters in the aerial extent and one meter or less in the vertical (DeGroot, 1996). DNAPL architecture is controlled by even smaller scale heterogeneities and depends heavily on release volume, rate and location (Kueper et al., 1993; Dekker and Abriola, 2000). Mass discharge resulting from nonlinear DNAPL distributions has been found to vary by orders of magnitude over a vertical spacing of only 15-30 cm (Guilbeault et al., 2005). Therefore, the number of soil cores necessary to characterize the precise distribution of DNAPL saturations within a source zone may be unreasonable (eg. Rao et al., 1997; Jawitz et al., 1998 (ES&T), 2000; Meinardus et al., 2002).

#### *1.4.2 - Partitioning Interwell Tracer Test*

Partitioning interwell tracer tests (PITTs) offer an alternative to soil coring (Jin et al., 1995; Annable et al., 1998a, 1998b). PITTs are conducted by passing a pulse of partitioning and non-partitioning tracers through a DNAPL source zone. Tracers are mixed with water and injected as a pulse into the ground through extraction wells. Once the pulse has been injected, clean water is pumped into the injection wells. The tracers flow through the contaminated zone and are pumped out of the extraction wells. Tracer concentration measurements over time are measured from the extracted water to create breakthrough curves (BTC).

Multiple hydraulic patterns can be used to conduct a PITT such as the line drive flow pattern (e.g. Annable et al., 1998b) and the five-spot pattern (Brooks et al., 2002). The tracers are chemicals that can be added to water and used to trace the flow path of the water without changing its physical properties (Jin et al., 1995). Non-partitioning tracers do not interact with the NAPL phase, while partitioning tracers interact with the NAPL, causing the partitioning pulse to lag behind the non-partitioning pulse. Partitioning tracers are selected that partition into the NAPL to different extents, and the comparison of tracer BTCs (e.g. partitioning and non-partitioning) permits estimation of an overall NAPL saturation along the flow path of the tracer. The overall NAPL saturation is estimated as:

$$S_n = \frac{M_1^p - M_1^{np}}{(K_p^{C_i} - 1)M_1^{np} + M_1^p} \quad (1.12)$$

where  $M_1^p$  and  $M_1^{np}$  are the first moments of the partitioning and non-partitioning tracer, respectively, and  $K_p^{C_i}$  is the concentration dependant partition coefficient [ $L_{aq}^3 \cdot L_{NAPL}^{-3}$ ] of the partitioning tracer (Jin et al., 1995). The assumptions implicit in the PITT method include: the tracer partition coefficient is independent of tracer concentration; local equilibrium partitioning of the tracer exists between the two phases; all of the NAPL is hydraulically accessible to the tracers; tracer interaction with the porous media is insignificant compared to NAPL/tracer interactions; tracer lost due to biodegradation or volatilization in the time frame of the PITT is insignificant.

The PITT has been used in the field to quantify the amount of NAPL in source zones (Annable et. al., 1998a; Annable et. al., 1998b; Jawitz et. al., 1998;

Rao et. al., 2000; Londergan et. al., 2001; Brooks et. al., 2002; Meindardus et. al., 2002; Ramsburg et. al., 2005). In one field test PITT results estimated an overall NAPL saturation between 4.6% and 5.4% while soil coring gave a saturation of 6.7% (Annable et. al., 1998a; Annable et. al., 1998b). The variation in PITT estimation occurs because a saturation estimate is made at each extraction well. Since the NAPL is not homogeneous throughout the swept zone, different saturations are calculated from tracers that take different flow paths. This information can be used to gain a qualitative understanding of which portion of the swept zone may have more contaminant, characterized by later tracer arrival times and more tracer tailing. Brooks et al. (2002) discuss that in addition to multiple extraction well locations, multiple tracers can give different estimates of NAPL saturation. For example, in their field test, 2-octanol gave an estimate of 22 L of NAPL while n-hexanol gave an estimate of 71 L.

Additionally, PITTs may also underestimate NAPL saturations from 30-60% when the NAPL is distributed as both ganglia and pools (Rao et al., 2000). One reason this occurs is that the tracers may not interact with all of the NAPL mass due to flow bypassing (Rao et al., 2000; Moreno-Babero and Illangasekare, 2006). When tracers are unable to access all of the NAPL phase, they will not be retarded to the same extent as they would if complete interaction occurred. This reduction in retardation results in the tracer tests determining that less NAPL is present than actually is. Additionally, underestimation of NAPL saturation may be due to nonequilibrium interactions of the tracer and the NAPL (Jin et al., 1997; Rao et al., 2000; Dai et al., 2001). When nonequilibrium mass transfer occurs,

there is resistance to tracer partitioning in the NAPL phase. This leads to less tracer mass partitioning into the NAPL phase than would occur under equilibrium conditions. As with flow bypassing, nonequilibrium mass transfer reduces the retardation, resulting in underestimation of NAPL saturation. Lastly, a BTC with an extensive tail can result in incomplete measurement of tracer mass. This may occur either because the partitioning tracer test is not conducted for enough time to collect the entire BTC or because tracer concentrations fall below detection limits. Because this tracer mass is not accounted for, the retardation coefficient is again underestimated, leading to NAPL mass underestimation. However, this problem can be corrected for by first extrapolating the BTC tail and then performing moment analysis (Skopp, 1984; Pope et al., 1994; Cain et al., 2000; Rao et al., 2000; Brooks et al., 2002).

PITTs are advantageous because they directly detect NAPL, but can be expensive due to the production of contaminated water during the test (Istok et al., 2002; NRC, 2005). While PITTs are more effective than soil cores at determining the NAPL saturation of a large area, they determine NAPL architecture from estimates of NAPL saturation averaged over the entire volume swept by the tracers (Rao et al., 2000; Ramsburg et al., 2005). Thus, the method cannot identify if the overall saturation produced during PITT data analysis results from homogeneously distributed ganglia, heterogeneously scattered pools, or mixture of both. To produce estimates of the spatial distribution of NAPL saturation on the scale necessary to quantify source zone architecture, a high

density of tracer sample locations would be necessary, which is costly to conduct (James et. al., 1997; Jawitz et al., 1998).

#### *1.4.3 - Push-Pull Test*

A hydraulic alternative to the PITT is to inject and extract the partitioning tracers from a single well. This method is called a push-pull test. The push-pull test has been examined through numerical simulations (Schroth et. al., 2001; Davis et. al., 2005) and through laboratory and field tests (Istok et. al., 2002). The same partitioning and non-partitioning tracers typically employed for PITTs are pumped into the subsurface during the “push” phase. The flow is then reversed and the tracers are pumped back out through the same well during the “pull” phase.

As in PITT data analysis, BTCs from push-pull tracer tests are also analyzed to estimate NAPL saturation. However, because the tracers are inserted and removed from the same well, a NAPL volume cannot typically be calculated from retardation of the different tracer BTCs (Istok et. al., 2002). Instead, the NAPL saturation of the swept area is calculated from the *apparent* dispersion of the tracer data obtained during the pull portion of the test (Schroth et. al., 2001). Apparent dispersion is a function of retardation and actual hydrodynamic dispersion. Interpretation of both PITT and push-pull tracer data assumes linear equilibrium partitioning between the tracers and NAPL, though it has been acknowledged that the partitioning may be nonlinear (Wise, 1999; Wise et. al., 1999). Additionally, mass transfer of the tracers may be limited by diffusion within the NAPL (Willson et. al., 2000; Moreno-Barbero and Illangasekare,

2006). If designed correctly, push-pull tests may produce better estimates of local NAPL saturation than PITTs. Since a push-pull test does not cover as large a volume as a PITT, the saturation value is averaged over a smaller distance and provides a higher resolution description of the area studied.

### ***1.5 Tracer DNAPL Interactions***

Given that the quantification of many source zone architecture metrics relies on partitioning tracer evaluation of the source zone, it is important to understand how these tracers partition between the aqueous and DNAPL phases. It is necessary to first understand the equilibrium behavior of the tracer-DNAPL-aqueous system because it is the thermodynamic driving force behind the chemical interactions that occur during transport. Interactions in this ternary system become increasingly complex when moving through a porous media due to complicated flow patterns and nonequilibrium partitioning. Therefore, a thorough understanding of the processes controlling partitioning tracer transport is necessary before the results of partitioning tracer tests can be used to estimate source zone architecture metrics.

#### ***1.5.1 - Liquid-Liquid Equilibrium***

Many liquid compounds are not completely miscible due to difference in chemical properties such as polarity. When these compounds are combined, they will not form a homogeneous mixture, but will equilibrate into two separate phases. Each phase will contain all components, but will have different

component compositions. A dilute solution has a lower Gibbs energy than its pure components, which is why a mixture of two unlike components equilibrates as two separate, dilute mixtures as opposed to two separate, pure phases.

It is, however, difficult to measure Gibbs free energy; therefore, thermodynamic equations have been manipulated so that more measurable terms are used to describe liquid-liquid equilibrium (LLE). At equilibrium, the fugacities ( $f$ ) of each component in each phase must be equal (Sandler, 2006):

$$\bar{f}_i^I(T, P) = \bar{f}_i^{II}(T, P) \quad (1.13)$$

The fugacity can be thought of as the tendency of a substance to prefer one phase over another. The value a component's fugacity in a mixture is different than that in the pure phase and is defined as:

$$\bar{f}_i = f_i x_i \gamma_i \quad (1.14)$$

In equations 1.13 and 1.14,  $\bar{f}_i$  is the fugacity of component  $i$  in the mixture [-],  $f_i$  is the fugacity of component  $i$  [-] at its reference state (usually the pure component),  $x_i$  is the mole fraction of component  $i$  [-], and  $\hat{\gamma}_i$  is the activity coefficient of component  $i$  [-]. The activity coefficient accounts for the component deviations from ideal behavior due to being in a mixture. The activity coefficient of component  $i$  is a function of both component  $i$  and the other components in the mixture. An activity coefficient of 1 means that the mixture is ideal and the fugacity of that component in the mixture is equal to the mole fraction of the component in the mixture multiplied by the fugacity of the pure

component. When equation 1.13 is substituted into equation 1.14, the resulting equation is:

$$x_i^I \gamma_i^I(T, P) = x_i^{II} \gamma_i^{II}(T, P) \quad i = 1, 2, \dots, c \quad (1.15)$$

Additionally the mole fractions of each component in each phase must sum to 1.

$$\sum_{i=1}^c x_i^I = 1 \quad \text{and} \quad \sum_{i=1}^c x_i^{II} = 1 \quad (1.16)$$

Equation 1.15 demonstrates that the liquid-liquid phase separation is a due to the nonidealities of the solution. If the solution were ideal in both phases, all activity coefficients would equal 1 making  $x_i^I = x_i^{II}$ , for all  $i$  species which would lead to a single phase of one composition. In environmental systems, a less rigorous approach employs an analogy to Raoult's Law to describe the partitioning of contaminants between aqueous and DNAPL phases of dilute solutions (Ramsburg et al., 2010).

$$x_i^{aq} = x_i^{aq,sol} x_i^{DNAPL} \quad (1.17)$$

In equation 1.17,  $x_i^{aq}$  is the mole fraction of component  $i$  in the aqueous phase [-],  $x_i^{aq,sol}$  is the aqueous solubility mole fraction [-] of component  $i$ , and  $x_i^{DNAPL}$  is the mole fraction of component  $i$  in the DNAPL phase [-].

However, if the solution is not dilute (i.e. activity coefficient  $\neq 1$ ), activity coefficients become important and need to be estimated for the system. Most often, this is done using thermodynamic models that estimate the excess Gibbs free energy. One model that is useful for predicting activity coefficients of organic compounds is the Universal Quasi Chemical Theory (UNIQUAC) (Abrams and

Prausnitz, 1975). This model is based on statistical mechanical theory that calculates excess Gibbs energy [ $M \cdot L^2 \cdot T^{-2} \cdot Mol^{-1}$ ] as:

$$\frac{G^{ex}}{RT} = \frac{G^{ex}(combinatorial)}{RT} + \frac{G^{ex}(residual)}{RT} \quad (1.18)$$

where the combinatorial piece accounts for nonidealities due to molecular size and shape and the residual piece accounts for energy differences between the molecules in the mixture. The activity coefficients of each species are calculated as:

$$\ln \gamma_i = \ln \gamma_i(combinatorial) + \ln \gamma_i(residual) \quad (1.19)$$

$$\ln \gamma_i(combinatorial) = \ln \frac{\hat{\phi}_i}{x_i} - \frac{z}{2} \hat{q}_i \ln \frac{\hat{\phi}_i}{\hat{\theta}_i} + l_i - \frac{\hat{\phi}_i}{x_i} \sum_j x_j l_j \quad (1.20)$$

$$\ln \gamma_i(residual) = \hat{q}_i \left[ 1 - \ln \left( \sum_j \hat{\theta}_j \tau_{ji} \right) - \sum_j \frac{\hat{\theta}_j \tau_{ij}}{\sum_k \hat{\theta}_k \tau_{kj}} \right] \quad (1.21)$$

$$l_i = \frac{(\hat{r}_i - \hat{q}_i)z}{2 - (\hat{r}_i - 1)} \quad (1.22)$$

$$\hat{\theta}_i = \frac{x_i \hat{q}_i}{\sum_j x_j \hat{q}_j} = \text{area fraction of species } i \quad (1.23)$$

$$\hat{\phi}_i = \frac{x_i \hat{r}_i}{\sum_j x_j \hat{r}_j} = \text{volume fraction of species } i \quad (1.24)$$

$\hat{r}_i$  and  $\hat{q}_i$  are surface area and volume size parameters [-], respectively, that are evaluated from molecular structure information,  $z$  is the coordination number (usually assumed to be ten) and  $\tau_{ij}$ ,  $\tau_{ji}$ , and  $\tau_{kj}$  are the binary interaction parameters [-]. Two binary interaction parameters exist for each component, one

for each phase. The UNIQUAC interaction parameters are typically regressed from experimentally determined vapor-liquid or liquid-liquid equilibrium data.

Another thermodynamic model that is used to estimate activity coefficients is the UNIVersal Functional-group Activity Coefficient (UNIFAC) model (Fredenslund et al., 1975). The UNIFAC model is based on the UNIQUAC and also has a combinatorial term depending on volume and surface area and a residual term resulting from interaction energies between the molecules. In UNIQUAC, the combinatorial piece is calculated from group contribution parameters and the residual term has adjustable binary interaction parameters. In the UNIFAC model, both the combinatorial and residual pieces are calculated from group contribution methods. To use the UNIFAC model, functional subgroups in each molecule must first be identified. Then

$$\ln \gamma_i(\text{combinatorial}) = \ln \frac{\phi_i'}{x_i} + 1 - \frac{\phi_i'}{x_i} - \frac{z}{2} \hat{q}_i \left( 1 + \ln \frac{\phi_i}{\theta_i} - \frac{\phi_i}{\theta_i} \right) \quad (1.25)$$

$$\phi_i' = \frac{x_i \hat{r}_i^{3/4}}{\sum_j x_j \hat{r}_j^{3/4}} \quad (1.26)$$

$$\ln \gamma_i(\text{residual}) = \sum_k \nu_k^{(i)} [\ln \Gamma_k - \ln \Gamma_k^{(i)}] \quad (1.27)$$

$$\ln \Gamma_k = Q_k \left[ 1 - \ln \left( \sum_m \Theta_m \Psi_{mk} \right) - \sum_m \frac{\Theta_m \Psi_{km}}{\sum_n \Theta_n \Psi_{nm}} \right] \quad (1.28)$$

$$\Theta_m = \frac{X_m Q_m}{\sum_n X_n Q_n} = \text{surface area fraction of group} \quad (1.29)$$

$$\Psi_{mn} = \exp \left[ \frac{-(u_{mn} - u_{nn})}{kT} \right] \quad (1.30)$$

In these equations  $\Gamma_k$  is the activity coefficient of group k in the mixture [-],  $\nu_k^{(i)}$  is the number of k groups present in species i [-], and  $\Gamma_k^{(i)}$  is the residual contribution to the activity coefficient of group k in a pure fluid of species i molecules [-],  $u_{mn}$  is a measure of interaction energy between groups m and n [ $M \cdot L^2 \cdot T^{-2} \cdot Mol^{-1}$ ], and  $Q_k$  is the surface parameter for functional group k [-].

Once activity coefficients are estimated (using UNIQUAC, UNIFAC or another of many methods), equation 1.25 can be used for any number of components i. However, the addition of any new component will change the activity coefficients for each species in the mixture. When the mixture is comprised of three or more components, a mole balance, equation (1.16) must also be solved (Sandler, 2006).

$$N_i = N_i^I + N_i^II \quad (1.31)$$

Often the equilibrium compositions of three component mixtures are of interest. These LLE data are frequently displayed in a ternary phase diagram (Figure 1.3). The most common type of ternary diagram, type one, is formed when two of the three binary pairs are completely miscible and the third binary pair is only partially miscible. Also common are type two diagrams where two of the three binary pairs are partially miscible and only one pair is fully miscible (Sorensen, 1979).

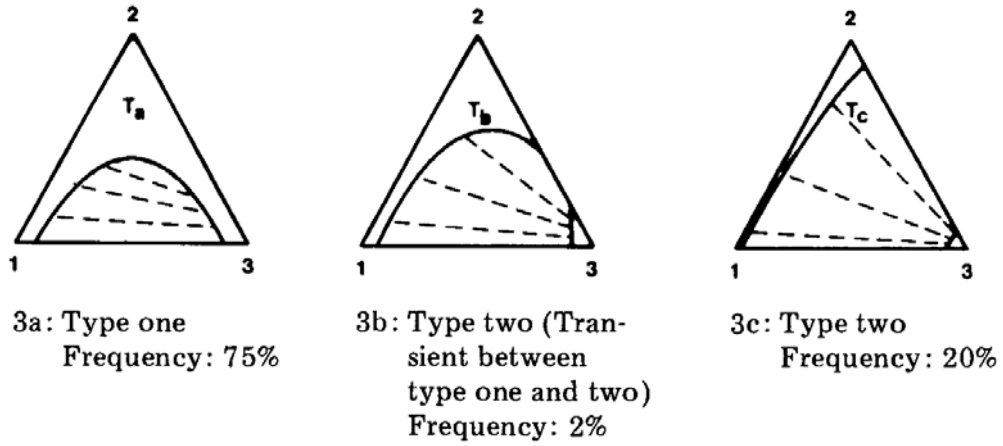


**Figure 1.3** Type one and Type two ternary phase diagrams. Reproduced from Sorensen, 1979.

Each apex represents a pure component species and the mole fraction of that species decreases linearly with the distance along the perpendicular bisector for that axis that represents the species. Therefore, each side of the triangle is a binary mixture that does not contain the species at the opposite apex. The bimodal curve, or curves (solid line), in each diagram separate the single phase regions (outside the curves) from the two phase region (inside the curves). Tie lines (dashed line) connect two points corresponding to the equilibrium compositions of the two phases. Any initial composition in the two phase region will separate into two phases, each having a composition lying on the bimodal curve that is connected by the tie line (Sorensen, 1979).

Alcohol partitioning tracers at equilibrium with DNAPL show type two interactions. Water forms partially miscible pairs with both the alcohol tracer and the DNAPL, while the alcohol tracer and the DNAPL are fully miscible. Therefore, type two interactions will be the focus of the equilibrium experiments in this study.

Another way to examine the LLE system is to compare the amount of tracer in the DNAPL phase the amount in the aqueous phase. This can be done on either a mole fraction basis where,

$$K_p^{m_i} = \frac{x_{tracer}^{NAPL}}{x_{tracer}^{aq}} \quad (1.32)$$

or on a concentration basis where,

$$K_p^{c_i} = \frac{C_{tracer}^{NAPL}}{C_{tracer}^{aq}} \quad (1.33)$$

Both  $K_p^{m_i}$  and  $K_p^{c_i}$  have units of  $[L_{aq} \cdot L_{NAPL}^{-1}]$ . Though one partition coefficient is often used to describe the partitioning of a single tracer between the aqueous and DNAPL phases, literature suggests that partitioning is concentration dependant (Wise, 1999; Wise et al., 1999). In the dilute region, a linear partition coefficient approximation is a safe assumption; however, as concentration increases to form less ideal solutions, this approximation is no longer valid. Therefore, care must be taken to understand how the partition coefficient was measured and under what conditions the measurement is valid.

### 1.5.2 - Surface Interactions

In systems comprised of two liquid phases, chemical interactions at the interface of the two phases can be important. Of particular importance in this study are compounds that both adsorb at the interface and partition between phases. In systems of interest, the compound is dissolved in one liquid phase, then adsorbs to the surface of the second liquid phase and then partitions into that second liquid phase. This is controlled by the equilibrium partition coefficient, the diffusion coefficients of the solute in both phases and the volume ratio of the two phases (Ferrari et al., 1997).

The adsorption process can be quantified through interfacial tension measurements, and, according to Ferrari et al. (1997), can be best described by a Langmuir isotherm (eqs. 1.34 and 1.35).

$$\Gamma_0 = \Gamma_\infty \frac{C_{aq}}{a_L + C_{aq}} \quad (1.34)$$

$$\gamma = \gamma_0 - \Gamma_\infty RT \ln \left( 1 + \frac{C_{aq}}{a_L} \right) \quad (1.35)$$

$\Gamma_0$  is the tracer equilibrium surface concentration [ $\text{Mol}\cdot\text{L}^{-2}$ ],  $\Gamma_\infty$  is the maximum tracer surface concentration [ $\text{Mol}\cdot\text{L}^{-2}$ ], and  $a_L$  is the bulk tracer concentration at which 50% of  $\Gamma_\infty$  has been reached [ $\text{M}\cdot\text{L}^{-3}$ ],  $\gamma$  is the interfacial tension measured at  $C_{aq}$  [ $\text{M}\cdot\text{T}^{-2}$ ] and  $\gamma_0$  is the interfacial tension of the two pure liquid phases [ $\text{M}\cdot\text{T}^{-2}$ ]. Both of these equations assume an equilibrium system. Laboratory measurements of concentration and surface tension are fit to equation 1.35 to determine  $\Gamma_\infty$  and  $a_L$ . The surface adsorption isotherm can then be produced from equation 1.34.

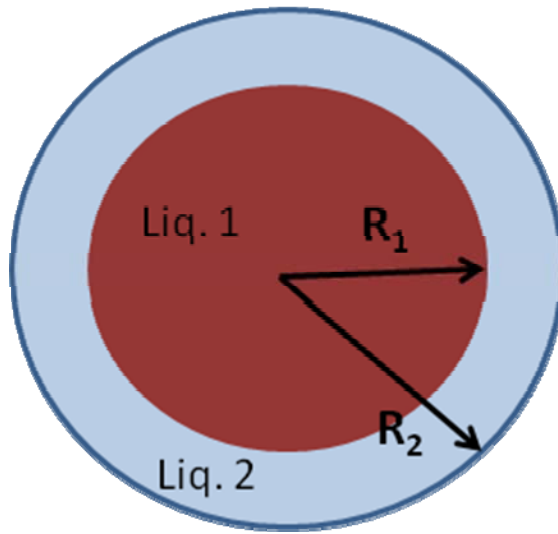


**Figure 1.4** A diagram of the conceptual model used by Liggieri et al. (1997) to discuss surface interactions.

This Langmuir isotherm can then be used in equations describing the dynamic process of solute partitioning from one liquid phase into another with a resistance at the liquid-liquid interface. The conceptual model of this process proposed by Liggieri et al. (1997) relates well to the systems of interest in this work.

This conceptual model is as follows. There exists a spherical drop of liquid 1 with radius  $R_1$  (Figure 1.4). This drop is surrounded by a shell of the second liquid phase, with radius  $R_2$ . The solute adsorption,  $\Gamma$  [ $\text{Mol}\cdot\text{L}^{-2}$ ], varies due to incoming and outgoing diffusive fluxes at the interface

$$\frac{d\Gamma}{dt} = -D_1 \left. \frac{\partial C}{\partial r} \right|_{r=R_1^-} + D_2 \left. \frac{\partial C}{\partial r} \right|_{r=R_1^+} \quad (1.36)$$

where  $C(r,t)$  is the solute concentration [ $\text{M}\cdot\text{L}^{-3}$ ] at time  $t$  and distance  $r$  from the origin, and  $D_1$  and  $D_2$  are the solute diffusion coefficients [ $\text{L}^2\cdot\text{T}^{-1}$ ] in phases 1 and 2 respectively. Equation 1.36 is used as the boundary condition at the interface ( $r=R_1$ ) for Ficks equation written for both bulk phases (equations 1.37 and 1.38).

$$\frac{\partial C}{\partial t} = D_1 \left( \frac{\partial^2 C}{\partial r^2} + \frac{2}{r} \frac{\partial C}{\partial r} \right) \quad \text{for } 0 < r < R_1 \quad (1.37)$$

$$\frac{\partial C}{\partial t} = D_2 \left( \frac{\partial^2 C}{\partial r^2} + \frac{2}{r} \frac{\partial C}{\partial r} \right) \quad \text{for } R_1 < r < R_2 \quad (1.38)$$

The initial conditions are as follows:

$$C(r,0) = C_0 \quad \text{for } 0 < r < R_1 \quad (1.39)$$

$$C(r,0) = 0 \quad \text{for } R_1 < r < R_2 \quad (1.40)$$

The other boundary conditions are:

$$\left. \frac{\partial C}{\partial r} \right|_{r=R_2^-} = 0 \quad (1.41)$$

$$\left. \frac{\partial C}{\partial r} \right|_{r=0} = 0 \quad (1.42)$$

Additionally, local equilibrium is assumed at the interface so that

$$C(R_1^-, t) = K_p^{c_i} C(R_1^+, t) \quad (1.43)$$

Lastly, an equilibrium relationship exists between the boundary concentration,  $C(R_1^-, t)$ , and the solute adsorption,  $\Gamma$ . In this case, the relationship is represented by the Langmuir isotherm shown in equation 1.34.

### *1.5.3 - Tracer Mass Transport in Porous Media*

As discussed in Chapter 1 - Infiltration and Entrapment, DNAPL is distributed in the subsurface both as small ganglia droplets and larger, high saturation pools. Tracer interactions with each type of distribution differ due to larger diffusion time scales for pooled regions and the greater accessibility of DNAPL surface area of the ganglia droplets. Generally research tends to focus on transport mechanisms important in tracer/ganglia interactions and tracer/pool interactions separately and then combine knowledge of these two types of interactions to study heterogeneous source zones. The models most appropriate for each type of interaction are described below.

#### *1.5.3.1 - Mass Transport Models in Regions of Entrapped DNAPL Saturation*

Brusseau et al., (1989) provide a review of multiple modeling approaches used to predict tracer mass transport in regions comprised of DNAPL ganglia. In all of these approaches, the DNAPL phase is assumed to be immobile and the aqueous phase mobile. The simplest modeling approach is to assume that

transport occurs under equilibrium conditions and that a linear sorption isotherm can be used to describe tracer partitioning between the DNAPL and aqueous phases. This 1-D transport model is then a simplified version of the advective-dispersive transport equation:

$$R \frac{\partial C_{Aq}}{\partial t} = D_H \frac{\partial^2 C_{Aq}}{\partial x^2} - v \frac{\partial C_{Aq}}{\partial x} \quad (1.44)$$

where  $D_H$  is the hydrodynamic dispersion coefficient [ $L^2 \cdot T^{-1}$ ],  $v$  is the pore water velocity [ $L \cdot T^{-1}$ ], and  $R$  is the retardation coefficient, defined as:

$$R = 1 + \left( \frac{S_n K_p^{c_i}}{(1 - S_n)} \right) \quad (1.45)$$

$\rho_b$  is the soil bulk density [ $M \cdot L^{-3}$ ],  $n$  is the soil porosity [-], and  $S_n$  is the DNAPL phase saturation [-].

In order for the local equilibrium assumption to be valid, the rate of tracer adsorption into the DNAPL must be fast relative to the rate of advection of the tracer in the aqueous phase. Often this is not the case and a kinetic limitation needs to be added to the model to improve its performance. One such model is the linear driving force model, again described by Brusseau et al. (1989), which incorporates a first order mass transfer resistance through an immobile aqueous boundary layer surrounding the DNAPL.

$$n \cdot S_{aq} \frac{\partial C_{aq}}{\partial t} + q \frac{\partial C_{aq}}{\partial x} - n \cdot S_{aq} \cdot D_H \frac{\partial^2 C_{aq}}{\partial x^2} = -\hat{k}(C_{aq} - C_{int}) \quad (1.46)$$

where  $\hat{k}$  is the lumped mass transfer coefficient [ $T^{-1}$ ] and  $C_{int}$  is the aqueous concentration [ $M \cdot L^{-3}$ ] at the interface between the two phases and is assumed to be in equilibrium with the DNAPL concentration ( $C_n$ ):

$$C_{\text{int}} = \frac{C_n}{K_p^{C_i}} \quad (1.47)$$

The tracer inside the DNAPL is assumed to be well mixed and is described as:

$$n.S_n \frac{\partial C_n}{\partial t} = \hat{k}(C_{aq} - C_{\text{int}}) \quad (1.48)$$

Resistance to tracer transport can also occur within the DNAPL itself. In this case a dual diffusion model which incorporates both the resistance to mass transport in the immobile aqueous boundary layer and diffusional resistance inside the DNAPL droplet. The aqueous phase transport is still described by equation 1.46, but the DNAPL phase equation is no longer well mixed. Diffusion within the DNAPL is assumed to be Fickian and the radial tracer distribution within the DNAPL ganglia is formulated as (Rasmuson and Neretnieks, 1980):

$$\frac{\partial C_{n,r}}{\partial t} = D_n \left( \frac{\partial^2 C_{n,r}}{\partial r^2} + \frac{2}{r} \frac{\partial C_{n,r}}{\partial r} \right) \quad (1.49)$$

$$D_n \frac{\partial C_{n,r=b}}{\partial r} = k_f (C_{aq} - C_{\text{int}}) \quad (1.50)$$

$$\frac{\partial C_{n,r=0}}{\partial r} = 0 \quad (1.51)$$

where  $C_{n,r}$  is the component concentration [ $\text{M}\cdot\text{L}^{-3}$ ] within the DNAPL at radial position,  $r$ ,  $D_n$  is the tracer diffusion coefficient in the DNAPL [ $\text{L}^2\cdot\text{T}^{-1}$ ],  $b$  is radius of the DNAPL droplet [ $\text{L}$ ], and  $k_f$  is mass transfer coefficient [ $\text{L}\cdot\text{T}^{-1}$ ]. The radius of the spherical, singlet DNAPL droplet is estimated from the grain size of the porous media. Previous studies have measured the average droplet radius of entrapped DNAPL at various sand fractions (Powers et al. 1992; Schnaar and Brusseau, 2005). Schnaar and Brusseau (2005) and Ramsburg et al. (2011)

developed regressions to relate an effective DNAPL drop radius to the mean diameter of granular medium.

#### *1.5.3.2 - Mass Transport Models in Pool Dominated or Heterogeneous DNAPL Saturations*

Partitioning tracer test saturation estimates are further complicated in regions with highly heterogeneous or pooled source zones (Jin et al., 1997; Rao et al., 2000; Brooks et al., 2002; Jalbert et al., 2003; Moreno-Barbero and Illangasekare, 2005, 2007). Jin et al. (1997) simulated partitioning tracer tests in a source zone with a large pooled region and reported that the PITTs DNAPL mass estimation errors as high as 50%. Therefore different modeling approaches have been tried to better examine tracer interactions in pooled and heterogeneous systems. These approaches include using either a mass transfer coefficient (e.g. Imhoff and Pirestani, 2004; Jalbert et al., 2003) or a modified equilibrium partition coefficient (Moreno-Barbero et al., 2007) to account for resistance to tracer mass transfer in highly saturated DNAPL zones.

One conceptual model suggested for modeling tracer mass transport in heterogeneous regions is to visualize multiple high saturation pools as one large immobile DNAPL domain located between two aqueous domains as shown in Figure 1.5 (Imhoff and Pirestani, 2004).

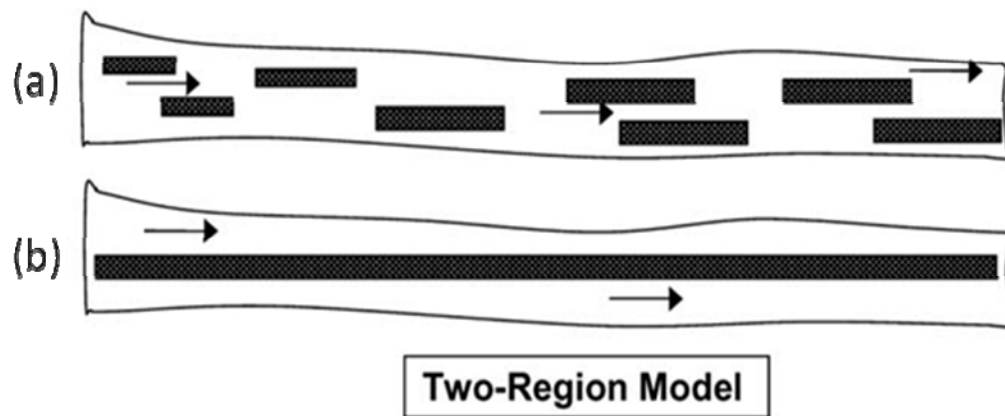


**Figure 1.5** Adapted from Imhoff and Pirestani (2004). The top picture (a) represents a more “real” system where the DNAPL is distributed in many regions of high saturation. This scenario can be modeled as shown in (b) using a two-region model, where the DNAPL is distributed as a single large pool. The large pool is immobile and is surrounded by a mobile aqueous phase.

Tracer mass transfer is assumed to occur between the mobile and immobile domains due to a mass transfer coefficient and a linear concentration driving force. Mathematically this model is described:

$$\phi_a^m \frac{\partial C_{aq}^m}{\partial T} + \left(1 - \frac{\phi_a^m}{R}\right) R \frac{\partial C_{aq}^{im}}{\partial T} = \frac{1}{Pe} \frac{\partial^2 C_{aq}^m}{\partial X^2} - \frac{\partial C_{aq}^m}{\partial X} \quad (1.52)$$

$$\left(1 - \frac{\phi_a^m}{R}\right) R \frac{\partial C_{aq}^{im}}{\partial T} = \omega (C_{aq}^m - C_{aq}^{im}) \quad (1.53)$$

where,

$$\phi_a^m = \frac{\theta_a^m}{\theta_a} \quad (1.54)$$

$$\omega = \frac{\gamma L}{\theta_a \nu_a} \quad (1.55)$$

In the proceeding equations  $\phi_a^m$  is the fraction of aqueous phase in the mobile domain [-],  $C_a^m$  and  $C_a^{im}$  are the aqueous tracer concentrations in the mobile and immobile domains [ $M \cdot L^{-3}$ ], respectively,  $\omega$  is a dimensionless mass transfer coefficient,  $\theta_a$  is the volume fraction of aqueous phase in the entire domain [-],  $\theta_a^m$  is the volume of aqueous phase in the mobile domain normalized by the volume of the entire domain [-],  $\gamma_m$  is the first order mass transfer coefficient for transport between the mobile and immobile domains [ $T^{-1}$ ].  $T$  is dimensionless time and  $X$  is dimensionless length.

Here, the mass transfer coefficient accounts for two resistances; the resistance between mobile aqueous phase and the immobile aqueous phase (assumed to be the dominant resistance) and that between the immobile aqueous phase and the immobile DNAPL phase. This model was tested by running partitioning tracer

tests in a 30 cm column filled with fine sand, surrounding a coarse sand block filled with TCE-DNAPL. Conservative tracer data was used to calibrate flow parameters and the partitioning tracer data along with the known saturation was used to fit the mass transfer coefficient. Using this procedure, the mobile/immobile model was able to reproduce the partitioning data, including the tails. However, this technique is not useful in field situations without an independent method to evaluate the mass transfer coefficient evaluation.

Another method for modeling tracer transport in heterogeneous flow fields is to use a two site partitioning model (Brusseau, 1992; Hatfield et al., 1993; Nkeddi-Kizza et al., 1984; Cussler, 1984; van Genuchten and Wagenet, 1989; Sardin et al., 1991). Jalbert et al. (2003) use a model similar to that of Selim et al. (1976) that assumes some fraction of the tracer-DNAPL interactions (F) occur at equilibrium and that the rest (1-F) exhibit rate limited, first order partitioning. The hypothesis is that the ganglia within the source zone will have equilibrium interactions with the partitioning tracers, while the higher saturation areas will provide mass transfer resistance.

$$(1 - S_n) \frac{\partial C_{aq}}{\partial t} + S_n \frac{\partial C_{n1}}{\partial t} + S_n \frac{\partial C_{n2}}{\partial t} = (1 - S_n) D_H \frac{\partial^2 C_{aq}}{\partial x^2} - (1 - S_n) v \frac{\partial C_{aq}}{\partial x} \quad (1.56)$$

$$C_{n1} = F K_p^{c_i} C_a \quad (1.57)$$

$$\frac{\partial C_{n2}}{\partial t} = \hat{k} [(1 - F) K_p^{c_i} C_{aq} - C_{n2}] \quad (1.58)$$

where  $C_{n1}$  is the DNAPL tracer concentration associated with equilibrium sorption [ $M \cdot L^{-3}$ ],  $C_{n2}$  is the DNAPL tracer concentration associated with the rate-limited partitioning [ $M \cdot L^{-3}$ ], and F is the fraction of DNAPL undergoing

equilibrium interactions [-]. This model was tested using a heterogeneous PCE spill in a 2-D box. Tracer test BTCs were measured in sampling points along the side of the tank and in an extraction well further downgradient. Flow parameters were fit to the conservative tracer data and then the mass transfer coefficient, saturation and  $F$  are fit to the partitioning BTC. Jalbert et al. (2003) found that their two site model gives more accurate predictions of saturation than the method of moments. However, the saturation values necessary to obtain good BTC fits still under predict the actual saturation measured with gamma radiation. The authors hypothesize that this under prediction occurs because the tracers do not interrogate the entire DNAPL volume due to the low permeability of the high saturation areas. Additionally, this model needs both an independent method for calculating the mass transfer coefficient and an independent method for estimating  $F$  to be able to estimate saturations from PITTs.

Moreno-Barbero et al. (2007) took a different approach to understanding tracer mass transport in heterogeneous regions of the subsurface. Instead of using a mass transfer coefficient to describe the rate limited partitioning, Moreno-Barbero et al. (2007) focused on modifying the equilibrium driving force behind the mass transport (the equilibrium partition coefficient). This was done in an intermediate-scale tank (4.87 x 1.21 x 0.05 m) with a heterogeneous PCE source zone. Partitioning tracers were then run through the box and concentration measurements were collected at 29 sample ports. Saturation was then estimated using the method of moments on the port data. As discussed previously, the method of moments assumes equilibrium partitioning. When equilibrium

conditions are not met, saturation is under predicted, especially in areas of high saturation. In order to make more accurate saturation predictions, Moreno-Barbero et al. (2007) employed effective partition coefficients in the method of moments. These effective partition coefficients were determined using batch experiments in which samples were taken at 15 min, and 1, 2, 6, 12 and 24 hours, generating a possible range of partition coefficients. No relationship between partition coefficient and time was assumed, the measurements were simply used to give a range of possible effective partition coefficient values. The lowest effective partition coefficient (measured at 15 min) and the highest partition coefficient (the actual equilibrium value) can then be used in the method of moments to create a range of possible saturations. By applying this procedure to the tank Moreno-Barbero et al. (2007) were able to more effectively predict local saturations within the tank.

The effective partition coefficient proposed by Moreno-Barbero et al. (2007) may be able to provide good estimates of saturation in the 2-D box studies when there is some knowledge about the location of high and low saturation areas, as well as tracer contact time with the DNAPL. However, in the field, we are not likely to have this type of knowledge. As concluded by Moreno-Barbero et al. (2007), this approach may be able to bracket the saturation range of the test, but this range may turn out to be too large to draw any conclusions about the source zone architecture.

#### *1.5.4 - Mass Transfer Coefficient Correlations*

Most of the mass transport models described above require estimation of a mass transfer coefficient. These mass transfer coefficients can be fit to BTC data if the saturation is known; however, to be useful for saturation estimation, an independent method for calculating the mass transfer coefficient is necessary. There are many correlations related to dissolution of pure component DNAPLs. When considering partitioning tracers, one approach is to employ a correlation developed for dissolution. The assumption here is that a tracer partitioning into and out of the DNAPL behaves similar to pure component dissolution. To be clear, there are two assumption here: (i) the kinetics of mass exchange are the same irrespective of whether the tracer is partitioning into or out of the DNAPL; and (ii) exchange kinetics for tracers (multi-component scenario) are similar to those experienced during pure component dissolution. Dissolution correlations are available for both ganglia and pools. What follows below is an overview of the most applicable mass transfer coefficient correlations for ganglia and pools.

##### *1.5.4.1 - Ganglia Dissolution Correlations*

Several mass transfer coefficient correlations have been developed for NAPL ganglia dissolution (e.g., Powers et al., 1992; Powers et al., 1994; Imhoff et al., 1994). Powers et al. (1992) measured the effects of porous media grain size and uniformity, NAPL type and aqueous phase velocity on the dissolution of styrene and TCE ganglia in 1-D column experiments. These correlations were developed by measuring dissolution of the NAPL from various size sand fractions. A linear regression was performed on all measured parameters to

develop the most appropriate Sherwood number correlation for determination of the mass transfer coefficient.

The lumped mass transfer coefficient  $\hat{k}$  describes tracer mass transport in an immobile aqueous phase boundary layer surrounding each TCE-DNAPL droplet. The mass transfer coefficient is calculated using the empirical relationship developed by Powers et al. (1992):

$$Sh' = \frac{\hat{k}d_{50}^2}{D_{aq}} = 57.7(Re)^{0.61}(d_{50})^{0.64}(U_i)^{0.41} \quad (1.59)$$

where  $Sh'$  is the Sherwood number [-],  $d_{50}$  is the mean particle diameter [L],  $D_{aq}$  is the aqueous phase diffusion coefficient [ $L^2 \cdot T^{-1}$ ],  $Re$  is the Reynolds number [-], and  $U_i$  is the uniformity index [-]. In these experiments, the NAPL droplets were assumed to be spherical and their radius dependant on grain diameter. The lumped mass transfer coefficient incorporates specific interfacial area of the spherical ganglia droplets. Though this empirical relationship was developed for the dissolution of pure-component NAPLs, it has been shown to be capable of describing mass exchange in ganglia systems comprising multiple components (Ramsburg et al., 2011).

In 1994, Powers and coauthors expanded their work to include the affect of NAPL blob geometry and the changing NAPL surface area as dissolution occurs. Experiments similar to those of Powers et al. (1992) were conducted and the following regression was developed:

$$Sh' = 4.13(Re)^{0.589} \left( \frac{d_{50}}{d_M} \right)^{0.673} (U_i)^{0.369} \left( \frac{\theta_n}{\theta_{n0}} \right)^B \quad (1.60)$$

$$B = 0.518 + 0.114 \left( \frac{d_{50}}{d_M} \right) + 0.10U_i \quad (1.61)$$

where  $d_M$  is the diameter of a “medium” sand grain (0.05 cm),  $\theta_n$  is the volume fraction of NAPL in the system [-], and  $\theta_{n0}$  is the initial volume fraction of NAPL in the system [-]. The addition of the NAPL volume fraction terms allow for the mass transfer coefficient to change as the NAPL dissolves and the B coefficient allows for the blob shape to depend on porous medium characteristics.

In their 2003 paper, Nambi and Powers discuss the reworking of the Powers et al. (1994) model to produce a correlation that explicitly contains saturation. In this process, it was shown that Reynolds number and NAPL saturation were the only two statistically significant parameters, which allowed the reworked correlation to be written as:

$$Sh' = 44.7(\text{Re})^{0.526} (S_n)^{0.937} \quad (1.62)$$

Imhoff et al. (1994) also developed a mass transfer coefficient correlation by measuring the dissolution of residual TCE-DNAPL in a column experiment. In this case, the DNAPL saturation was measured directly, using gamma attenuation.

$$Sh = 340(\theta_n)^{0.87} (\text{Re})^{0.71} \left( \frac{x}{d_{50}} \right)^{-0.31} \quad (1.63)$$

where  $x/d_{50}$  is the dimensionless distance into the region of residual TCE-DNAPL. This model is valid for:  $0 \leq \theta_n \leq 0.04$ ,  $0.0012 \leq \text{Re} \leq 0.021$ , and  $1.4 \leq x/d_{50} \leq 180$ . With these independent means of calculating mass transfer coefficients, the transport models described above can be fit to tracer BTCs to estimate an average saturation of NAPL ganglia in the region swept by the tracers.

#### *1.5.4.2 - Pool Dissolution Correlations*

Because the kinetics of NAPL pool dissolution may be different than those for NAPL ganglia dissolution, mass transfer correlations have also been developed from pool dissolution studies. Again, the use of existing correlations allows independent calculation of the mass transfer correlation (i.e., model predictions not fits); therefore it is important to determine whether any pool dissolution correlations can also describe partitioning tracer transport in systems of high DNAPL saturation. Much of the experimental work in the pool dissolution literature examines single component NAPL dissolution from a single pool (Lee and Chrysikopoulos, 2002; Seagren et al., 1999a). Some researchers have added complexity to their experiments by either examining dissolution of one component from a two component pool (Seagren et al., 2003) or by developing mass transfer correlations for applicable over a wider range of saturations (Nambi and Powers, 2003). Numerical modeling approaches have also been used to generate dissolution data that are then employed to develop mass transfer correlations (Kim and Chrysikopoulos, 1999; Chrysikopoulos and Kim, 2000).

Seagren et al. (1999a; 1999b) examined the dissolution from a toluene pool (i.e., a single component NAPL) using both the equilibrium assumption and the mass transfer correlation of Pfannkuch (1984). The Pfannkuch correlation was developed using dissolution data of an LNAPL trapped as a pool on a capillary fringe (Hoffman, 1969 as referenced in Pfannkuch, 1984). Results showed dissolution flux to be independent of pore water velocity for velocities

less than 2 m/day; above 2 m/day the flux was found to generally increase with velocity. The correlation developed from Hoffman's data is:

$$Sh = \frac{k_f l_x}{D_z} = 0.55 + 0.025(Pe)^{1.5} \quad (1.64)$$

$$Pe = \frac{v d_{50}}{D_{aq}} \quad (1.65)$$

where  $Pe$  is the Peclet number [-],  $l_x$  [L] is the NAPL pool length in the x-direction, and  $D_z$  [ $L^2T^{-1}$ ] is vertical transverse hydrodynamic dispersion coefficient. This correlation was then tested with the experimental data (flux vs. velocity) of Seagren et al. (1999b) which used a  $Pe$  range (56-792) outside of that range supported by the data employed to develop the correlation (0.65-41.7).

Seagren et al. (1999b) found that for pore water velocities of less than 18 m/day, predictions of mass flux with the nonequilibrium model using the Pfannkuch correlation did not appreciably differ from those of the local equilibrium model. Above 18 m/day, the two models deviate, indicating a non-equilibrium response, but the Pfannkuch correlation does not capture the dissolution flux data. The Pfannkuch correlation predicts that dissolution will continually increase with increasing velocity, while, Seagren et al. (1999b) observed that the dependence of the flux on velocity appeared to diminish at velocities  $> 20$  m/day. It appears that since the correlation was developed at lower  $Pe$  numbers where flux does increase with increasing velocity, the correlation is not able to capture the leveling out of the flux data at higher  $Pe$  numbers. Seagren et al. (1999b) fit a mass transfer coefficient to those dissolution flux data that were  $< 95\%$  of the local equilibrium flux prediction. This process

produced a single mass transfer coefficient of 4.76 m/d, which, when used in the nonequilibrium model, was able to satisfactorily reproduce the steady state dissolution flux for the velocities used in the laboratory experiments.

Lee and Chrysikopoulos (2002) also developed a correlation for dissolution of a single component pool under multiple velocities. The experimental setup consisted of a 3-D sand aquifer cell (150 cm x 40 cm x 17 cm) containing a cylindrical TCE-DNAPL pool in glass beads (7.6 cm diameter and 0.5 cm deep). Water was flowed through the cell at pore water velocities (again determined as  $Q/nS_{aq}A$ , with  $S_{aq} = 1$ ) of 0.51, 1.21, 1.50 and 3.35 cm/hr and concentration measurements were taken at ports downstream sampling ports. The mass transfer coefficient at each velocity was estimated from the concentration measurements using an analytical solution for circular pool dissolution from (Chrysikopoulos, 1995) assuming that

$$\hat{k} = \frac{1}{A_{pool}} \int k^*(t, x, y) d^2 A_{pool} \quad (1.66)$$

where  $k^*$  is the local mass transfer coefficient [ $L \cdot T^{-1}$ ]. These mass transfer coefficients were then fit to a Sherwood correlation to give

$$Sh = \frac{\hat{k} \pi^{1/2} r_{pool}}{D_e} = 1.30 (Pe_x)^{0.12} (Pe_y)^{0.44} \quad (1.67)$$

$$Pe_{x,r} = \frac{v_x r_{pool}}{D_x} \quad (1.68)$$

$$Pe_{y,r} = \frac{v_x r_{pool}}{D_y} \quad (1.69)$$

where  $r_{pool}$  [L] is the pool radius,  $D_e = D_{aq}/\tau$  is the effective molecular diffusion coefficient [ $L^2 T^{-1}$ ],  $D_x = \alpha_L v_x + D_e$  and  $D_y = \alpha_T v_x + D_e$  are the longitudinal and

transverse hydrodynamic dispersion coefficients [ $L^2T^{-1}$ ], respectively, and  $\alpha_L$  and  $\alpha_T$  [L] are the longitudinal and transverse aquifer dispersivities, respectively. The correlation represented by equations 1.67-1.69 was not validated against independent experimental data sets.

Seagren and Moore (2003) performed dissolution experiments examining the dissolution of naphthalene from a two component NAPL compound (naphthalene and nonane). The addition of a second component created the potential for resistance to mass transfer in both the aqueous and NAPL phases – making this work more akin to partitioning tracer transporting out of a NAPL phase. The experiments were conducted in a rectangular column filled with glass beads, containing a LNAPL pool sitting on top of water. Seagren and Moore (2003) conducted 15 experiments, quantifying the dissolution of naphthalene at pore water velocities between 0.1 – 60 m/day by measuring concentrations from an effluent sampling valve.

Mass transfer coefficients were fit to the flux data measured at each velocity. Predictions from the nonequilibrium model using this mass transfer coefficient and from the local equilibrium model were compared. The local equilibrium model was able to give reasonable estimates of naphthalene flux up to pore water velocities of 10 m/d; therefore, nonequilibrium mass transfer analysis focused on velocities of 10 m/d – 60 m/d. It was determined that there was no statistically significant dependence of mass transfer coefficient on velocity and that the average mass transfer coefficient of 0.407 m/day used in the nonequilibrium model was able to predict dissolution flux data.

Seagren and Moore (2003) proposed the following conceptual model as to why the mass transfer coefficient was not a function of velocity. The overall mass transfer coefficient can be thought of as dependent on both the mass transfer coefficient in the aqueous phase and the mass transfer coefficient in the NAPL phase, each of which is inversely proportional to an aqueous phase boundary layer and a NAPL phase boundary layer respectively. At low velocities, the mass transfer coefficient is small because the thickness of the aqueous boundary layer is relatively thick. As the velocity increases, the thickness of the aqueous phase boundary layer decreases, causing the mass transfer coefficient to increase. For a multi-component NAPL, at a certain velocity, the aqueous boundary layer becomes small enough that resistance in the NAPL phase starts to dominate mass transfer. Mass transfer in the NAPL phase does not depend on aqueous phase velocity, causing the overall mass transfer coefficient to no longer depend on velocity.

All of the studies summarized to this point have examined pool dissolution from pools at early times, meaning that dissolution is not studied as pools age and decrease in saturation. Nambi and Powers (2003) however, examined pool dissolution from high initial saturations, until the aqueous NAPL concentration resulting from dissolution falls below analytical detection limits (3 orders of magnitude reduction in concentration). Their objective was to develop a mass transfer correlation that can be used to estimate dissolution rates for a range of NAPL saturations that were initially entrapped at high saturations. The experiment was conducted in a 2-D box with either one or two 5 cm long course

lenses (varying width 1.5 – 3 cm) surrounded by a finer sand. A pure o-toluidine NAPL at initial saturations from 0.3-0.8 was emplaced in the course lens(es), water was flowed through the box at different rates and the dissolved phase concentrations were measured at both the local port and at the effluent. During the experiment, they were able to visually determine that the NAPL dissolved in a relatively uniform manner, and not preferentially around the pool edges, perhaps suggesting water flow through the pool. Pore water velocities used are estimated in the course lens, assuming flow lines remain parallel through the fine and course lens.

Concentrations measured at the local port were used to generate the mass transfer coefficient relationship. They found that at initial, high saturations (defined by Nambi and Powers as greater than 0.3), dissolution occurs under approximately equilibrium conditions and mass transfer coefficients cannot be quantified. For lower saturations, 90 data sets from 9 experiments were used to develop the following mass transfer coefficient:

$$Sh = \frac{\hat{k}L^2}{D_{aq}} = 37.2(S_n)^{1.24} (Re)^{0.61} \quad (1.70)$$

where  $L$  is the characteristic length [L]. The correlation is valid for  $0.01 < S_n < 0.35$  and  $0.018 < Re < 0.134$ . Parameters representing sand grain size, intrinsic permeability and pool width were also included in the regression process, but none of these parameters were found to be statistically significant ( $p < 0.05$ ). This mass transfer correlation differs from others because it was developed from experiments with high initial saturations and were dissolved to saturations around

1% - that is the inclusion of the saturation history (via experimental design) is important.

Pool dissolution correlations have also been developed by producing data with 3-D transport models and fitting power law correlations of the Sherwood number to the 3-D results (Kim and Chrysikopoulos, 1999; Chrysikopoulos and Kim, 2000). Both studies use the 3-D advection-dispersion-reaction equation to simulate dissolution from single component pools of both rectangular and elliptical geometries. It is assumed that a concentration boundary layer exists with solubility concentrations at the NAPL-water interface and a bulk concentration above this concentration boundary layer of zero. The principal difference between the two studies is that Kim and Chrysikopoulos (1999) develop mass transfer correlations for overall mass transfer coefficients from the entire pool and Chrysikopoulos and Kim (2000) develop correlations for local mass transfer coefficients that correspond to distinct locations above the pool.

Kim and Chrysikopoulos (1999) numerically simulated 121 rectangular pools (with  $l_x \times l_y$  ranging from 5 x 5 m to 10 x 10 m) and 121 elliptical pools (with semiaxes  $a \times b$  ranging from 2.5 x 2.5 m to 5 x 5 m) at velocities of 0.3, 0.5, 0.7 and 1 m/day. A form of the advective-dispersive equation:

$$R \frac{\partial C_{aq}}{\partial t} = D_x \frac{\partial^2 C_{aq}}{\partial x^2} + D_y \frac{\partial^2 C_{aq}}{\partial y^2} + D_z \frac{\partial^2 C_{aq}}{\partial z^2} - v_x \frac{\partial C_{aq}}{\partial x} \quad (1.71)$$

The source of dissolution concentration is found in the boundary conditions:

$$C(0, x, y, z) = 0 \quad (1.72)$$

$$C(t, \pm\infty, y, z) = 0 \quad (1.73)$$

$$C(t, x, \pm\infty, z) = 0 \quad (1.74)$$

$$C(t, x, y, 0) = C_s \quad x, y \in R_r \quad (1.75)$$

$$\frac{\partial C(t, x, y, 0)}{\partial z} = 0 \quad x, y \in R_r \quad (1.76)$$

$$C(t, x, y, \infty) = 0 \quad (1.77)$$

where  $C_s$  is the solubility concentration [ $M \cdot L^{-3}$ ] and  $R_r$  is the domain defined by the rectangular NAPL-water interfacial area [ $L^2$ ]. Equation 1.75 implies that the NAPL and aqueous phase are in equilibrium at  $z = 0$ , with the concentration along  $z = 0$  equal to the NAPL solubility. For an elliptical pool, equations 1.74 and 1.75 are replaced with equations 1.76 and 1.77, respectively.

$$C(t, x, y, 0) = C_s \quad x, y \in R_e \quad (1.78)$$

$$\frac{\partial C(t, x, y, 0)}{\partial z} = 0 \quad x, y \in R_e \quad (1.79)$$

where  $R_e$  is the domain defined by the elliptic NAPL pool.

The mass transfer coefficients generated by these simulations were then used to develop two overall Sherwood correlations, one for each geometry. The correlation developed for rectangular pools is:

$$Sh = \frac{\hat{k}L}{D_e} = 1.58(Pe_x)^{0.34} (Pe_y)^{0.43} \quad (1.80)$$

$$Pe_x = \frac{v_x L}{D_x} \quad (1.81)$$

$$Pe_y = \frac{v_y L}{D_y} \quad (1.82)$$

In these equations the characteristic length,  $L$ , is the square root of pool area.

For elliptical pools, the Sherwood correlation is:

$$Sh = \frac{\hat{k}L}{D_e} = 1.74(Pe_x)^{0.33}(Pe_y)^{0.40} \quad (1.83)$$

$$Pe_x = \frac{v_x \hat{a}}{D_x} \quad (1.84)$$

$$Pe_y = \frac{v_x \hat{b}}{D_y} \quad (1.85)$$

where  $\hat{a}$  and  $\hat{b}$  are the length of the major and minor semiaxes [L] of the pool, respectively. Both correlations are valid for pore water velocities from 0.1 – 1.0 m/d and  $D_x$ ,  $D_y$ , and  $D_z$ , from  $2.5-8.3 \times 10^{-2} \text{ m}^2/\text{hr}$ ,  $2.5-8.3 \times 10^{-3} \text{ m}^2/\text{hr}$ , and  $2.5-8.3 \times 10^{-3} \text{ m}^2/\text{hr}$ , respectively ( $\alpha_L/10 = \alpha_T = \alpha_V$ ).

The elliptical correlation was tested by comparing it to data developed by Lee et al. (1998) using a fully saturated bench scale aquifer with a circular TCE-DNAPL pool at pore water velocities from 0.1 – 0.4 m/day. The authors state that the overall correlation performs well, but note that it slightly over predicts the experimental mass transfer coefficients at each velocity. This over prediction of the mass transfer coefficients was also reported by Lee and Chrysikopoulos (2002) who used the elliptical mass transfer correlation to predict Sherwood numbers for their experimental data. They found that the correlation developed from the numerical work always over predicted the  $Sh$  by about a factor of two. They hypothesize that this may be due to the fact that the correlation was developed with pools of longitudinal size ranging from 2.5 – 5 m, while the pool in the experimental work was only 0.076 m.

The work of Chrysikopoulos and Kim (2000) uses the same conceptual model and numerical procedures to estimate local mass transfer coefficients for rectangular and elliptical pools. The difference is that the local mass transfer coefficients correspond to specific locations above the pool. The local  $Sh$  correlation determined for rectangular pools is:

$$Sh = \frac{k^* x' y'}{D_e L} = \beta_1 (Pe'_x)^{(\beta_2)(Pe'_y)^{(\beta_3)}} \quad (1.86)$$

$$Pe'_x = \frac{v_x x'}{D_x} \quad (1.87)$$

$$Pe'_y = \frac{v_x y'}{D_y} \quad (1.88)$$

$$x' = x - l_{x0} \quad (1.89)$$

$$y' = y - \left( l_{y0} + \frac{l_y}{2} \right) \quad (1.90)$$

where  $l_{x0}$  and  $l_{y0}$  are the Cartesian coordinates of the origin [-]. Since Chrysikopoulos and Kim (2000) are calculating local mass transfer coefficients,  $\beta$  values are dependent on pool shape and hydrodynamics and are calculated as

$$\beta_1 = 0.01 l_x^{-0.53} \frac{l_y^{1.16}}{2} v_x^{-0.11} \quad (1.91)$$

$$\beta_2 = 0.69 l_x^{-0.13} v_x^{-0.01} \quad (1.92)$$

$$\beta_3 = 1.35 \frac{l_y^{-0.55}}{2} v_x^{-0.01} \quad (1.93)$$

where  $l_x$  and  $l_y$  are the lengths of the pool [L] in the x and y directions, respectively. A similar correlation was developed for elliptical pools.

$$Sh = \frac{k^*|x|y''}{D_e L} = \gamma_1 (Pe_{x,e})^{\gamma_2} (Pe_{y,e})^{\gamma_3} \quad (1.94)$$

$$Pe_{x,e} = \frac{v_x |x|}{D_x} \quad (1.95)$$

$$Pe_{y,e} = \frac{v_x y''}{D_y} \quad (1.96)$$

$$y'' = y - l_{y,0} \quad (1.97)$$

Again, the coefficients in the Sherwood correlation are dependent on geometry and hydrodynamics.

$$\gamma_1 = 0.10(2\hat{a})^{-3.26} (\hat{b})^{-1.51} (v_x)^{-1.21} \quad (1.98)$$

$$\gamma_2 = 5.31(2\hat{a})^{0.27} (\hat{b})^{-0.20} (v_x)^{0.21} \quad (1.99)$$

$$\gamma_3 = 7.65(2\hat{a})^{0.10} (\hat{b})^{-0.19} (v_x)^{0.24} \quad (1.100)$$

Both the rectangular and elliptical correlations are valid for pore water velocities ranging from 0.1 – 1.0 m/d. The rectangular correlation is valid for pools with dimensions of 0.2 x 0.2 m to 10.0 x 10.0 m and the elliptical correlation for pools with semiaxes ranging from 0.1 x 0.1 m to 5 x 5 m. These correlations were not tested against laboratory data.

Mass transfer correlations developed from ganglia dissolution experiments have been used with a linear driving force model to predict solute partitioning into and out of DNAPL ganglia (Ramsburg et al., 2011); it may be possible that similarly developed pool dissolution correlations can be used to predict partitioning tracer transport into and out of DNAPL pools. The previous section

examines the available pool dissolution correlations that have been developed through both experimental and modeling work looking at both single component and multi-component NAPL dissolution. These correlations will be tested to determine if pool dissolution correlations can be used in a transport model to predict partitioning tracer transport in systems containing pooled and heterogeneous DNAPL distributions.

## **Chapter 2: OBJECTIVES AND HYPOTHESES**

Accurate characterization of DNAPL source zones remains a substantial challenge to effective remediation (US EPA, 1993, 2004; NRC, 2005; Abriola et al., in press). Although soil coring and direct push sampling techniques are the most common methods for DNAPL mass delineation (Costanza and Davis, 2000; Guilbeault et al., 2005; Kram et al., 2001; Meinardus et al., 2002; NRC, 2005), partitioning tracer tests offer an alternative approach to characterization. In fact, quantification of several source zone architecture metrics relies upon successful implementation of partitioning tracer tests. Partitioning tracer tests can be employed to characterize large volumes of the subsurface by estimating spatially averaged saturations (Annable et al., 1998a; 1998b; Brooks et al. 2002; Jin et al., 1995). In partitioning interwell tracer tests (PITTs) the average DNAPL saturation between the injection and observation wells is related to the observed retardation of the tracer(s) through a temporal moment analysis (e.g. Annable et al. 1998a; Brooks et al., 2002; Jawitz et al., 2003; Jin et al., 1995; Saripalli et al., 1997). The spatial resolution of a DNAPL saturation estimate from a PITT is directly related to the distance between the observation points. Thus, high resolution estimates of DNAPL architecture are often economically prohibitive due to the density of sampling locations and the amount of contaminated water produced during the tests. However, the use of partitioning tracers in a “push-pull” flow scheme reduces the volume of subsurface interrogated, and hence the volume of contaminated water produced, thereby increasing the resolution of local estimation of saturation.

In order for partitioning tracer tests to accurately characterize the subsurface, the equilibrium and transport processes governing their interactions in the source zone needs to be well understood. Tracer partitioning between a NAPL and aqueous phase has been examined at a variety of scales, ranging from batch experiments (Dai et al., 2001; Dwarakanath and Pope, 1998; Thal et al., 2007; Wang et al., 1998; Wise et al 1999; Young et al., 1999), to laboratory flow studies (Dai et al., 2001; Jin et al., 1995; Moreno-Barbero and Illangasekare, 2005, 2006, 2007; Wilson and Mackay, 1995) to field-scale research and application (Annable et al., 1998a, 1998b; Brooks et al., 2002; Jawitz et al., 1998; Meinardus et al., 2002; Nelson and Brusseau, 1996; Ramsburg et al., 2005; Rao et al., 1997, 2000). This body of research largely assumes that tracer partitioning is linear. A notable exception is the work of Wise and co-workers (1999a, 1999b) that used a Langmuir-type isotherm to represent observed partitioning nonlinearities. Other assumptions commonly employed in tracer data analysis include local equilibrium and complete hydraulic accessibility to the DNAPL (Annable et al., 1998a; Wilson et al., 2000). Spatial variability of aquifer properties or DNAPL distributions, however, will promote non-uniform flow fields which may lead to nonequilibrium conditions (Brooks et al., 2002; Imhoff and Pirestani, 2004; Jalbert et al., 2003; Meinardus et al., 2002; Moreno-Barbero and Illangasekare, 2005, 2006; Rao et al., 2000; Wilson et al., 2000). Flow field heterogeneity can also result in hydraulic isolation of DNAPL and underestimation of contaminant mass during tracer tests (Moreo-Barbero and Illangasekare, 2006; Rao et al., 2000). In addition, diffusive transport (within

immobile aqueous phase and DNAPL zones) and adsorption at the DNAPL-aqueous interface may influence tracer transport, and consequently decrease the accuracy of DNAPL saturation estimates (Garcia et al., 1993; Willson et al., 2000).

The overall objective of this work is to explore the influence of nonlinear partitioning, non-equilibrium mass exchange and non-uniformity in DNAPL spatial distribution when employing alcohol tracer tests to characterize local-scale source zone architecture. Understanding each of these influences may allow for the design of a partitioning tracer test that quantifies source zone architecture metrics by exploiting specific influences.

Equilibrium partitioning defines the thermodynamic driving force for tracer exchange between the aqueous phase and DNAPL. Hence, it is important to fully understand the equilibrium phase behavior of the tracer-water-NAPL system before examining kinetic transport processes. Complete characterization of the liquid-liquid equilibria will establish the concentration dependence of the tracer distribution between the aqueous phase the DNAPL. Doing so will permit: (i) identification of the region(s) over which the partitioning is approximately linear; and (ii) assessment of common thermodynamic models to predict the partitioning behavior.

Though the literature related to partitioning tracer transport is extensive, few studies have rigorously examined how surface capacity, and diffusional resistances within each phase influence tracer mass transport within regions comprising DNAPL ganglia and regions comprising DNAPL pools. Furthermore,

no studies have attempted to manipulate the relative mass transfer influences with the objective of distinguishing between ganglia dominated and pool dominated heterogeneous source zones. The central hypothesis of this work is that the relative importance of diffusion within each phase will be different for DNAPL present as ganglia and DNAPL present in pools. Diffusional resistance in the DNAPL is expected to be more important in pools because of the longer diffusion path length, compared to those within ganglia.

To examine the overall objective and hypothesis, the following specific objectives and hypotheses have been identified:

**Objective 1: Measure the liquid-liquid-equilibrium of each 1-pentanol, 1-hexanol, and 2-octanol (three representative tracers) in a TCE-water system.**

Partition coefficients of tracers used within DNAPL source zones are generally assumed to be linear. This assumption leads some to evaluate partition coefficients using a single point measurement. Here batch experiments will be used to characterize tracer absorption over the entire range of possible tracer concentrations in systems comprising TCE-DNAPL, water and the alcohol tracer. Results from this characterization will be used to: (i) show whether or not equilibrium partitioning is linear; and (ii) if partitioning is nonlinear, elucidate regions over which partitioning may be approximated as linear.

It is hypothesized that the *partitioning of all short-chain alcohols commonly employed as tracers between TCE-DNAPL and water is nonlinear*. The basis for this assumption is that there is greater capacity for the alcohol to hydrogen bond with water in the aqueous phase, resulting in nonideal (i.e.,

nonlinear) distributions. Further, it is hypothesized that alcohol partitioning within a dilute region may be approximated as linear. Part of this research aims to establish the limits of the linear assumption for each of the three alcohols. Thus, the detailed LLE characterization of the three alcohol tracers (1-pentanol, 1-hexanol, and 2-octanol) in a TCE-water system allows for better tracer test design by greatly reducing uncertainty related to the concentration dependant phase distribution of the tracer. Data related to this objective are presented and interpreted in Chapter 4.

**Objective 2: Compare the measured liquid-liquid-equilibrium behavior of each alcohol to the behavior predicted using UNIFAC**

Thermodynamic models based upon the calculation of the excess Gibbs energy are useful for modeling phase equilibria. There are several types of excess Gibbs energy models, but one that holds particular relevance here is Universal Functional Activity Coefficient (UNIFAC) theory. These thermodynamic models typically regress interaction parameters for compounds using existing vapor-liquid equilibria. UNIFAC is potentially beneficial to the research described here because the model employs group contributions to build each solute present in the system. Thus, the predictive capability of UNIFAC is theoretically much greater as one can examine untested solutes by building each solute from specific functional groups. This potentially useful approach, however, needs to be rigorously examined by comparing model predictions of the phase equilibria to observations developed in Objective 1. Particular emphasis will be placed on evaluating the distribution of alcohol between the two phases (i.e. partitioning).

It is hypothesized that *thermodynamic models will require compound specific calibration to capture liquid-liquid-equilibria considered herein*. Simulations related to this objective are presented and interpreted in Chapter 4 in conjunction with the equilibrium data of Objective 1.

**Objective 3: Explore the processes controlling partitioning tracer mass transport in columns containing uniform distributions of entrapped TCE-DNAPL**

In order to evaluate the utility of partitioning tracer tests for differentiating ganglia dominated source zones from pool dominated source zones, the processes controlling mass transfer in each end member (all ganglia or all pools) must be elucidated. Potential limitations to partitioning in a DNAPL source zone include resistances in the aqueous phase, at the interface and within the DNAPL. A stationary aqueous boundary layer surrounding the DNAPL may provide diffusional resistance to transport within the boundary layer. Additionally, tracers may accumulate at the DNAPL-water interface before partitioning into the DNAPL. Upon partitioning into the DNAPL, diffusional resistance to mass transfer throughout the DNAPL may provide a kinetic limitation to tracer transport.

It is hypothesized that *mass transfer kinetics in regions of residual saturation will be influenced by a combination of these three resistances*. This hypothesis was tested by conducting partitioning tracer tests in column systems with residual saturation of TCE-DNAPL. The resulting breakthrough curves will be compared to predictions from models that incorporate the three resistances to

tracer transport. Using the models to examine each resistance separately and in combination, will allow for the determination of the resistances that dominate transport in systems of TCE-DNAPL ganglia. The models used in this objective were developed through collaboration with Mr. Ali Boroumand, Dr. Linda M. Abriola, Dr. John A. Christ, and Dr. C. Andrew Ramsburg. All codes were written or adapted by Mr. Boroumand for use in modeling the experiments described herein, and all assessments of experimental breakthrough curves were made in collaboration with Mr. Boroumand. Data and simulations related to this objective are presented and interpreted in Chapter 5.

**Objective 4: Assess mass transfer kinetics in systems containing a single pool of TCE-DNAPL.**

Objective 4 complements objective 3 by examining partitioning tracer transport at the other end of the pool fraction spectrum, a pool-dominated source zone. It is anticipated that the characterization of transport for end-member pool fraction will allow for a better understanding of partitioning tracer behavior in heterogeneous source zones. DNAPL pools have both a longer diffusion path length and a lower surface area to volume ratio than DNAPL ganglia. Therefore, more diffusional resistance may be encountered by tracers partitioning out of DNAPL pools, leading to long tailing in tracer BTCs. It is hypothesized that *characterization of diffusional resistance within the DNAPL will be necessary to predict tracer mass transfer in regions containing pooled DNAPL.*

This hypothesis was tested by conducting partitioning tracer tests in a 2-D aquifer cell, containing one, large, high-saturation TCE-DNAPL pool. The

pooled region in this system is anticipated to have a much longer diffusion path length than the entrapped TCE-DNAPL in Objective 3. Assessment of effluent and port BTCs was conducted using a numerical model developed by Mr. Ali Boroumand and Dr. Linda M. Abriola. All codes were written or adapted by Mr. Boroumand for use in modeling the experiments described herein. Data and simulations related to this objective are presented and interpreted in Chapter 6.

**Objective 5: Examine the influence of injection and extraction flow rates during a push-pull test conducted in heterogeneous DNAPL source zones.**

This objective will employ push-pull tests within a 2-D aquifer cell experiment to assess the influence of flow rate on mass transfer kinetics and flux-averaged effluent concentrations in heterogeneous source zones. Examining a range of pool fractions with tracer tests conducted at various flow rates may allow for the determination of how to best conduct push-pull tests to distinguish between ganglia dominated and pool dominated source zones. It is hypothesized that *push-pull tests employing a slow injection flow rate, followed by a fast extraction flow rate will permit the discrimination of ganglia dominated zones from pool dominated zones.* The use of different flow rates for the “push” and “pull” phases of the partitioning tracer test may take advantage of equilibrium and nonequilibrium processes to help distinguish ganglia dominated and pool dominated source zones. A slow “push” may allow tracer concentrations to build up in the NAPL. The fast “pull” will then create nonequilibrium conditions, especially for the tracer mass associated with NAPL pools. This nonequilibrium

may cause tracer BTC tails to be longer if the region is dominated by pools than if it is dominated by ganglia.

Experiments related to Objective 5 use TCE-DNAPL source zones described by a low, mid and high pool fraction. For each pool fraction a series of three partitioning tracer tests will be conducted using a combination of “fast” and “slow” flows for each push and pull step. One tracer test employed a slow injection, followed by a fast extraction; another employed a fast injection, followed by a slow extraction; another employed a fast injection, followed by a fast extraction. Effluent data from these experiments were used to construct four breakthrough curves (three partitioning tracers and one nonpartitioning tracer) per pool fraction per flow-rate combination (nine sets of effluent data each producing four breakthrough curves). These effluent data are interrogated to explore potential relationships between pool fraction and the influence of non-equilibrium on effluent curves. Data from each of the nine experiments are modeled using a fine scale numerical simulator developed by Mr. Ali Boroumand in collaboration with Dr. Linda M. Abriola. All codes were written or adapted by Mr. Boroumand for use in modeling the push-pull experiments described herein. Simulations are compared to experimental data for model validation. Data and simulations related to this objective are presented and interpreted in Chapter 7.

**Objective 6: Explore the influence of DNAPL architectural features on push-pull test breakthrough curves.**

Objective 5 examines the influence of kinetic mass transport in heterogeneous architectures by conducting both laboratory and modeling push-

pull experiments in three source zones of different pool fraction. These push-pull tests may also be sensitive to source zone architecture features other than pool fraction. Therefore, objective 6 focuses on determining whether push-pull tests can be used to distinguish differences in vertical and horizontal DNAPL distribution.

It is hypothesized that *push-pull partitioning tracer tests are able to distinguish differences in the vertical extent of DNAPL within the interrogated volume, but cannot distinguish horizontal extent.* The basis for this hypothesis is that the number of tracer flow paths interacting with the DNAPL is highly dependent on the vertical spread. As tracer flow paths are primarily horizontal, the larger fraction of the vertical dimension containing DNAPL the more tracer solution will contact the DNAPL. A smaller vertical spread results in less tracer flow paths interacting with the DNAPL. Contrastingly, the horizontal extent of DNAPL does not as strongly impact the number of tracer flow paths intersecting the DNAPL phase. A large horizontal extent of DNAPL may cause more tracer mass in each interacting flow path to partition into the DNAPL, but will not affect the tracer mass whose flow paths do not contact the DNAPL. This hypothesis was tested by running push-pull tests in the 2-D push-pull model written by Mr. Boroumand (validated in objective 5) through source zones contrived to highlight differences in vertical and horizontal DNAPL distribution. Simulations related to this objective are presented and interpreted in Chapter 8.

## CHAPTER 3 – MATERIALS AND METHODS

### 3.1 – Materials

2-propanol (HPLC grade), 1-pentanol (99%), 1-hexanol (98%), 2-octanol (97%), and trichloroethene (TCE) (ACS grade) were obtained from Sigma Aldrich and used as received. 2-propanol (IPA) is miscible with water and used as a solvent in preparing samples for analysis. Relevant properties of 1-pentanol, 1-hexanol, 2-octanol and TCE are shown in Table 3.1. All aqueous solutions were made using water purified to have resistivity  $> 18.1 \text{ M}\Omega\cdot\text{cm}$  and TOC  $< 10$  ppb using a MilliQ A-10 system (Millipore).

**Table 3.1** Physical properties of alcohol tracers and TCE

Alcohol	$K_p^{C_i}$ ( $L_{\text{aq}}/L_{\text{TCE-DNAPL}}$ )	Density (g/mL)	Solubility, in aq. (mg/L)	Solubility, aq. in (mg/L)	Purity %
1-pentanol	3.8 <sup>a,f</sup>	0.815 <sup>b,d</sup>	2.19%w <sup>b,d</sup>	7.46%w <sup>b,d</sup>	99
1-hexanol	18.6 <sup>a,f</sup>	0.820 <sup>a,d</sup>	0.706%w <sup>a,d</sup>	7.42%w <sup>a,d</sup>	98
2-octanol	317 <sup>a,f</sup>	0.82 <sup>a,d</sup>	0.127 <sup>a,d</sup>	3.40%w <sup>a,d</sup>	97
trichloroethene	-	1.45 <sup>b,c</sup>	0.098 <sup>a,e</sup>	0.032 <sup>b,d</sup>	ACS grade

<sup>a</sup>20 °C; <sup>b</sup>25 °C; <sup>c</sup>temperature was not reported; <sup>d</sup>Riddick and Bunger (1970); <sup>e</sup>Horvath et al. (1999); <sup>f</sup>Dwarakanath and Pope, 1998

For transport experiments (1-D column and 2-D box) TCE-DNAPL was dyed with  $10^{-4}$  M Oil-Red-O (Alfa Aesar) for the purpose of visualization. Previous research has shown that the addition of Oil-Red-O at this concentration does not significantly affect the relevant physical properties of the DNAPL (Taylor et al., 2001), nor the partitioning behavior of the tracers (Willson et al., 2000).

Federal Fine Ottawa sand (30-140 mesh) was obtained from U.S. Silica and used as the background packing media for all column and aquifer cell experiments. Federal fine is quartz sand comprised of 99.7% Silicon Dioxide (U.S. Silica) and has an intrinsic permeability of  $4.2 \times 10^{-11} \text{ m}^2$  (Suchomel et al., 2007). The grain size distribution of Federal Fine is shown below in Figure 3.1 (U.S. Silica). For the aquifer cell used to examine transport in pooled source zones (Chapter 6) Federal Fine was used as received. Federal Fine was sieved in 200 g batches on a shaker for 10-15 min to obtain the 45-50 sand fraction and the 40-50 sand fraction for 1-D column experiments (Chapter 5) and heterogeneous source zone aquifer cells (Chapter 7), respectively. F-70 sand was obtained from U.S. Silica and used as received to create all low permeability layers. F-70 has is also a quartz sand that is 99.7% Silicon Dioxide (U.S. Silica) and has an intrinsic permeability of  $8.2 \times 10^{-12} \text{ m}^2$  (Suchomel et al., 2007). A grain size distribution of F-70 is shown below in Figure 3.2.

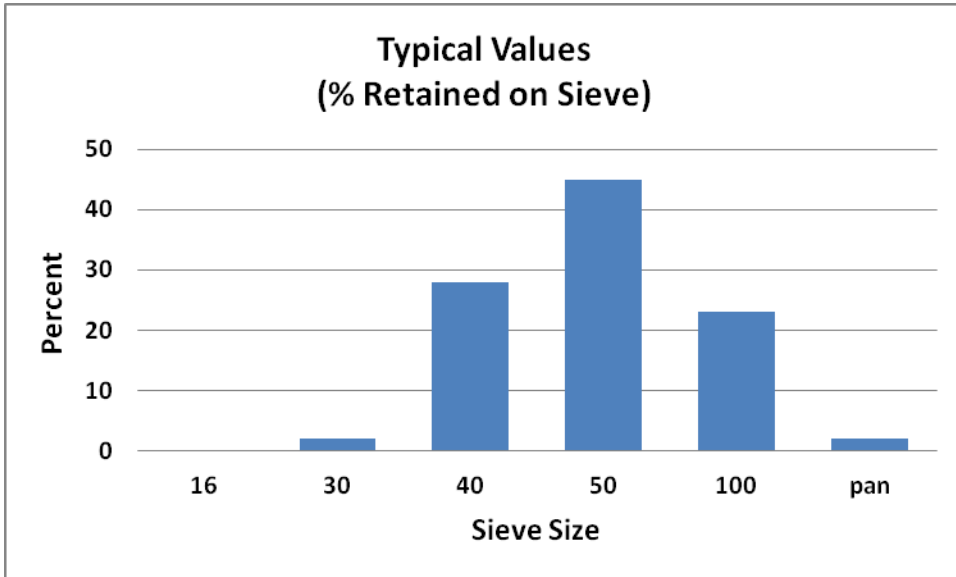


**Figure 3.1** Sieve analysis for Ottawa Federal Fine.

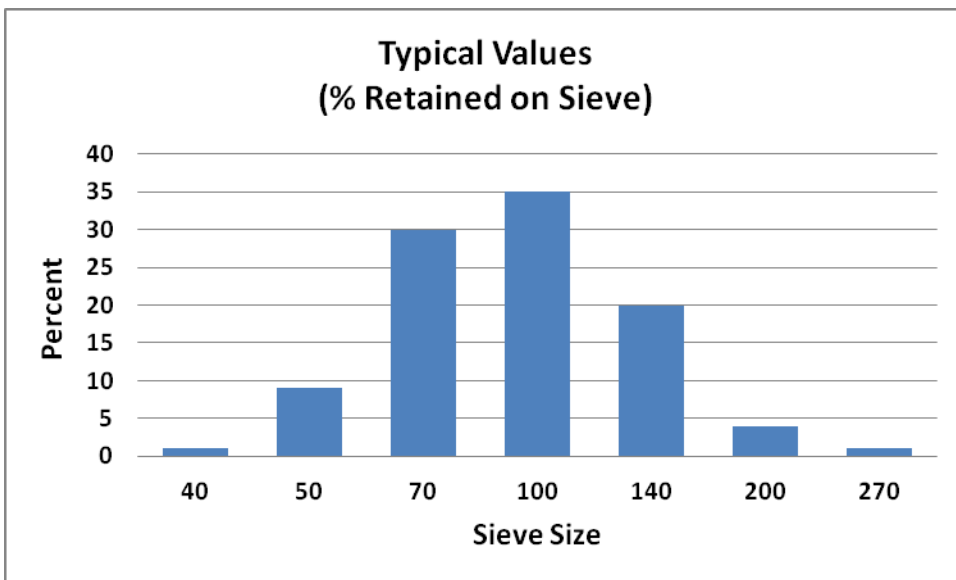


**Figure 3.2** Sieve analysis for F-70.

### **3.2 - Analytical Methods**

#### **3.2.1 - Alcohol and TCE Concentrations - Gas Chromatography**

Aqueous phase samples collected from batch experiments for alcohol and TCE were diluted using Milli-Q water and isopropanol (IPA), respectively. DNAPL samples collected from the batch experiments were diluted (~10x) using IPA. Aqueous phase samples from 1-D column and 2-D box experiments were analyzed without dilution.

Alcohol and TCE concentrations were quantified in duplicate using a Hewlett-Packard 6890 Gas Chromatograph (GC) equipped with a DB-5 (0.32 mm diameter, 30 m long) column and flame ionization detector at 250°C. A five-point calibration curve was obtained each day of use and checked using a calibration standard every 20 samples. Both the method for alcohol measurement and TCE measurement used nitrogen and hydrogen at a total flow rate of 18.1 mL/min. The method for alcohol quantification used a split injection with a split ratio of 0.5:1. The oven started at 35 °C for 2 min and ramped 35 °C/ min to a temperature of 115°C. The TCE quantification used a splitless injection and a simple temperature method of 35 °C for 5 min. The detection limit for each 1-pentanol, 1-hexanol, and 2-octanol is 1 mg/L. The detection limit for TCE is 5 mg/L.

#### **3.2.2 - Bromide and Chloride Concentrations - Ion Chromatography**

Bromide (non-reactive tracer) and chloride concentrations were quantified using a Dionex ICS-2000 Ion Chromatograph (IC) equipped with an AS-18 column (4 x 250 mm). The IC was calibrated with a six-point standard curve every fifteen samples. 25 µL of aqueous sample was injected pumped through the

IC at a flow rate of 1 mL/min. Potassium hydroxide at a concentration of 23.0 mM was used as the eluent.

### *3.2.3 - DNAPL Water Content - Karl Fischer Titration*

Water contents were quantified in duplicate using a Mettler Toledo DL38 Karl Fischer Titrator. Prior to each day of use the titrator was calibrated with an AquaStar 1% water standard. Calibration was checked with the water standard every ten samples.

### *3.2.4 - DNAPL Phase Density - Pycnometer*

Density of the DNAPL phase was measured in triplicate with a 2 mL glass pycnometer that was calibrated with water prior to each day of use.

### *3.2.5 - Interfacial Tension – Drop Shape Analyzer*

Equilibrium interfacial tensions (IFT) between the aqueous and organic phases were quantified via drop shape analysis (IT Concept Tracker). Depending on which equilibrium phase (NAPL or aqueous) was more dense, either the pendant (NAPL more dense) or the sessile up (aqueous more dense) drop configuration was used. NAPL drop volumes of approximately 20  $\mu$ L were created in a reservoir containing the corresponding equilibrium aqueous phase. Volumes varied slightly, dependant on interfacial tension. Interfacial tension measurements were taken every 20 seconds for 5 min. The overall interfacial tension was taken to be a 4 min average of steady-state measurements.

### ***3.3 - Experimental Methods***

#### ***3.3.1 - Liquid-Liquid-Equilibrium***

Liquid-liquid equilibrium (LLE) experiments permit accurate quantification of the partitioning over all possible alcohol concentrations while also allowing assessment of interfacial tension between the aqueous phase and the DNAPL. Initial overall compositions (comprising various amounts of water, tracer and TCE) were created in triplicate within 35 mL borosilicated glass centrifuge tubes (Corning, part number: 8422-35) with PTFE lined screw-cap closures (Kimble Chase part number 45066C). Tubes were subsequently equilibrated for 72 hr on oscillating shakers (LabQuake, model T415110) located within a controlled temperature room (Harris Environmental) operating at  $22.0\pm 0.1^{\circ}\text{C}$ . Previous experiments suggest 72 hr is sufficient for these types of systems to reach equilibrium (Gossett, 1987; Ramsburg and Pennell, 2002). After equilibration, the tubes were centrifuged at 1500 rpm and  $22^{\circ}\text{C}$  for 10 min (Beckman Coulter Avanti J-25) prior to careful separation and sampling (see analytical methods below) of the aqueous phase and DNAPL.

#### ***3.3.2 - 1-D Column Experiments***

All 1-D transport experiments were conducted in Kontes borosilicate glass columns (4.8 cm i.d.). The 45-50 mesh Ottawa Sand (see materials section) was selected to generate DNAPL ganglia that exist primarily as singlets (Schnaar and Brusseau, 2005; Ramsburg et al., 2010a). The column was saturated with  $\text{CO}_2$  for half an hour before being saturated with water at 1 mL/min for approximately 10 hours. Conservative, nonreactive tracer tests were conducted at a flow rate of

2.2mL/min pre and post TCE-DNAPL emplacement to estimate dispersivity and confirm the uniformity of the emplaced DNAPL distribution (Pennell et al., 1993). Here a pulse of approximately 2.7 pore volumes (PV) of an aqueous solution containing 0.01 M Br<sup>-</sup> was followed by 2 PV of 0.01 M Cl<sup>-</sup>.

TCE (dyed with Oil-Red-O) was pumped into the column at 0.5 mL/min using a Hamilton Syringe Pump until no aqueous phase could be seen. Pressure was then increased by injecting TCE into the column by hand to force out as much aqueous phase as possible. Once no additional aqueous phase could be seen in the effluent line, it was assumed that maximum saturation had been reached. To establish residual saturation, water was flushed through the column at 1 mL/min (in both directions) until no more TCE-DNAPL flowed out the column.

Partitioning tracer tests were conducted using 2 PV pulses introduced at the same flow rate. For non-equilibrium column studies, a fast flow rate (2.2 mL/min) and short packed length (5.0 cm) were selected to promote the observation of non-equilibrium conditions so that partitioning kinetics could be quantified. A column experiment was also run at 0.5 mL/min, attempting to achieve equilibrium partitioning. In columns where multiple tracer pulses were introduced to the system, they were conducted successively, ensuring that no concentration from the previous pulse was detected in the effluent before the next pulse began. Effluent samples were collected over short intervals through the peak of the BTC and over increasingly longer intervals as the test continued using a fraction collector (Retriever II, ISCO). Dissolution of the TCE-DNAPL was prevented by using Milli-Q water saturated with TCE for all aqueous solutions

introduced to the column. This experimental procedure ensured that each BTC was associated with the same saturation of TCE-DNAPL.

### *3.3.3 2-D Box Experiments – Pooled Source Zone*

Experiments examining tracer transport in a pool dominated source zone (Chapter 6) were completed in a 2-D aquifer cell. The aquifer cell (Figure 3.3) is constructed out of two pieces of flat polish, annealed, float glass (each piece 70 x 42 x 1.5 cm) held together with a 5 cm wide frame on the bottom and sides that creates a 1.4 cm gap between the pieces of glass. Note the dimensions shown in Figure 3.3 (63 x 39.5 cm) are smaller than those mentioned above because a portion of the glass sits inside the frame so that the structure is stable and airtight. The front piece of glass has 24 sampling ports for measuring local tracer BTCs; exact location of these ports is shown in Table 3.2. Each end of the metal frame has a fully screened well to encourage even flow through the box. Ottawa Federal Fine (30-140 mesh) sand is used as the background porous media and F-70 is used to create all low permeability layers. The box is wet packed, ensuring that 2 inches of Milli-Q water remain above the sand layer at all times during the process. A Hamilton Syringe Pump was used to pump TCE through an injection needle (gauge 18) packed into the box. Flow through the boxes was regulated by maintaining constant head at both the inlet and outlet. For the pooled source zone experiments, all solutions are pumped into the screened well on the left hand side of the box and out of the screened well on the right hand side of the box. Additional details on the packing structure, TCE-DNAPL source zone and partitioning tracer test parameters can be found in Chapter 6, Section 6.2.1.

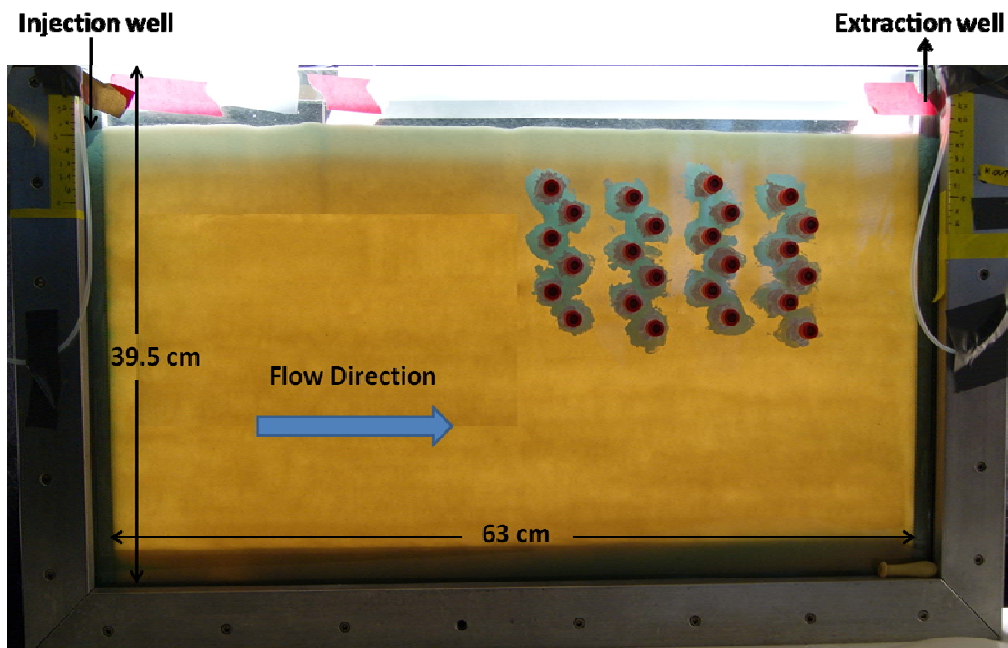


**Figure 3.3** 2-D box setup used to conduct partitioning tracer experiments in Chapter 6.

**Table 3.2** Locations of the local sampling ports shown in Figure 3.1.

<b>Port</b>	<b>Distance from Well (cm)</b>	<b>Distance from Bottom (cm)</b>	<b>Port</b>	<b>Distance from Well (cm)</b>	<b>Distance from Bottom (cm)</b>
<b>1A</b>	33.0	29.5	<b>3A</b>	45.0	29.5
<b>1B</b>	34.0	27.5	<b>3B</b>	46.0	27.5
<b>1C</b>	33.0	25.5	<b>3C</b>	45.0	25.5
<b>1D</b>	34.0	23.5	<b>3D</b>	46.0	23.5
<b>1E</b>	33.0	21.5	<b>3E</b>	45.0	21.5
<b>1F</b>	34.0	19.5	<b>3F</b>	46.0	19.5
<b>2A</b>	39.0	28.5	<b>4A</b>	100.0	28.5
<b>2B</b>	40.0	26.5	<b>4B</b>	102.0	26.5
<b>2C</b>	39.0	24.5	<b>4C</b>	100.0	24.5
<b>2D</b>	40.0	22.5	<b>4D</b>	102.0	22.5
<b>2E</b>	39.0	20.5	<b>4E</b>	100.0	20.5
<b>2F</b>	40.0	18.5	<b>4F</b>	102.0	18.5

### 3.3.4 - 2-D Box Experiments – Heterogeneous Source Zone

Experiments examining tracer transport in heterogeneous source zones (Chapter 7) were also completed in a 2-D aquifer cell. This aquifer cell (Figure 3.4) is slightly larger with two pieces of flat polish, annealed, float glass (each piece 107 x 52 x 1.5 cm). It is held together with a similar frame, that also creates at 1.4 cm gap between the pieces of glass. Again, the dimensions shown in Figure 3.4 (100 x 49.5 cm) are smaller than those mentioned above because a portion of the glass sits inside the frame so that the structure is stable and airtight. The front piece of glass has 25 sampling ports for measuring local tracer BTCs. Only the first two columns of ports were used in the heterogeneous source zone experiments. The exact locations of the ports used in these experiments are shown in Table 3.3. Each end of the metal frame has a fully screened well to encourage even flow through the box. Ottawa Federal Fine (30-140 mesh) sand is used as the background porous media and F-70 is used to create all low permeability layers. The box is wet packed, ensuring that 2 inches of Milli-Q water remain above the sand layer at all times during the process. A Hamilton Syringe Pump was used to pump TCE through an injection needle (gauge 18) packed into the box. Flow through the boxes was regulated by maintaining constant head at both the inlet and outlet. These experiments were run with a push-pull flow scheme, using the left-hand well as both the injection well and the extraction well. Additional details on packing structure, TCE-DNAPL source zones and partitioning tracer test parameters can be found in Chapter 7, Sections 7.3-7.5.

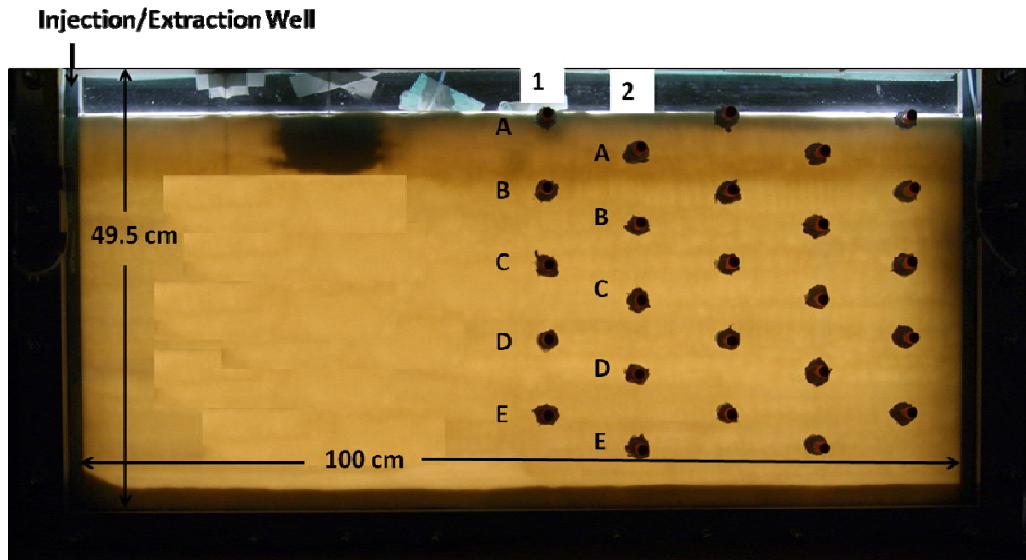


**Figure 3.4** 2-D box setup used to conduct push-pull experiments in heterogeneous source zones in Chapter 7.

**Table 3.3** Locations of the local sampling ports shown in Figure 3.2.

<b>Port</b>	<b>Distance from Well (cm)</b>	<b>Distance from Bottom (cm)</b>	<b>Port</b>	<b>Distance from Well (cm)</b>	<b>Distance from Bottom (cm)</b>
<b>1A</b>	53.0	10.0	<b>2A</b>	63.0	6.0
<b>1B</b>	53.0	18.5	<b>2B</b>	63.0	14.5
<b>1C</b>	53.0	27.0	<b>2C</b>	63.0	23.0
<b>1D</b>	53.0	35.5	<b>2D</b>	63.0	31.5
<b>1E</b>	53.0	44.0	<b>2E</b>	63.0	40

### 3.3.5 - *Light Transmission Imaging*

The light transmission (LT) system and methods employed in this research are based upon that described in Suchomel and Pennell (2006). LT was used to image the packed boxes before and after the introduction of TCE-DNAPL. In addition, LT was used to monitor the TCE-DNAPL saturation distribution over the course of tracer testing. For LT imaging, the aquifer cell was illuminated with a light bank (Kino Flo Inc.) placed directly behind the system. A Sony  $\alpha$ 330 (10.2 mega pixels) digital camera was then used to take images of the entire box. Images captured in the absence of DNAPL permit accurate quantification of the location and shape of the low permeability lenses. For images captured with TCE-DNAPL present, the LT data permit quantification of the local DNAPL saturations. Quantification of DNAPL saturation is based upon image hues that are correlated to saturation with calibration curves developed using the method of Darnault et al. (1998). This method produces a pixel-by-pixel estimation of thickness-averaged saturation. Saturation, however, is a REV based property of the phase. Recent work by Christ et al. (2012) has demonstrated that the pixel-by-pixel estimates of saturation must be upscaled to better represent the physical definition of saturation. Following the guidance of Christ et al. (2012) thickness averaged saturation distributions were estimated over a 0.98 cm x 0.98 cm averaging window using Matlab 10.0 (Mathworks, Inc.). (This is compared to a pixel size of 0.02 cm x 0.02 cm). Two types of averaging were applied: i) discrete block averaging, which uses averaging windows that do not overlap; ii) continuous averaging, which uses overlapping averaging windows. Additional

details on these averaging methods can be found in Christ et al. (2012). The saturation calculations were summed over the entire source zone and compared to the known volume of injected TCE. Additionally, the Matlab 10.0 script was used to calculate pool fraction. For these experiments, a unit volume of porous media was defined as pooled if the TCE-DNAPL saturation is greater than 17%, and ganglia if the saturation is less than 17%. The value of 17% was chosen as the cutoff because this was the residual saturation determined by column experiments in Chapter 4. The Matlab 10.0 scripts used to estimate spatial saturation distribution and calculate pool fraction were provided by Dr. John Christ and Mr. Doug Walker.

### ***3.4 - Mathematical Modeling***

Mathematical modeling was used to examine data produced in all laboratory experiments. The purpose of modeling the experiments is two-fold: first it is of interest to determine whether mathematical models are able to predict experimental results; second, when models have been validated with laboratory data, they can be used to conduct additional experiments. This allows for further data generation at a much faster rate than can be accomplished with laboratory experiments. The models used to describe each type of experiment (LLE, 1-D transport and 2-D transport) are discussed in detail below.

#### ***3.4.1 - Thermodynamic modeling of LLE***

The phase behavior of each alcohol in the water-alcohol-TCE ternary was predicted using an isothermal flash calculation performed in Matlab version R2009b (The MathWorks, Inc) (e.g., Smith and Van Ness, 1987). UNIFAC

(Fredenslund et al., 1975) was employed to estimate activity coefficients using available structural parameters (Hansen et al., 1991). Greater detail on this model can be found in Chapter 1, Section 1.5.1. Water was assigned as  $1 \times \text{H}_2\text{O}$  (group 7). 1-pentanol was assigned as  $1 \times \text{CH}_3$  (group 1) +  $4 \times \text{CH}_2$  (group 1) +  $1 \times \text{OH}$  (group 5). 1-hexanol was assigned as  $1 \times \text{CH}_3$  (group 1) +  $5 \times \text{CH}_2$  (group 1) +  $1 \times \text{OH}$  (group 5). 2-octanol was assigned as  $2 \times \text{CH}_3$  (group 1) +  $5 \times \text{CH}_2$  (group 1) +  $1 \times \text{CH}$  (group 1) +  $1 \times \text{OH}$  (group 5). TCE was assigned as  $1 \times \text{HC}=\text{C}$  (group 2) +  $2 \times \text{Cl}-\text{C}=\text{C}$  (group 37). Interaction parameters used for each of these groups are shown in Table 3.4. Iteration convergence was established when successive changes to molar phase fractions and component mole fractions were less than  $1 \times 10^{-10}$ .

**Table 3.4** UNIFAC group interaction parameters ( $\alpha_{ij}$ ).

$\alpha_{ij}$	group 1 C-C	group 2 C=C	group 5 -OH	group 7 H <sub>2</sub> O	group 37 Cl-C=C
group 1 C-C	0 <sup>a</sup>	74.54 <sup>b</sup>	644.6 <sup>b</sup>	1300 <sup>b</sup>	-0.505 <sup>c</sup>
group 2 C=C	292.3 <sup>b</sup>	0 <sup>a</sup>	724.4 <sup>b</sup>	785.6 <sup>d</sup>	237.3 <sup>c</sup>
group 5 -OH	328.2 <sup>b</sup>	470.7 <sup>b</sup>	0 <sup>a</sup>	353.5 <sup>c</sup>	253.9 <sup>c</sup>
group 7 H <sub>2</sub> O	342.4 <sup>b</sup>	-26.52 <sup>d</sup>	-229.1 <sup>c</sup>	0 <sup>a</sup>	651.9 <sup>d</sup>
group 37 Cl-C=C	41.90 <sup>c</sup>	-3.167 <sup>c</sup>	640.9 <sup>c</sup>	1100 <sup>d</sup>	0 <sup>a</sup>

<sup>a</sup> by definition; <sup>b</sup> Magnussen et al. (1981); <sup>c</sup> Gmehling et al. (1982); <sup>d</sup> Cooling et al. (1992)

### 3.4.2 - Partitioning Tracer Transport - Ganglia

A number of conceptual approaches for interphase partitioning behavior, including equilibrium, linear driving force, dual diffusion and surface resistance, were implemented in a numerical simulator to explore the mechanisms controlling tracer transport in systems of entrapped ganglia. All models used to produce BTCs for the column experiments were developed by Mr. Ali Boroumand and Dr. Linda Abriola and numerically coded into Matlab by Mr. Boroumand. All models assume that transport occurs only in the aqueous phase, with an immobile TCE-DNAPL, distributed uniformly as spherical singlets. This assumption is supported by visualization of DNAPL distributions within similar size fractions of sandy media (Schnaar and Brusseau, 2005). Within the model, TCE-DNAPL dissolution is assumed negligible and the flow is uniform, consistent with the experimental methods employed. Based upon the above assumptions, flow and mass balance equations for the two fluid phases (aqueous and DNAPL) need not be explicitly written.

The governing equation for 1-D tracer mass transport is a simplified version of the multiphase advective-dispersive-reactive transport equation, where tracer interaction occurs only with the DNAPL:

$$nS_n \frac{\partial C_n}{\partial t} + nS_{aq} \frac{\partial C_{aq}}{\partial t} = nS_{aq} (\alpha|v| + D_{aq}) \frac{\partial^2 C_{aq}}{\partial x^2} - nS_{aq} v \frac{\partial C_{aq}}{\partial x} \quad (3.1)$$

Here  $C_{aq}$  is the bulk phase aqueous concentration [ $M \cdot L^{-3}$ ],  $C_n$  is average concentration of the tracer contained within the DNAPL [ $M \cdot L^{-3}$ ], and  $v$  is the pore water velocity [ $L \cdot T^{-1}$ ].  $\alpha$ ,  $D_{aq}$ ,  $S_{aq}$ ,  $S_n$ , and  $n$  are the dispersivity [ $L$ ], solute

diffusivity in the aqueous phase [ $L^2 \cdot T^{-1}$ ], aqueous saturation [-], DNAPL saturation [-], and porosity [-], respectively, which are assumed to be temporally and spatially invariant.

The alternative conceptual modeling approaches employed here for tracer partitioning vary in the way the source/sink term  $nS_n \frac{\partial C_n}{\partial t}$  is represented. These models differ in their assumptions pertaining to transport within the DNAPL (completely mixed versus diffusive transport) and descriptions of solute exchange between the DNAPL and aqueous phase (equilibrium, linear driving force kinetics, and surface resistance). Detailed presentations of these models are available elsewhere (e.g., Brusseau and Rao, 1989; Liggieri et al., 1997). What follows below are brief descriptions of how each approach was implemented for one dimensional alcohol transport in a medium containing entrapped TCE-DNAPL. Irrespective of the alternative approaches adopted to represent the sink/source term, all models employed third and second type boundary conditions for the column inlet and outlet, respectively. Equations were discretized using a Crank-Nicholson finite difference approach and solved numerically.

#### 3.4.2.1 - *Equilibrium*

Here it is assumed that the flow rate is sufficiently slow such that the DNAPL and aqueous concentrations reach equilibrium at the grid resolution scale of the model. Defining  $K_p^{C_i}$  as the concentration-based equilibrium partitioning coefficient (Ramsburg et al., 2010b) of the tracer between the DNAPL and aqueous phases, yields:

$$nS_n \frac{\partial C_N}{\partial t} = nS_n K_p^{C_i} \frac{\partial C_{aq}}{\partial t} \quad (3.2)$$

### 3.4.2.2 - Linear Driving Force

The linear driving force approach assumes that diffusion across an immobile aqueous phase boundary layer can be represented by a first order mass transfer expression. Intra-DNAPL diffusional resistance is ignored, and distribution of components inside the DNAPL is assumed uniform. Component concentrations at the interface of the boundary layer and the DNAPL are assumed to be in equilibrium, while a linear concentration gradient exists within the stagnant aqueous film surrounding each DNAPL droplet. The source/sink term becomes:

$$nS_n \frac{\partial C_n}{\partial t} = \hat{k} \left( C_{aq} - \frac{C_n}{K_p^{C_i}} \right) \quad (3.3)$$

Here  $\hat{k}$  is a lumped mass transfer coefficient [ $T^{-1}$ ]. For the model results presented herein, the lumped mass transfer coefficient was evaluated using an empirical correlation developed for NAPL dissolution (Powers et al., 1992). Ramsburg et al. (2010a) have recently shown that the Powers et al. (1992) and Imhoff et al. (1994) correlations are capable of, and offer similar performance when, describing the mass transfer of chlorinated solvent degradation products within columns containing uniform saturations of DNAPL.

### 3.4.2.3 - Dual Diffusion

In this approach, as with the linear driving force model, interphase mass transfer occurs through an immobile aqueous boundary layer surrounding DNAPL ganglia. Thus, Equation 3.3 remains valid for the source/sink term. The assumption that the DNAPL is well mixed is, however, relaxed. Diffusion within the NAPL is assumed to be Fickian and the radial distribution of tracer concentration within the NAPL droplets satisfies (Rasmuson and Neretnieks, 1980):

$$\frac{\partial C_{n,r}}{\partial t} = D_n \left( \frac{\partial^2 C_{n,r}}{\partial r^2} + \frac{2}{r} \frac{\partial C_{n,r}}{\partial r} \right) \quad (3.4)$$

subject to the following boundary conditions:

$$D_n \frac{\partial C_{n,r=b}}{\partial r} = k_f \left( C_{aq} - \frac{C_{n,r=b}}{K_p^{C_i}} \right) \quad (3.5)$$

$$\frac{\partial C_{n,r=0}}{\partial r} = 0 \quad (3.6)$$

Here  $C_{n,r}$  is the component concentration within the DNAPL [ $M \cdot L^{-3}$ ] at radial position,  $r$  [L],  $D_n$  is solute diffusion coefficient in the DNAPL [ $L^2 \cdot T^{-1}$ ],  $b$  is radius of the DNAPL droplet [L], and  $k_f$  is the mass transfer coefficient [ $L \cdot T^{-1}$ ]. Equation 3.5 (continuity of fluxes) assumes no surface accumulation at the DNAPL-aqueous interface.

Previous studies have measured the average singlet radius of entrapped NAPL for various sand fractions (Powers et al. 1992; Schnaar and Brusseau, 2005). Schnaar and Brusseau (2005) and Ramsburg et al. (2010a) developed regressions that relate an effective DNAPL drop radius to the saturation and

textural characteristics of the granular medium. The correlation of Ramsburg et al. (2010a) is employed herein to estimate ganglia size. To convert from  $k_f$  to  $\hat{k}$ , the model assumes that all of the DNAPL surface area is accessible to the tracer, and that this surface area can be calculated assuming a uniform distribution of spherical droplets:

$$\hat{k} = k_f \left( \frac{3nS_{aq}}{b} \right) \quad (3.7)$$

An existing numerical model (Mendoza-Sanchez and Cunningham, 2007) was adapted to simultaneously solve the system of Equations. Equation 3.5 serves to couple the aqueous phase and DNAPL transport equations at the interface. The solution was validated against an existing semi-analytical solution (Rasmuson and Neretnieks, 1980). Accuracy of the dual diffusion algorithm was verified through comparisons with linear driving force solutions for an extreme (high) DNAPL diffusion coefficient.

#### *3.4.2.4 - Dual Diffusion and Surface Partitioning*

A key assumption in both the linear driving force and dual diffusion conceptual models is that mass fluxes toward and away from the DNAPL/aqueous interface are equal, such that no surface accumulation occurs. In a surface partitioning model, tracer accumulation at the interface is permitted, adding a third resistance to tracer mass transport. The approach employed herein is based largely on the work of Liggieri et al. (1997), who studied adsorption kinetics of

alkylphosphines oxides at a water/hexane interface. A mass balance equation within the interface is expressed as:

$$\frac{\partial \Gamma}{\partial t} = k_f (C_{aq} - C_{int}) - D_n \frac{\partial C_{n,r=b}}{\partial r} \quad (3.8)$$

where  $\Gamma$  is the accumulation of mass at the interface [ $M \cdot L^{-2}$ ]. In this formulation, Equation 3.8 replaces Equation 3.5. The left hand side of Equation 3.8 is

rewritten as  $\frac{\partial \Gamma}{\partial C_{int}} \frac{\partial C_{int}}{\partial t}$  and a local equilibrium assumption is invoked at the

interface, with  $\Gamma$  represented by a Langmuir isotherm expression. Using this approach, the maximum capacity at the interface between the aqueous phase and DNAPL is not reached until  $C_n$  becomes equal to the effective solubility of tracer in the DNAPL ( $K_p^{C_i} C_{aq}$ ). The system of equations is solved iteratively. At the

start of each time step, the known isotherm parameters and the  $C_{int}$  from the previous time step are used to estimate the accumulation term coefficient  $\left( \frac{\partial \Gamma}{\partial C_{int}} \right)$ .

The system of equations is then solved for new interface concentrations, which are compared with the original values (Ervin et al., 2011). Iterations are performed until the convergence criterion ( $0.001 \text{ mg/m}^2$ ) is reached and all equations are satisfied.

### 3.4.3 - Partitioning Tracer Transport – Pooled Source Zone

As with column experiment modeling, all models used to produce BTCs for 2-D aquifer cell experiments were developed by Mr. Ali Boroumand and Dr. Linda Abriola and numerically coded into Matlab by Mr. Boroumand. A 2-D

numerical linear driving force model is used to simulate partitioning tracer transport in the 2-D aquifer cells (Chapters 6 - 8). Flow is described using the 2-D groundwater flow equation:

$$S_s \frac{\partial \phi}{\partial t} = \frac{\partial}{\partial x} \left( K \frac{\partial \phi}{\partial x} \right) + \frac{\partial}{\partial y} \left( K \frac{\partial \phi}{\partial y} \right) \quad (3.9)$$

where,

$$K = \frac{k_{rw} \rho_{aq} g}{\mu_{aq}} \quad (3.10)$$

where  $S_s$  [ $L^{-1}$ ] is the specific storage,  $\phi$  is hydraulic head [ $L$ ],  $K$  [ $L \cdot T^{-1}$ ] is the hydraulic conductivity of the porous medium (here assumed to be isotropic),  $k_{rw}$  is the relative permeability [ $L^2$ ],  $\mu_{aq}$  is the dynamic viscosity of the aqueous phase [ $M \cdot L^{-1} \cdot T^{-1}$ ], and  $g$  is the gravitational constant [ $L \cdot T^{-2}$ ]. A relative permeability function is necessary to account for the reduction in permeability due to the presence of the TCE-DNAPL. The Kaluarachichi and Parker (1992) relative permeability function is used to account for the reduction in permeability:

$$k_{rw} = S_{aq}^{0.5} \left( 1 - \left( 1 - S_{aq}^{1/m} \right)^m \right)^2 \quad (3.11)$$

$$m = 1 - \frac{1}{n_{vg}} \quad (3.12)$$

where  $k_r$  [ $L^2$ ] is the reduced permeability due to the presence of the TCE-DNAPL and  $n_{vg}$  [-] is the Van Genuchten parameter that represents the uniformity of the pore size distribution. Herein, a value of 0.7 was employed because it has been previously used to model similar sands (Rathfelder and Abriola, 1996).

Because the model is confined, no flow boundary conditions apply to both the top and bottom boundary:

$$\left. \frac{\partial \phi}{\partial y} \right|_{y=0} = 0 \quad (3.13)$$

$$\left. \frac{\partial \phi}{\partial y} \right|_{y=H} = 0 \quad (3.14)$$

where H is the packed height of the 2-D aquifer cell [L]. Flow is controlled by prescribing head (from experimental piezometric head readings) in the fully screened inlet and outlet wells:

$$\phi|_{x=0} = h_1 \quad (3.15)$$

$$\phi|_{x=L_{\text{box}}} = h_2 \quad (3.16)$$

where  $h_1$  and  $h_2$  are the heads [L] at the left and right hand side of the box, respectively and  $L_{\text{box}}$  [L] is the length of the 2-D box. The inlet and outlet wells were modeled as very high permeability columns added to the sides of the domain. The exact locations of the tubing used for experimental injection and extraction were modeled inside the screened wells.

Again, tracer transport is assumed to occur only in the aqueous phase as described by the 2-D transport equation:

$$nS_{aq} \frac{\partial C_{aq}}{\partial t} + \hat{k} \left( C_{aq} - \frac{C_n}{K_p^{C_i}} \right) = \frac{\partial}{\partial x} \left( nS_{aq} (\alpha_{ij} |v| + D_{aq}) \frac{\partial C_{aq}}{\partial y} \right) - nS_{aq} v \frac{\partial C_{aq}}{\partial x} \quad (3.17)$$

where  $\alpha_{ij}$  is the 2-D dispersivity [L]. The longitudinal dispersivity is determined by fitting to the bromide data and the vertical dispersivity is assumed to be

0.1\*longitudinal dispersivity. The transport boundary conditions on the top and bottom of the domain are:

$$\left. \frac{\partial C_{aq}}{\partial y} \right|_{y=0} = 0$$

(3.18)

$$\left. \frac{\partial C_{aq}}{\partial y} \right|_{y=H} = 0 \tag{3.19}$$

When combined with the no flow boundary conditions at the top and bottom (eqs 3.13 and 3.14), equations 3.18 and 3.19 result in no advective or dispersive flux at these boundaries. No dispersive flux is allowed on either side of the domain:

$$\left. \frac{\partial C_{aq}}{\partial x} \right|_{x=0} = 0 \tag{3.20}$$

$$\left. \frac{\partial C_{aq}}{\partial x} \right|_{x=L_{box}} = 0 \tag{3.21}$$

The DNAPL phase equation is the same as equation 3.2. As with the 1-D linear driving force model, it is assumed that diffusion across an immobile aqueous phase boundary layer can be represented using a first order mass transfer expression.

For the model results presented herein, the lumped mass transfer coefficient was evaluated using the Nambi and Powers (2003) empirical correlation developed for NAPL pool dissolution. Further detail on the development of this correlation can be seen in Chapter 1, Section 1.5.4.2. In

order to account for continued tracer partitioning into the TCE-DNAPL during the flow interruption in experiments 2 and 3 (Chapter 6, Section 6.2.2) the Nambi and Powers (2003) correlation was modified slightly according to the method of Unger et al. (1998). Unger et al. (1998) modified the Powers et al. (1994) dissolution correlation so that NAPL dissolution would occur during periods of no flow due to diffusion. This was accomplished by adding 0.01 to the Reynolds number. This term is large enough to allow for slight dissolution to occur during no flow periods, but does not significantly impact the mass transfer coefficient as long as the pore water velocity is greater than 0.07 cm/min (Unger et al., 1998). The slowest pore water velocity used for experiments in Chapter 6 is 0.25 cm/min, well above 0.07 cm/min. Therefore, to account for mass transport during the flow interruptions, the Nambi and Powers (2003) correlation was modified to:

$$Sh = \frac{\hat{k}L^2}{D_{aq}} = 37.7(S_n)^{1.24} (0.01 + Re^{0.61}) \quad (3.22)$$

The model employs a Crank-Nicholson finite difference approach to solve the aqueous-phase transport equation and DNAPL phase component mass balance (assumes complete mixing). Light transmission images of the experimental system before TCE-DNAPL injection allow for the exact geometry of the 2-D box (i.e. the location of low and high permeability layers) to be input into the model domain. The exact TCE-DNAPL saturation distribution is added to the domain using light transmission results after TCE-DNAPL injection. The domain is discretized into 5 mm x 5 mm grid blocks, which is similar to the averaging window used to estimate pool fraction from the light transmission pictures. Hydraulic conductivity values for each sand type are estimated from intrinsic

permeability (Section 3.1) and then refined using known experimental velocities and piezometric head readings.

The flow field is solved using MODFLOW, which is called from the Matlab code written by Mr. Boroumand. A transient flow field is used any time the influent or effluent head values are changed (e.g. start of experiment, flow interruption, reversal of flow in push-pull tests). MODFLOW is called once at the beginning of each simulation and all flow fields are calculated. Once the flow fields are established, the Matlab code then computes the transport of each tracer through the flow fields in sequential order. A time step of 20 seconds was used for all simulations, upon determining that a smaller time step produced the same BTCs. Flux averaged tracer concentrations are output for the effluent well (right-hand side of the aquifer cell), and local tracer concentrations can be output at any location in the domain. Here this functionality is used to output local tracer BTCs at the locations presented in Table 3.2.

#### *3.4.4 - Partitioning Tracer Transport - Heterogeneous DNAPL Distributions*

The model used to examine tracer transport in source zones with heterogeneous TCE-DNAPL distributions (Chapter 7) is the same as the 2-D model described above. The only difference here is that effluent BTCs are output for the left-hand well that is used as both the injection and extraction well.

## **CHAPTER 4 – EQUILIBRIUM PARTITIONING AND INTERFACIAL ADSORPTION OF SELECTED ALCOHOLS IN SYSTEMS COMPRISING ALCOHOL, TCE-DNAPL AND WATER**

### ***4.1 - Introduction***

Tracer partitioning between a NAPL and aqueous phase has been examined at a variety of scales, ranging from batch experiments (Dai et al., 2001; Dwarakanath, 1997; Dwarakanath and Pope, 1998; Thal et al., 2007; Wang et al., 1998; Wise et al 1999; Young et al., 1999), to laboratory flow studies (Dai et al., 2001; Jin et al., 1995; Moreno-Barbero and Illangasekare, 2005, 2006, 2007; Wilson and Mackay, 1995) to field-scale research and application (Annable et al., 1998a, 1998b; Brooks et al., 2002; Jawitz et al., 1998; Meindardus et al., 2002; Nelson and Brusseau, 1996; Ramsburg et al., 2005; Rao et al., 1997, 2000). This body of research largely assumes that tracer partitioning is linear. The notable exception is the work of Wise and co-workers (1999a, 1999b) that used a Langmuir-type isotherm to represent observed partitioning nonlinearities.

The goal of this work is to explore the equilibrium conditions within the aqueous phase, the DNAPL and at the interface between the two phases. This was accomplished through a series of batch experiments using three, representative alcohol tracers: 1-pentanol, 1-hexanol, and 2-octanol. These three tracers were selected based: 1) upon use in previous tracer tests (e.g. Jin et al., 1997; Wilson et al., 2000; Brooks et al., 2002; Jalbert et al., 2003; Ramsburg et al., 2005; Moreno-Barbero et al., 2007; Hartog et al., 2010); 2) upon known adsorption to the aqueous-DNAPL interface (Chang and Franses, 1994; Kim et

al., 2007; Zhu et al., 2009), so that the importance of a surface resistance in mass transport could be evaluated.

## **4.2 - Results and Discussion**

### *4.2.1 – Equilibrium Partitioning*

The ternary phase diagram for each alcohol is shown in Figure 4.1. Each alcohol exhibits Type II ternary phase behavior, which results from two partially miscible pairs (alcohol/water and TCE/water) and one fully miscible pair (TCE/alcohol) (Sorensen et al., 1979). Also shown in Figure 4.1 is the UNIFAC prediction (dashed line) of the binodal curves that separate the two phase region from the DNAPL phase region (upper left curve) and the aqueous region (a small region, not visible in Figure 4.1, located in the lower right corner of the phase diagram). Tie lines (solid lines) connect the two points corresponding to the measured, equilibrium compositions of the two phases. Any initial composition located between the binodal curves will separate into two phases each having a composition lying on the binodal curves that is connected by a tie line.

The nonlinear partitioning of each tracer between the TCE-DNAPL and aqueous phase is shown in Figure 4.2. The nonlinearity in the partitioning behavior means that  $K_p^{C_i}$  is a function of phase composition. (Herein partition coefficients refer to concentration based partition coefficients ( $K_p^{C_i}$ ) with units of  $[L^3/L^3]$  as opposed to mol fraction based partition coefficients ( $K_p^{X_i}$ ) which are unitless). As additional tracer is added to the system, the DNAPL phase composition is increasingly dominated by the alcohol. This creates more favorable

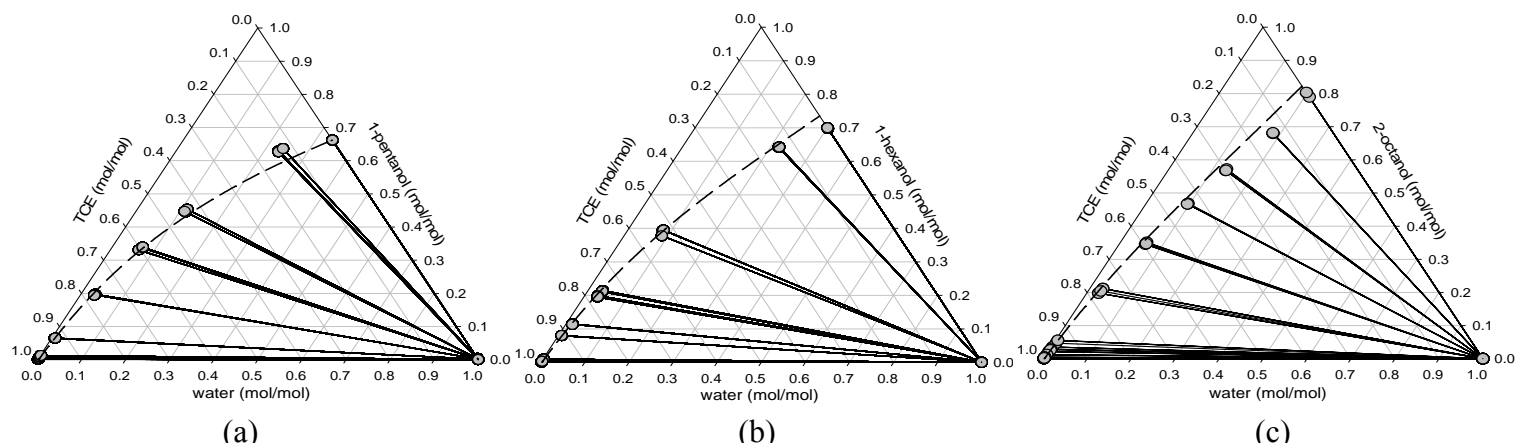


**Figure 4.1** Ternary phase diagrams at  $22.0 \pm 0.1^\circ\text{C}$  for 1-pentanol (a), 1-hexanol (b), and 2-octanol (c) developed from liquid-liquid equilibrium batch experiments. Experimental data are shown as tie lines. UNIFAC predictions of the binodal curves defining each two phase region are shown as dotted lines. The binodal curve defining the aqueous phase is not visible but exists in the lower right corner of each phase diagram.

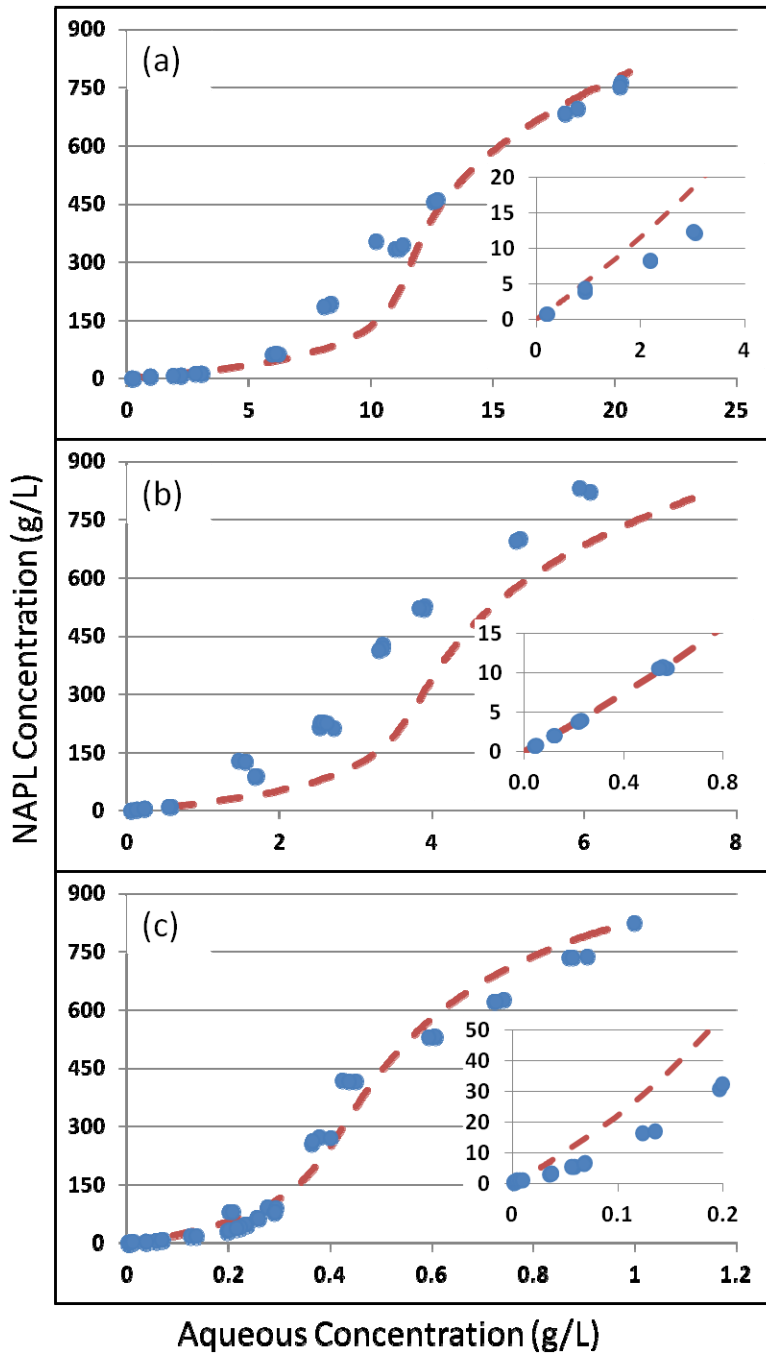


**Figure 4.2** The distribution of 1-pentanol (a), 1-hexanol (b) and 2-octanol (c) between the DNAPL and aqueous phases  $22.0 \pm 0.1^\circ\text{C}$  as established by liquid-liquid equilibrium data (circles). Dashed line shows UNIFAC predictions using literature interaction parameters. Note that data span the range of possible aqueous concentrations but that differences in solubility necessitate change in the horizontal range for each panel. Insets show dilute range.

tracer (and water) interactions in the DNAPL phase, and a shift away from the deviations from Raoult's Law that are exhibited at low alcohol concentrations.

Evident in Figure 4.2 is a region at lower concentration where the partitioning data can be approximated as linear, above which the partition coefficient increases with increasing concentration. The assumption of linear partitioning appears to be applicable below approximately 3,000 mg/L, 600 mg/L and 200 mg/L for 1-pentanol, 1-hexanol and 2-octanol, respectively (Figure 4.2). A Linear, weighted, least squares regression was employed in the dilute region of each alcohol tracer to determine the linear partition model (Ramachandran et al., 1996). The resulting partition coefficients (at  $22.0 \pm 0.1^\circ\text{C}$ ) for 1-pentanol, 1-hexanol and 2-octanol in a TCE-DNAPL/water system are  $4.20 \pm 0.10$ ,  $17.4 \pm 0.2$ , and  $149 \pm 8$   $L_{\text{aq}}/L_{\text{DNAPL}}$ , respectively (Figure 4.3).

It is noted that all three of these measured values represent a different amount of partitioning than has been previously reported (Table 4.1). The discrepancy between measured and literature values for the partitioning of 2-octanol (in a TCE/water system) is approximately 113%. This large discrepancy for 2-octanol is consistent with the fact that 2-octanol exhibited the greatest nonlinearity (Figure 4.2). In addition, both  $K_p$  values for 2-octanol appearing in Table 4.1 (317 and 332) were estimated based upon equivalent alkane carbon number (Dwarakanath and Pope, 1998; Thal et al., 2007). While these estimates may hold value when screening alcohols, the data shown in Figure 4.2 demonstrate the need for careful measurement of partition coefficients prior to application.

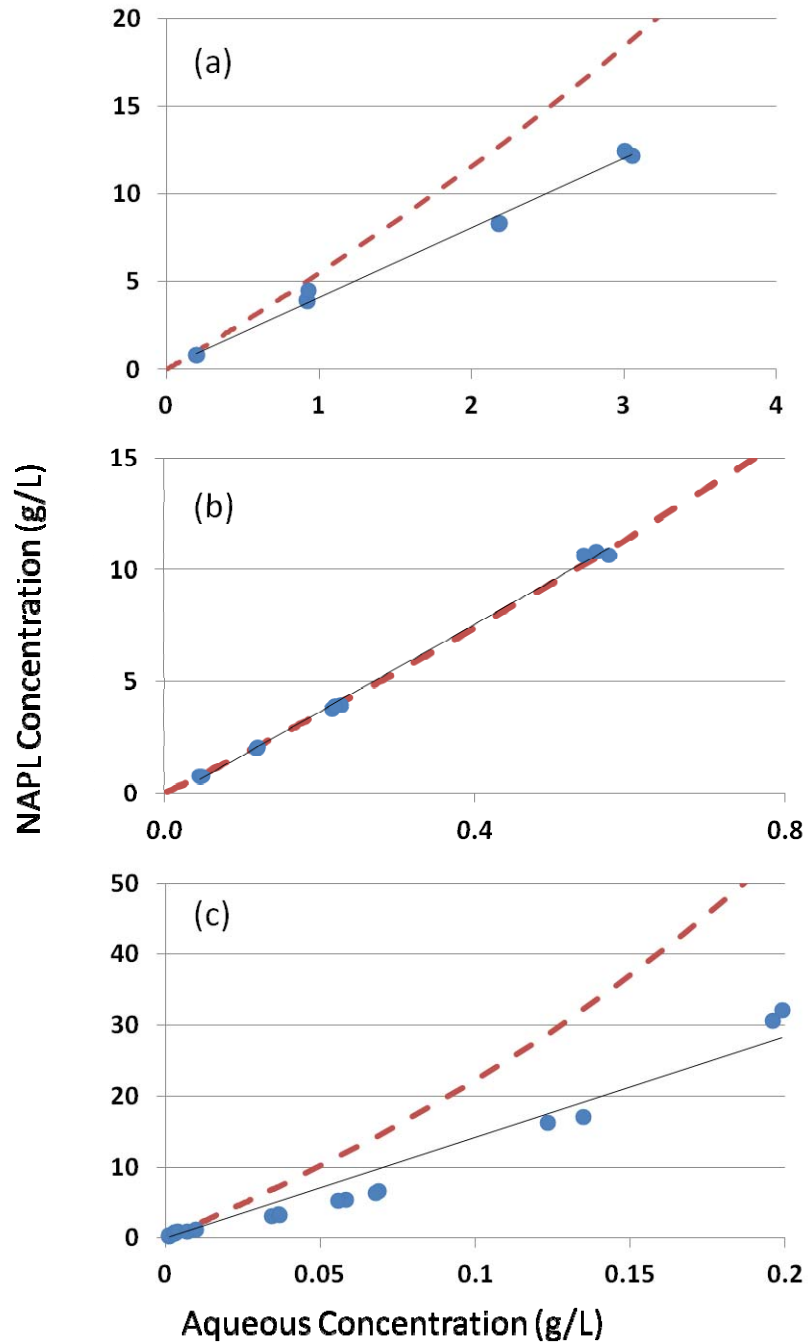


**Figure 4.3** Dilute regions for each 1-pentanol (a), 1-hexanol (b) and 2-octanol (c) partitioning between the DNAPL and aqueous phases  $22.0 \pm 0.1^\circ\text{C}$  as established by liquid-liquid equilibrium data (circles). Dashed line shows UNIFAC predictions using literature interaction parameters. Solid line shows weighted, linear, least squares regression. Note again the change in the horizontal range for each panel.

**Table 4.1** Reported partition coefficients for 1-pentanol, 1-hexanol and 2-octanol.

Tracer	$K_p^{C_i}$ ( $L_{aq}/L_{DNAPL}$ )	Initial Aqueous Concentration for Measurement of $K_p^{C_i}$	Reference
1-pentanol	3.80 <sup>a,c</sup> 3.8 <sup>b,c</sup> 3.73 <sup>a,d</sup> 3.39 <sup>a,c</sup>	1000 mg/L 1000 mg/L range not reported <sup>d</sup> 500 mg/L	Dwarakanath and Pope, 1998 Wang et al., 1998 Willson et al., 2000 Thal et al., 2007
1-hexanol	18.6 <sup>a,e</sup> 18.6 <sup>a,c</sup> 18.6 <sup>b,c</sup> 18.0 <sup>a,d</sup> 18.2 <sup>a,f</sup> 12.4 <sup>a,c</sup>	not reported <sup>e</sup> 1000 mg/L 1000 mg/L range not reported <sup>d</sup> not applicable <sup>f</sup> 500 mg/L	Jin et al., 1997 Dwarakanath and Pope, 1998 Wang et al., 1998 Willson et al., 2000 Istok et al., 2002 Thal et al., 2007
2-octanol	317 <sup>a,g</sup> 332 <sup>a,g</sup>	not applicable <sup>g</sup> not applicable <sup>g</sup>	Dwarakanath and Pope, 1998 Thal et al., 2007

<sup>a</sup> temperature was not reported, <sup>b</sup> 25°C, <sup>c</sup> single-point measurement, <sup>d</sup> regression of measurements at multiple concentrations though concentration range was not reported, <sup>e</sup> measurement method was not reported, <sup>f</sup> value estimated using method in Lyman et al. (1990), <sup>g</sup> estimated using an equivalent alkane carbon number for 2-octanol that was produced by employing the known 2-octanol partition coefficient between water and PCE-DNAPL (Ramsburg et al. 2005).

#### 4.2.2 – UNIFAC Modeling

The UNIFAC predictions of alcohol partitioning between the DNAPL and aqueous phases are also shown in Figures 4.2 and 4.3 (dashed line). The group contribution parameters used in the UNIFAC prediction (Chapter 3, Table 3.3) are able to predict the general shape over the entire partitioning range for each alcohol. The model performance is especially good for 1-pentanol and 2-octanol. The relatively poorer performance of UNIFAC when describing the partitioning of 1-hexanol results from an inability to accurately capture the 1-hexanol/water mutual solubility which shifts the curve to the right in Figure 4.2. Note, however, that the shape of the UNIFAC prediction is similar to that of the data. UNIFAC predictions for alcohol partitioning in the dilute region are shown in Figure 4.3. In the dilute region, the UNIFAC model over predicts the amount of alcohol partitioning. The UNIFAC predictions of linear partition coefficients within the dilute regions are  $5.8 L_{aq}/L_{DNAPL}$ ,  $18.4 L_{aq}/L_{DNAPL}$  and  $232.6 L_{aq}/L_{DNAPL}$  for 1-pentanol, 1-hexanol and 2-octanol, respectively (Figure 4.3). The superior UNIFAC predictions for the 1-hexanol within the dilute region are suspected to be spurious and related to the previously described inaccuracy in the 1-hexanol/water mutual solubilities.

#### 4.2.3 - Fitting UNIFAC Parameters

The inability of UNIFAC to capture the 1-hexanol data was further examined by adjusting group interaction parameters in an attempt to visually fit the model to the 1-hexanol data. Note that only one set of interaction parameters

was adjusted in any fitting attempt. A better prediction of the hexanol data can be accomplished by adjusting either parameter describing the interaction between –OH and H<sub>2</sub>O groups (groups 5 and 7 in Table 3.3). Either the –OH/H<sub>2</sub>O or the H<sub>2</sub>O/OH interaction parameter can be adjusted to the values shown in Table 4.2 to capture the 1-hexanol/water mutual solubility point. No other values that allow UNIFAC to capture the 1-hexanol/water mutual solubility point were found. The results of the adjusted UNIFAC predictions are shown in Figure 4.4. Adjustments were also attempted with the C=C-Cl interaction parameters (group 37) which are less well established, but this group does not help capture the 1-hexanol-water mutual solubility point. While the adjustment of these parameters enables the model to better predict the 1-hexanol data, the same adjustment leads to poorer UNIFAC model predictions for both 1-pentanol and 2-octanol. On a least squares basis the adjusted model error was 3 times and 2 times higher than the corresponding original model error for 1-pentanol and 2-octanol, respectively. In the linear range, the adjusted model predicts partition coefficients of 6.5  $L_{aq}/L_{DNAPL}$ , 21.6  $L_{aq}/L_{DNAPL}$ , 273.0  $L_{aq}/L_{DNAPL}$  for 1-pentanol, 1-hexanol and 2-octanol, respectively. UNIFAC parameters are estimated from thousands of data points stored in the Dortmund Data Bank (Gmehling et al., 1977) and both H<sub>2</sub>O and –OH groups are well characterized interaction parameters. Therefore, even though adjustment of these parameters allows for better prediction of the hexanol data set, it is not recommended that these adjusted interaction parameters be employed when making predictions of LLE.

**Table 4.2** Adjusted interaction parameters that visually allow the UNIFAC model to capture the hexanol, water mutual solubility point. Literature interaction parameters shown in parentheses.

$\alpha_{ij}$	group 5 -OH	group 7 H <sub>2</sub> O
group 5 -OH	0 <sup>a</sup>	500 (353.5 <sup>b</sup> )
group 7 H <sub>2</sub> O	-200 (-229.1 <sup>b</sup> )	0 <sup>a</sup>

<sup>a</sup> by definition; <sup>b</sup> Gmehling et al. (1982)

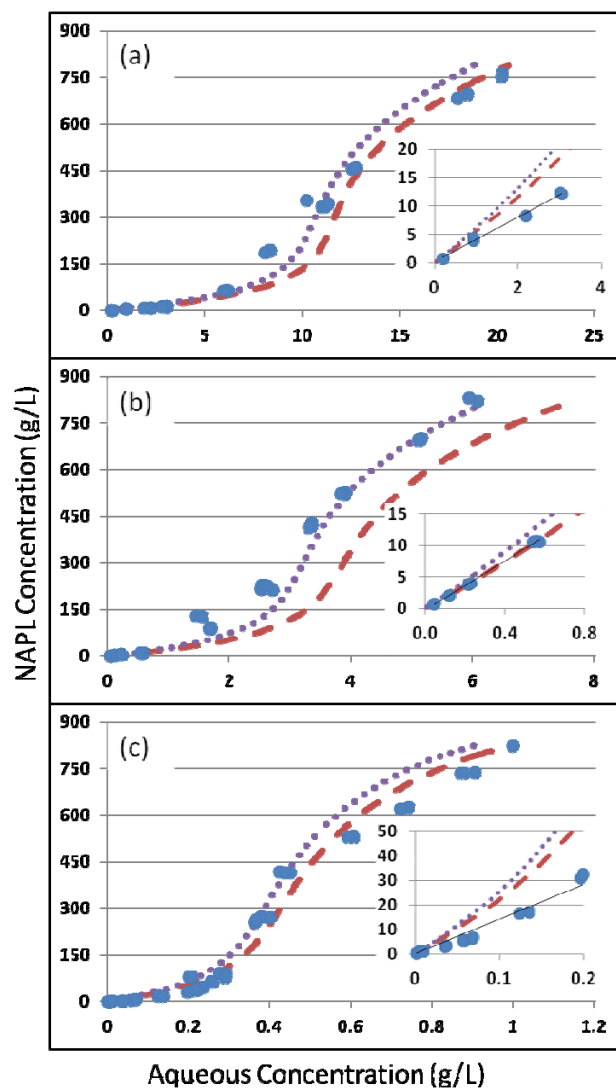


**Figure 4.4** The distribution of 1-pentanol (a), 1-hexanol (b) and 2-octanol (c) between the DNAPL and aqueous phases  $22.0 \pm 0.1^\circ\text{C}$  as established by liquid-liquid equilibrium data (circles). Dashed line shows UNIFAC predictions using literature interaction parameters, dotted line shows UNIFAC predictions using an adjusted OH/H<sub>2</sub>O interaction parameter. Note that data span the range of possible aqueous concentrations but that differences in solubility necessitate change in the horizontal range for each panel. Insets show dilute range with the regressed, linear partitioning model (solid line).

#### 4.2.4 - Adsorption of the Selected Tracers at the TCE-DNAPL/Water Interface

LLE experiments were also used to study interactions of the alcohol tracers and the aqueous/organic interface. Surface accumulation for 1-pentanol, 1-hexanol and 2-octanol at the DNAPL-aqueous interface was quantified by measuring equilibrium IFTs over a range of solute concentrations (200-1300 mg/L for 1-pentanol, 35-4600 mg/L for 1-hexanol, and 170-900 mg/L for 2-octanol). The two Langmuir parameters  $\Gamma_\infty$  (maximum surface accumulation,  $M \cdot L^{-2}$ ) and  $a_L$  (half saturation concentration,  $M \cdot L^{-3}$ ) were obtained by fitting Equation 13 to the IFT data using a nonlinear, least squares approach (Figure 4.5):

$$\gamma = \gamma_0 - \Gamma_\infty RT \ln \left( 1 + \frac{C_{aq}}{a_L} \right) \quad (4.1)$$

where  $C_{aq}$  is the bulk tracer concentration ( $M \cdot L^{-3}$ ), and  $\gamma_0$  and  $\gamma$  are the interfacial tensions ( $M \cdot T^{-2}$ ) measured in the absence of the alcohol and at alcohol concentration  $C$ , respectively. Fitted isotherm parameters (shown in Table 4.3) suggest that 2-octanol has a half saturation concentration ( $a_L$ ) that is two orders of magnitude less than that of 1-pentanol. The low  $a_L$  of 2-octanol implies that the interface becomes saturated at relatively low concentrations. The capacity of the interface ( $\Gamma_\infty$ ) was found to decrease with increasing alcohol carbon chain length, though all values are on the same order of magnitude. The interfacial capacities shown in Table 4.3 suggest that surface accumulation (at any given time during the column experiment) will represent a small fraction of the overall mass in the system. The importance of this mass is discussed in more detail in Chapter 5 when modeling the transport of these tracers in column experiments.

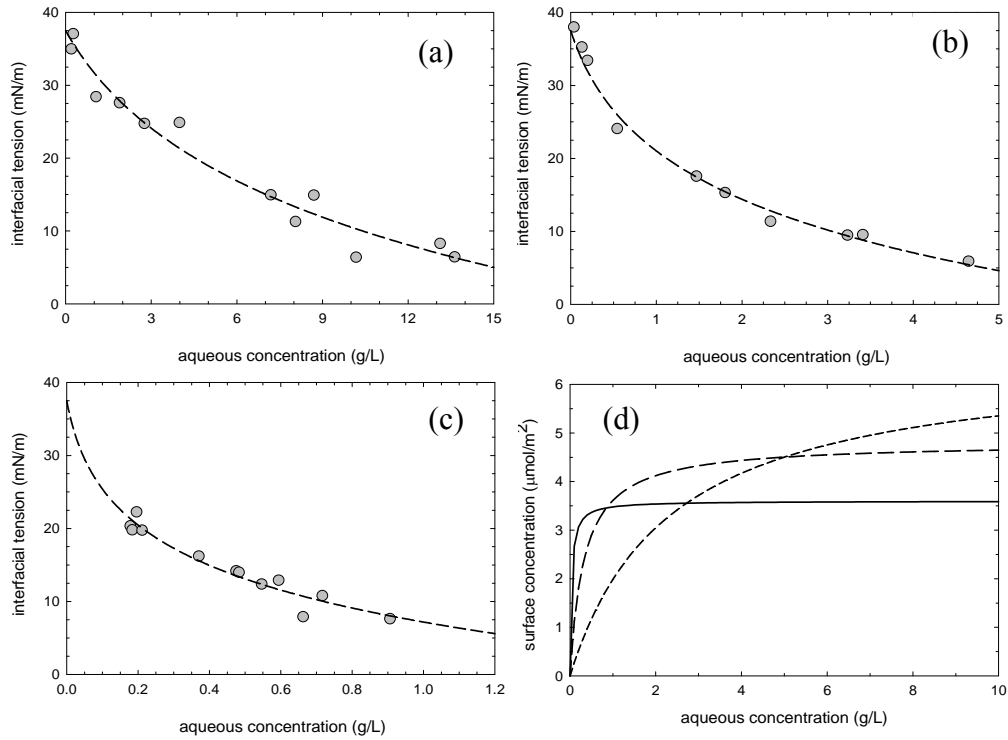


**Figure 4.5** TCE-DNAPL-water interfacial tension at  $22\pm 2^\circ\text{C}$  as a function of 1-pentanol (a), 1-hexanol (b), and 2-octanol (c) aqueous concentrations. Note that the horizontal range changes for each panel. Dashed lines in panels a-c represent nonlinear least squares fits of Equation 9. Langmuir adsorption isotherms (d) produced using fitted parameters (Table 4.3) for 1-pentanol (short dash), 1-hexanol (long dash), and 2-octanol (solid).

**Table 4.3** Isotherm parameters for tracers at a TCE-DNAPL-water interface.

Tracer	$\Gamma_{\infty}$ ( $\mu\text{mol}/\text{m}^2$ )	$a_L$ ( $\mu\text{mol}/\text{m}^3$ )	$a_L$ (mg/L)	$R^2$
1-pentanol	6.6 $\pm$ 1.5	(2.6 $\pm$ 1.1) $\times 10^7$	2330 $\pm$ 1000	0.960
1-hexanol	4.8 $\pm$ 0.5	(3.2 $\pm$ 0.6) $\times 10^6$	330 $\pm$ 60	0.989
2-octanol	3.6 $\pm$ 0.4	(2.7 $\pm$ 0.8) $\times 10^5$	35 $\pm$ 11	0.936

Values determined by a nonlinear least squares fit of Equation 9 to equilibrium interfacial tensions measured at 22 $\pm$ 2°C. Uncertainties represent standard error in parameter estimates.

### 4.3 - Conclusions

In this chapter the partitioning of three, straight-chain alcohols was found to be nonlinear function (i.e., dependent upon phase composition). These findings, together with those in Wise et al. (1999), suggest a need for more thorough characterization of alcohol partition coefficients prior to application for source zone assessment. When nonlinearity is neglected, interpretation of partitioning tracer data leads to a systematic over estimations of NAPL saturation (Wise 1999). The partitioning of many tracers, however, may be approximately linear at low concentration. Care must be taken when designing and interpreting the results from tests employing partitioning tracers as analysis may prove difficult due to the convoluted effects of poor characterization of  $K_p^{C_i}$  (over estimation of  $S_n$ ) and the hydraulic accessibility of the NAPL (under estimation of  $S_n$ ). Few studies report the concentrations at which partition coefficients were measured, and those that do report the data employed to evaluate  $K_p^{C_i}$  often evaluate the partition coefficient at concentrations that are much lower than those introduced to the subsurface (Jawitz et al., 1998; Brooks et al., 2002; Meinardus et al., 2002; Jalbert et al., 2003; Ramsburg et al., 2005; Moreno-Barbero et al., 2007; Hartog et al., 2010). The injection concentrations employed in these field tests may be within the linear partitioning range, but without thorough characterization of the tracer/NAPL interactions the range over which the linear assumption is valid remains unknown. While the use of low injection concentrations minimizes the potential implications relating to nonlinear partitioning, concentrations must be high enough to avoid the influence of tracer-

soil interactions and analytical detection limits. Our thermodynamically rigorous characterization of 1-pentanol, 1-hexanol and 2-octanol interactions with TCE suggests that concentrations should not exceed 3,000 mg/L, 500 mg/L and 200 mg/L, respectively, if the data analysis is to be simplified by assuming linear partitioning.

Transport models, and consequently, saturation estimates are very sensitive to the partition coefficient. Though UNIFAC offers an effective tool for predicting alcohol/chlorinated ethene/water phase behavior, the group contribution method tends to over predict the partition coefficients in the dilute range (where data appear linear). This over prediction of the partition coefficient may lead to underestimation of NAPL saturation. Therefore, measurement of the partition coefficient over the range of concentrations to be employed provides the best foundation for accurate estimates of NAPL saturation from partition tracer test data.

The equilibrium sorption isotherms developed in this work show that 1-pentanol, 1-hexanol and 2-octanol do accumulate at the aqueous/DNAPL interface. This surface accumulation may regulate tracer mass flux across this interface (Ferrari et al., 1997; Liggieri et al., 1997; Ravera et al., 1997, 2000). However, the maximum accumulation of the three tracers is small (on the order of micrometers per square meter). To understand the implications of surface accumulation, the equilibrium sorption isotherms need to be incorporated into a transport model that can quantify the affect surface accumulation has on overall transport.

## **CHAPTER 5 - PARTITIONING KINETICS OF TRACERS WITHIN TCE-DNAPL GANGLIA**

### ***5.1 - Introduction***

Partitioning tracer transport in systems of residual NAPL has been studied both experimentally and numerically (e.g. Jin et al., 1997; Saripalli et al., 1997; Dai et al., 2001; Hartog et al., 2010). Generally, equilibrium conditions and linear sorption isotherms are assumed so that tracer partitioning between the NAPL and aqueous phases can be described using the simplest modeling approach. When this model is used, overall saturations can be estimated by simply calculating partitioning tracer retardation coefficients. The results of Chapter 4 in addition to the work of Wise (1999; Wise et al., 1999), show that tracer partitioning may often be nonlinear. Kinetic limitations may necessitate more complicated models such as a linear driving force model (e.g. Brusseau et al., 1989) to adequately describe tracer transport. Additionally, diffusive transport (within immobile aqueous phase and DNAPL zones) and adsorption at the DNAPL–aqueous interface may influence tracer transport, and consequently decrease the accuracy of DNAPL saturation estimates (Chang and Franses, 1994; Gracia et al., 1993; Kim et al., 2007; Willson et al., 2000; Zhu et al., 2009).

The goal of Chapter 5 is to explore the relative importance of the processes that may control the extent and rate of interphase alcohol tracer partitioning in domains containing uniformly entrapped TCE-DNAPL. In contrast to previous investigations, independent measurement and/or estimation of system physical and chemical properties leads to unambiguous data interpretation and eliminates

the need for curve fitting. Focus is placed on conditions which promote nonequilibrium mass exchange to elucidate the processes controlling the temporal distribution of the solute within the multiphase environment. We specifically examine the importance of aqueous, NAPL and surface resistances to tracer mass transfer. This is done through a series of column experiments, using the representative alcohol tracers studied in Chapter 4.

## **5.2 - Results and Discussion**

### *5.2.1 – Nonequilibrium Mass Transfer Coefficients*

Breakthrough curves from the column tracer experiments are presented in Figure 5.1, with experimental parameters listed in Table 5.1. Comparison of the curve for the non-partitioning tracer (Figure 5.1a) with that for each alcohol tracer (Figures 5.1b-d) reveals the influence of partitioning – retardation during transport. Also shown in Figure 5.1 are numerical predictions for the equilibrium, linear driving force, and dual diffusion models developed using literature values of  $K_p^{C_i}$ : 3.80 for 1-pentanol (Dwarakanath and Pope, 1998; Wang et al. 1998); 18.6 for 1-hexanol (Dwarakanath and Pope, 1998; Wang et al. 1998); and 317 for 2-octanol (Dwarakanath and Pope, 1998). Here, literature values were used in the model to examine the predictive power of the model when partition coefficients are not robustly quantified. These BTCs are later compared to model predictions using the partition coefficients quantified in Chapter 4. Inspection of Figure 5.1 reveals that neither the equilibrium nor the non-equilibrium (linear driving force) models capture the observed breakthrough of 1-hexanol and 2-octanol (Figures 5.1c and 5.1d). The inability of the linear driving

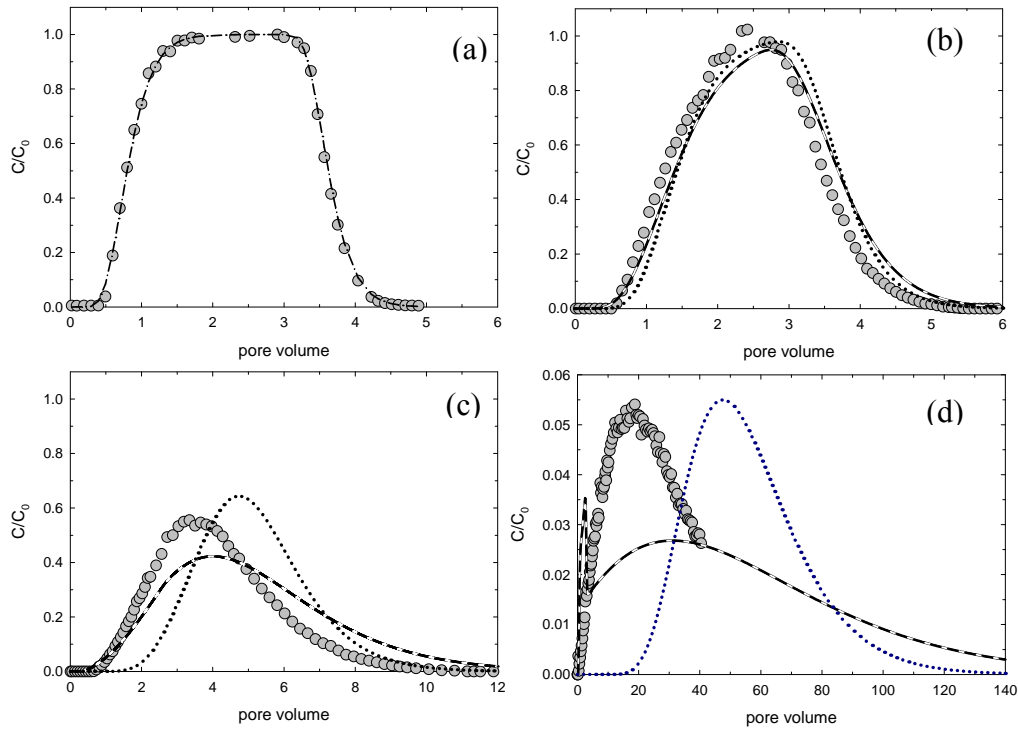


**Figure 5.1** Breakthrough curves for bromide (a), 1-pentanol (b), 1-hexanol (c), and 2-octanol (d) tracer tests conducted at  $22 \pm 2^\circ\text{C}$ . Dispersivity was fit (dash-dot) to bromide data. Predictive simulations using literature values for the partition coefficients are also shown using equilibrium (dotted), linear driving force (solid), and dual diffusion (dashed) models. Literature values employed for partition coefficients were 3.80, 18.6, and 317  $L_{\text{aq}}/L_{\text{NAPL}}$  for 1-pentanol, 1-hexanol, and 2-octanol, respectively. Note that the pore volume scale changes for each panel, and the normalized concentration scale changes for panel d.

**Table 5.1** Parameters related to column experiments and simulations.

sand (Ottawa, IL)	45-50 mesh	45-50 mesh
uniformity index ( $U_i$ )	1.09	1.09
median grain diameter ( $d_{50}$ )	0.326 mm	0.326 mm
column length ( $L$ )	5.0 cm	4.9 cm
pore volume ( $PV$ )	36 mL	35 mL
porosity ( $n$ )	0.39	0.39
TCE-NAPL saturation ( $S_n$ )	16.8%	13.1%
ganglia diameter <sup>a</sup> ( $d_{NAPL}$ )	0.297 mm	0.297 mm
flow rate ( $Q$ )	2.2 mL·min <sup>-1</sup>	0.56 mL·min <sup>-1</sup>
pore water velocity ( $v$ )	0.32 cm·min <sup>-1</sup>	0.091 cm·min <sup>-1</sup>
dispersivity ( $\alpha$ )	3.2 mm	1.5 mm
molecular diffusivity in water ( $D_{aq}$ ) <sup>b</sup>		
1-pentanol	$0.80 \times 10^{-5} \text{ cm}^2 \cdot \text{s}^{-1}$	
1-hexanol	$0.76 \times 10^{-5} \text{ cm}^2 \cdot \text{s}^{-1}$	
2-octanol	$0.65 \times 10^{-5} \text{ cm}^2 \cdot \text{s}^{-1}$	
molecular diffusivity in TCE ( $D_n$ ) <sup>c</sup>		
1-pentanol	$2.4 \times 10^{-5} \text{ cm}^2 \cdot \text{s}^{-1}$	
1-hexanol	$2.2 \times 10^{-5} \text{ cm}^2 \cdot \text{s}^{-1}$	
2-octanol	$1.9 \times 10^{-5} \text{ cm}^2 \cdot \text{s}^{-1}$	
lumped mass transfer coefficient ( $\hat{k}$ ) <sup>d</sup>		
1-pentanol	$2.34 \times 10^{-3} \text{ s}^{-1}$	-
1-hexanol	$2.19 \times 10^{-3} \text{ s}^{-1}$	-
2-octanol	$1.98 \times 10^{-3} \text{ s}^{-1}$	$8.45 \times 10^{-4} \text{ s}^{-1}$
pulse width – all pulses ( $PW$ )	2.3 PV	10.3 PV
influent concentration ( $C_0$ )		
1-pentanol	1070 mg·L <sup>-1</sup>	-
1-hexanol	380 mg·L <sup>-1</sup>	-
2-octanol	180 mg·L <sup>-1</sup>	195 mg·L <sup>-1</sup>
effluent recovery		
1-pentanol	98.8%	-
1-hexanol	94.6%	-
2-octanol <sup>e</sup>	70.4%	89.6%

<sup>a</sup> Calculated using correlation of Ramsburg et al. (2010). <sup>b</sup> Calculated using the correlation of Hayduk and Laudie (1974) at 22°C. <sup>c</sup> Calculated with correlation of Wilke-Chang at 22°C. <sup>d</sup> Calculated using the correlation of Powers et al. (1992) at 22°C. <sup>e</sup> Effluent recovery lower due to incomplete quantification of BTC tail.

force model to capture either pulse is particularly interesting, given the apparent agreement between the model and data in the case of 1-pentanol. Breakthrough curves simulated with the linear driving force model can be characterized as having lower peak values and greater tailing than the data, suggesting that the model is over predicting tracer partitioning. The relatively poor performance of the linear driving force model could suggest that other resistances to mass transfer are influencing tracer transport.

To explore the possibility that diffusion within the DNAPL is influencing tracer transport, the assumption of a well-mixed DNAPL was relaxed. Application of the dual diffusion model to these scenarios produces BTCs that are coincident with those obtained using the linear driving force model. The deviations between simulated BTCs for the two models were quantified using normalized sum of squared differences, yielding differences of 0.57%, 0.02%, and 5.9% for 1-pentanol, 1-hexanol and 2-octanol, respectively. The similarities between predictions of the linear-driving force and dual diffusion models suggest that diffusion within the NAPL singlets occurs rapidly relative to transport to the NAPL-water interface, such that it does not influence the breakthrough of 1-hexanol or 2-octanol. Sensitivity analyses (not shown) determined that diffusional resistance in the NAPL phase does not become important until the radius of the ganglia droplet is doubled. From this analysis, it appears that diffusional resistance within the NAPL may be important for tracer mass transport through regions containing pools, but is not controlling mass transfer for the entrapped ganglia systems examined herein. Additional sensitivity analyses (not

shown) were conducted to determine whether or not the laboratory data could be reproduced by fitting the value of the mass transfer coefficient in either the linear driving force or dual diffusion models. Results suggest that adjustment of the mass transfer coefficient does not improve either model's ability to fit the 1-hexanol or 2-octanol effluent data.

The two hypotheses most likely to explain the inability of these models to capture the 1-hexanol and 2-octanol BTCs are: (i) a resistance to tracer mass transport exists at the interface between the aqueous and NAPL phase that modulates the rate of the tracer flux into the NAPL droplet; of (ii) values of  $K_p$  are inaccurate due to insufficient characterization of tracer partitioning.

The first hypothesis is supported by the fact that all three alcohols are known to accumulate at the aqueous/organic interface (Graciaa et al., 1993; Chang and Franses, 1994; Kim et al., 2007; Zhu et al., 2009). Surface accumulation has been shown to regulate mass flux through the interface for some partitioning solutes (Ferrari et al., 1997; Liggieri et al., 1997; Ravera et al., 1997; Ravera et al., 2000). Neglecting this accumulation of the tracer at the interface may result in the observed over prediction of tracer partitioning. Thus we incorporated the equilibrium isotherm parameters determined with the LLE batch experiments (Table 4.4) into surface partitioning transport model.

Results from these transport simulations suggest that the surface resistance model produces BTCs for all three tracers that are indistinguishable from those produced using the linear driving force model (0.09%, 0.16% and 0.20% for 1-pentanol, 1-hexanol and 2-octanol, respectively). Here predicted accumulations at

the interface are negligible compared to mass within the pulse (0.04%, 0.10%, and 0.15% for 1-pentanol, 1-hexanol and 2-octanol, respectively). Thus, surface accumulation alone cannot explain the discrepancies between the laboratory data and model predictions shown in Figures 5.1c and 5.1d.

The second hypothesis that may explain the inability of the models capture the tracer breakthrough data relates to errors made when assessing the tracer partition coefficients. To test this hypothesis, we employed the rigorously characterized partition coefficients measured in the LLE batch experiments in the linear driving force model. These partition coefficients are appropriate for modeling the column system because the pulse concentrations used for each tracer lie within the linear partition range.

Use of these measured partition coefficients greatly improved performance of the linear driving force model (Figure 5.2). In addition, simulation of the all three tracer tests using the dual diffusion model and measured  $K_p^{C_i}$  results in BTCs that are within 0.1% of linear driving force model predictions. The linear driving force model is capable of capturing the transport because the two diffusion resistances (i.e. film resistance and intra-NAPL resistance) operate in series and the intra-NAPL resistance is negligible. In the case of 1-pentanol, both the measured (4.2) and literature (3.9) values for  $K_p^{C_i}$  produce simulations that are visually similar. The smaller partition coefficient produces a slightly better prediction, with the two BTCs differing by 0.1%.

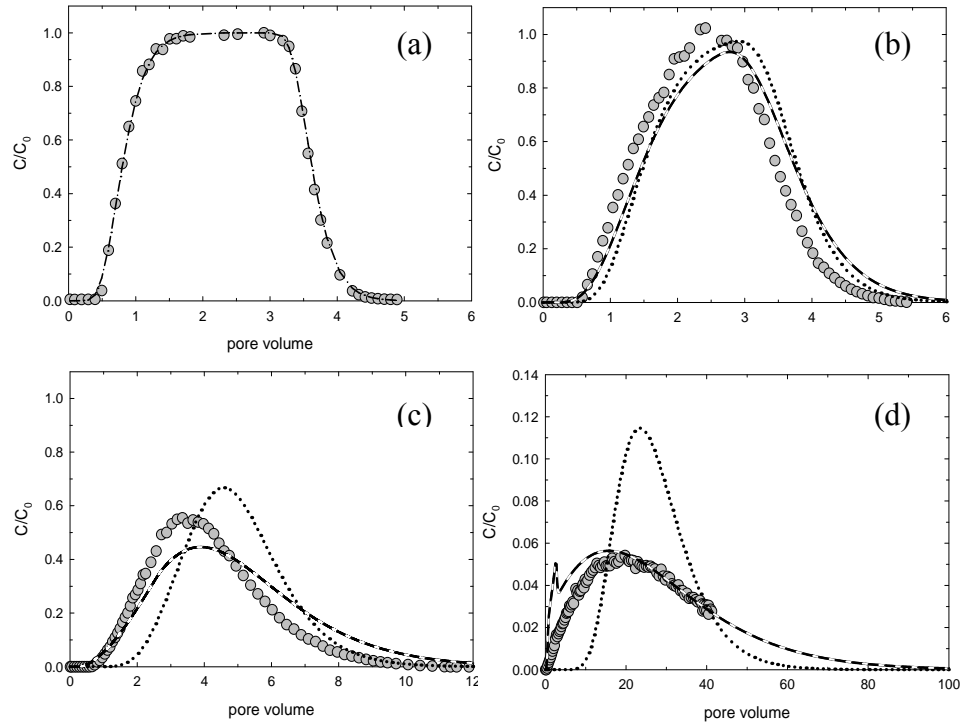


**Figure 5.2** Breakthrough curves for bromide (a), 1-pentanol (b), 1-hexanol (c), and 2-octanol (d) tracer tests conducted at  $22 \pm 2^\circ\text{C}$ . Dispersivity was fit (dash-dot) to bromide data. Predictive simulations using measured values for the partition coefficients are also shown using equilibrium (dotted), linear driving force (solid), and dual diffusion (dashed) models. Values of the partition coefficient employed in these simulations were 4.20, 17.4, and 149  $L_{\text{aq}}/L_{\text{NAPL}}$  for 1-pentanol, 1-hexanol, and 2-octanol, respectively, at  $22.0 \pm 0.1^\circ\text{C}$ . Note that the pore volume scale changes for each panel, and the normalized concentration scale changes for panel d.

In the case of 1-hexanol, the measured partition coefficient (17.4) yields a visually better prediction as compared to that obtained using the literature value (18.6). Use of the measured  $K_p^{C_i}$  within the linear driving force model for 1-hexanol, however, still slightly over predicts partitioning - lower  $C/C_0$  values and the greater tailing in the prediction compared to that observed in the column experiment. A duplicate 1-hexanol tracer test in a similar column (data not shown) produced a similar result. This consistently poorer prediction for 1-hexanol data cannot be explained by the phenomena examined here. Attempts to fit the linear driving force model to the experimental data by adjusting the partition coefficient suggest that  $K_p^{C_i}$  must be reduced to  $13 \text{ L}_{\text{aq}}/\text{L}_{\text{NAPL}}$ . This fitted  $K_p^{C_i}$  value, although consistent with that reported by Thal et al. (2007) (12.4), is 75% of the measured value of 17.4, and outside of the error bounds associated with the batch measurements. It is important to note that simultaneous fitting of saturation and mass transfer coefficient is not a viable option, as adjustment of these parameters also influences the 1-pentanol and 2-octanol simulations.

Model performance for 2-octanol was greatly improved when the measured  $K_p^{C_i}$  ( $149 \text{ L}_{\text{aq}}/\text{L}_{\text{NAPL}}$ ) is employed with overall good visual agreement between the prediction and observations. The initial rise of the predicted BTC, however, exhibits a small perturbation where effluent concentrations increase sharply before the pulse is turned off. It is hypothesized that the source of this perturbation relates to the differences in the time scales of mass transfer and advection, such that aqueous phase concentrations change more quickly from advection than from tracer absorption. Sensitivity analyses conducted by Mr. Ali

Boroumand (not shown) determined that the perturbation is not evident when the mass transfer coefficient is increased by approximately 30%.

### *5.2.2 - Slow flow mass transfer kinetics*

To further examine the relationship between this perturbation and time scales of mass transport, an additional column experiment was run at  $\frac{1}{4}$  of the previous flow rate. The results of this experiment, along with equilibrium and linear driving force model predictions are shown in Figure 5.3. Although the flow rate was much slower, experimental conditions still promoted nonequilibrium mass exchange. While the linear driving force model performs well, the predicted BTC does not exhibit the perturbation observed at higher flow rates. The slower flow rate reduces both the pore water velocity and the mass transfer coefficient; however, the flow rate is reduced by 75%, while the mass transfer coefficient is only reduced by 55%. Thus, the time scales for mass transfer and advection are more similar and the perturbation is not apparent. The lack of an observed perturbation in either experiment may suggest that the mass transfer correlation employed herein does not capture the precise velocity dependence for 2-octanol exchange. It is, however, important to recognize the surprisingly robust performance of the mass transfer correlation across all three tracers, given that existing correlations are based upon dissolution of a pure-component NAPL (not absorption and dissolution of components introduced to characterize the multiphase, multicomponent system).

To more broadly explore the effects of uniform DNAPL saturation on the equilibrium assumption the linear driving force model was employed to identify a velocity at which LEA is a reasonable approximation of the partitioning process (taken here to be 5% difference between the simulated BTCs). The 18 simulation results shown in Figure 5.4 are for the partitioning alcohols and porous medium examined here, with transport lengths of 5, 10 and 100 cm.

These illustrative results, presented in terms of the hydraulic residence time within the zone  $\left(\frac{L}{nS_{aq}v}\right)$ , and the partitioning index (defined here as  $S_n K_p^{C_i}$ ), suggest that strong non-equilibrium conditions may be present when using tracers with high partition coefficients, or where local saturations may be high. It is interesting that the tracers with the higher partition coefficients are frequently used to assess DNAPL saturation in the field due the need for tracer separation when interrogating large volumes. Local exchange for these tracers, however, may be occurring under conditions of non-equilibrium.

Actual source zones, characterized by low overall saturations, typically comprise heterogeneous saturation distributions. Here, the local equilibrium assumption may be less appropriate due to flow bypassing and less accessibility to the DNAPL surface area (Moreno-Barbero and Illangasekare, 2005, 2006). Where DNAPL is accessible, the local length scale (characteristic length of contact between the tracer solution and DNAPL) will govern the applicability of the LEA. Unfortunately, confirmation of the LEA applicability or selection of an appropriate non-equilibrium model formulation requires that contact times (or lengths) are known *a priori* across the unknown DNAPL architecture.

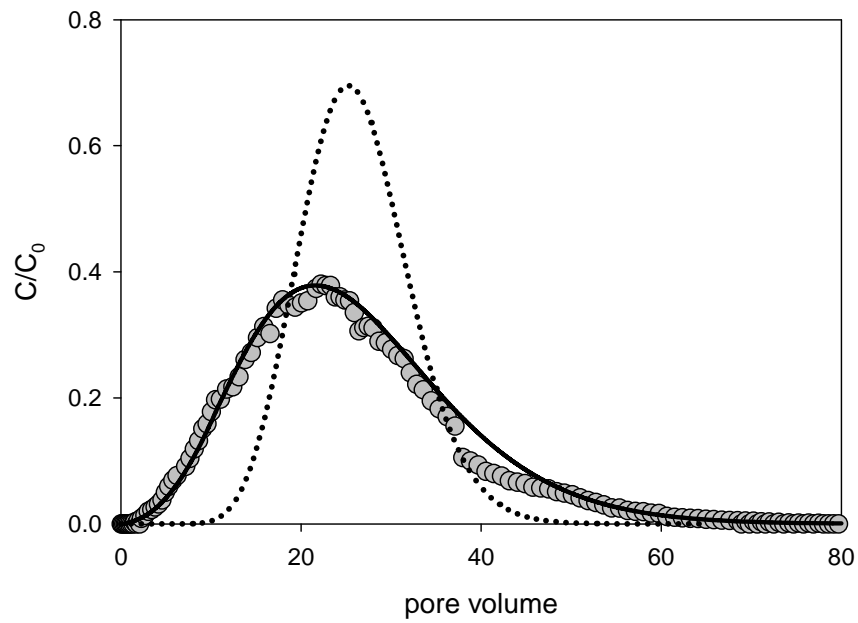


**Figure 5.3** Breakthrough curve of 2-octanol for experiment conducted at 0.5 mL/min ( $22\pm 2^\circ\text{C}$ ). Also shown are the linear driving force (solid) and equilibrium (dotted) predictions using the measured 2-octanol partition coefficient ( $149\text{ L}_{\text{aq}}/\text{L}_{\text{NAPL}}$ ).

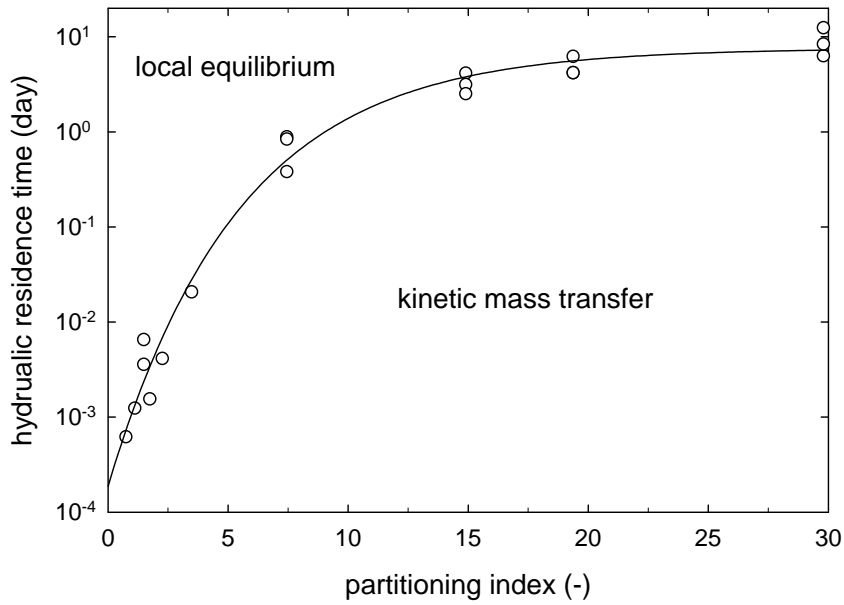


**Figure 5.4** Limitation of the local equilibrium assumption for partitioning alcohols in zones of uniformly entrapped DNAPL. The hydraulic residence time within the zone is  $\frac{L}{nS_{aq}v}$ , and the partitioning index is defined to be  $S_n K_p^{C_i}$ . The line is shown as a visual guide for the simulation results shown as open circles.

### ***5.3 - Conclusions***

Laboratory experiments and mathematical modeling were coupled to examine the partitioning of the three representative tracers under non-equilibrium conditions in systems comprised of TCE-DNAPL ganglia. Results suggest that a linear driving force model employing a mass transfer coefficient correlation developed from NAPL dissolution experiments is able to reproduce BTCs generated in the 1-D column systems. Additionally, neither accumulation of alcohol tracers at the interface between the NAPL and aqueous phase, nor diffusion within the TCE-DNAPL droplet are important resistances to partitioning tracer mass transfer in these ganglia systems.

Results also demonstrate that nonequilibrium effects increase with increasing partition coefficient and increasing NAPL saturation, suggesting that the validity of the LEA should be checked for the solute having the highest partition coefficient. While the column experiments were designed to be in non-equilibrium, the flow rate of the 2-octanol experiment would have had to be reduced to 0.01 mL/min (i.e., 0.5% of the initial rate) before the linear driving force model predictions were within 5% of those produced by an equilibrium simulation.

## CHAPTER 6 – PARTITIONING KINETICS ASSOCIATED WITH TCE-DNAPL POOLS

### *6.1 - Introduction*

Interpretation of partitioning tracer tests is made difficult by nonuniformity in the spatial distribution and saturation distribution of DNAPL within a source zone (Jin et al., 1997; Rao et al., 2000; Brooks et al., 2002; Jalbert et al., 2003; Moreno-Barbero and Illangasekare, 2005, 2007). This is particularly true when DNAPL pools are present due to flow bypass and diffusion limitations. Jin et al. (1997) simulated partitioning tracer tests in a source zone with a large pooled region and reported DNAPL mass estimation errors as high as 50%. Such errors are thought to be exacerbated by employing the local equilibrium assumption to interpret tracer signals obtained within heterogeneous sources - sources in which flow bypass becomes appreciable (e.g. Annable et al., 1998a; Brooks et al., 2002; Hartog et al., 2010).

Results presented in Chapter 5 show that partitioning tracer mass transport in regions comprising uniformly entrapped TCE-DNAPL ganglia can be described using a linear driving force model with a mass transfer coefficient correlation developed for NAPL dissolution. This chapter focuses on quantifying tracer mass transfer in a region containing a large TCE-DNAPL pool. The experiments and modeling described herein complement the work described in Chapter 5 by examining mass transfer of partitioning tracers at the opposite end of the pool fraction spectrum. It is envisioned that the characterization of both end members of pool fraction (i.e., 0 and 1) will provide a foundation for

understanding tracer transport in more realistic sources comprising a mixture of pools and ganglia.

The longer diffusional path length in a DNAPL pool (relative to ganglia), may mean that diffusion within the DNAPL is more relevant to tracer transport in regions having pooled DNAPL. To study kinetic processes controlling tracer transport in regions of pooled DNAPL, partitioning tracer tests are conducted in a 2-D aquifer cell with a source zone comprised of a large TCE-DNAPL pool. Concentration data are modeled to examine the feasibility of employing mass transfer correlations developed to describe dissolution from a NAPL pool when describing the kinetic mass transfer for partitioning tracers.

## ***6.2 – Experimental Design***

### *6.2.1 Aquifer Cell Packing Structure and TCE-DNAPL Source Zone*

In the aquifer cell experiments described in this Chapter, Ottawa Federal Fine (30-140 mesh) was used for the background sand and F-70 Ottawa Sand was used to create low permeability lenses and layers. The lens structure (Figure 6.1) comprises a 1 cm thick F-70 lens (28.2 cm long) at the up-gradient end of the box. Triangular mounds (3.6 cm tall) sit on each end of the lens in an effort to direct the TCE-DNAPL to fill the area above the lens, creating a large pool. This structure is not meant to mimic an observed structure within the subsurface. Rather, it is an alternative to previous use of similarly contrived, coarse lenses placed within a lower permeability matrix (e.g. Nambi and Powers, 2003; Moreno-Barbero and Illangasekare, 2006). Parameters pertaining to the packing structure are shown in Table 6.1.

A pooled TCE-DNAPL zone was created in the box by using a Hamilton Syringe Pump to inject TCE through a needle (gage 18) at 0.5 mL/min. The needle was packed into the box so that its tip was approximately 1 cm above the middle of the low permeability F-70 layer. 13.5 mL of TCE were pumped into the box with no background flow and were allowed to redistribute for 24 hours before any aqueous solution was flowed through the box.

The TCE-DNAPL distribution and corresponding light transmission results are shown in Figure 6.2. Light transmission results determine the pool fraction as 0.96, 0.94 and 0.93 on a pixel by pixel basis, a discrete block averaging basis and a continuum averaging basis, respectively (Christ et al., 2012). Details on this analysis can be found in Chapter 3, Section 3.3.5. A cutoff saturation of 0.17 was used to discriminate between pools and ganglia.

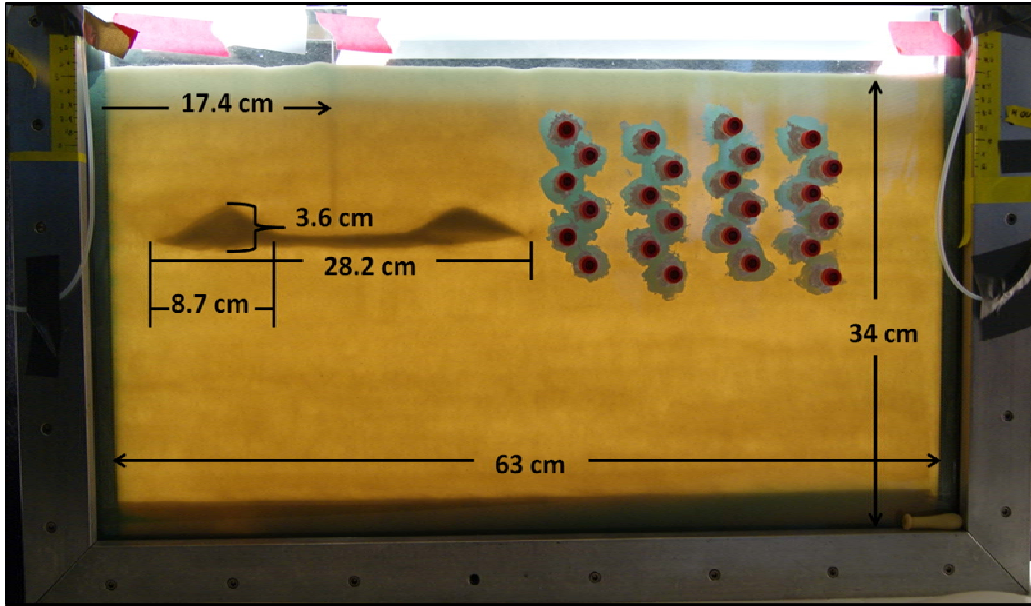


**Figure 6.1** Packing structure used to create the pooled source zone.

**Table 6.1** Relevant 2-D box parameters

<b>Parameter</b>	<b>Value</b>
<b>Mass Ottawa Federal Fine</b>	4868 g
<b>Mass F-70</b>	521 g
<b>Packed Height</b>	34 cm
<b>Average Bulk Density</b>	1.54 g/cm <sup>3</sup>
<b>Average Porosity</b>	0.42
<b>Total Pore Volume</b>	1303 mL
<b>TCE-DNAPL Volume</b>	13.5 mL
<b>Overall TCE-DNAPL Saturation</b>	1.04%
<b>Initial Pool Fraction</b>	
<b>Pixel x Pixel</b>	0.96
<b>Discrete Block Averaging</b>	0.94
<b>Continuum Averaging</b>	0.93

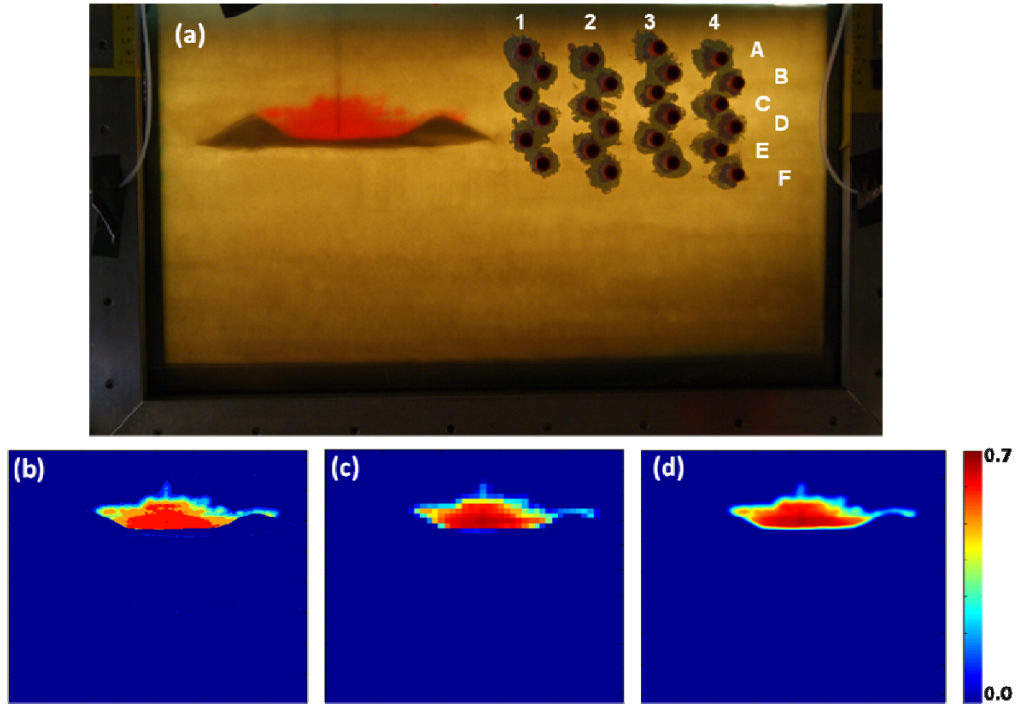


**Figure 6.2** 2-D aquifer cell used to examine partitioning tracer transport in a pooled TCE-DNAPL source zone. The photograph (a) sampling port labels (columns 1- 4 and rows A-F). Light transmission results are shown as a pixel by pixel saturation estimation (b), discrete averaging saturation estimation (c), and continuum averaging saturation estimation (d).

### 6.2.2 – Tracer Test Design

All tracer tests were conducted with a conventional, line-drive flow pattern, using the fully screened well on the left-hand side of the box as the influent and the fully screened well on the right-hand side as the effluent. The three tracer experiments, conducted in series, are described in Table 6.2. Each tracer pulse contained bromide, 1-pentanol, 1-hexanol, and 2-octanol. The background solution was comprised of Milli-Q water saturated with TCE. The first test used a tracer pulse of 0.31 PV followed by flushing with the background solution at 4.9 mL/min (without flow interruption). The second experiment used a 0.67 PV tracer pulse, followed by a 60 hour flow interruption, followed by flushing the background solution at 5.2 mL/min. The third experiment also used at 0.71 PV tracer pulse, and a 60 hour flow interruption, but was followed by flushing the background solution at 8.6 mL/min. For all three experiments, effluent samples were continuously collected over 4-5 minute intervals throughout the test using a fraction collector (Retriever II, ISCO). Additionally, 250  $\mu$ L samples were collected from the array of sampling ports (immediately downstream of the pool) approximately every pore volume using a 1 mL gas tight Hamilton syringe. Experiments were terminated when tracer concentrations were consistently observed to be below the analytical detection limit ( $\sim$ 1 mg/L). After each experiment, the background solution was flushed through the box at 5 mL/min for eight hours to remove any tracer that may have remained in the system.

**Table 6.2** Experimental Parameters for pooled TCE-NAPL in 2-D Box.

<b>Experiment</b>	1	2	3
<b>Flow</b>	4.9 mL/min	5.2 mL/min	8.6 mL/min
<b>PW Velocity</b>	0.25 cm/min	0.26 cm/min	0.43 cm/min
<b>Pulse Width</b>	0.31 PV	0.67 PV	0.71 PV
<b>Flow Interruption Duration</b>	None	60 hr	60 hr
<b>Bromide Conc.</b>	10 mM	11 mM	9 mM
<b>1-Pentanol Conc.</b>	983 mg/L	1003 mg/L	896 mg/L
<b>1-Hexanol Conc.</b>	381 mg/L	371 mg/L	326 mg/L
<b>2-Octanol Conc.</b>	134 mg/L	147 mg/L	129 mg/L
<b>Bromide Recovery</b>	93.3%	97.2%	95.9%
<b>1-Pentanol Recovery</b>	94.9%	99.6%	93.1%
<b>1-Hexanol Recovery</b>	91.7%	99.9%	85.5%
<b>2-Octanol Recovery</b>	83.5%	90.5%	79.8%

### **6.3 – Results**

Effluent data from each of the three experiments are shown in Figures 6.3 and 6.4. Also shown in both figures are dashed lines indicating the down-gradient edge of the pool during the flow interruption; this is the point at which interactions occurring during the flow interruption should first be visible. In contrast to column experiments conducted using uniform residual TCE-DNAPL saturations, the breakthrough of each tracer in the 2-D box occurred at approximately the same time (Figure 6.3). The lack of tracer separation in the effluent was attributed to the larger volume of the 2-D system, relative to that of the pool (TCE-DNAPL pool comprises 1% of the total volume); therefore, most of the tracer flowing through the system did not contact the pool (i.e., flow bypass). Although the overall (effective) saturation employed for the pool experiments (1%) is lower than that employed for the ganglia column experiments (16.8%), local saturations in the pool experiments were much greater (~70%).

No effect of the flow interruption is seen for experiment 2 on a linear scale (Figure 6.3 b). In experiment 3, a dip and recovery in concentration due to the flow interruption is seen around the dashed line indicating the edge of the pool during the flow interruption (Figure 6.3 C). The effect of the flow interruption is visible for both experiments 2 and 3 on a log-scale (Figure 6.4). Here there is significant tailing compared to experiment 2 where no flow interruption was employed. This suggests that diffusion within the DNAPL pool may be relevant when considering tracer transport, and deviations from local equilibrium. There is little difference between BTC tails of experiments 2 and 3.

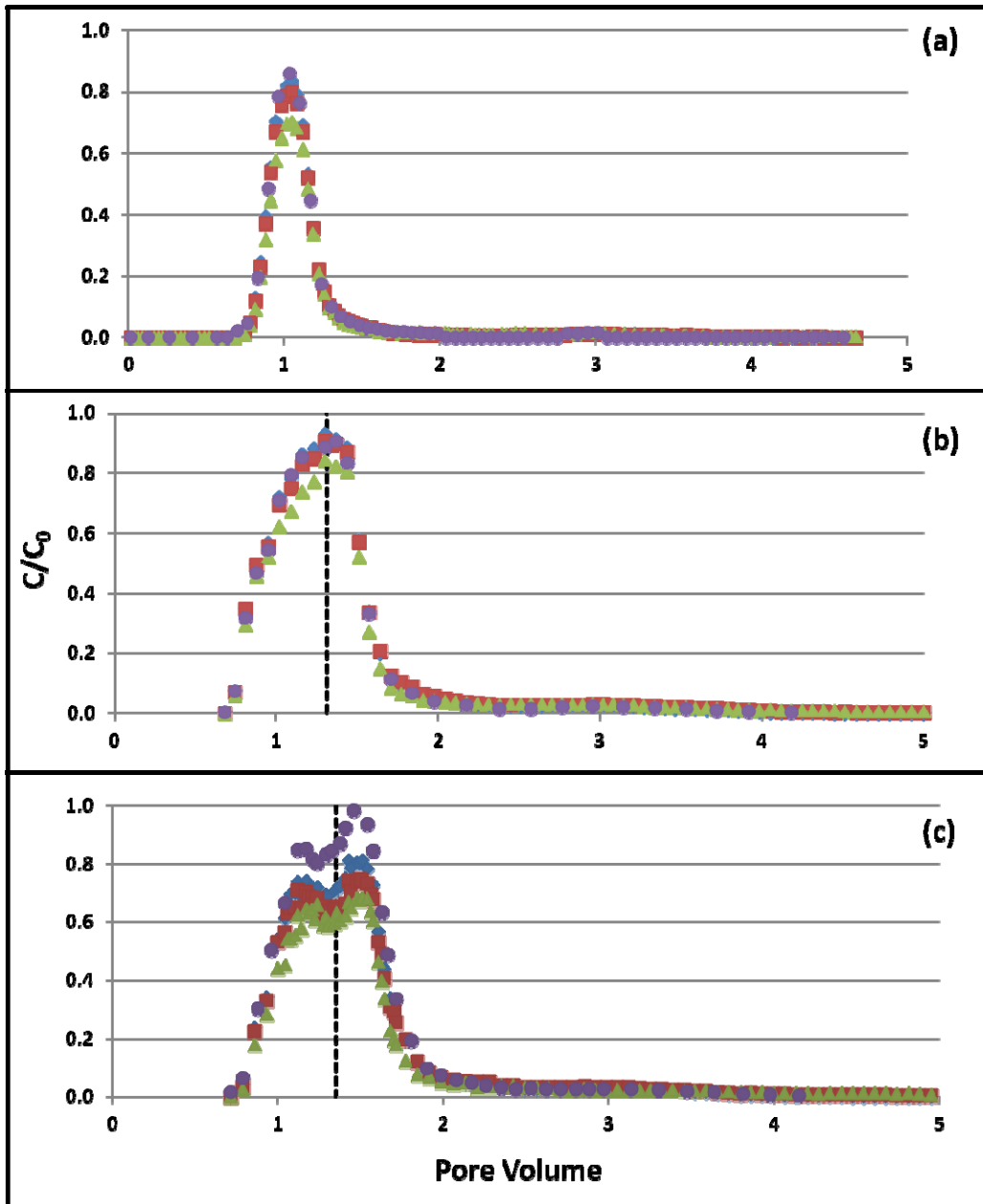


**Figure 6.3** Effluent concentrations for 2-D box experiments 1 (panel a), 2 (panel b) and 3 (panel c). Bromide (circle), 1-pentanol (diamond), 1-hexanol (square) and 2-octanol (triangle) concentrations are shown on all three plots. Also included for experiments 2 and 3 is the dashed line indicating the location of the downgradient edge of the TCE-DNAPL pool during the flow interruption.

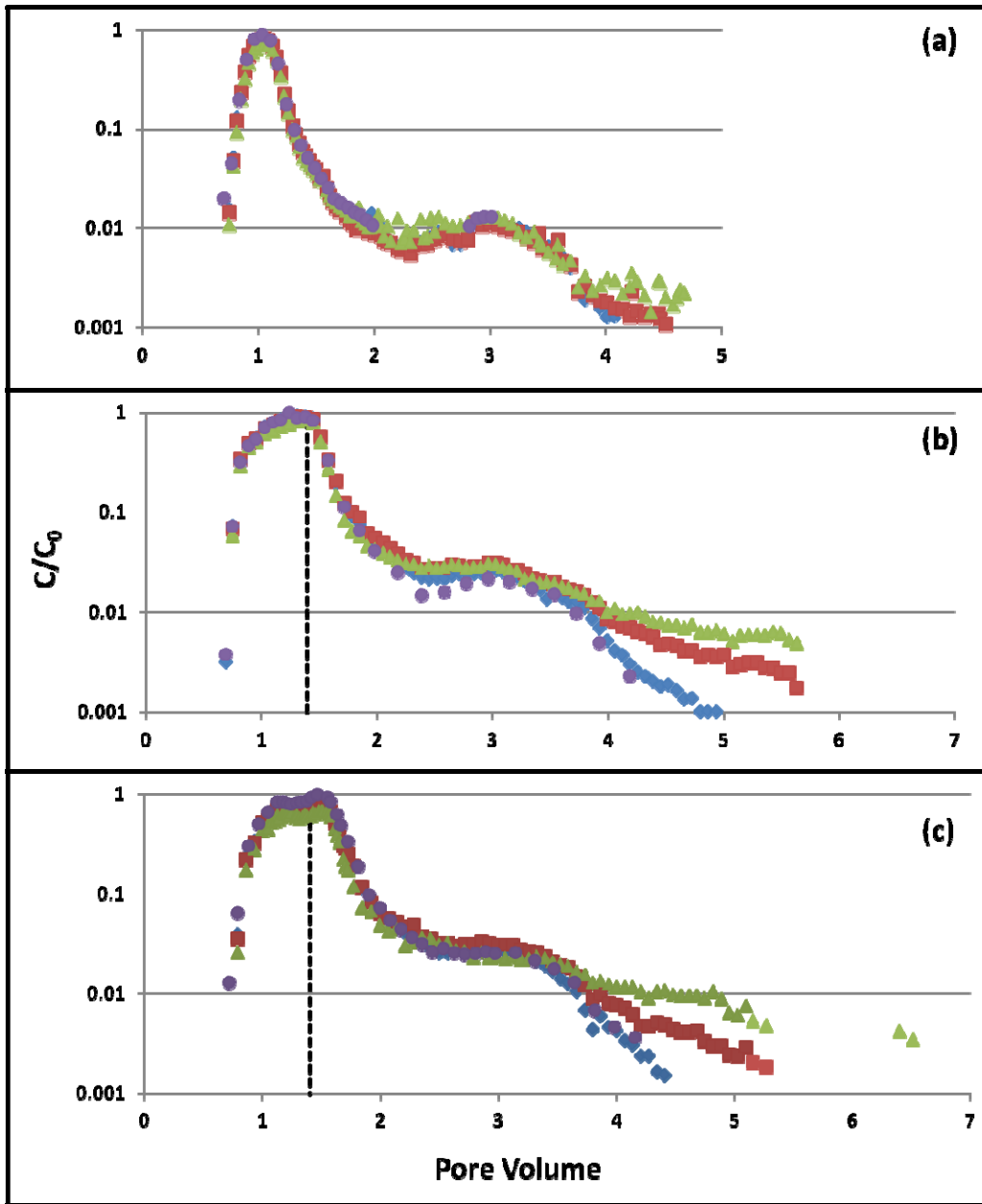


**Figure 6.4** Effluent concentrations for 2-D box experiments 1 (panel a), 2 (panel b) and 3 (panel c). Bromide (circle), 1-pentanol (diamond), 1-hexanol (square) and 2-octanol (triangle) concentrations are shown on all three plots. Also included for experiments 2 and 3 is the dashed line indicating the location of the downgradient edge of the TCE-DNAPL pool during the flow interruption. Note the y-axis is log scale to enable better visualization of BTC tails.

This observation suggests that the increased flow rate of experiment 3 may not have a large influence on the kinetics as assessed by examining the flux-averaged effluent concentrations (i.e., both experiments 2 and 3 are non-equilibrium transport where tailing is, perhaps, controlled by diffusion within the DNAPL).

As described in Chapter 1, Section 1.3.1, the method of temporal moments is commonly used to analyze partitioning tracer tests. A retardation factor is determined for each partitioning tracer by comparing the 1<sup>st</sup> temporal moment of the partitioning tracer to that of the conservative tracer (eq. 1.4). Using these retardation factors, saturation is then estimated as:

$$S_n = \frac{R - 1}{R + K_p^C - 1} \quad (6.1)$$

Temporal moments and corresponding estimates of retardation coefficient were calculated for each tracer in each experiment (Table 6.3) to enable a quantitative comparison of the three effluent curves. A few trends are visible in this Table 6.3. First, as tracer partition coefficient increases center of mass, standard deviation and skew all increase. This is expected, due to the increased tailing of higher partitioning tracers. Additionally, TCE-DNAPL saturation underestimated. This underestimation is expected in source zones with high saturation pools, where flow bypassing is common (e.g. Annable et al., 1998a; Brooks et al., 2002; Hartog et al., 2010). Jin et al. (1997) recommend that estimated retardation coefficients lie between 1.2 and 4.0 to obtain the best overall saturation estimates. When estimated retardation coefficients are less than 1.2, noise in the data has a large impact on BTC interpretation. When estimated retardation coefficients are greater than 4.0, tracer test durations become unreasonable (Annable et al., 1998a).

**Table 6.3** Moment calculations for pooled box experiments. Reported moments include the center of mass, standard deviation and skew. Also shown are estimated retardation coefficients and overall TCE-NAPL saturation estimates.

Experiment	Tracer	Center of Mass	Standard Deviation	skew	R	Estimate Overall $S_n$	Fraction of Actual $S_n^1$
<b>1</b>	<b>Bromide</b>	1.09	0.26	0.08	-	-	-
	<b>Pentanol</b>	1.17	0.47	0.38	1.09	2.04%	1.96
	<b>Hexanol</b>	1.17	0.48	0.42	1.09	0.52%	0.50
	<b>2-Octanol</b>	1.22	0.55	0.56	1.14	0.09%	0.09
<b>2</b>	<b>Bromide</b>	1.33	0.46	0.26	-	-	-
	<b>Pentanol</b>	1.35	0.51	0.39	1.03	0.60%	0.58
	<b>Hexanol</b>	1.40	0.61	0.68	1.08	0.44%	0.42
	<b>2-Octanol</b>	1.44	0.70	1.04	1.11	0.08%	0.08
<b>3</b>	<b>Bromide</b>	1.42	0.46	0.22	-	-	-
	<b>Pentanol</b>	1.44	0.48	0.27	1.01	0.34%	0.33
	<b>Hexanol</b>	1.51	0.64	0.76	1.06	0.45%	0.43
	<b>2-Octanol</b>	1.63	0.96	2.90	1.10	0.13%	0.13

<sup>1</sup>The fraction of actual saturation is calculated as the estimate of overall saturation divided by the actual overall saturation, 1.04%

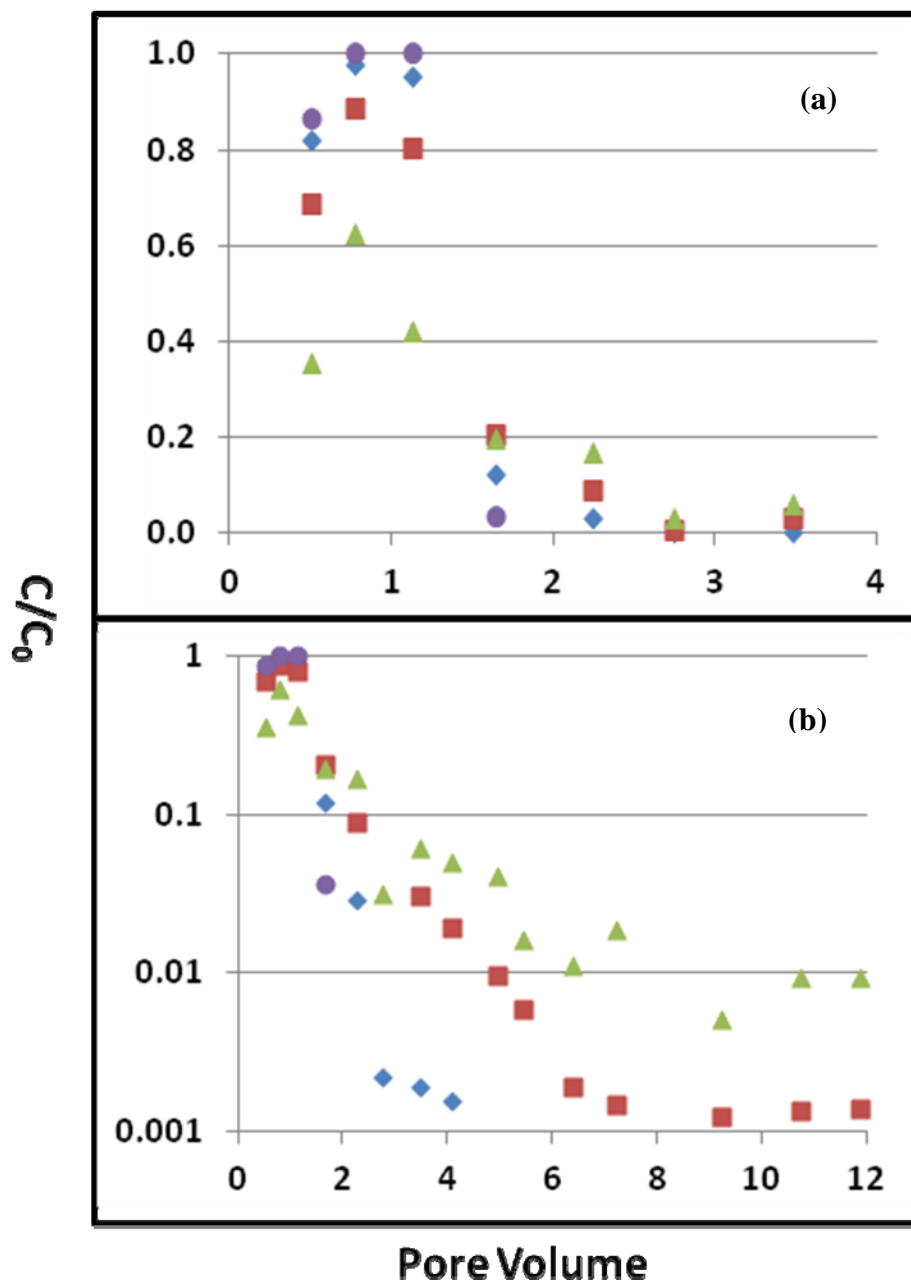


**Figure 6.5** Concentration measurements shown on linear (a) and log (b) scales, taken from local the local port 2C (Figure 6.2) during experiment 2. Bromide (circle), 1-pentanol (diamond), 1-hexanol (square) and 2-octanol (triangle) concentrations are shown on both plots. Note the change in x-axis scale between panels a and b.

Therefore, when a suite of tracers is used, tracer BTCs that result in estimated retardation coefficients between 1.2 and 4.0 should be employed in the method of moments to provide the best estimates of overall saturation. Due to a combination of low overall saturation and flow bypassing, retardation factors shown in Table 6.3 do not fall within this recommended range. Therefore, it is unsurprising that overall saturation estimates are inaccurate.

Unlike the effluent data, the effect of the high saturation pool is visible in the local port data. Shown in Figure 6.5 are data from sampling port 2C (Figure 6.2) taken during experiment 2. These data are representative of BTCs whose flow paths interacted with the DNAPL pool. The complete set of port data is presented later in this chapter (Section 6.3.2). Here, tracer separation is seen both in the difference separation of the maximum  $C/C_0$  values of each tracer (Figure 6.5 a) and in the stronger tailing of the higher partitioning tracers (Figure 6.5 b).

### *6.3.1 Numerical Modeling of Effluent BTCs*

A quantitative transport model is necessary to explain both the local and effluent BTCs generated in the above partitioning tracer tests. In Chapter 5, it was shown that a mass transfer coefficient correlation developed for DNAPL dissolution can be used to predict tracer partitioning in ganglia dominated systems (Ervin et al., 2011). It is therefore plausible that a correlation developed through dissolution from DNAPL pools may provide adequate predictions of tracer partitioning to/from DNAPL pools. The literature review discussed in Chapter 1, Section 5.4.2 identifies six pool dissolution studies that provide mass transfer

coefficients that may be applicable to tracer transport in the pooled box experiments.

The Nambi and Powers (2003) correlation was employed in the 2-D linear driving force model described in Chapter 3, Section 3.4.3 to produce effluent BTCs for all three experiments (Figures 6.6 – 6.8). The Nambi and Powers (2003) correlation was selected because it was developed for both local scale and overall dissolution. Additionally, this correlation includes a saturation term which may be useful for predicting transport in source zones with heterogeneous DNAPL saturations. The only adjustable parameter in the model is longitudinal dispersivity which was fit to bromide data in each experiment (dispersivity is 0.13 cm, 0.21 cm and 0.51 cm for experiments 1, 2, and 3, respectively). Note here that transverse dispersivity is assumed to be 10% of the longitudinal value. In order to account for continued tracer partitioning into the DNAPL during the flow interruption the Nambi and Powers (2003) correlation was modified to contain an additional kinetic term to account for mass exchange during periods of no flow (see description in Chapter 3, Section 3.4.3).

Overall the model appears to capture the general shape of the effluent breakthrough curve produced in experiment 1 (Figure 6.6). When viewed on the log-scale (panel b in Figure 6.6), it becomes apparent that the model is able to capture the slight dip and recovery in concentrations seen between approximately 1.8 and 3 pore volumes, but over predicts the subsequent increase in concentrations. The remainder of the tail concentrations ( $> 4$  PV) are well captured by the model. Effluent breakthrough curves from Experiments 2 and 3

have more difficult shapes to capture as seen in Figures 6.7 and 6.8. As seen in the table of sum of squared errors (Table 6.4), the model error is 5-10 times higher in experiments 2 and 3, compared to experiment 1. It is hypothesized that model does a poorer job at capturing the effluent data from experiments 2 and 3 because it is incapable of accurately describing the transient flow field during and after the flow interruption. The model employed for these simulations assumes confined flow. The box, however, is unconfined. During experiments where the flow is steady (e.g., Experiment 1) the confined model does a good job at capturing the flow field. The flow interruptions, however, are physically created by instantaneously stopping the influent and effluent flow to the box. This then creates a situation where the location of the water becomes transient, as the gradient decays to the equilibrium state (i.e., level water table at an elevation corresponding to the volume of water within the box). A similar transient period occurs when the flow to and from the box is instantaneously re-established at the end of the flow interruption period. This inconsistency between the physical experiment and numerical model is explored further when examining the port data from each experiment.

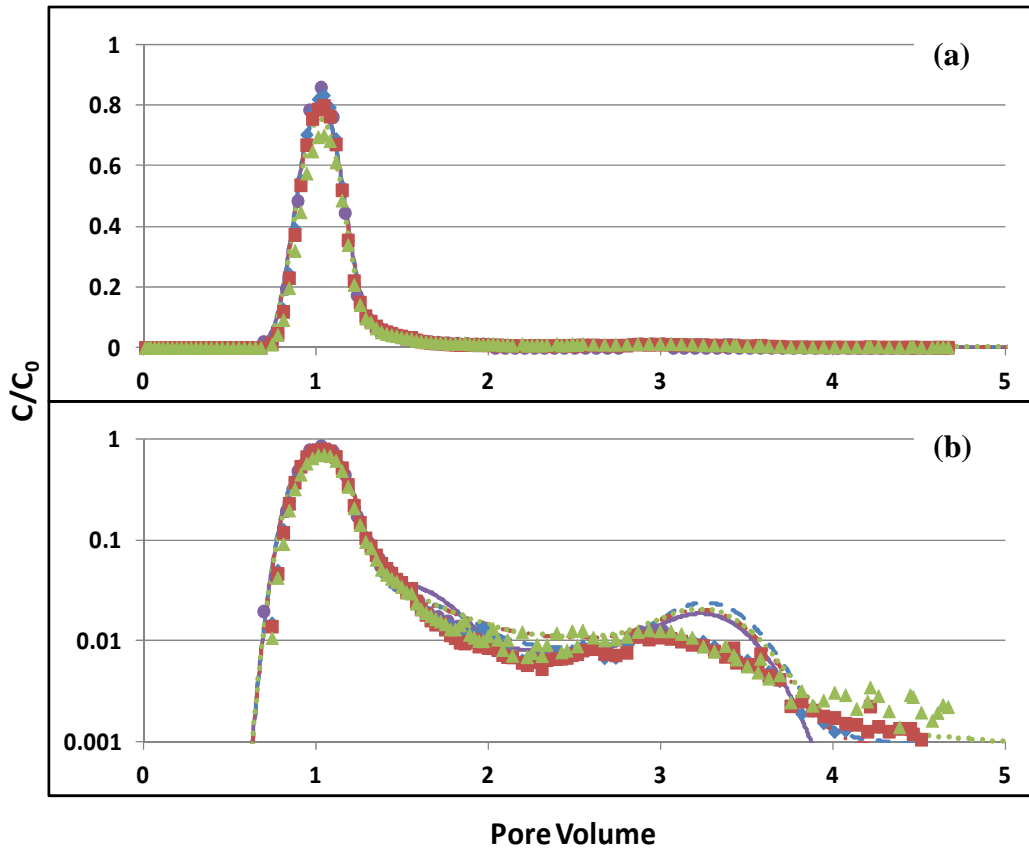


**Figure 6.6** Comparison of experiment 1 effluent data and model simulations using the Nambi and Powers (2003) mass transfer coefficient correlation. Bromide (circles and solid line), pentanol (diamonds and dashed line), hexanol (squares and dash-dot line) and 2-octanol (triangles and dotted line) are included. The model was fit to the bromide data by adjusting dispersivity. All partitioning tracer breakthrough curves were subsequently predicted using this fitted dispersivity.

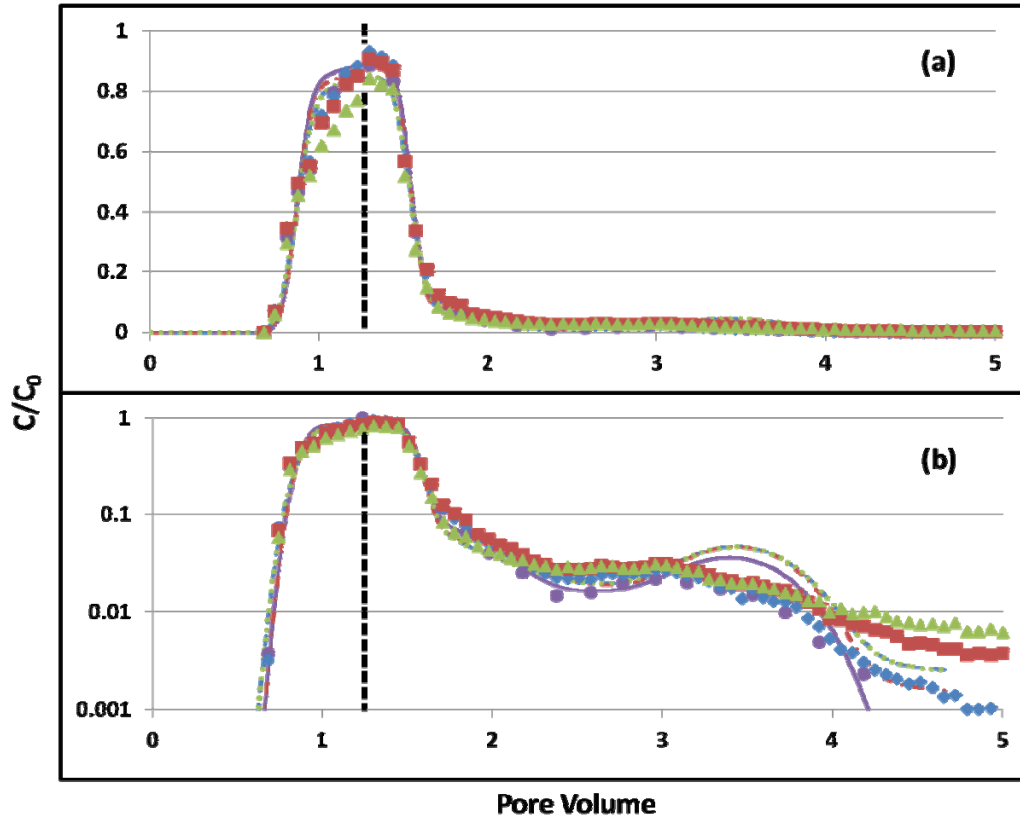


**Figure 6.7** Comparison of experiment 2 effluent data and model simulations using the Nambi and Powers (2003) mass transfer coefficient correlation. Bromide (circles and solid line), pentanol (diamonds and dashed line), hexanol (squares and dash-dot line) and 2-octanol (triangles and dotted line) are included. The dashed vertical line indicates the location of the downgradient edge of the TCE-DNAPL pool during the flow interruption. The model was fit to the bromide data by adjusting dispersivity. All partitioning tracer breakthrough curves were subsequently predicted using this fitted dispersivity.

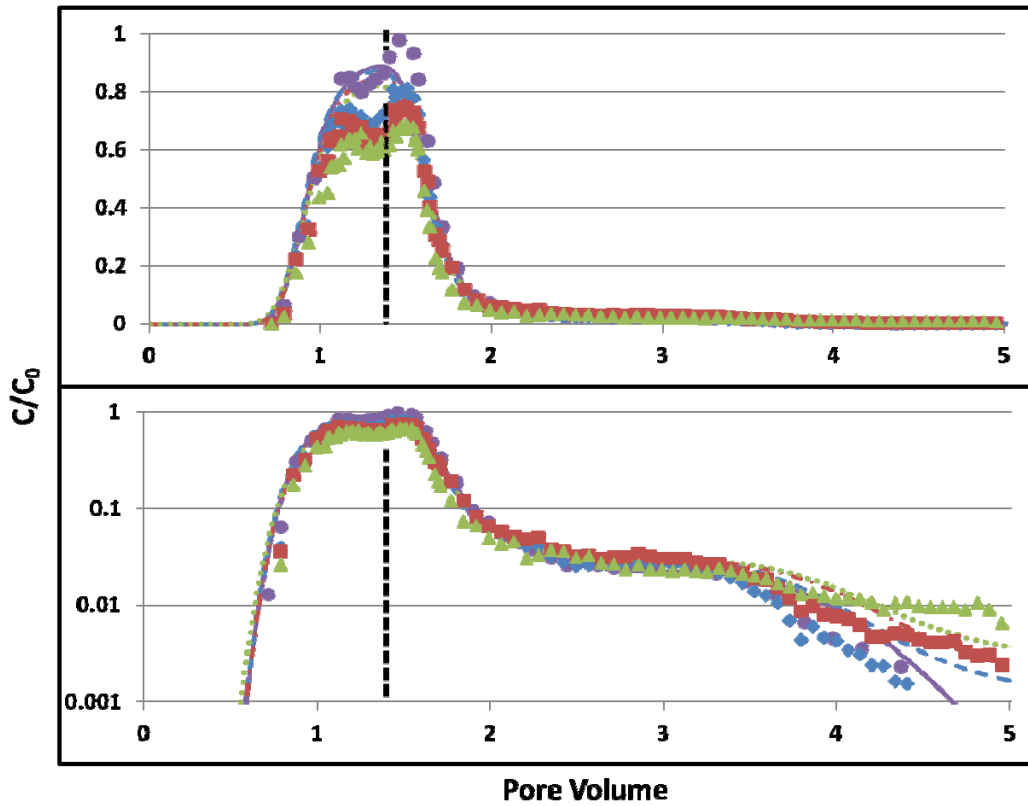


**Figure 6.8** Comparison of experiment 3 effluent and model simulations using the Nambi and Powers (2003) mass transfer coefficient correlation. Bromide (circles and solid line), pentanol (diamonds and dashed line), hexanol (squares and dash-dot line) and 2-octanol (triangles and dotted line) are included. The dashed vertical line indicates the location of the downgradient edge of the TCE-DNAPL pool during the flow interruption. The model was fit to the bromide data by adjusting dispersivity. All partitioning tracer breakthrough curves were subsequently predicted using this fitted dispersivity.

**Table 6.4** Sum of squared error between experimental effluent data and model predictions for each tracer in experiments 1-3. Recall that experiment 1 does not employ a flow interruption, while experiments 2 and 3 each employ a 60 hour flow interruption.

<b>Experiment</b>	<b>Sum of Squared Error Bromide</b>	<b>Sum of Squared Error 1-Pentanol</b>	<b>Sum of Squared Error 1-Hexanol</b>	<b>Sum of Squared Error 2-Octanol</b>
<b>1</b>	0.02	0.03	0.02	0.06
<b>2</b>	0.10	0.08	0.12	0.11
<b>3</b>	0.20	0.43	0.51	0.75

### *6.3.2 Local Concentrations as Established from the Array of Sampling Ports*

Samples collected from the ports shown in Figure 6.1 were used to construct local BTCs in an effort to examine the influence of the pool on the spatial distribution of tracer concentrations within the box. These local BTCs were subsequently examined by interrogating local concentration predictions produced during each of the aforementioned model simulations. Emphasis here is placed on assessing the Nambi and Powers (2003) mass transfer correlation for predicting the partitioning of these tracers. Local BTCs are shown for experiment 1 in Figures 6.9 - 6.12 grouped by column (see Figure 6.2). For this experiment, bromide was not analyzed in the port samples collected during this experiment.

Simulations for each partitioning tracer match the data well for most ports. The dispersivity value fit to the bromide effluent curve was used to predict tracer BTCs at each sampling port. Shown in Table 6.5 are the sum of squared errors between the measured port data and the model predictions of local concentration. These errors are included to aid in quantitative comparison of model performance at each port; however, caution should be employed in direct comparison of these values because of the low number of experimental data points available at each port. In column 1, predictions for port 1E slightly under predict maximum  $C/C_0$  values, but still capture the general shape of the data. For port 1D, the port most affected by the combination of the low permeability berm and the TCE-DNAPL pool, the simulations accurately captures the data. In column 2, the data for all of the ports, except 2D are well reproduced. However, even the predictions at port 2D are able to capture the overall shape and low  $C/C_0$  values seen in the data.

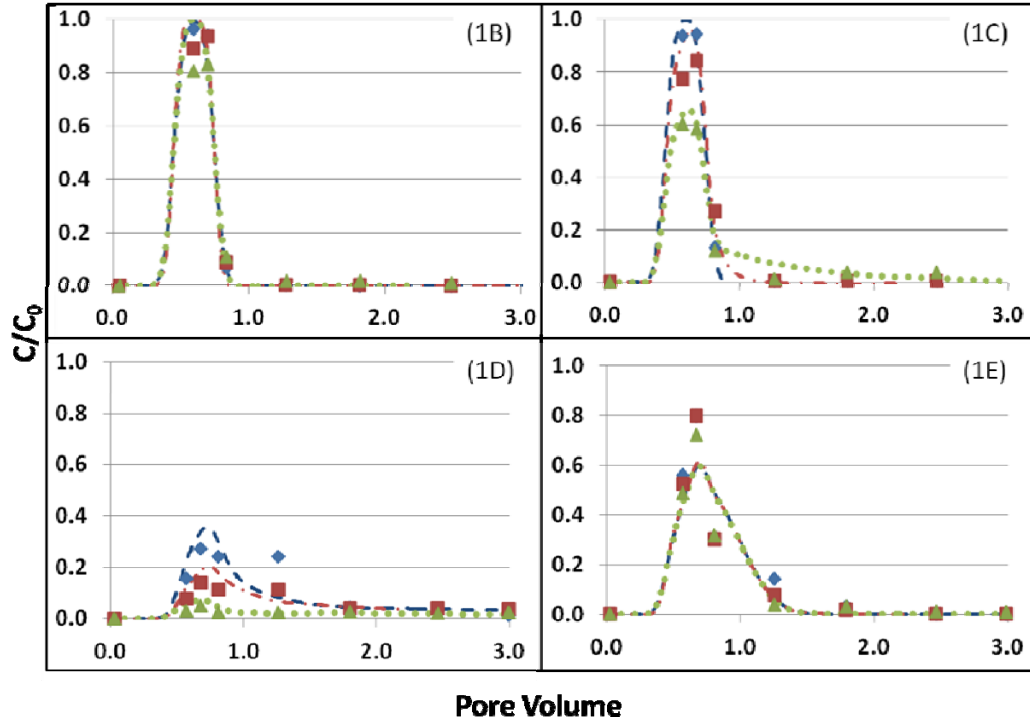


**Figure 6.9** Comparison of column 1 port data from experiment 1 and model predictions using the Nambi and Powers (2003) mass transfer coefficient correlation. 1-pentanol (diamonds, dashed line), 1-hexanol (squares, dash-dot line) and 2-octanol (triangles, dotted line) are included. Panel labels correspond to specific ports shown in Figure 6.2.

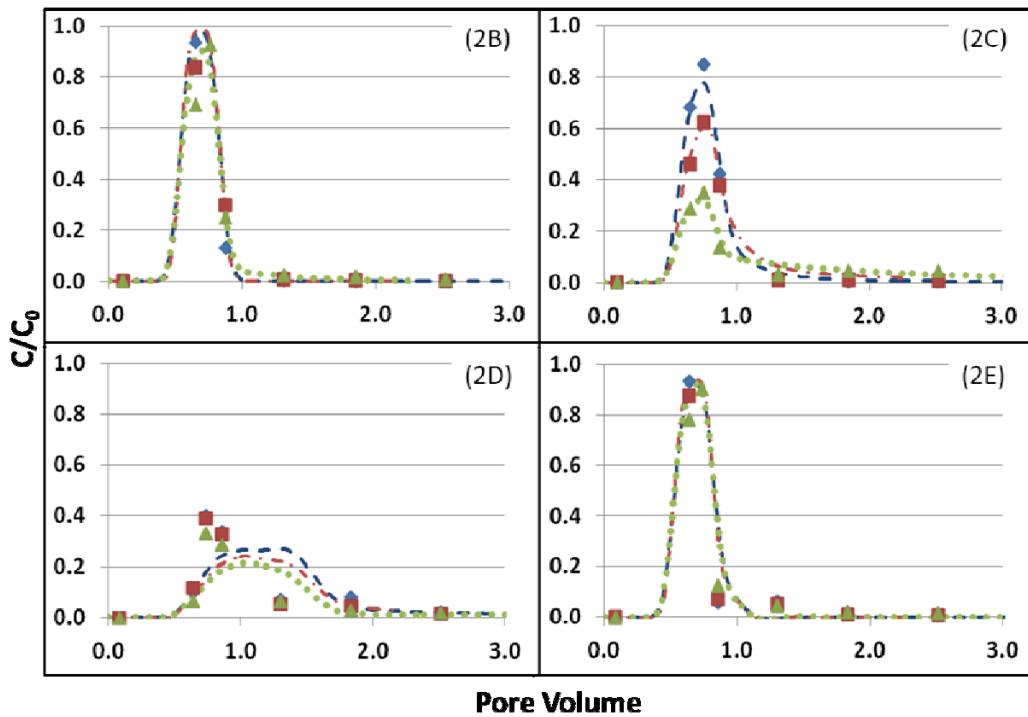


**Figure 6.10** Comparison of column 2 port data from experiment 1 and model predictions using the Nambi and Powers (2003) mass transfer coefficient correlation. 1-pentanol (diamonds, dashed line), hexanol (squares, dash-dot line) and 2-octanol (triangles, dotted line) are included. Panel labels correspond to specific ports show in Figure 6.2.

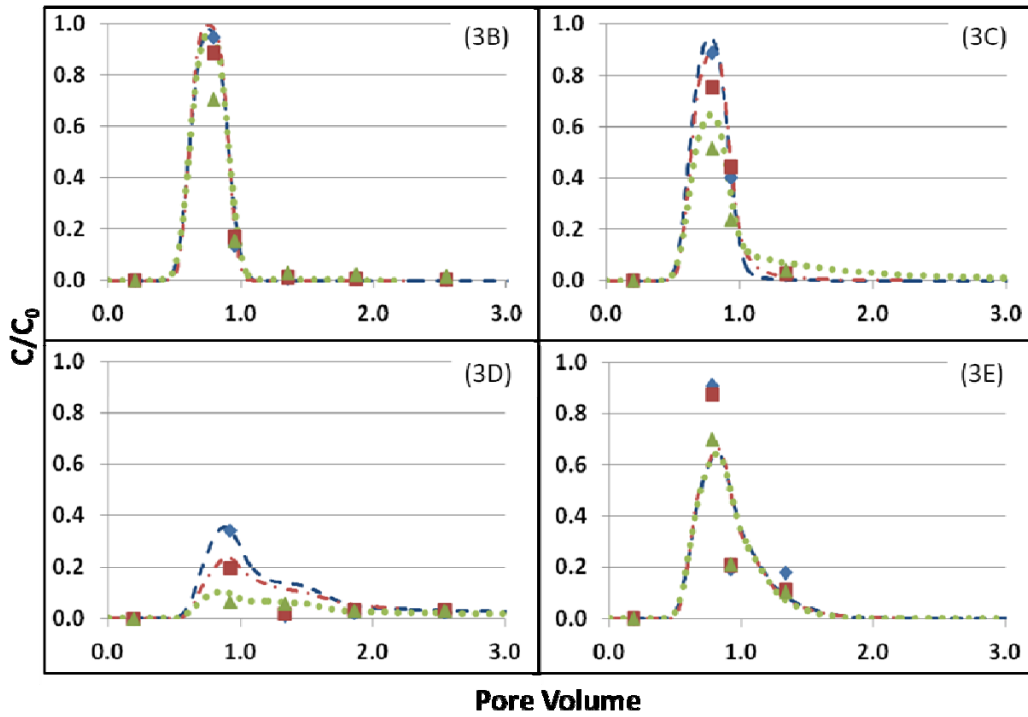


**Figure 6.11** Comparison of column 3 port data from experiment 1 and model predictions using the Nambi and Powers (2003) mass transfer coefficient correlation. 1-pentanol (diamonds, dashed line), hexanol (squares, dash-dot line) and 2-octanol (triangles, dotted line) are included. Panel labels correspond to specific ports show in Figure 6.2.

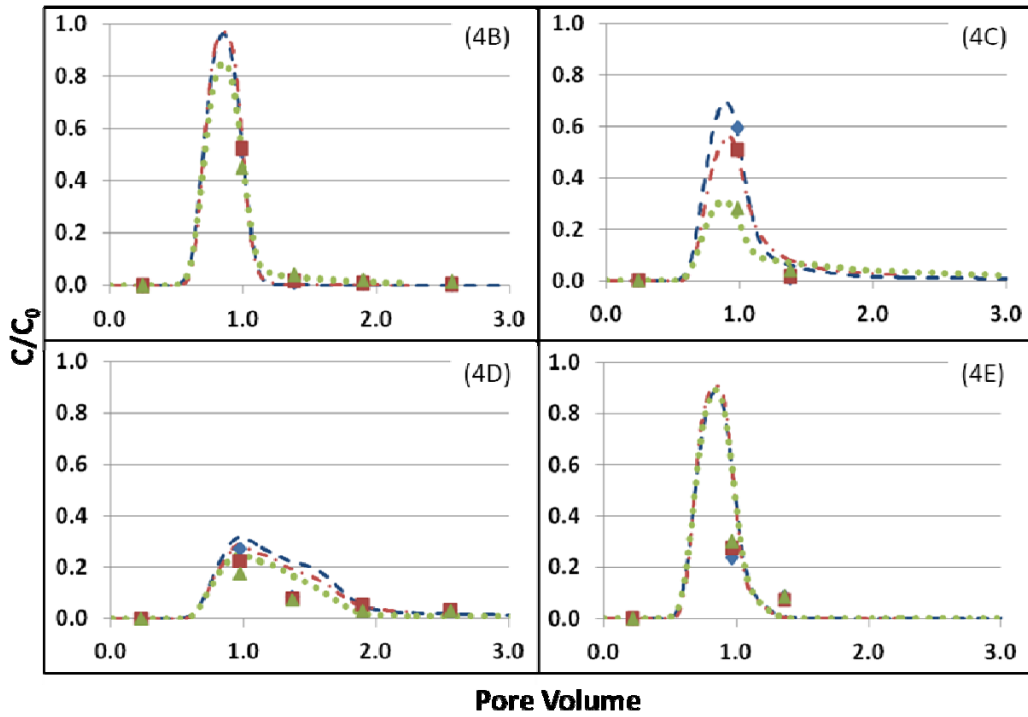


**Figure 6.12** Comparison of column 4 port data from experiment 1 and model predictions using the Nambi and Powers (2003) mass transfer coefficient correlation. 1-pentanol (diamonds, dashed line), hexanol (squares, dash-dot line) and 2-octanol (triangles, dotted line) are included. Panel labels correspond to specific ports show in Figure 6.2.

**Table 6.5** Sum of squared error between experimental data and model predictions at local sampling ports for experiment 1.

<b>Port</b>	<b>Sum of Squared Error 1-Pentanol</b>	<b>Sum of Squared Error 1-Hexanol</b>	<b>Sum of Squared Error 2-Octanol</b>
<b>1B</b>	0.02	0.02	0.04
<b>1C</b>	0.01	0.03	0.01
<b>1D</b>	0.04	0.01	0.00
<b>1E</b>	0.10	0.08	0.05
<b>2B</b>	0.08	0.05	0.04
<b>2C</b>	0.01	0.01	0.00
<b>2D</b>	0.10	0.10	0.07
<b>2E</b>	0.13	0.08	0.08
<b>3B</b>	0.03	0.02	0.09
<b>3C</b>	0.01	0.02	0.03
<b>3D</b>	0.02	0.01	0.00
<b>3E</b>	0.18	0.14	0.09
<b>4B</b>	0.00	0.01	0.01
<b>4C</b>	0.00	0.00	0.00
<b>4D</b>	0.02	0.02	0.01
<b>4E</b>	0.03	0.12	0.09

Results for column 3 are similar to column 1 and those for column 4 are similar to column 2. This is because columns 1 and 3 are horizontally aligned as are columns 2 and 4 (see Figure 6.2). Comparison between columns 1 (or 3) and 2 (or 4), however suggests a fine-scale local variation in concentration. Though these two sets of ports (columns 1 and 3 versus columns 2 and 4) are only vertically offset by 1 cm, the differences in the breakthrough curves are distinct (e.g. ports C, D, and E for columns 1 and 2). This shows that the scale of vertical heterogeneity around the low permeability berm and TCE pool is on the order of 1 cm, highlighting the importance of precise alignment of the local ports in the model domain.

The same modeling procedure was applied to the local port data from experiment 2 (Table 6.2). Recall, the two principal differences in this experiment are that the pulse volume is 0.67 PV (compared to 0.31 PV in experiment 1) and a 60 hour flow interruption was employed after pumping in the pulse. Local breakthrough curves established from port samples and model simulations are shown in Figures 6.13 – 6.16. A table of sum of squared errors is provided below in Table 6.6. Here, it is again seen that model performance is not as good as was observed for experiment 1. In general, predictions of the B and C ports are able to capture the bromide data, and somewhat able to capture the partitioning tracer data. In the D ports, neither the bromide or partitioning tracer data is well captured. In the E ports, the model captures some of the bromide behavior, but underpredicts partitioning for all partitioning tracers.

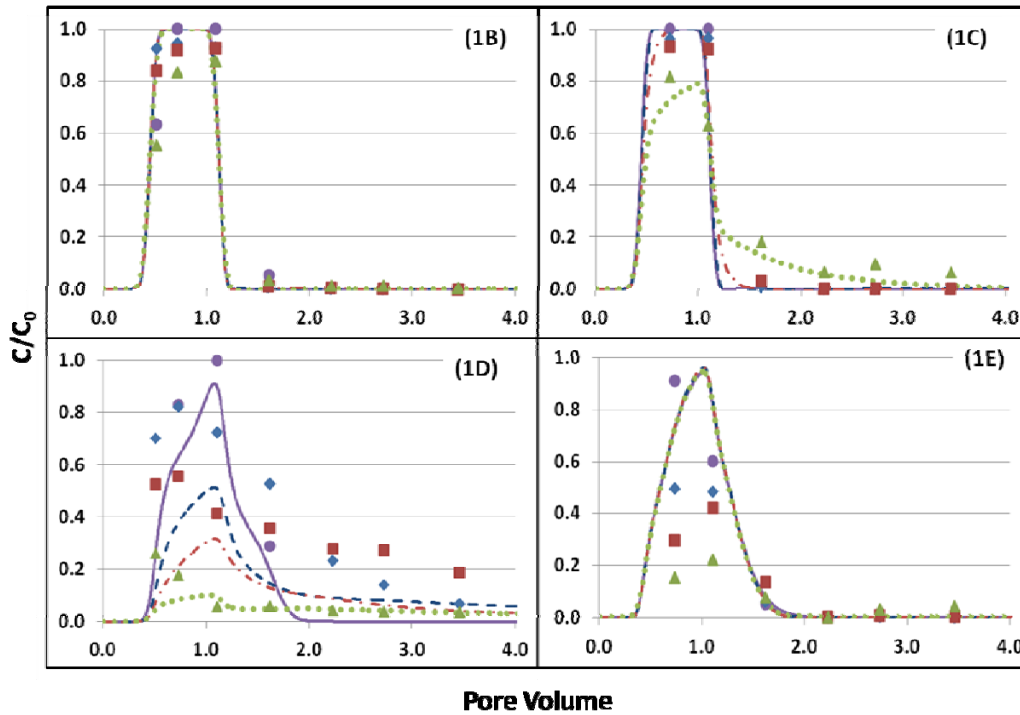


**Figure 6.13** Comparison of column 1 port data from experiment 2 and model predictions using the Nambi and Powers (2003) mass transfer coefficient correlation. Bromide (circles, solid line), 1-pentanol (diamonds, dashed line), 1-hexanol (squares, dash-dot line) and 2-octanol (triangles, dotted line) are included. Panel labels correspond to specific ports show in Figure 6.2.

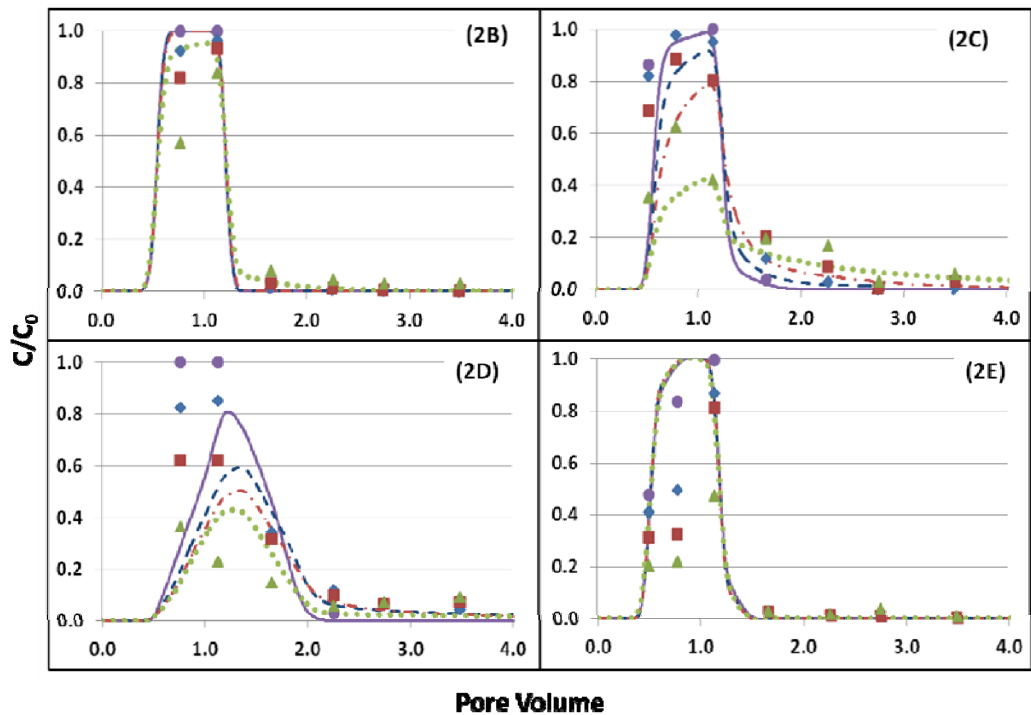


**Figure 6.14** Comparison of column 2 port data from experiment 2 and model predictions using the Nambi and Powers (2003) mass transfer coefficient correlation. Bromide (circles, solid line), 1-pentanol (diamonds, dashed line), 1-hexanol (squares, dash-dot line) and 2-octanol (triangles, dotted line) are included. Panel labels correspond to specific ports show in Figure 6.2.

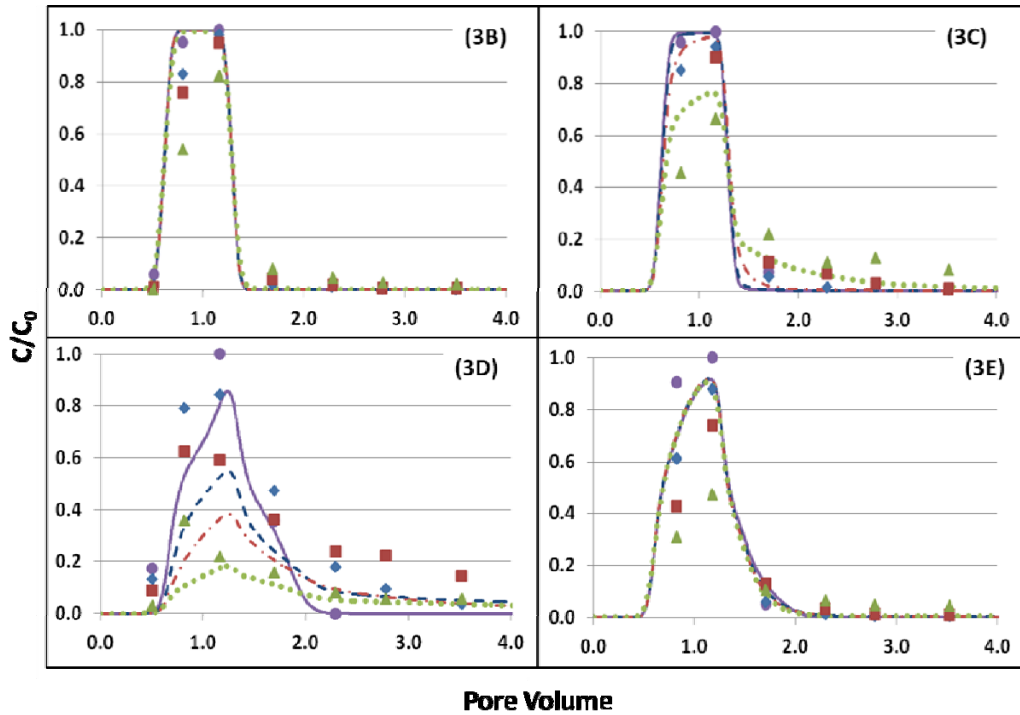


**Figure 6.15** Comparison of column 3 port data from experiment 2 and model predictions using the Nambi and Powers (2003) mass transfer coefficient correlation. Bromide (circles, solid line), 1-pentanol (diamonds, dashed line), 1-hexanol (squares, dash-dot line) and 2-octanol (triangles, dotted line) are included. Panel labels correspond to specific ports show in Figure 6.2.

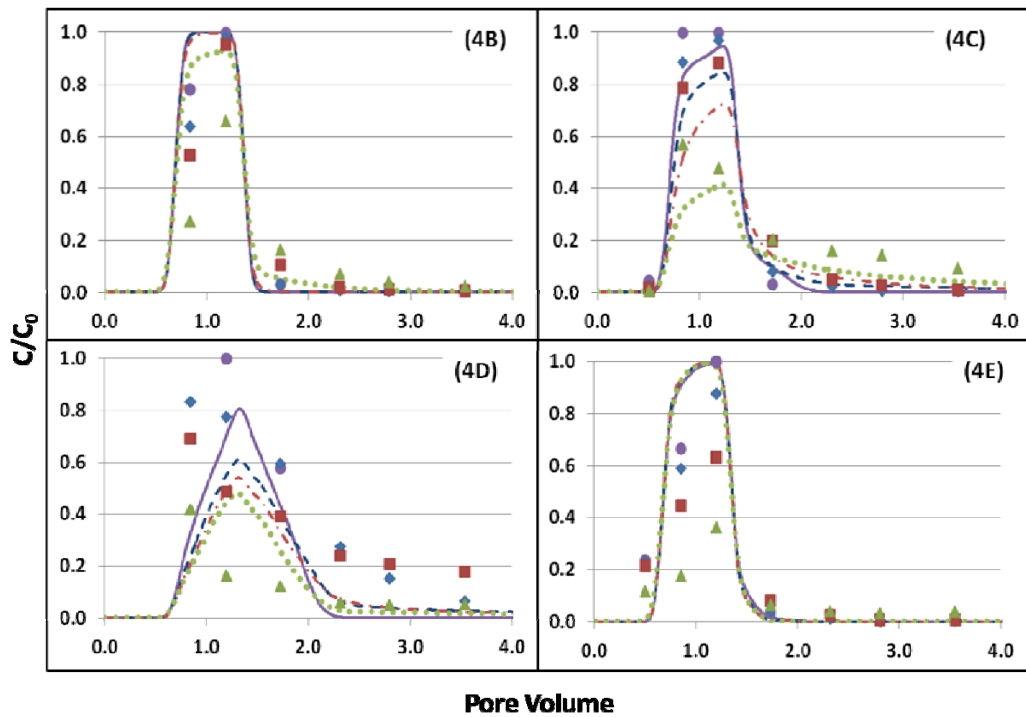


**Figure 6.16** Comparison of column 4 port data from experiment 2 and model predictions using the Nambi and Powers (2003) mass transfer coefficient correlation. Bromide (circles, solid line), 1-pentanol (diamonds, dashed line), 1-hexanol (squares, dash-dot line) and 2-octanol (triangles, dotted line) are included. Panel labels correspond to specific ports show in Figure 6.2.

**Table 6.6** Sum of squared error between experimental data and model predictions at local sampling ports for experiment 2.

<b>Port</b>	<b>Sum of Squared Error Bromide</b>	<b>Sum of Squared Error 1-Pentanol</b>	<b>Sum of Squared Error 1-Hexanol</b>	<b>Sum of Squared Error 2-Octanol</b>
<b>1B</b>	0.07	0.04	0.05	0.16
<b>1C</b>	0.13	0.07	0.03	0.02
<b>1D</b>	0.24	0.76	0.52	0.06
<b>1E</b>	0.09	0.18	0.37	0.70
<b>2B</b>	0.00	0.01	0.03	0.14
<b>2C</b>	0.44	0.50	0.42	0.16
<b>2D</b>	0.59	0.52	0.25	0.10
<b>2E</b>	0.05	0.24	0.44	0.72
<b>3B</b>	0.00	0.03	0.06	0.24
<b>3C</b>	0.01	0.02	0.32	0.09
<b>3D</b>	0.07	0.39	0.33	0.07
<b>3E</b>	0.06	0.01	0.11	0.34
<b>4B</b>	0.04	0.12	0.20	0.44
<b>4C</b>	0.04	0.06	0.11	0.09
<b>4D</b>	0.11	0.51	0.34	0.16
<b>4E</b>	0.11	0.18	0.41	0.97

Recall that the confined flow model employed herein is a reasonable model of the physical flow in experiment 1, but may be a poor representation of flow in experiments 2 and 3 (due to the flow interruption). To be clear, the model can incorporate transient flow fields, but cannot simulate a transient water table. Specifically, it is hypothesized that it is critical to model the flowfield created when flow is restarted after the flow interruption. Instantaneously raising head on the lefthand side and lowering it on the righthand side, may cause the flow field to curve down and around the pool more than it does during steady flow. This idea is supported by the data. Consider the comparison of data and simulation in ports D and E in column 1 (other columns show similar comparisons). Note that the model underpredicts the data in port D and over predicts the data in port E. The flow field for this simulation (Figure 6.17) shows that velocity is generally horizontal from the pool to the ports. In the simulation there is more partitioning in port D (which is more or less level with the pool) than port E (which is slightly below the pool). The data, however, illustrate the opposite trend. There is greater partitioning in port E data and port D data, suggesting that the flow from the pool is migrating downward.

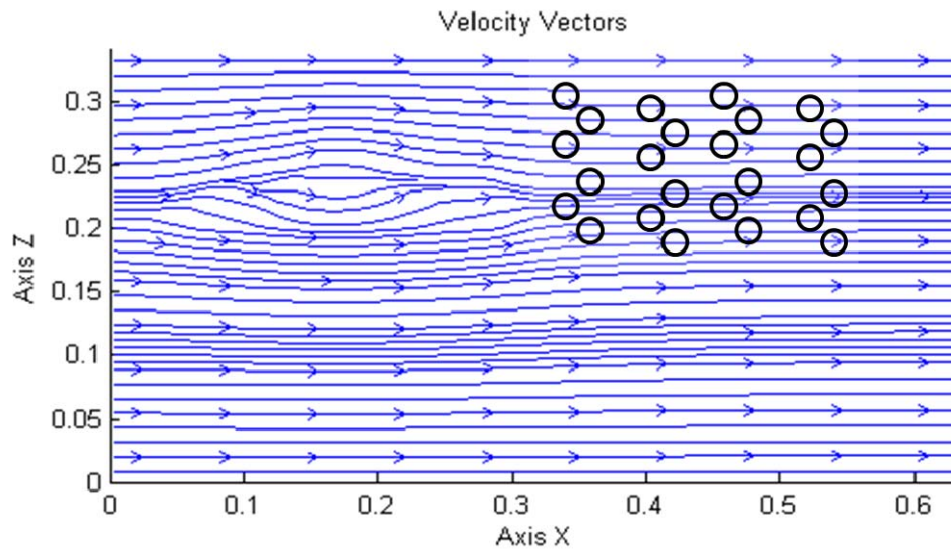


**Figure 6.17** Flow field generated by the confined model immediately upon restarting flow after the flow interruption.

Below, shown in Figures 6.18 – 6.21, are the model predictions of local port BTCs for experiment 3. A table of sum of squared errors is also included below in Table 6.7. Model performance for experiment 3 is similar to that of experiment 3. Recall, the principal difference between experiments 2 and 3 is the flow rate (5.2 mL/min in experiment 2 and 8.6 mL/min in experiment 3). Note that measurements were not taken from the “B” ports in this experiment because the higher flow rate was thought to have lowered the water table close to these port locations. Experiment 3 also employed a flow interruption, which again seems introduce discrepancies between the data and the model. The model is able to capture the bromide data well in all of the C ports except for column 4 where the peak concentration is over predicted. Partitioning behavior is also best captured in the C ports. In the D ports, the model tends to over predict partitioning and under predict spreading. Predictions of the E ports show very little partitioning, though partitioning is seen in the experimental data. As with experiment 2, model predictions of local port data have sum of squared errors that are on average 5 times those seen in experiment 1. Here, it is again hypothesized that the confined model is not able to produce the flow dynamics caused by the flow interruption.

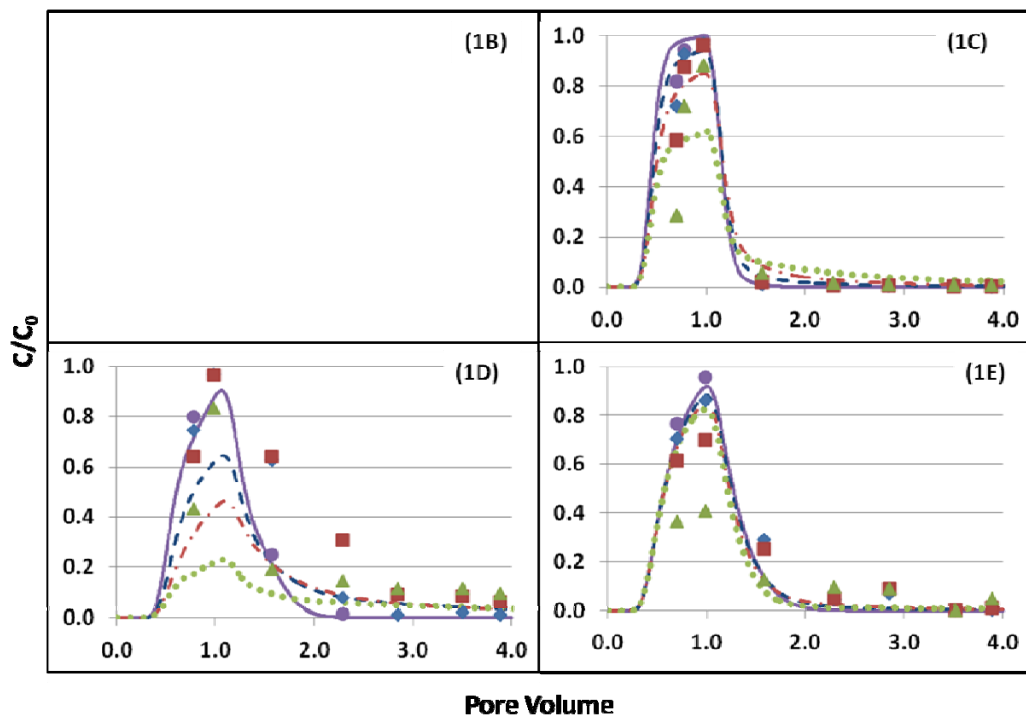


**Figure 6.18** Comparison of column 1 port data from experiment 3 and model predictions using the Nambi and Powers (2003) mass transfer coefficient correlation. Bromide (circles, solid line), 1-pentanol (diamonds, dashed line), 1-hexanol (squares, dash-dot line) and 2-octanol (triangles, dotted line) are included. Panel labels correspond to specific ports show in Figure 6.2. Note port samples were not taken from port 1B in this experiment.

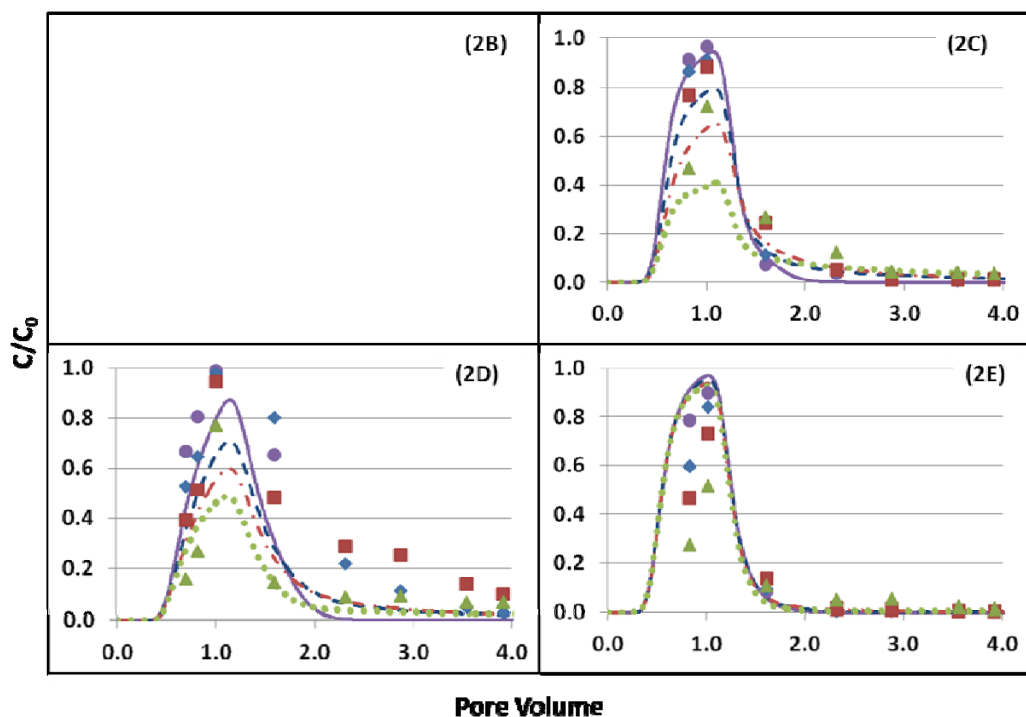


**Figure 6.19** Comparison of column 2 port data from experiment 3 and model predictions using the Nambi and Powers (2003) mass transfer coefficient correlation. Bromide (circles, solid line), 1-pentanol (diamonds, dashed line), 1-hexanol (squares, dash-dot line) and 2-octanol (triangles, dotted line) are included. Panel labels correspond to specific ports show in Figure 6.2. Note port samples were not taken from port 2B in this experiment.

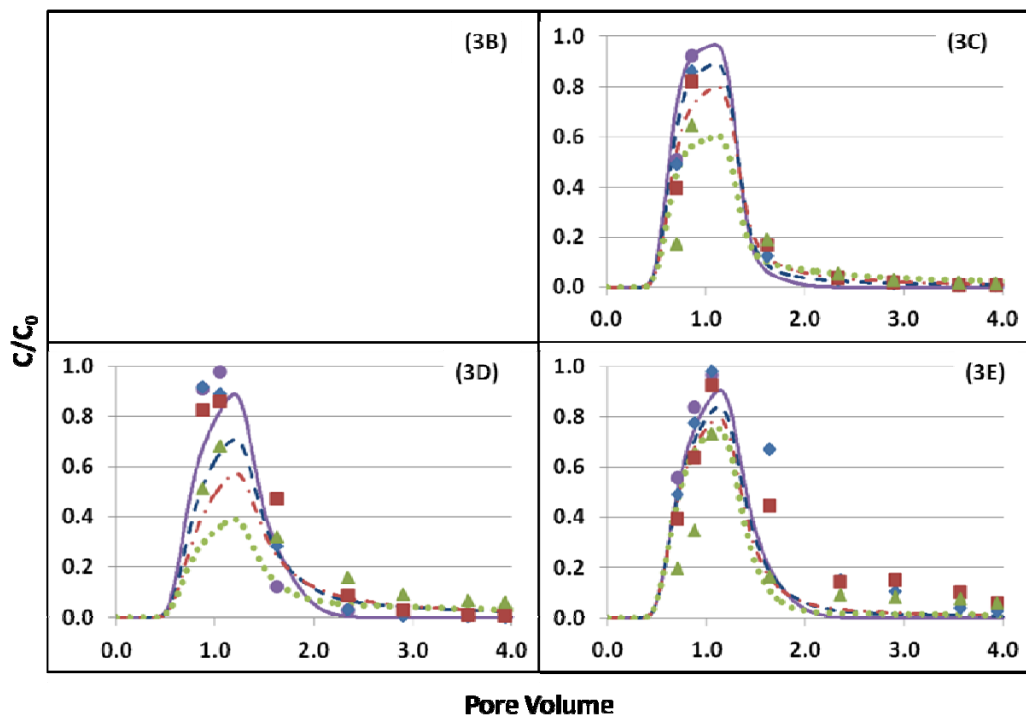


**Figure 6.20** Comparison of column 3 port data from experiment 3 and model predictions using the Nambi and Powers (2003) mass transfer coefficient correlation. Bromide (circles, solid line), 1-pentanol (diamonds, dashed line), 1-hexanol (squares, dash-dot line) and 2-octanol (triangles, dotted line) are included. Panel labels correspond to specific ports show in Figure 6.2. Note port samples were not taken from port 3B in this experiment.

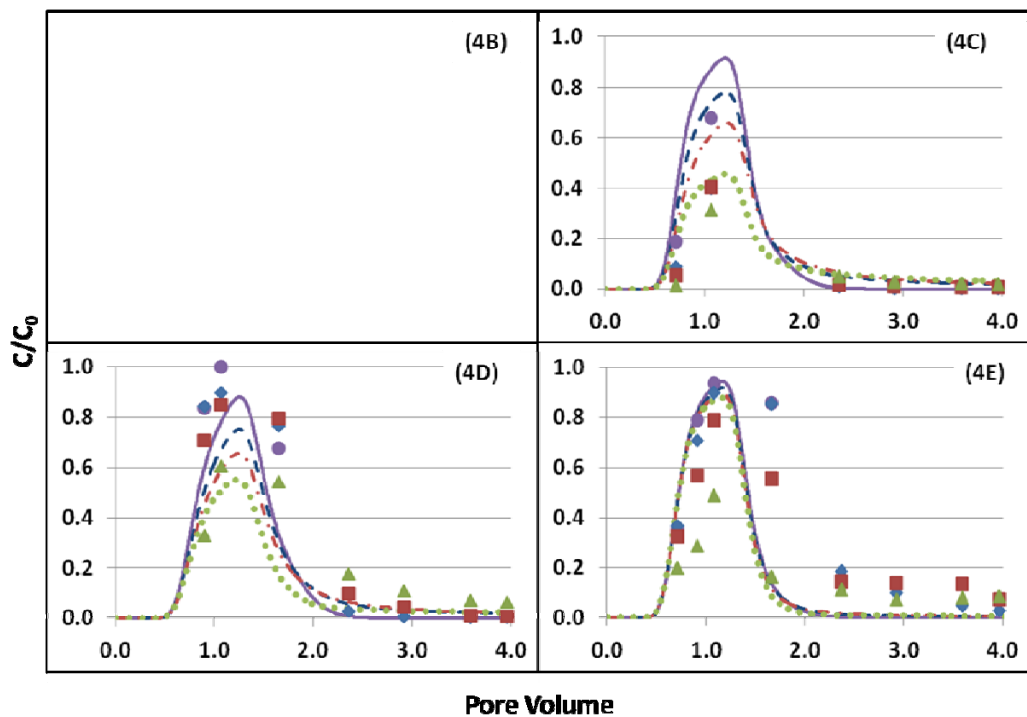


**Figure 6.21** Comparison of column 4 port data from experiment 3 and model predictions using the Nambi and Powers (2003) mass transfer coefficient correlation. Bromide (circles, solid line), 1-pentanol (diamonds, dashed line), 1-hexanol (squares, dash-dot line) and 2-octanol (triangles, dotted line) are included. Panel labels correspond to specific ports show in Figure 6.2. Note port samples were not taken from port 4B in this experiment.

**Table 6.7** Sum of squared error between experimental data and model predictions at local sampling ports for experiment 3.

<b>Port</b>	<b>Sum of Squared Error Bromide</b>	<b>Sum of Squared Error 1-Pentanol</b>	<b>Sum of Squared Error 1-Hexanol</b>	<b>Sum of Squared Error 2-Octanol</b>
<b>1C</b>	0.03	0.03	0.06	0.17
<b>1D</b>	0.01	0.36	0.62	0.48
<b>1E</b>	0.19	0.03	0.05	0.28
<b>2C</b>	0.05	0.02	0.03	0.09
<b>2D</b>	0.11	0.22	0.35	0.21
<b>2E</b>	0.15	0.28	0.15	0.19
<b>3C</b>	0.01	0.04	0.11	0.15
<b>3D</b>	0.25	0.47	0.35	0.13
<b>3E</b>	0.02	0.10	0.23	0.55
<b>4C</b>	0.07	0.15	0.08	0.04
<b>4D</b>	0.22	0.38	0.42	0.19
<b>4E</b>	0.53	0.58	0.32	0.50

### 6.3.3 - Assessment of Pool Dissolution Mass Transfer Correlations

Results from the experiments conducted in this chapter suggest that the Nambi and Powers (2003) correlation in concert with the linear driving force model is capable of describing tracer partitioning (absorption and dissolution) within DNAPL pools. This section presents results from additional simulations conducted using other correlations for the mass transfer coefficient. Six additional dissolution correlations were considered. Shown in Figures 6.22 – 6.26 are results using pool correlations of Pfannkuch (1984), Kim and Chrysikopoulos (1999), Seagen et al. (1999), and Seagren and Moore (2003). These correlations are discussed in Chapter 1 (see Section 1.5.4.2). Also displayed in these figures are results generated using ganglia dissolution correlations developed in Powers et al. (1992) and Powers et al. (1994) (the latter being the version reworked by Nambi (1999)). Since the Powers et al. (1992) correlation was shown capable of describing tracer mass transport in ganglia dominated systems in Chapter 5, it was included here to determine effectiveness in pool dominated systems. DNAPL saturation is one of the terms used to calculate the Sherwood number in the reworked Powers et al. (1994) correlation, which may be important for regions of heterogeneous DNAPL saturation. Therefore, the reworked Powers et al. (1994) correlation was also included in the analysis of sensitivity to mass transfer coefficient correlation.

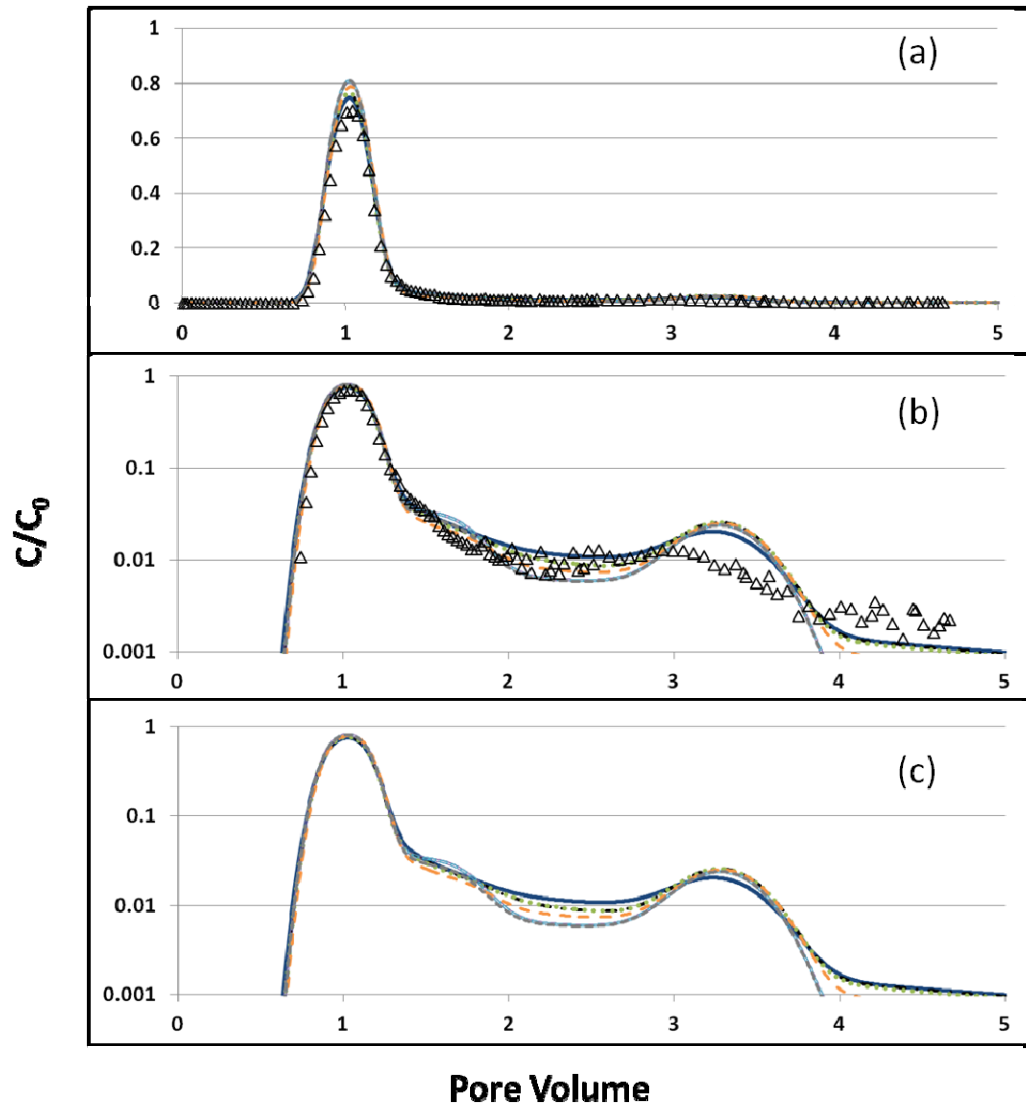


**Figure 6.22** Results of mass transfer coefficient correlation sensitivity study for the experiment 1, 2-octanol effluent data set. The 2-octanol data (open triangles), Nambi and Powers (2003) (blue, solid), reworked Powers et al. (1994) (black, dot-dash), Powers et al. (1992) (green, dotted), Pfannakuch (1984) (purple, open solid), Kim and Chrysikopoulos (1999) (light blue, open dash), Seagren et al. (1999) (orange, long dash), and Seagren and Moore (2003) (grey, short dash) predictions are all displayed. Panels b and c are shown on semi-log scale to show the tailing of each BTC. Panel c is shown without the 2-octanol data to better enable visualization of the model predictions.

**Table 6.8** Sum of squared error between 2-octanol experimental effluent data and model predictions shown in Figure 6.22 using the seven mass transfer correlations discussed above.

<b>Correlation</b>	<b>Sum of Squared Error 2-Octanol</b>
Nambi and Powers, 2003	0.06
Powers et al., 1994	0.07
Powers et al., 1992	0.07
Pfannakuch, 1984	0.13
Kim and Chrysikopoulos, 1999	0.13
Seagren et al., 1999	0.10
Seagren and Moore, 2003	0.13

Displayed in Figure 6.22 are 2-octanol effluent curves produced by the seven mass transfer correlations (six in addition to Nambi and Powers (2003)). Both the data and model BTCs are displayed in panels a and b on a linear and a semi-log scale, respectively. In panel c, the data is removed so that simulation results are more easily distinguished. Shown in Table 6.8 are the sum of squared errors of the 2-octanol predictions using each mass transfer correlation. In Figure 6.22 it can be seen that each simulation matches the data reasonably well. All of the correlations slightly under predict partitioning (panel a), but the Powers et al. (1992), reworked Powers et al. (1994) and the Nambi and Powers (2003) correlations come closest to capturing the maximum  $C/C_0$  value of the data. Similarly, these three correlations better capture the tailing seen between pore volumes 4 and 5 (panel b). Though all of the correlations are able to capture the general behavior of the effluent BTC, the squared error of predictions generated using the Powers et al. (1992), Powers et al. (1994) and the Nambi and Powers (2003) correlations is approximately half the sum of squared error resulting from the other correlations (Table 6.8). It is therefore concluded that these three mass transfer correlations work best for describing overall tracer transport through the pooled box system.

The local port 2-octanol BTCs produced for all seven mass transfer coefficient correlations are shown for each column in Figures 6.23-6.26. In these figures and the sum of squared error table (Table 6.9), it is shown that all correlations produce essentially the same BTCs for ports 1B, 1E, 2E, 3B, 3E and 4E, suggesting that these ports are not greatly impacted by the TCE pool.

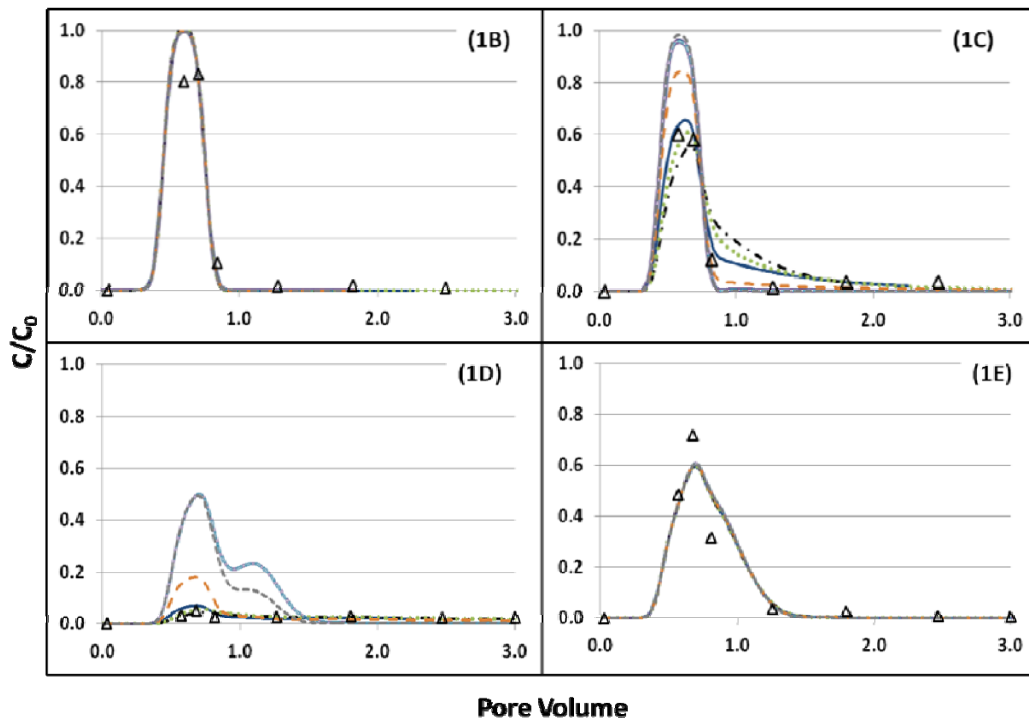


**Figure 6.23** Results of mass transfer coefficient correlation sensitivity study for experiment 1, column 1, 2-octanol port samples. The 2-octanol (open triangles), Nambi and Powers (2003) (blue, solid), reworked Powers et al. (1994) (black, dot-dash), Powers et al. (1992) (green, dotted), Pfannakuch (1984) (purple, open solid), Kim and Chrysikopoulos (1999) (light blue, open dash), Seagren et al. (1999) (orange, long dash), and Seagren and Moore (2003) (grey, short dash) predictions are all displayed.

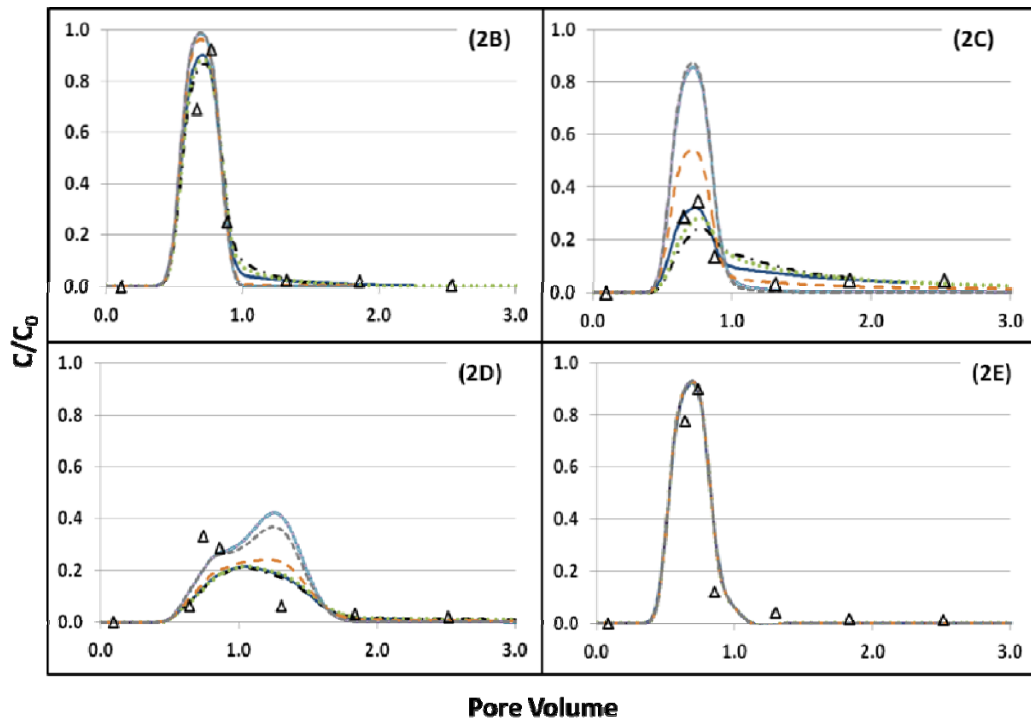


**Figure 6.24** Results of mass transfer coefficient correlation sensitivity study for experiment 1, column 2, 2-octanol port samples. The 2-octanol (open triangles), Nambi and Powers (2003) (blue, solid), reworked Powers et al. (1994) (black, dot-dash), Powers et al. (1992) (green, dotted), Pfannakuch (1984) (purple, open solid), Kim and Chrysikopoulos (1999) (light blue, open dash), Seagren et al. (1999) (orange, long dash), and Seagren and Moore (2003) (grey, short dash) predictions are all displayed.

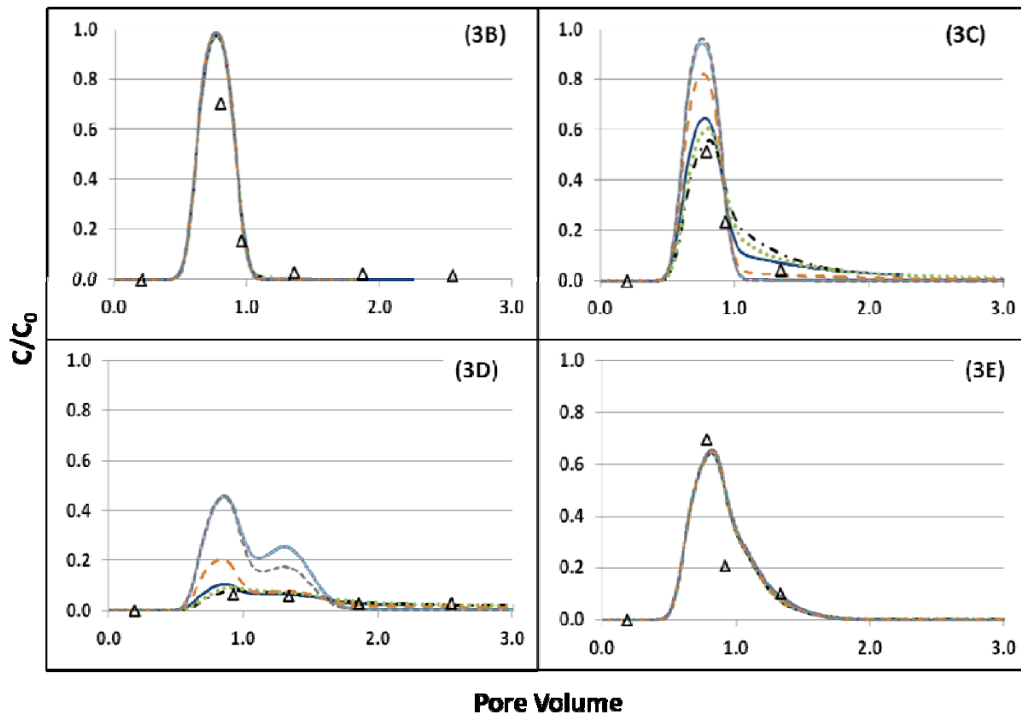


**Figure 6.25** Results of mass transfer coefficient correlation sensitivity study for experiment 1, column 3, 2-octanol port samples. The 2-octanol (open triangles), Nambi and Powers (2003) (blue, solid), reworked Powers et al. (1994) (black, dot-dash), Powers et al. (1992) (green, dotted), Pfannakuch (1984) (purple, open solid), Kim and Chrysikopoulos (1999) (light blue, open dash), Seagren et al. (1999) (orange, long dash), and Seagren and Moore (2003) (grey, short dash) predictions are all displayed.

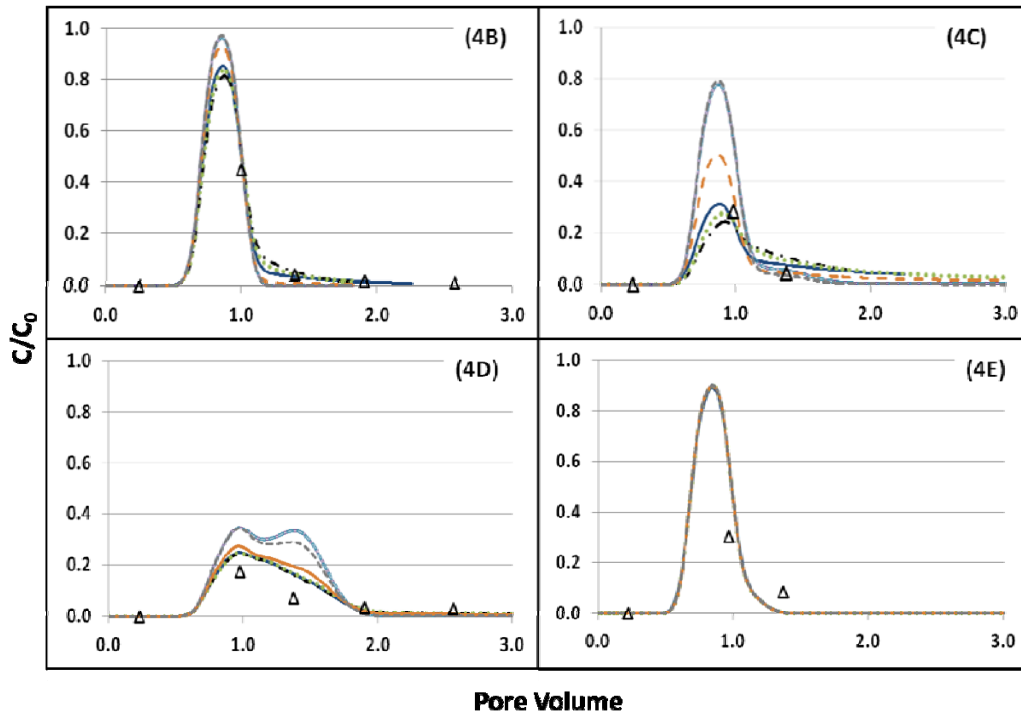


**Figure 6.26** Results of mass transfer coefficient correlation sensitivity study for experiment 1, column 3, 2-octanol port samples. The 2-octanol (open triangles), Nambi and Powers (2003) (blue, solid), reworked Powers et al. (1994) (black, dot-dash), Powers et al. (1992) (green, dotted), Pfannakuch (1984) (purple, open solid), Kim and Chrysikopoulos (1999) (light blue, open dash), Seagren et al. (1999) (orange, long dash), and Seagren and Moore (2003) (grey, short dash) predictions are all displayed.

**Table 6.9** Sum of squared error of 2-octanol port data and model predictions of local concentration. Errors are shown for each of the seven mass transfer coefficient correlations discussed above.

Port	Nambi and Powers, 2003	Powers et al., 1994	Powers et al., 1992	Pfannakuch, 1984	Kim and Chrysikopoulos, 1999	Seagren et al., 1999	Seagren and Moore, 2003
1B	0.04	0.05	0.05	0.04	0.04	0.04	0.04
1C	0.01	0.05	0.03	0.19	0.19	0.09	0.22
1D	0.00	0.00	0.00	0.44	0.44	0.04	0.41
1E	0.05	0.05	0.05	0.05	0.05	0.05	0.05
2B	0.04	0.03	0.04	0.08	0.08	0.07	0.08
2C	0.00	0.03	0.02	0.57	0.57	0.09	0.60
2D	0.07	0.07	0.07	0.14	0.14	0.07	0.11
2E	0.08	0.07	0.07	0.07	0.07	0.07	0.07
3B	0.09	0.09	0.09	0.09	0.09	0.09	0.09
3C	0.03	0.03	0.03	0.19	0.19	0.10	0.21
3D	0.00	0.00	0.00	0.16	0.16	0.01	0.13
3E	0.09	0.08	0.09	0.09	0.09	0.09	0.09
4B	0.01	0.01	0.01	0.01	0.01	0.01	0.01
4C	0.00	0.01	0.00	0.34	0.09	0.01	0.09
4D	0.01	0.01	0.01	0.10	0.10	0.03	0.08
4E	0.09	0.10	0.10	0.10	0.10	0.10	0.10

However, results in the other ports show a definite separation among the correlations. Again, the Powers et al. (1992), reworked Powers et al. (1994) and the Nambi and Powers (2003) correlations produce BTCs that are most consistent with the 2-octanol data. The Pfannkuch (1984), Kim and Chrysikopoulos (1999), and Seagen and Moore (2003) BTCs show relatively little partitioning and are, in fact, quite close to bromide predictions (not shown). All three of these correlations were developed to predict overall, not local, dissolution behavior. Therefore, it is unsurprising that they are unable to capture local partitioning tracer transport.

Interestingly, though Seagen et al. (1999) report a single mass transfer coefficient rather than a correlation related to system parameters, their mass transfer coefficient allows for model predictions that generally match port data. Seagen et al. (1999) used the same data set as Pfannkuch (1984) to develop their overall mass transfer coefficient. The Pfannkuch (1984) correlation always predicts increasing mass flux from the pool with increasing water velocity, even though the data show that eventually flux plateaus and stops increasing with increased velocity. Seagen et al. (1999) were attempting to improve this part of the correlation and came up with a mass transfer coefficient that allows flux calculated from a nonequilibrium model to plateau, similar to the data. This may be why the Seagen et al. (1999) correlation performs better, at high velocities, it provides a better description of mass flux from a pool. Though the Seagen et al. (1999) correlation does outperform some of the other correlations, it still under predicts partitioning and performance is not as good as either the Powers et al.

(1992), Powers et al. (1994) or the Nambi and Powers (2003). However, since it is a single value and not a correlation dependent on system parameters that may be unknown, this correlation may be useful as a first approximation of local tracer partitioning.

Figures 6.23 – 6.26 above are redisplayed below showing only BTCs resulting from the Powers et al. (1992), the reworked Powers et al. (1994), and the Nambi and Powers (2003) correlations. Again, it can be seen that all three correlations produce reasonable predictions of the 2-octanol BTCs for the port data. Examination of the errors shown in Table 6.9 determines that the two Powers et al. correlations (1992, 1994) result in average squared errors that are 1.5 times larger than those resulting from the Nambi and Powers (2003) correlation. Therefore, the Nambi and Powers (2003) correlation appears to be the best overall option for describing partitioning tracer transport in domains containing DNAPL pools.

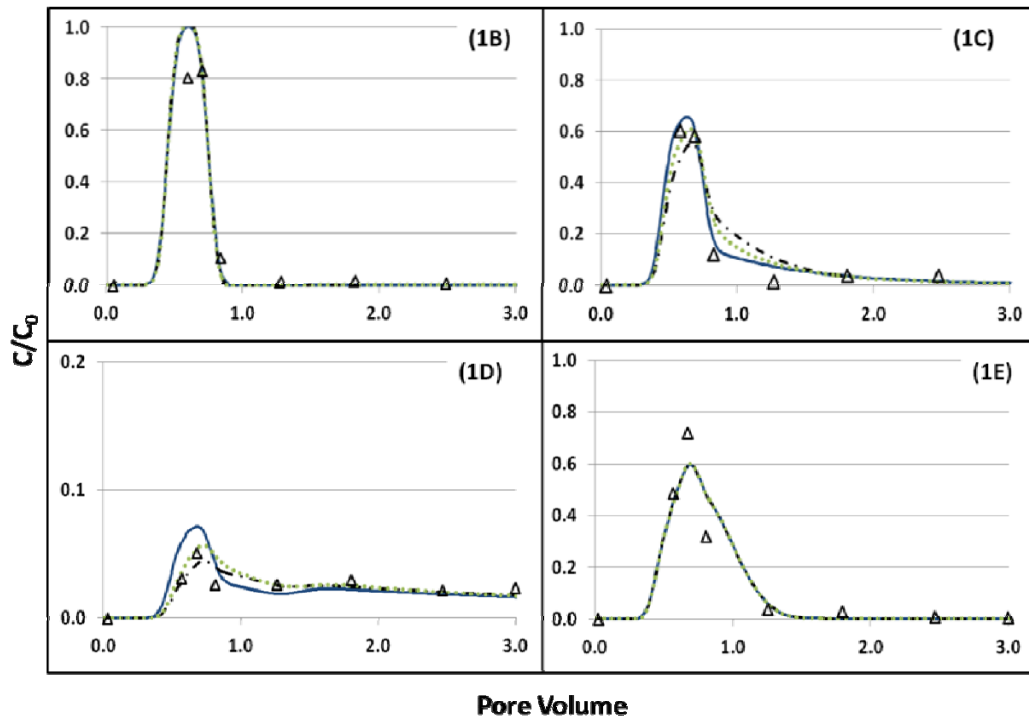


**Figure 6.27** Results of mass transfer coefficient correlation sensitivity study for experiment 1, column 1, 2-octanol port samples. The number of BTCs is reduced to show only 2-octanol data (open triangles), Nambi and Powers (2003) (blue, solid), reworked Powers et al. (1994) (black, dot-dash) and Powers et al. (1992) (green, dotted). Note the y-axis adjustment for port 1D.

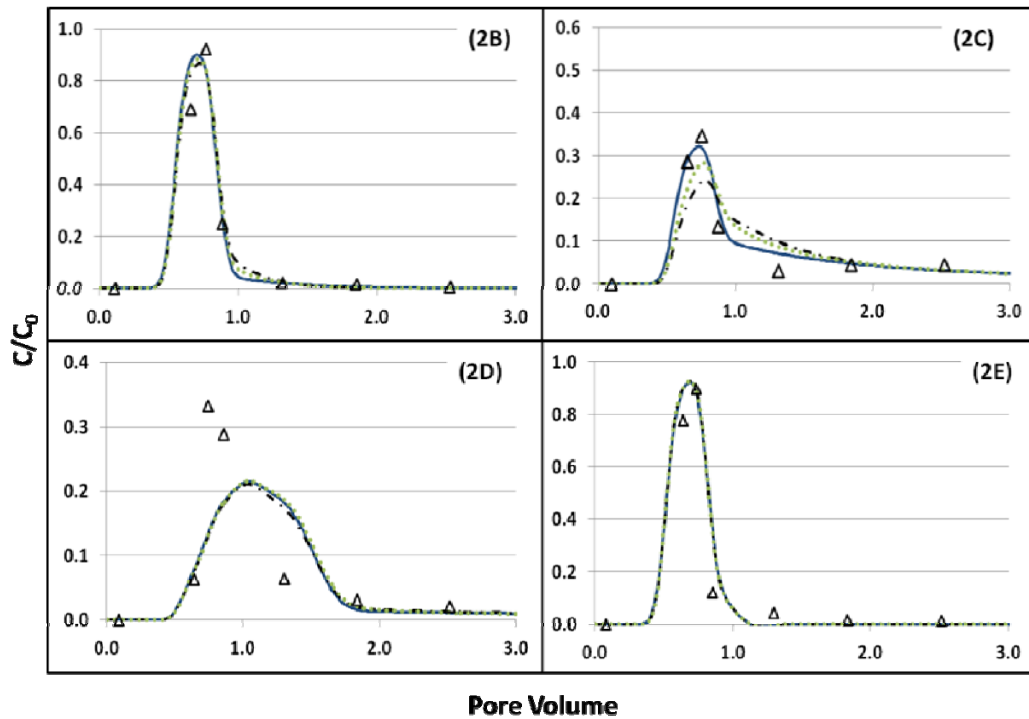


**Figure 6.28** Results of mass transfer coefficient correlation sensitivity study for experiment 1, column 2, 2-octanol port samples. The number of BTCs is reduced to show only 2-octanol data (open triangles), Nambi and Powers (2003) (blue, solid), reworked Powers et al. (1994) (black, dot-dash) and Powers et al. (1992) (green, dotted). Note the y-axis is adjustment for ports 2C and 2D.

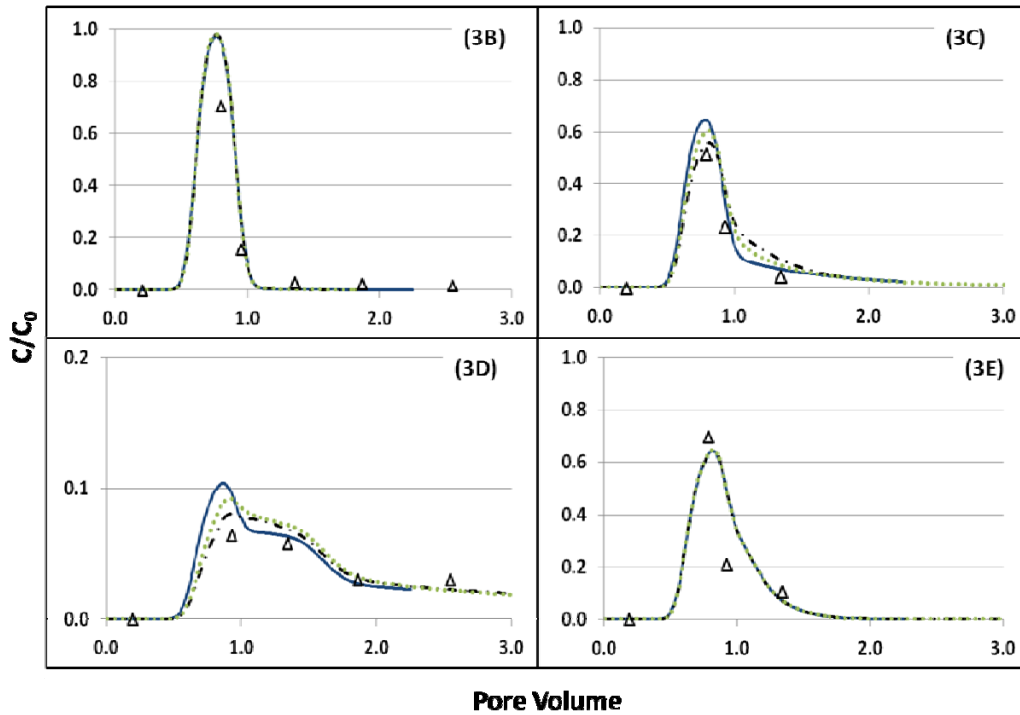


**Figure 6.29** Results of mass transfer coefficient correlation sensitivity study for experiment 1, column 3, 2-octanol port samples. The number of BTCs is reduced to show only 2-octanol data (open triangles), Nambi and Powers (2003) (blue, solid), reworked Powers et al. (1994) (black, dot-dash) and Powers et al. (1992) (green, dotted). Note the y-axis adjustment for port 3D.

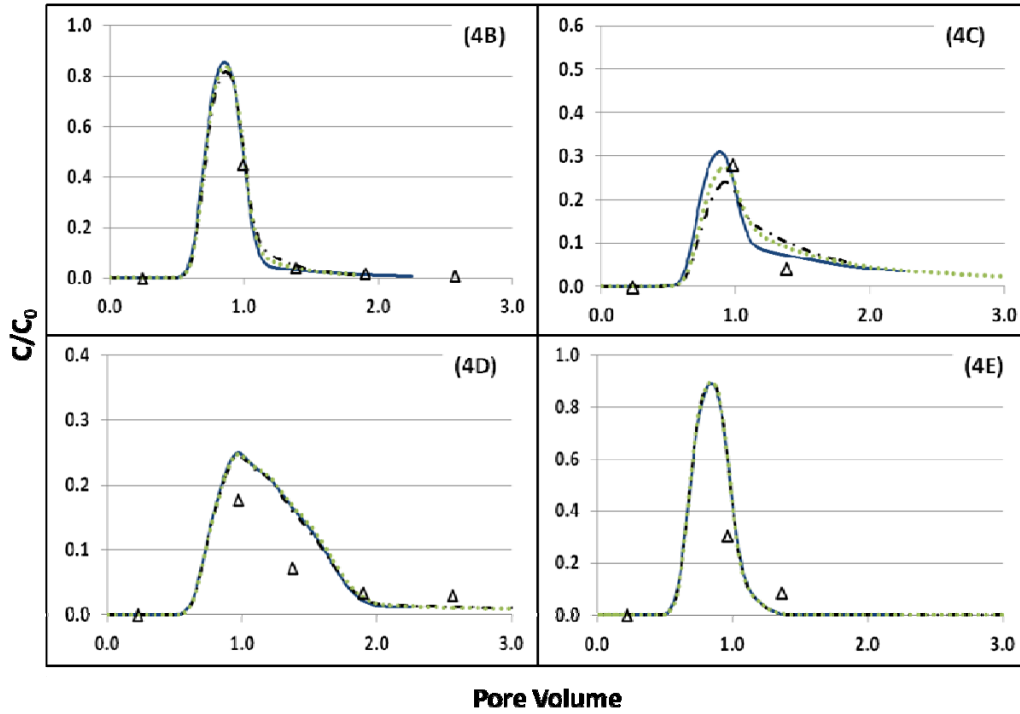


**Figure 6.30** Results of mass transfer coefficient correlation sensitivity study for experiment 1, column 2, 2-octanol port samples. The number of BTCs is reduced to show only 2-octanol data (open triangles), Nambi and Powers (2003) (blue, solid), reworked Powers et al. (1994) (black, dot-dash) and Powers et al. (1992) (green, dotted). Note the y-axis is adjustment for ports 2C and 2D.

#### **6.4 – Conclusions**

Focus in this chapter is placed on quantifying tracer transport in a source zone comprised of a single large TCE-DNAPL pool. Three conventional partitioning tracer tests were conducted in a 2-D aquifer cell with a large TCE-DNAPL pool in the source zone. Results demonstrated that a 2-D linear driving force model employing a mass transfer coefficient correlation developed from DNAPL dissolution experiments is able to predict partitioning tracer transport for the experiment that did not employ a flow interruption. Model predictions were able to capture the behavior of both the effluent data and local port BTCs downgradient of the TCE-DNAPL pool. The model does not capture the local port behavior of the two experiments that employed a flow interruption. It is hypothesized that the confined nature of the model does not capture the flow dynamics of the experimental system upon restarting flow after the flow interruption.

The linear driving force model was used to examine five mass transfer correlations developed from NAPL pool dissolution studies as well as two correlations developed from ganglia dissolution studies. It was determined that the Nambi and Powers (2003) correlation (developed from a DNAPL pool dissolution study) and the Powers et al. (1992, 1994) correlations (developed from ganglia dissolution studies) are all able of providing good predictions of partitioning tracer transport. By comparison of the sum of squared errors, it was determined that the Nambi and Powers (2003) correlation performs slightly better than the other two correlations.

Results produced in Chapters 5 and 6 allow for quantitative understanding of partitioning tracer transport at both end members of pool fraction. It is anticipated understanding partitioning tracer transport at both ends of the pool fraction spectrum will provide the foundation necessary for quantifying partitioning tracer transport in heterogeneous DNAPL source zones.

## **CHAPTER 7 – ASSESSMENT OF HETEROGENEOUS DNAPL ARCHITECTURE USING A PUSH-PULL TEST**

### ***7.1 - Introduction***

Partitioning tracer tests are usually employed to estimate overall source zone saturation (e.g. Annable et al., 1998a; Annable et al., 1998b; Hartog et al., 2010) or to evaluate the change in overall saturation due to the implementation of remedial technologies (e.g. Jin et al., 1995; Jawitz et al., 1998; Rao et al., 2000; Brooks et al., 2002; Meinardus et al., 2002). Partitioning tracers, however, may hold promise in aiding efforts aimed at estimating source zone architecture. This chapter describes laboratory experiments and mathematical modeling used to evaluate the information that can be obtained from localized push-pull partitioning tracer tests conducted within DNAPL source zones. These experiments and simulations build upon the results described in Chapters 5 and 6, where the tracer partitioning in ganglia and pooled regions were evaluated. The goal of the research described in Chapter 7 is to evaluate if these end-member models of DNAPL architecture can be integrated to elucidate features of the DNAPL distribution when interpreting breakthrough curves obtained from push-pull tracer tests. Here push-pull tracer tests are conducted in three heterogeneous source zones, each having a different pool fraction (low, mid and high), to examine if variations in injection and extraction flow rates can aid in distinguishing pool fraction.

## 7.2 - Push-Pull Test Design

Three push-pull tests, each employing a different combination of injection and extraction rates, were conducted in 2-D aquifer cell experiments. A description of the aquifer cell is provided in Chapter 3, Section 3.3.4. Three different packing structures were used to create a low, mid and high pool fraction source zone. Combinations of fast (8.5 mL/min) and slow (0.05 mL/min) flow rates were selected in an attempt to highlight the difference in transport time scales between ganglia and pools. Target flow rates for each experiment are shown below in Table 7.1. 8.5 mL/min was chosen as the fast flow rate because it provides a similar pore water velocity to that employed in the nonequilibrium column experiments (Chapter 5). 0.5 mL/min was selected as the slow flow rate. This slow flow rate represents a compromise between a desire to achieve 2-octanol equilibrium partitioning and the practicability of using slow flow (i.e., long test durations in the field).

**Table 7.1** Tracer test flow rates for mixed source zone experiments.

Condition	Push		Pull	
	Q (mL/min)	v (m/hr)	Q (mL/min)	v (m/hr)
1	8.5	0.25	8.5	0.25
2	0.5	0.02	8.5	0.25
3	8.5	0.25	0.5	0.02

Using a fast flow rate for both phases of a test (condition 1) is most favorable for field implementation because of the cost and organizational issues associated with running long field tests. The increased residence time due to the slow push in condition 2 should allow more tracer mass to partition into the DNAPL. The fast “pull” phase would then force the system into non-equilibrium, possibly visualizing any diffusional resistance to mass transport in the DNAPL pools as long tailing signals. Condition 3 switches the order of flow rates used in condition 2 to force the tracers all the way through the source zone and then allow for partitioning during the pull phase to be close to equilibrium. By changing the injection and extraction flow rates of each push-pull test, the three experiments should show if differences in transport time scales between ganglia dominated and pool dominated systems can be manipulated to estimate pool fraction.

In each of these nine, push-pull experiments, approximately 1800 mL of an aqueous tracer solution containing bromide, 1-pentanol, 1-hexanol and 2-octanol were flowed through the source zone from the left end-chamber (exact injection volumes for each test are shown in Tables 7.3, 7.5 and 7.7). To ensure that the tracer solution flowed completely through the source zone, the presence of each partitioning tracer was verified in aqueous samples taken from the first two columns of ports (see box configuration, Figure 3.2) immediately downgradient of the source. Flow was then reversed and background solution was flowed through the box from the right end-chamber. Effluent samples were collected from the left end chamber with a fraction collector (Retriever II, ISCO) in 20 mL increments during this “pull” phase until tracer tails began to flatten out. Then,

samples were collected approximately every 900 mL until tracer concentrations fell below the detection limit. All background solutions used after DNAPL was released into the box were saturated with TCE to minimize TCE-DNAPL dissolution from the source zone. All tracer concentrations were below their detection limit (see analytical methods in section 3.2.1) before the experiment was terminated and the next experiment initiated.

It should be noted that though TCE saturated water was used in attempt to minimize TCE-DNAPL dissolution from the source zone, DNAPL mass was lost from each source zone due to both dissolution and volatilization. The initial source zone mass corresponding to each test can be seen in the box parameter tables (7.3, 7.5 and 7.7). The greatest amount of source zone mass was lost in the mid pool fraction box (the first box to be conducted) where the order of experiments was slow-fast followed by fast-slow, followed by fast-fast. It was determined that most of the TCE-DNAPL mass loss occurred during the long duration of the fast-slow test. Therefore, the order of the tests in the low and high pool fraction boxes was revised to be fast-fast, followed by slow-fast, followed by fast-slow.

### ***7.3 - Assessment of Low Pool Fraction Source Zone***

The packing structure of the low pool fraction box is shown below in Figure 7.1. Here, F-70 lenses were staggered in an attempt to allow the TCE-DNAPL to pool along the lenses as well as run off the edges and form ganglia trails. The five lenses were packed toward the bottom of the box in an attempt to

create a large ganglia zone in the top half of the box. The location and size of each lens is shown in Table 7.2. 32 mL of TCE was injected into the box at 1 mL/min using a Hamilton Syringe Pump. This injection rate was used by Suchomel and Pennell (2006) to create high GTP (low pool fraction) source zones. After the TCE-DNAPL injection, the system was left undisturbed for 3 days to allow the TCE-DNAPL to redistribute. Shown in Figure 7.2 (Panel I) is the resulting TCE-DNAPL distribution and corresponding light transmission analysis. Light transmission results determine the source zone pool fraction as 0.34, 0.27 and 0.26 when calculated on a pixel by pixel basis, a discrete block averaging basis and a continuum averaging basis, respectively (Christ et al., 2012). Details on this analysis can be found in Chapter 3, Section 3.3.5. Also shown in Figure 7.2 are pictures and light transmission analysis of the source zones immediately preceding the slow-fast test (Panel II) and the fast-slow test (Panel III). In Figure 7.2, the source zone distributions for the first two tests (fast-fast and slow-fast) appear to be visually similar. However, the effects of dissolution and volatilization can be seen in the source zone corresponding to the third test (fast-slow). The TCE-DNAPL source zone volumes, corresponding pool fraction and additional box parameters are presented in Table 7.3.

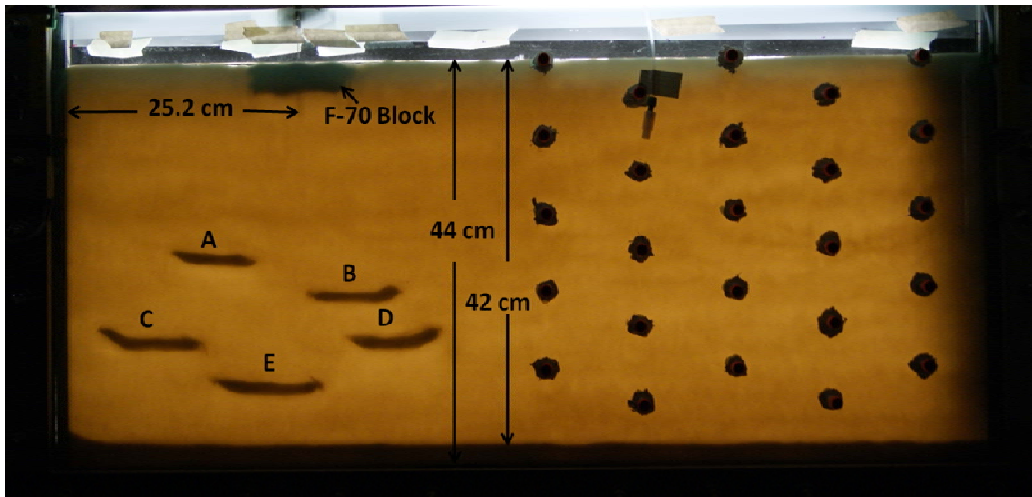


**Figure 7.1** Packing structure of the low pool fraction box. Included in the figure are the total packed height (44 cm), the height of the 40-50 sand (42 cm) and the distance from the injection/extraction well to the TCE-DNAPL injection needle (25.2 cm). The size and locations of all lenses are displayed in Table 7.2., below.

**Table 7.2** Size and location of the 5 lenses and F-70 block in the low pool fraction box

<b>Lens</b>	<b>Length (cm)</b>	<b>Thickness (cm)</b>	<b>Distance from Well to Front Edge of lens (cm)</b>	<b>Distance from bottom of box to bottom edge of lens (cm)</b>
<b>F-70 Block</b>	10.0	3.4	20.1	40.7
<b>A</b>	8.0	1.3	11.8	21.8
<b>B</b>	9.5	1.2	26.0	18.1
<b>C</b>	9.5	1.4	4.2	12.6
<b>D</b>	10.0	1.3	31.1	12.6
<b>E</b>	9.0	1.5	16.4	7.6

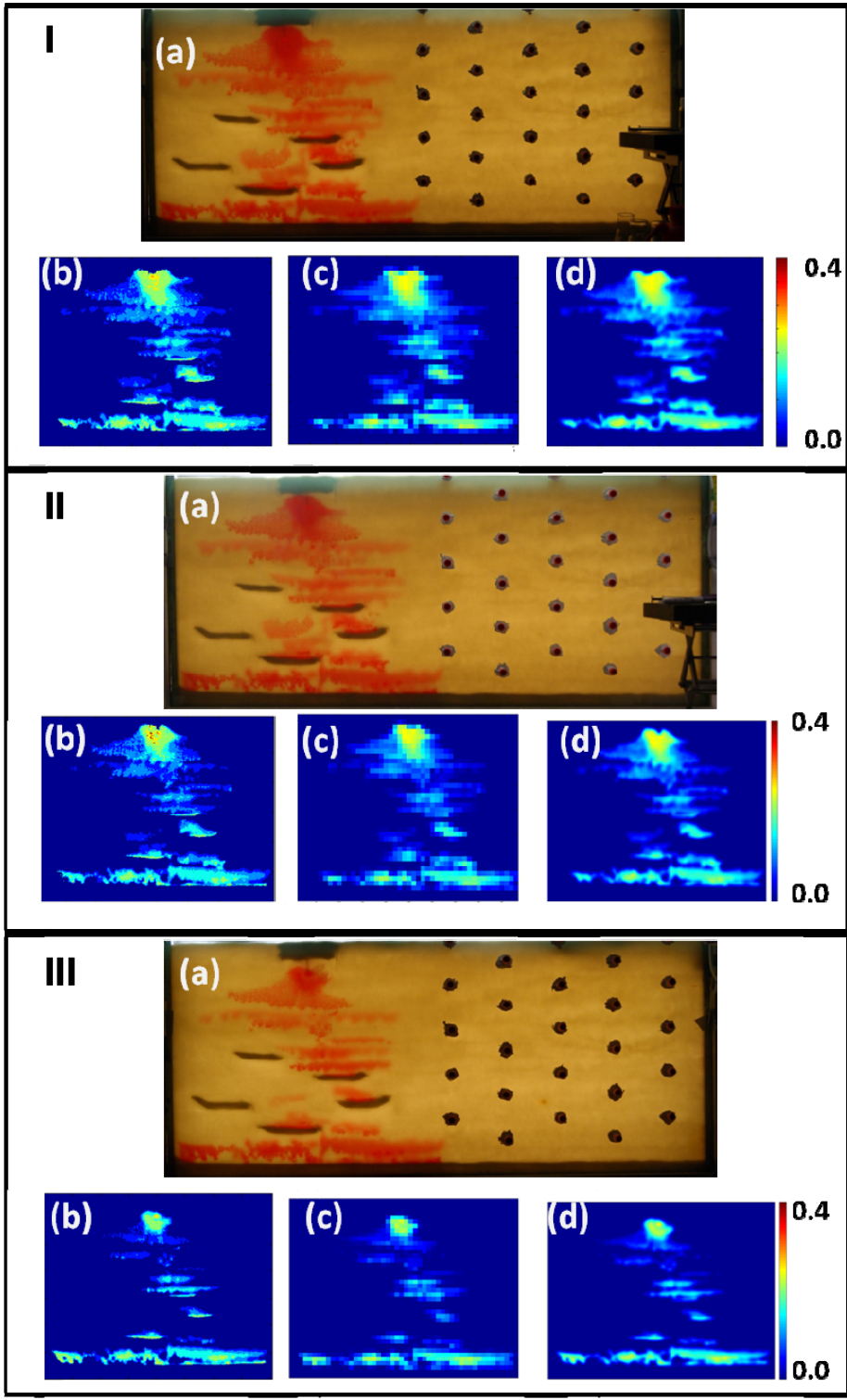


**Figure 7.2** Low pool fraction TCE-DNAPL spill shown as a photograph (a), pixel by pixel saturation (b), discrete averaging saturation (c), and continuum averaging saturation (d). Panels I, II and III show the source zone distribution before the fast-fast test, slow-fast test, and fast-slow test, respectively.

**Table 7.3** Low pool fraction box parameters.

	<b>Fast Injection Fast Extraction</b>	<b>Slow Injection Fast Extraction</b>	<b>Fast Injection Slow Extraction</b>
<b>Background sand (Ottawa, IL)</b>	Ottawa Federal Fine, 40-50 Sand Fraction		
<b>Uniformity Index (<math>U_i</math>)</b>	1.2		
<b>Median Grain Diameter (<math>d_{50}</math>)</b>	0.35 mm		
<b>Box Length</b>	100 cm		
<b>Packed Height</b>	44.2 cm		
<b>Mass Federal Fine</b>	9415 g		
<b>Mass F-70</b>	783 g		
<b>Bulk Density</b>	1.54 g/cm <sup>3</sup>		
<b>Porosity</b>	0.42		
<b>Pore Volume (PV)</b>	2780 mL		
<b>TCE Injected</b>	33.0 mL		
<b>TCE-DNAPL in Source Zone</b>	32.5 mL <sup>1</sup>	27.9 mL <sup>2</sup>	20.5 mL <sup>2</sup>
<b>Pool Fraction</b>			
<b>Pixel x Pixel</b>	0.34	0.27	0.32
<b>Discrete Block Avg.</b>	0.26	0.19	0.20
<b>Continuum Avg.</b>	0.26	0.19	0.21
<b>Tracer Solution Injection Volume</b>	1817.0 mL	1697.8 mL	1737.4 mL
<b>Swept Volume TCE-DNAPL Saturation<sup>3</sup></b>	1.8%	1.6%	1.2%
<b>Injection Flow</b>	8.4 mL/min	0.4 mL/min	7.4 mL/min
<b>Extraction Flow</b>	8.8 mL/min	8.5 mL/min	0.6 mL/min
<b>Average Injection Pore Water Velocity</b>	0.33 cm/min	0.02 cm/min	0.29 cm/min
<b>Average Extraction Pore Water Velocity</b>	0.35 cm/min	0.34 cm/min	0.02 cm/min
<b>Br- Conc.</b>	719 mg/L	719 mg/L	779 mg/L
<b>1-Pentanol Conc.</b>	842 mg/L	943 mg/L	984 mg/L
<b>1-Hexanol Conc.</b>	370 mg/L	345 mg/L	385 mg/L
<b>2-Octanol Conc.</b>	142 mg/L	119 mg/L	152 mg/L
<b>Bromide Recovery</b>	98%	95%	101%
<b>1-Pentanol Recovery</b>	93%	88%	100%
<b>1-Hexanol Recovery</b>	93%	88%	99%
<b>2-Octanol Recovery</b>	77%	78%	92%

<sup>1</sup>Any difference between the volume of TCE injected and the volume of TCE-DNAPL in the source zone is due to TCE-DNAPL flow into the end chamber and subsequent removal.

<sup>2</sup>Dissolution and volatilization result in changes in TCE-DNAPL source zone volume and pool fraction. Here TCE-DNAPL source zone volume is calculated using light transmission analysis.

<sup>3</sup>Swept volume TCE-DNAPL saturation is defined as the volume of TCE-DNAPL normalized by the injected tracer volume. Values vary slightly between each test due to the different injection volumes used.

The resulting BTCs of all three experiments are shown in Figures 7.3 – 7.5. As with previous BTCs, the x-axis is dimensionless time, but for push-pull tests time is represented as volume extracted ( $V_{\text{ext}}$ ) normalized by the pulse injection volume ( $V_{\text{inj}}$ ). The bromide curves for each test are approximately symmetrical, but as partition coefficient increases, the partitioning tracer curves become more asymmetrical. If all tracers exhibited equilibrium behavior, the breakthrough of each tracer (defined as  $C/C_0 = 0.5$ ) would occur at a  $V_{\text{ext}} / V_{\text{inj}}$  of 1. The partitioning of each tracer would be expressed as excess spreading or effective dispersion (compared to the bromide BTC).

In the fast-fast experiment, the breakthrough of each partitioning tracer occurs early, at a  $V_{\text{ext}} / V_{\text{inj}}$  of 0.8, 0.5 and 0.3 for pentanol, hexanol and 2-octanol, respectively. In the following two experiments, only 2-octanol exhibits early breakthrough ( $V_{\text{ext}} / V_{\text{inj}}$  between 0.3 and 0.5), with the breakthrough of the other tracers occurring at approximately  $V_{\text{ext}} / V_{\text{inj}} = 1$ .

Additionally, in the fast-fast and slow-fast experiments, (Figures 7.3 and 7.4) the partitioning tracers BTC have an inflection point before which the  $C/C_0$  value drops quickly with  $V_{\text{ext}} / V_{\text{inj}}$ , and after which the concentration signals level out and begin to tail. Again this behavior is more pronounced with the higher partitioning tracers. Since this inflection occurs in the bromide data, it appears to be due to a flow field effect that is exaggerated in the partitioning tracer curves. Less frequent sampling in the fast-slow test makes it difficult to conclude whether this behavior also occurred during that experiment.

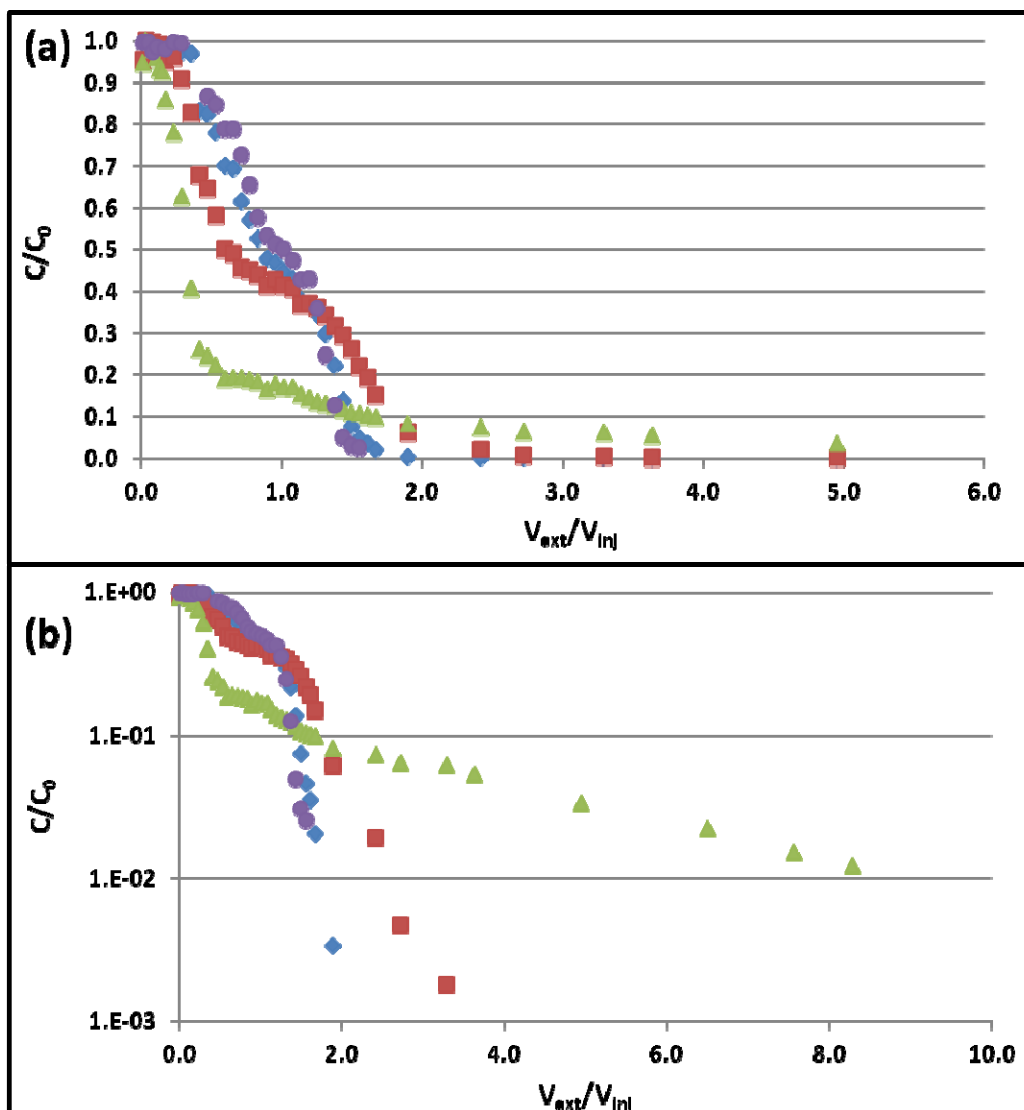


**Figure 7.3** Low pool fraction fast-fast breakthrough curves: bromide (circles), 1-pentanol (diamonds), 1-hexanol (squares) and 2-octanol (triangles). Data is shown on a linear y-axis scale, and for a shorter extraction time (a) to display the differences in the front of the BTCs and then on a log scale axis, for a longer extraction time (b) to highlight tracer tailing.

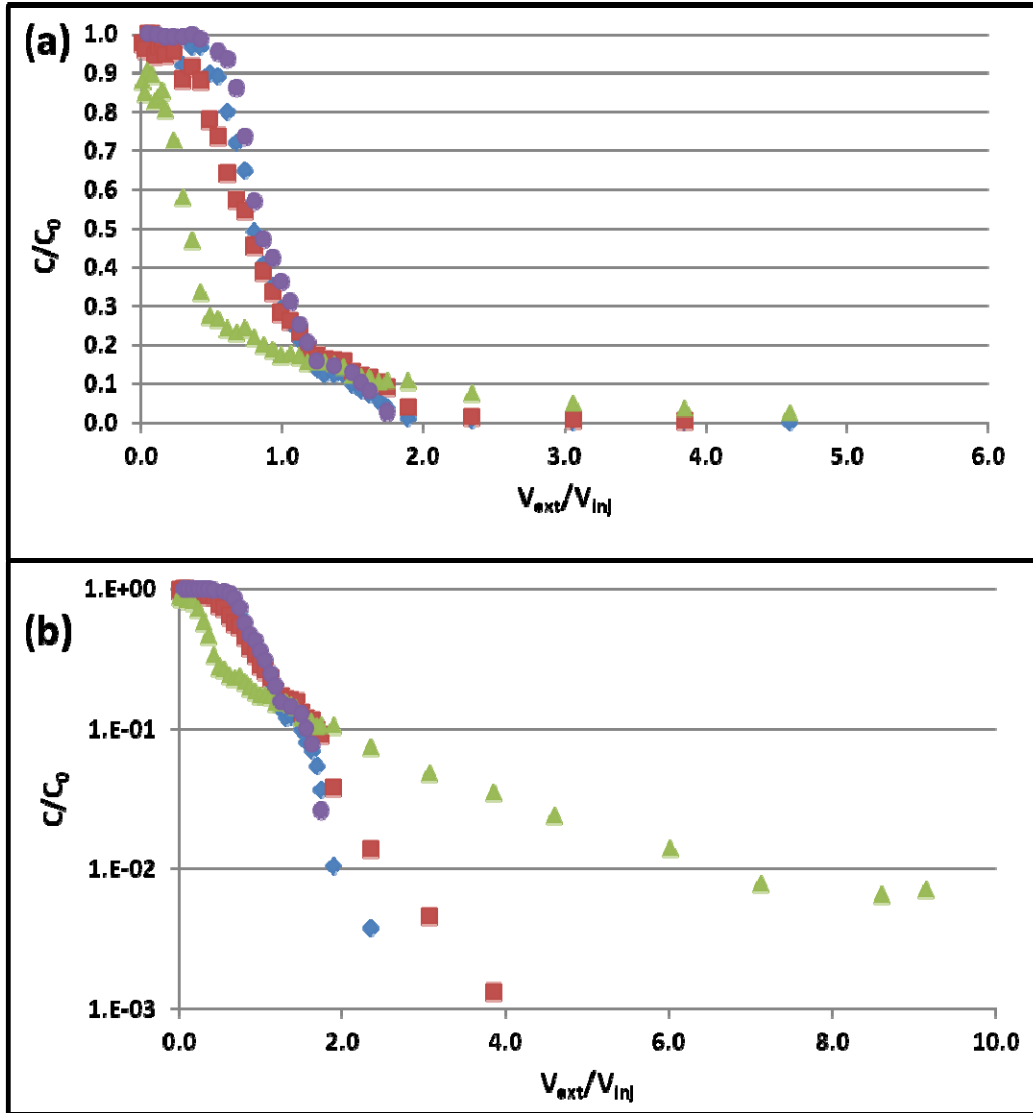


**Figure 7.4** Low pool fraction slow-fast breakthrough curves: bromide (circles), 1-pentanol (diamonds), 1-hexanol (squares) and 2-octanol (triangles). Data is shown on a linear y-axis scale, and for a shorter extraction time (a) to display the differences in the front of the BTCs and then on a log scale axis, for a longer extraction time (b) to highlight tracer tailing.

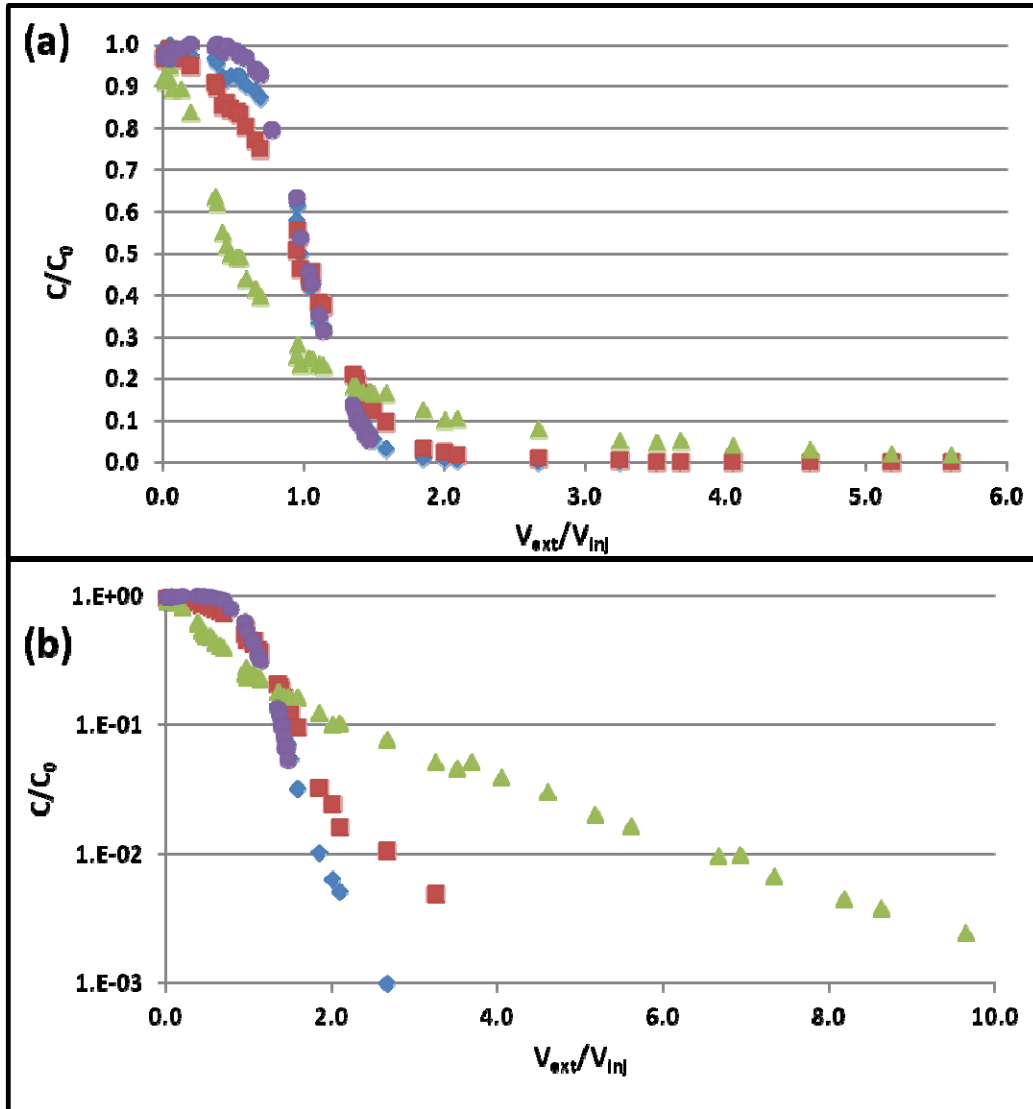


**Figure 7.5** Low pool fraction fast-slow breakthrough curves: bromide (circles), 1-pentanol (diamonds), 1-hexanol (squares) and 2-octanol (triangles). Data is shown on a linear y-axis scale, and for a shorter extraction time (a) to display the differences in the front of the BTCs and then on a log scale axis, for a longer extraction time (b) to highlight tracer tailing.

The data from these low pool fraction experiments are plotted in Figures 7.6 and 7.7 to facilitate comparison across experiments. The bromide and 1-pentanol curves have some slight variations among the three experiments, but are generally quite similar. The higher partitioning tracers show more distinct differences in the early part of the BTCs, but not necessarily in the tails. The 1-hexanol curves appear to exaggerate the slight differences seen in the corresponding bromide curves. For instance, at a  $V_{\text{ext}}/V_{\text{inj}}$  of approximately 1, the slope of the fast-fast bromide data flattens out for about 0.3 PV and then resumes a steep decline. The 1-hexanol data have a similar feature, but with a shallower and wider “flat” portion of the curve. A similar occurrence can be seen in the fast-slow data at a  $V_{\text{ext}}/V_{\text{inj}}$  of approximately 1.3. Contrastingly, the fast-fast and slow-fast 2-octanol BTCs are quite similar to each other, though their bromide signals are quite different. This suggests that partitioning interactions between 2-octanol and the TCE-DNAPL are quite strong. The fast-slow 2-octanol curve is slightly different from the other two. As mention above, the loss of TCE-DNAPL mass in the source zone corresponding to the fast-slow is apparent in Figure 7.2. As will be discussed in greater detail in Section 7.7.4, these BTC differences may result more from the evolving source zone architecture than from the differences in experimental flow rate.

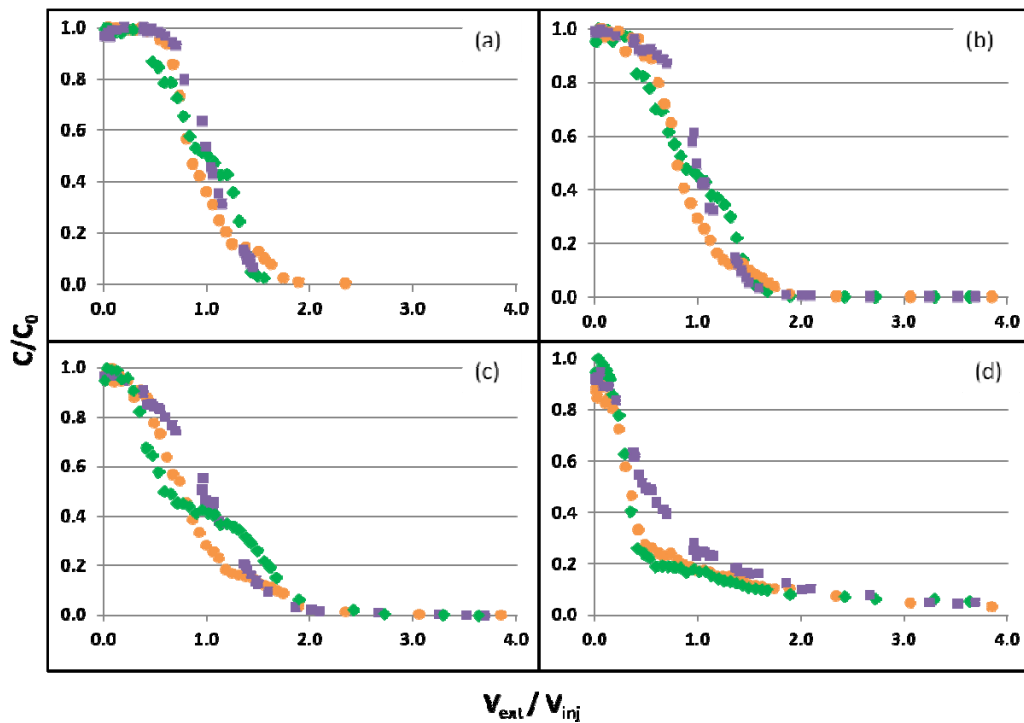


**Figure 7.6** Early time BTCs of low pool fraction bromide (a), 1-pentanol (b), 1-hexanol (c) and 2-octanol (d) BTCs for each experiment. The fast-fast BTCs are shown in diamonds; the slow-fast in circles; the fast-slow in squares.

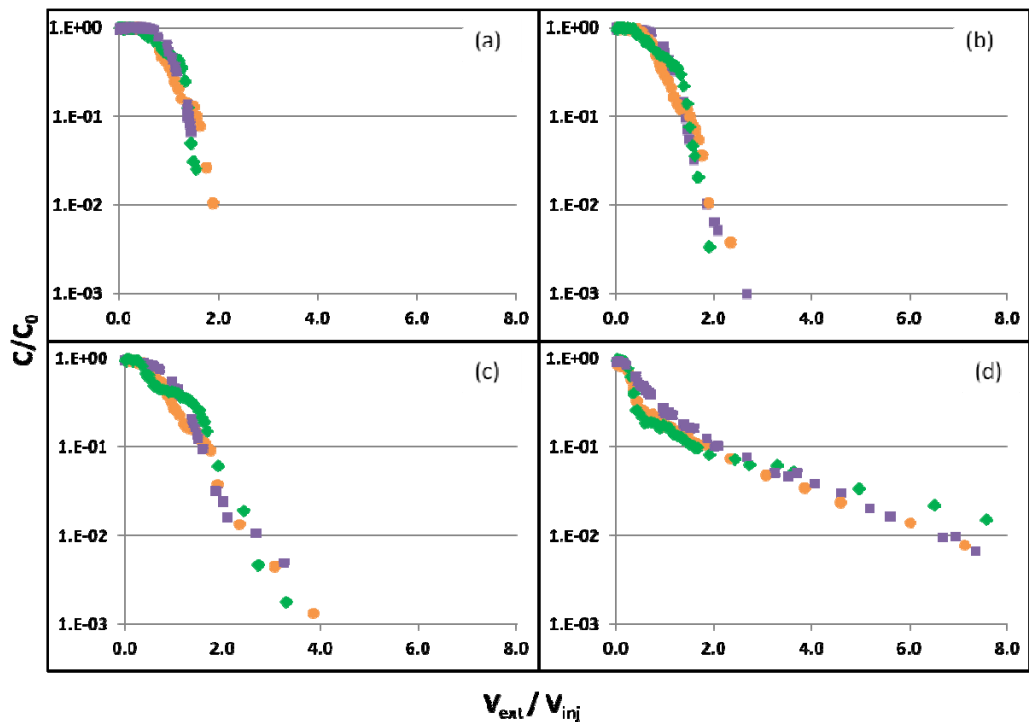


**Figure 7.7** Comparison of low pool fraction bromide (a), 1-pentanol (b), 1-hexanol (c) and 2-octanol (d) BTC tails for each experiment. The fast-fast BTCs are shown in diamonds; the slow-fast in circles; the fast-slow in squares. Note the y-axis is log scale.

#### ***7.4 - Assessment of Mid Pool Fraction Source Zone***

The packing structure of the mid pool fraction box is shown below in Figure 7.8. The main difference in packing structure compared to the low pool fraction is that a lens was added 3 cm below the injection needle to create more pooling. The location and size of each lens is shown in Table 7.4. 32 mL of TCE was injected at a flow rate of 0.5 mL/min. This slower flow was employed to create a higher pool fraction (Suchomel and Pennell, 2006). After TCE-DNAPL injection, the system was left undisturbed for 3 days to allow the TCE-DNAPL to redistribute. Shown in Figure 7.9 are the TCE-DNAPL source zone distributions and light transmission analysis corresponding to the three push-pull experiments. Light transmission results of the initial source zone determine the pool fraction as 0.68, 0.51 and 0.50 when calculated on a pixel by pixel basis, a discrete block averaging basis and a continuum averaging basis, respectively. It should be noted here that a light transmission picture of the source zone before the second test (fast-slow) is not available. However, the source zone at this time was visually similar to source zone corresponding to the first test (slow-fast), so its light transmission picture is used to estimate pool fraction and source zone volume. It can be seen in Figure 7.9 that significant dissolution occurred during the fast-slow test, resulting in a much different source zone upon running the fast-fast test. Though the source zone corresponding to the fast-fast test is visually different from the initial source zone, the pool fraction has only changed slightly (Table 7.3). TCE-DNAPL source zone volumes, corresponding pool fractions and additional box parameters are presented below in Table 7.3.

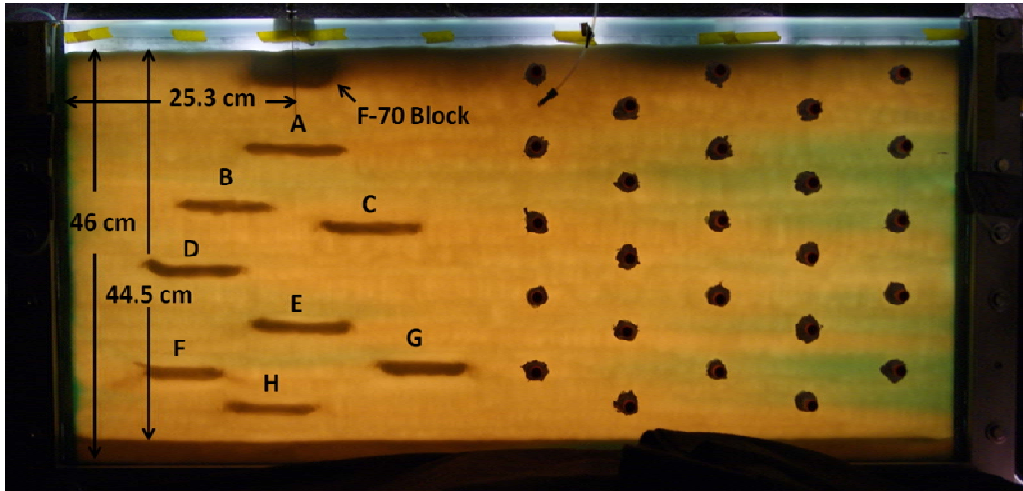


**Figure 7.8** Packing structure of the mid pool fraction box. Included in the figure are the total packed height (46 cm), the height of the 40-50 sand (44.5 cm) and the distance from the injection/extraction well to the TCE-DNAPL injection needle (25.3 cm). The size and locations of all lenses are displayed in Table 7.4., below.

**Table 7.4** Size and location of the 5 lenses and F-70 block in the mid pool fraction box

<b>Lens</b>	<b>Length (cm)</b>	<b>Thickness (cm)</b>	<b>Distance from Well to Front Edge of lens (cm)</b>	<b>Distance from bottom of box to bottom edge of lens (cm)</b>
<b>F-70 Block</b>	9.2	4.0	21.0	42.6
<b>A</b>	11.2	1.4	20.0	34.8
<b>B</b>	10.6	1.4	12.2	28.3
<b>C</b>	10.6	1.4	28.6	25.8
<b>D</b>	10.4	1.5	8.6	21.0
<b>E</b>	10.0	1.4	20.5	14.6
<b>F</b>	8.8	1.4	8.4	9.4
<b>G</b>	9.4	1.4	38.4	10.4
<b>H</b>	9.6	1.4	18.0	5.4

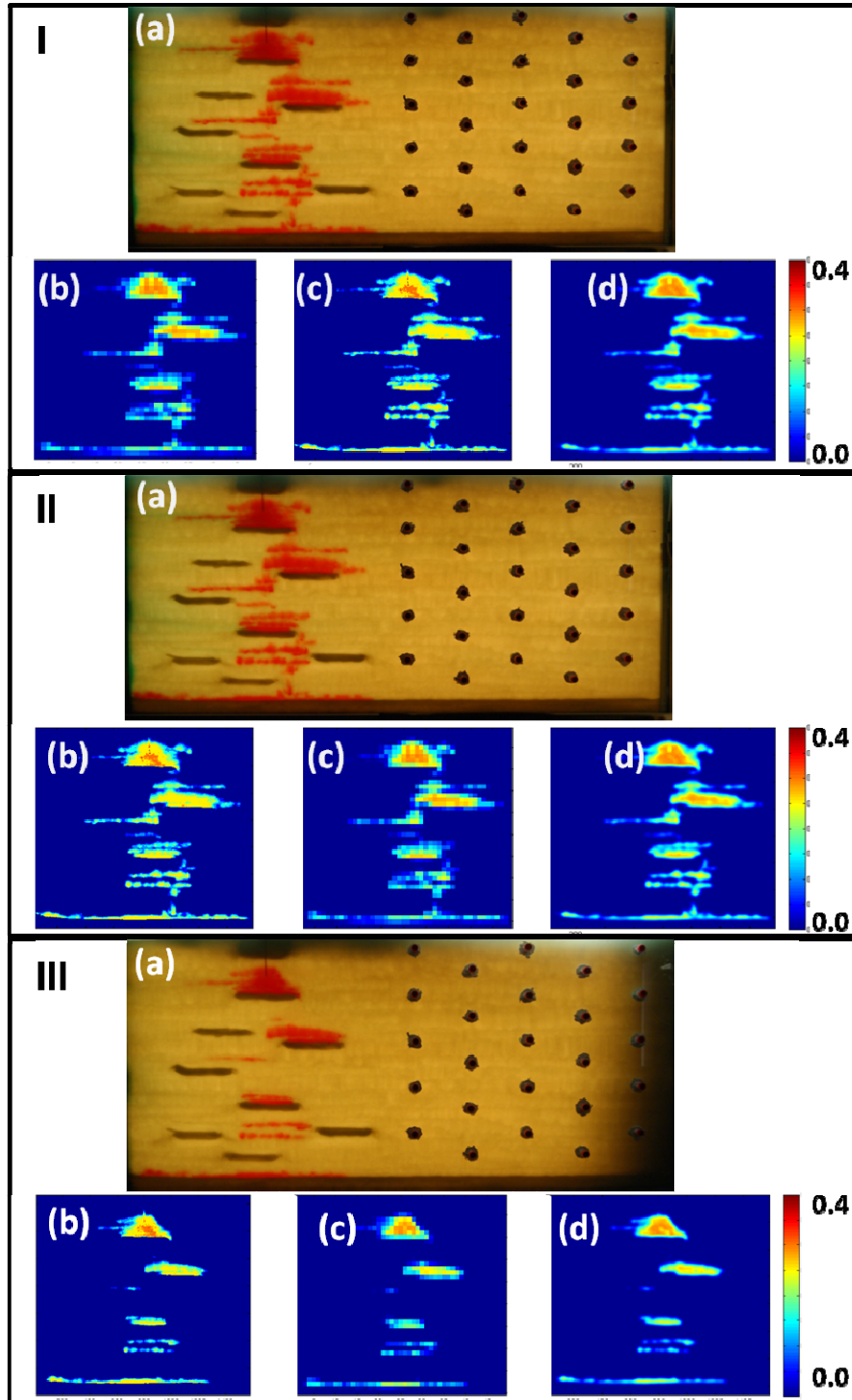


**Figure 7.9** Mid pool fraction TCE-DNAPL spill shown as a photograph (a), pixel by pixel saturation (b), discrete averaging saturation (c), and continuum averaging saturation (d). Panels I, II and III show the source zone distribution before the slow-fast test, fast-slow test, and fast-fast test, respectively.

**Table 7.5** Mid pool fraction box and corresponding tracer test parameters.

	<b>Fast Injection Fast Extraction</b>	<b>Slow Injection Fast Extraction</b>	<b>Fast Injection Slow Extraction</b>
<b>Background sand (Ottawa, IL)</b>	Ottawa Federal Fine, 40-50 Sand Fraction		
<b>Uniformity Index (<math>U_i</math>)</b>	1.2		
<b>Median Grain Diameter (<math>d_{50}</math>)</b>	0.35 mm		
<b>Box Length</b>	100 cm		
<b>Packed Height</b>	46 cm		
<b>Mass Federal Fine</b>	9998 g		
<b>Mass F-70</b>	1008 g		
<b>Average Bulk Density</b>	1.56 g/cm <sup>3</sup>		
<b>Average Porosity</b>	0.41		
<b>Pore Volume (PV)</b>	2891 mL		
<b>Volume TCE Injected</b>	32.0 mL		
<b>Volume of TCE-DNAPL in Source Zone</b>	15.1 mL <sup>3</sup>	30.8 mL <sup>1</sup>	30.8 mL <sup>2</sup>
<b>Pool Fraction</b>			
<b>Pixel x Pixel</b>	0.74	0.72	0.72
<b>Discrete Block Avg.</b>	0.50	0.51	0.51
<b>Continuum Avg.</b>	0.54	0.50	0.50
<b>Tracer Solution Injection Volume</b>	1941 mL	2191 mL	2082 mL
<b>Swept Volume TCE-DNAPL Saturation<sup>4</sup></b>	1.6 %	1.4 %	1.5 %
<b>Injection Flow</b>	8.6 mL/min	0.5 mL/min	8.5 mL/min
<b>Extraction Flow</b>	8.5 mL/min	8.7 mL/min	0.6 mL/min
<b>Injection PW Velocity</b>	0.33 cm/min	0.02 cm/min	0.33 cm/min
<b>Extraction PW Velocity</b>	0.33 cm/min	0.34 cm/min	0.02 cm/min
<b>Br- Conc.</b>	879 mg/L	790 mg/L	879 mg/L
<b>1-Pentanol Conc.</b>	851 mg/L	1044 mg/L	1061 mg/L
<b>1-Hexanol Conc.</b>	267 mg/L	360 mg/L	293 mg/L
<b>2-Octanol Conc.</b>	133 mg/L	121 mg/L	146 mg/L
<b>Bromide Recovery</b>	97%	105%	100%
<b>1-Pentanol Recovery</b>	99%	99%	89%
<b>1-Hexanol Recovery</b>	98%	98%	88%
<b>2-Octanol Recovery</b>	92%	88%	83%

<sup>1</sup>Any difference between the volume of TCE injected and the volume of TCE-DNAPL in the source zone is due to TCE-DNAPL flow into the end chamber and subsequent removal.

<sup>2</sup>No light transmission picture was taken for this test, so light transmission results from the slow-fast test are used to calculate TCE-DNAPL volume and pool fraction.

<sup>3</sup>Dissolution and volatilization result in changes in TCE-DNAPL source zone volume and pool fraction. Here TCE-DNAPL source zone volume is calculated using light transmission analysis.

<sup>4</sup>Swept volume TCE-DNAPL saturation is defined as the volume of TCE-DNAPL normalized by the injected tracer volume. Values vary slightly between each test due to the different injection volumes used.

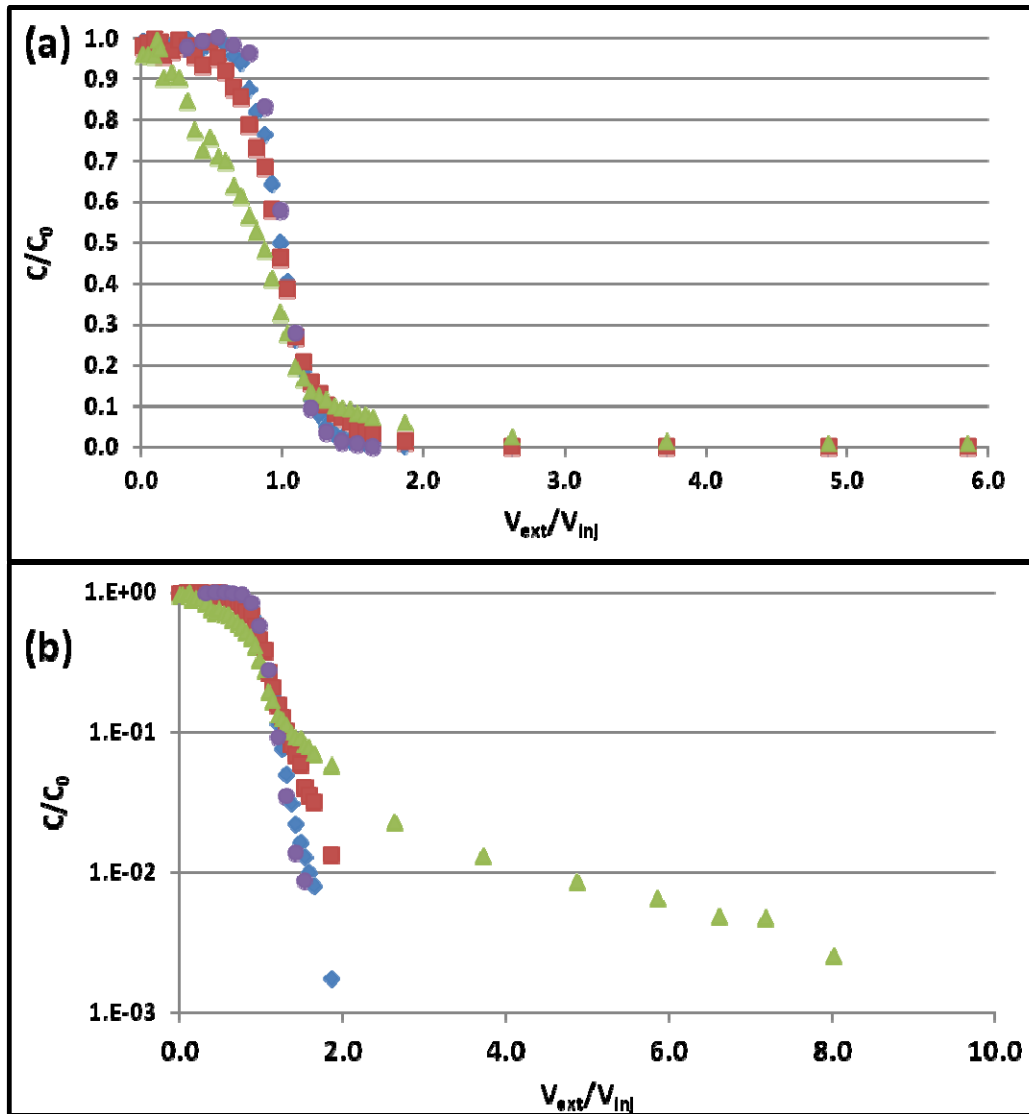


**Figure 7.10** Mid pool fraction fast-fast breakthrough curves: bromide (circles), 1-pentanol (diamonds), 1-hexanol (squares) and 2-octanol (triangles). Data is shown on a linear y-axis scale, and for a shorter extraction time (a) to display the differences in the front of the BTCs and then on a log scale axis, for a longer extraction time (b) to highlight tracer tailing.

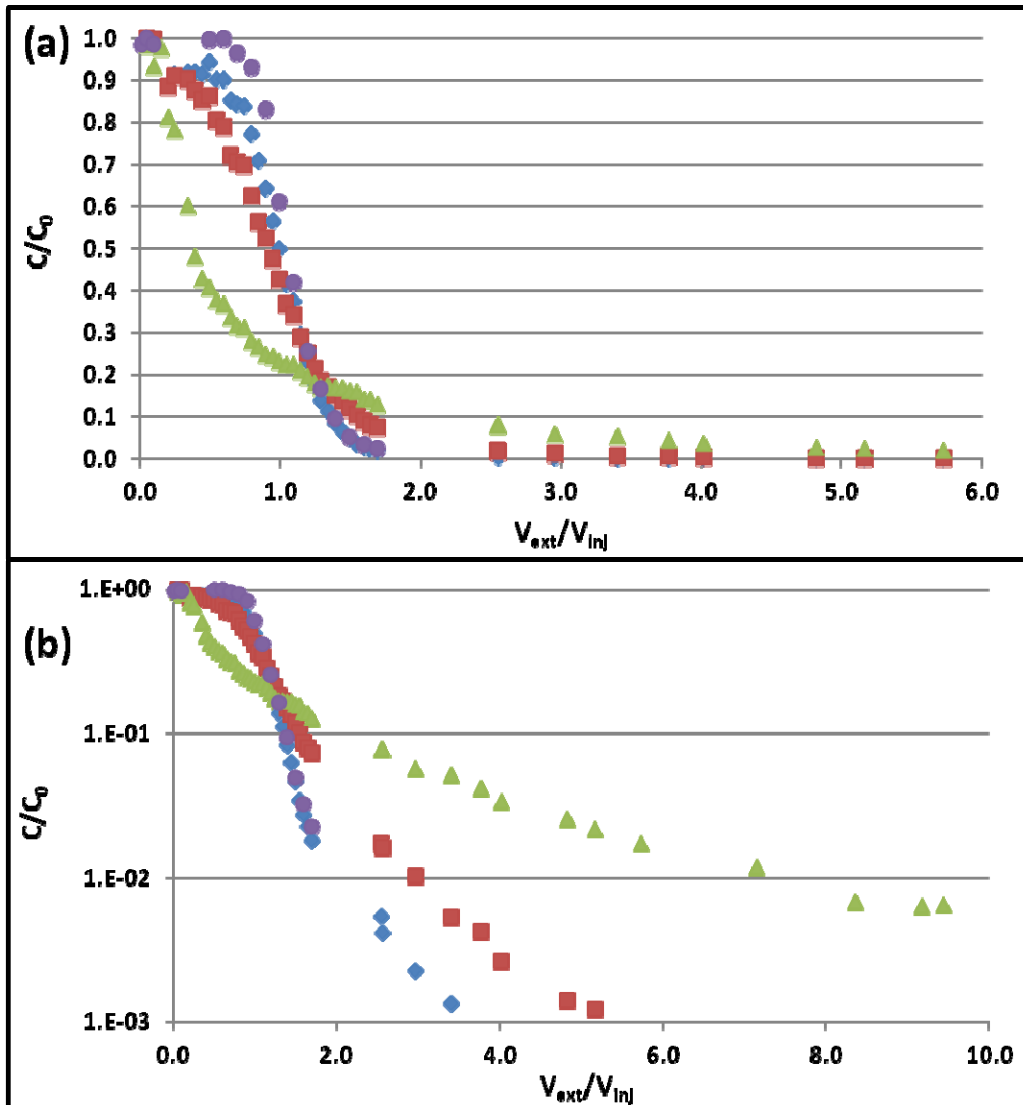


**Figure 7.11** Mid pool fraction slow-fast breakthrough curves: bromide (circles), 1-pentanol (diamonds), 1-hexanol (squares) and 2-octanol (triangles). Data is shown on a linear y-axis scale, and for a shorter extraction time (a) to display the differences in the front of the BTCs and then on a log scale axis, for a longer extraction time (b) to highlight tracer tailing.

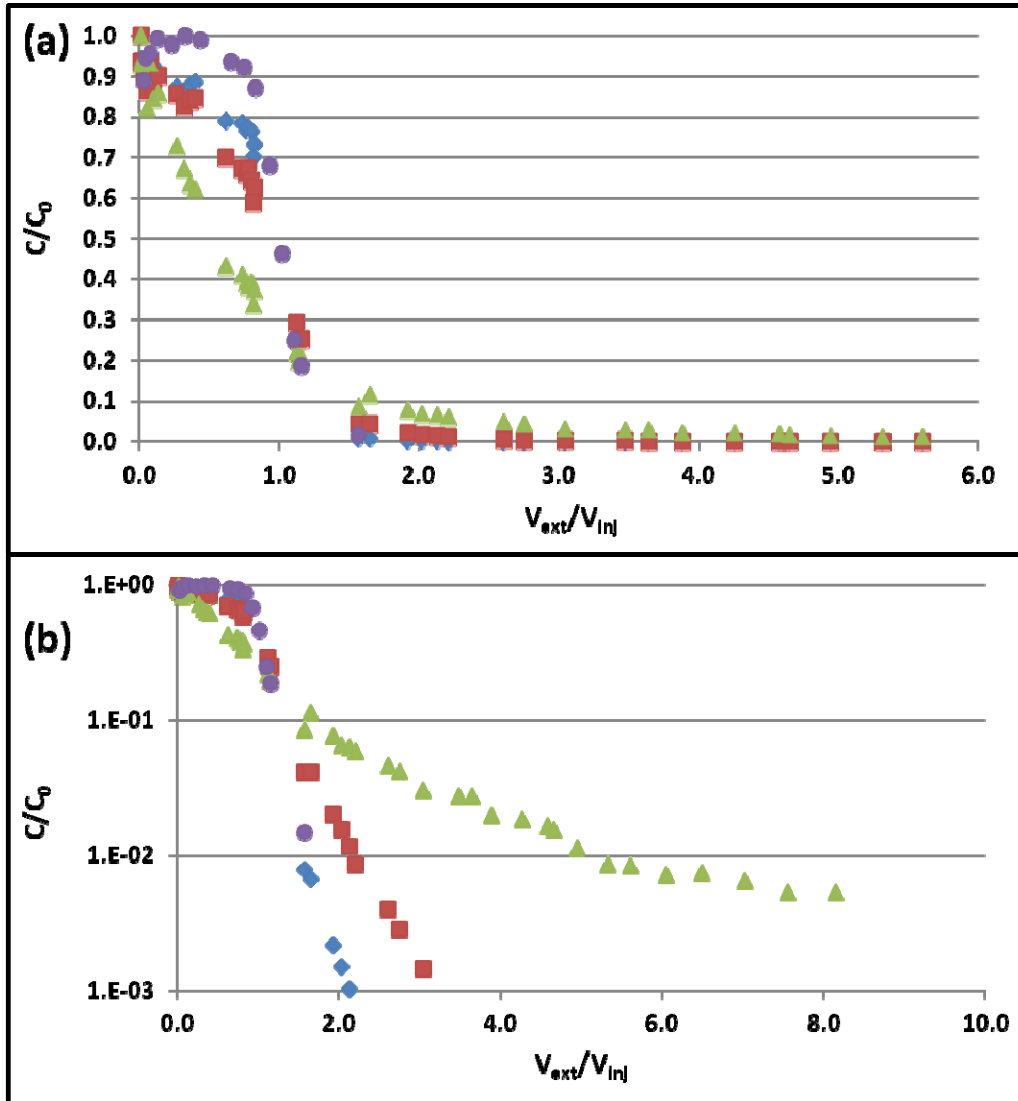


**Figure 7.12** Mid pool fraction fast-slow breakthrough curves: bromide (circles), 1-pentanol (diamonds), 1-hexanol (squares) and 2-octanol (triangles). Data is shown on a linear y-axis scale, and for a shorter extraction time (a) to display the differences in the front of the BTCs and then on a log scale axis, for a longer extraction time (b) to highlight tracer tailing.

BTCs resulting from the three push-pull tests are shown in Figures 7.10 – 7.12. Similar to the low pool fraction box, the asymmetry of each BTC increases with increasing tracer partition coefficient. Here, the same inflection point behavior is not seen except in the 2-octanol signal of the fast-fast test (Figure 7.10), at a  $V_{\text{ext}} / V_{\text{inj}}$  of approximately 0.4. In this case, the “flat” portion of the curve is not as pronounced as in the low pool fraction box. Additionally, the inflection point behavior is not seen in any of the bromide signals, indicating a difference in flow field between the mid and low pool fraction boxes.

The three push-pull experiments are compared on both linear and log scales in Figures 7.13 and 7.14. Overall, the bromide, 1-pentanol and 1-hexanol BTCs are similar, except that the slow-fast test exhibits slightly stronger tailing than the other two experiments. Upon first analysis, it appears that the fast-fast test provides a 2-octanol BTC distinct from the other two. However, it is important to remember that the fast-fast test was the last to be conducted in this box and that significant TCE-DNAPL dissolution had occurred before starting this test (Figure 7.9 and Table 7.5). Though the calculated pool fraction in the box only increased slightly, a comparison of panels I and III in Figure 7.9 shows that the TCE-DNAPL distributions are quite different. Therefore, it may be (as discussed later in Section 7.7.4) that the different fast-fast results are due more to the differences in DNAPL source zone than to differences in push-pull test flow rate.

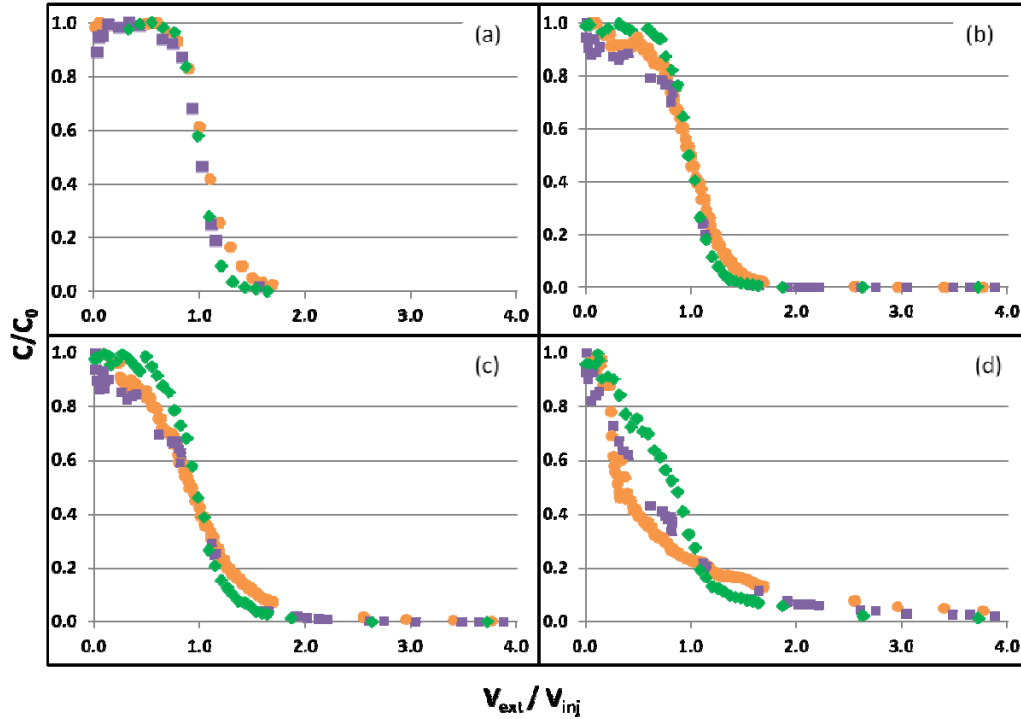


**Figure 7.13** Comparison of mid pool fraction bromide (a), 1-pentanol (b), 1-hexanol (c) and 2-octanol (d) BTCs for each experiment. The fast-fast BTCs are shown in diamonds; the slow-fast in circles; the fast-slow in squares.

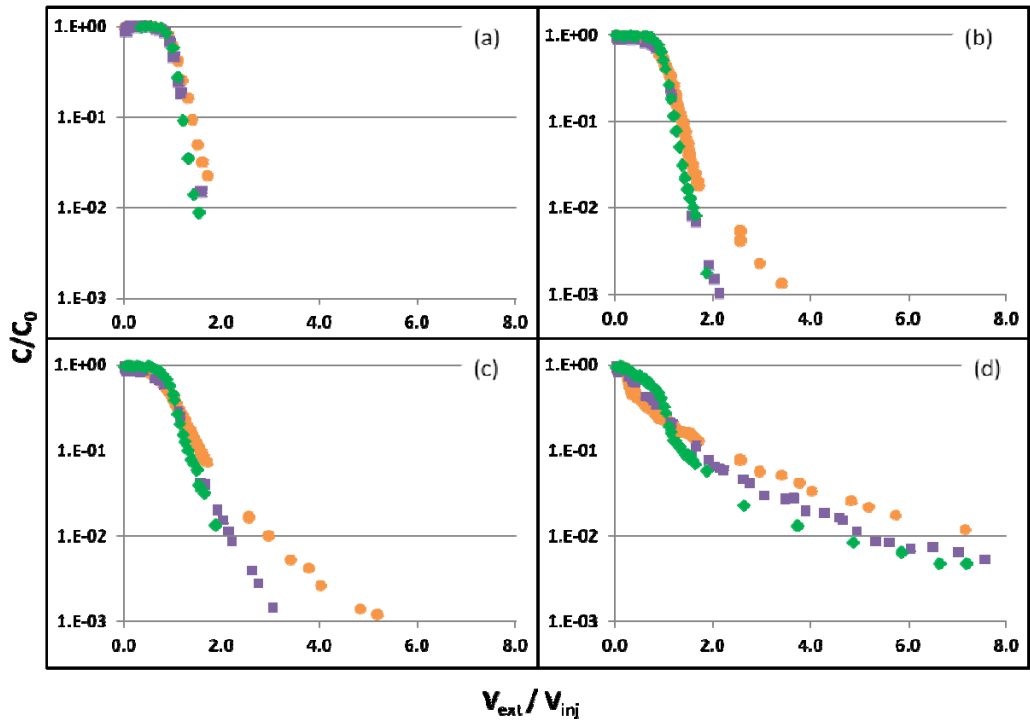


**Figure 7.14** Comparison of mid pool fraction bromide (a), 1-pentanol (b), 1-hexanol (c) and 2-octanol (d) BTC tails for each experiment. The fast-fast BTCs are shown in diamonds; the slow-fast in circles; the fast-slow in squares. Note the y-axis is log scale.

### ***7.5 - Assessment of High Pool Fraction Source Zone***

The packing structure of the high pool fraction box is shown below in Figure 7.15. In order to create even more pooling in the high pool fraction box, an additional injection needle was packed into the box to aid in delivery of the TCE. The thought here was that two injection points, each over a different low permeability lens, would cause more pooling. The exact location and size of each lens is shown in Table 7.6. 17 mL of TCE were injected at a flow rate of 0.1 mL/min through the needle to the right (Figure 7.6). The system was then allowed to redistribute over night prior to introducing an additional 15.1 mL of TCE through the needle to the left ( $Q=0.1$  mL/min). The entire system was then allowed to redistribute for two days. Light transmission results determine the initial source zone pool fraction as 0.85, 0.68 and 0.68 when calculated on a pixel by pixel basis, a discrete block averaging basis and a continuum averaging basis, respectively (Figure 7.16). All three source zones shown in Figure 7.16 are visually similar because (as displayed in Table 7.7) there is only 2.7 mL of TCE-DNAPL dissolved and/or volatilized from the source zone. All TCE-DNAPL source zone volumes, corresponding pool fractions and additional high pool fraction box parameters are presented below in Table 7.7.

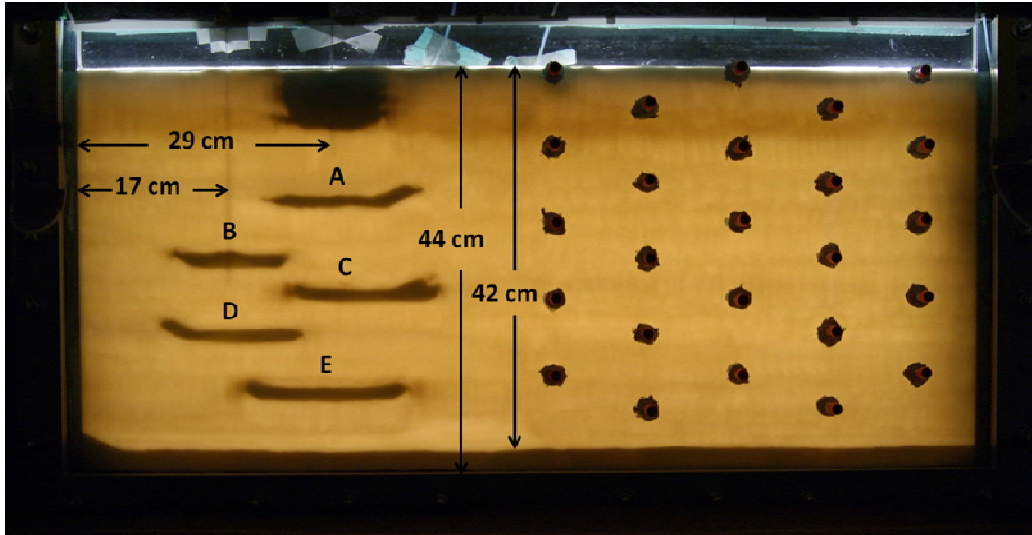


**Figure 7.15** Packing structure of the high pool fraction box. Included in the figure are the total packed height (44 cm), the height of the 40-50 sand (42 cm) and the distance from the injection/extraction well to both TCE-DNAPL injection needles (17 cm and 29 cm). The size and locations of all lenses are displayed in Table 7.4., below.

**Table 7.6** Size and location of the 5 lenses and F-70 block in the high pool fraction box

<b>Lens</b>	<b>Length (cm)</b>	<b>Thickness (cm)</b>	<b>Distance from Well to Front Edge of lens (cm)</b>	<b>Distance from bottom of box to bottom edge of lens (cm)</b>
<b>F-70 Block</b>	11.0	6.5	23.2	37.6
<b>A</b>	15.0	1.3	21.0	29.3
<b>B</b>	12.0	1.8	11.0	23.6
<b>C</b>	16.0	1.3	23.6	18.6
<b>D</b>	15.0	1.5	9.5	14.4
<b>E</b>	18.0	1.5	18.2	7.7

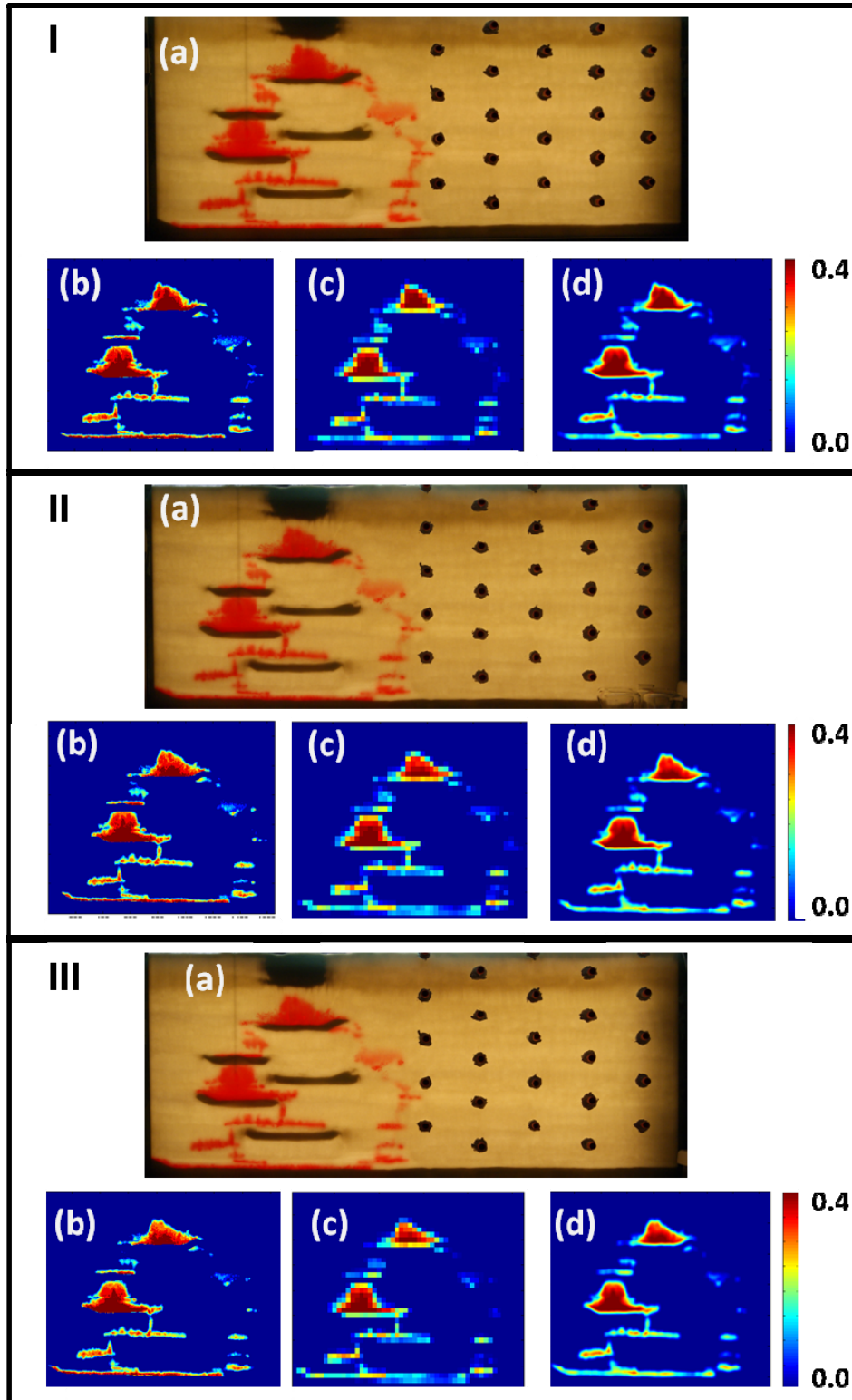


**Figure 7.16** High pool fraction TCE-DNAPL spill shown as a photograph (a), pixel by pixel saturation (b), discrete averaging saturation (c), and continuum averaging saturation (d). Panels I, II and III show the source zone distribution before the fast-fast test, slow-fast test, and fast-slow test, respectively.

**Table 7.7** High pool fraction box and corresponding tracer test parameters.

	<b>Fast Injection Fast Extraction</b>	<b>Slow Injection Fast Extraction</b>	<b>Fast Injection Slow Extraction</b>
<b>Background sand (Ottawa, IL)</b>	Ottawa Federal Fine, 40-50 Sand Fraction		
<b>Uniformity Index (<math>U_i</math>)</b>	1.2		
<b>Median Grain Diameter (<math>d_{50}</math>)</b>	0.35 mm		
<b>Box Length</b>	100 cm		
<b>Packed Height</b>	44 cm		
<b>Mass Federal Fine</b>	9325 g		
<b>Mass F-70</b>	990 g		
<b>Average Bulk Density</b>	1.54 g/cm <sup>3</sup>		
<b>Average Porosity</b>	0.42		
<b>Pore Volume (PV)</b>	2782 mL		
<b>Volume TCE Injected</b>	32.1 mL		
<b>Volume of TCE-DNAPL in Source Zone</b>	32.1 mL <sup>1</sup>	31.9 mL <sup>2</sup>	29.4 mL <sup>2</sup>
<b>Pool Fraction</b>			
<b>Pixel x Pixel</b>	0.85	0.86	0.86
<b>Discrete Block Avg.</b>	0.68	0.65	0.69
<b>Continuum Avg.</b>	0.68	0.70	0.70
<b>Tracer Solution Injection Volume</b>	1781 mL	1610 mL	1744.6 mL
<b>Swept Volume TCE-DNAPL Saturation<sup>3</sup></b>	1.8 %	2.0 %	1.8 %
<b>Injection Flow</b>	8.7 mL/min	0.4 mL/min	8.5 mL/min
<b>Extraction Flow</b>	8.3 mL/min	8.4 mL/min	0.5 mL/min
<b>Injection PW Velocity</b>	0.33 cm/min	0.02 cm/min	0.32 cm/min
<b>Extraction PW Velocity</b>	0.32 cm/min	0.32 cm/min	0.02 cm/min
<b>Br- Conc.</b>	719 mg/L	719 mg/L	63 mg/L
<b>1-Pentanol Conc.</b>	880 mg/L	930 mg/L	926 mg/L
<b>1-Hexanol Conc.</b>	368 mg/L	384 mg/L	411 mg/L
<b>2-Octanol Conc.</b>	104 mg/L	96 mg/L	99 mg/L
<b>Bromide Recovery</b>	102%	96%	100%
<b>1-Pentanol Recovery</b>	98%	99%	97%
<b>1-Hexanol Recovery</b>	98%	99%	95%
<b>2-Octanol Recovery</b>	95%	93%	92%

<sup>1</sup>Any difference between the volume of TCE injected and the volume of TCE-DNAPL in the source zone is due to TCE-DNAPL flow into the end chamber and subsequent removal.

<sup>2</sup>Dissolution and volatilization result in changes in TCE-DNAPL source zone volume and pool fraction. Here TCE-DNAPL source zone volume is calculated using light transmission analysis.

<sup>3</sup>Swept volume TCE-DNAPL saturation is defined as the volume of TCE-DNAPL normalized by the injected tracer volume. Values vary slightly between each test due to the different injection volumes used.

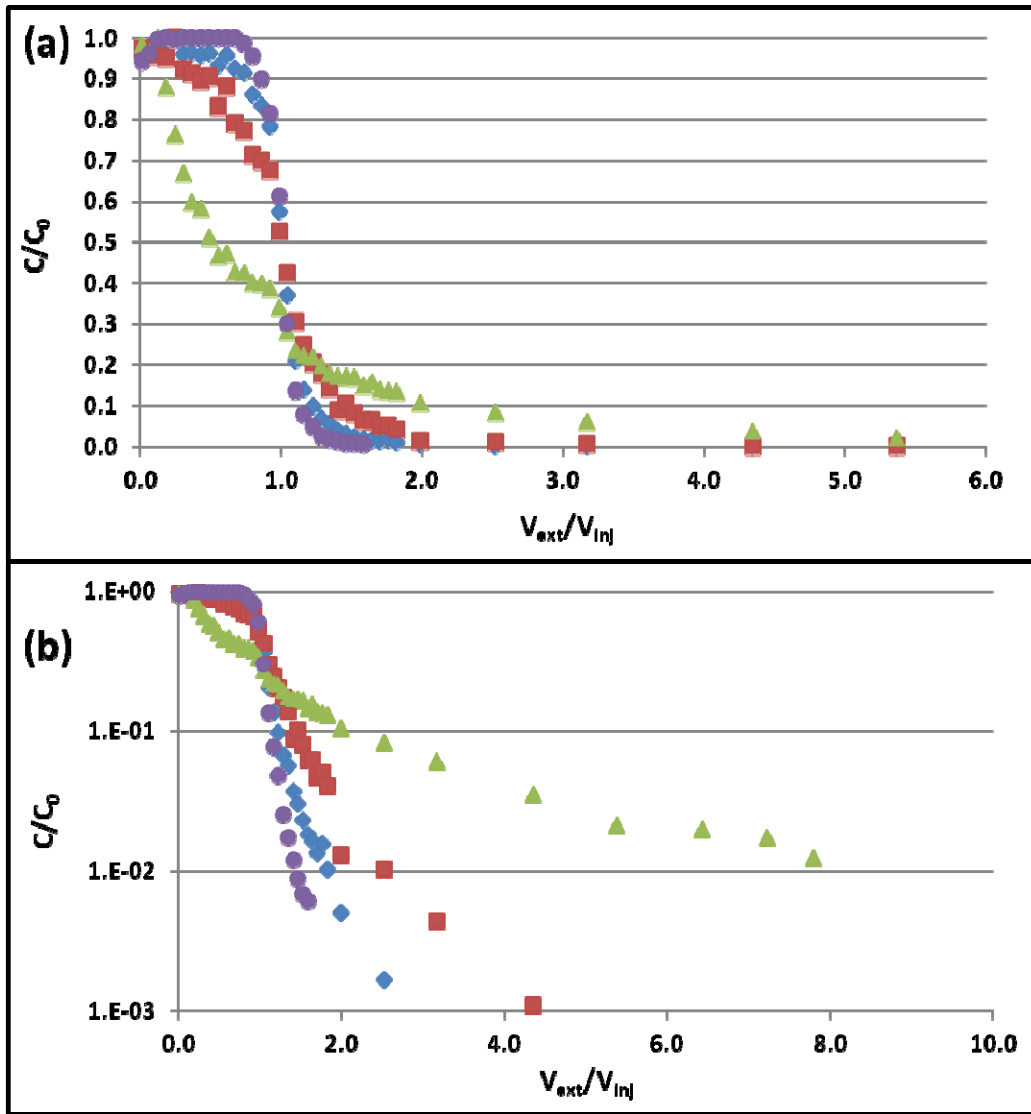


**Figure 7.17** High pool fraction fast-fast breakthrough curves: bromide (circles), 1-pentanol (diamonds), 1-hexanol (squares) and 2-octanol (triangles). Data is shown on a normal y-axis scale, and for a shorter extraction time (a) to display the differences in the front of the BTCs and then on a log scale axis, for a longer extraction time (b) to highlight tracer tailing.

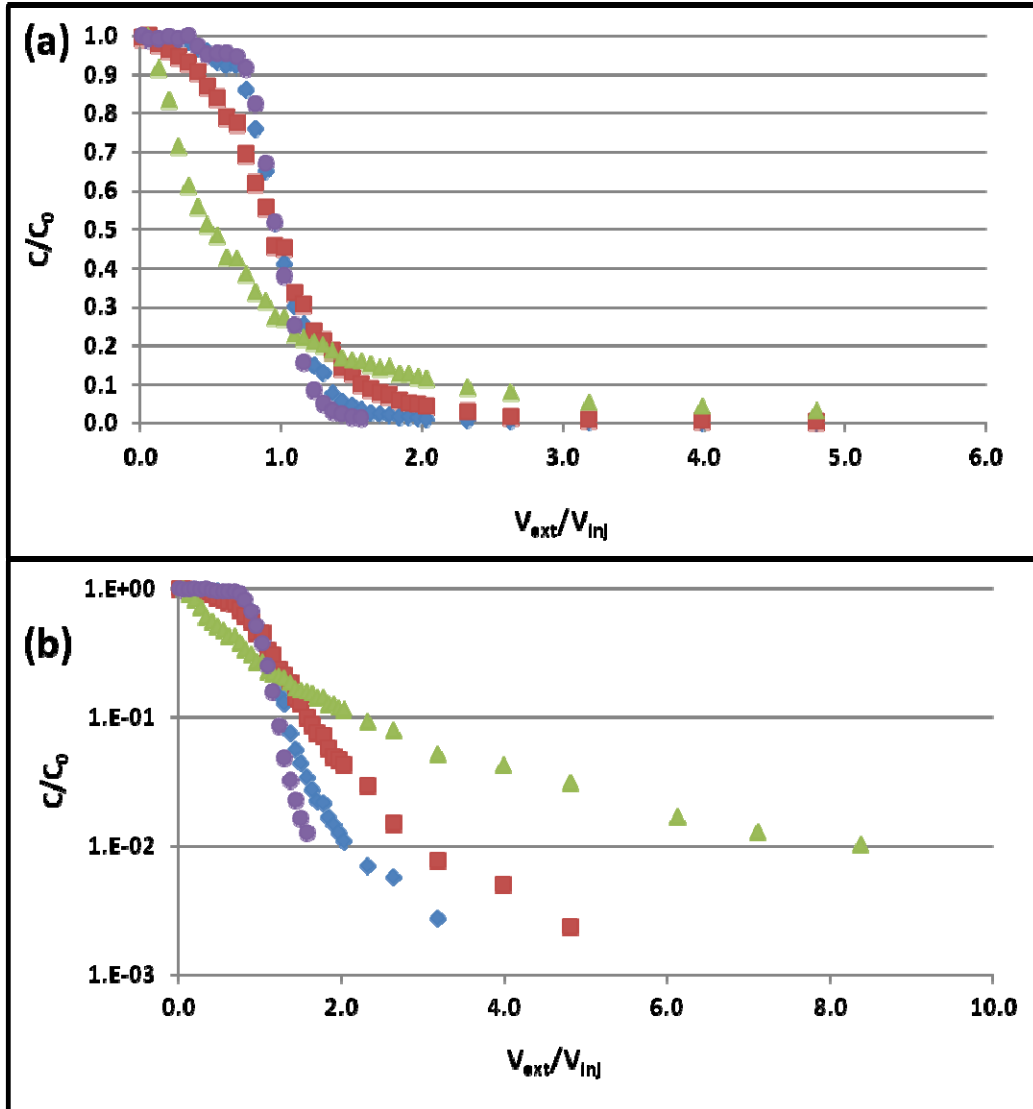


**Figure 7.18** High pool fraction slow-fast breakthrough curves: bromide (circles), 1-pentanol (diamonds), 1-hexanol (squares) and 2-octanol (triangles). Data is shown on a normal y-axis scale, and for a shorter extraction time (a) to display the differences in the front of the BTCs and then on a log scale axis, for a longer extraction time (b) to highlight tracer tailing.

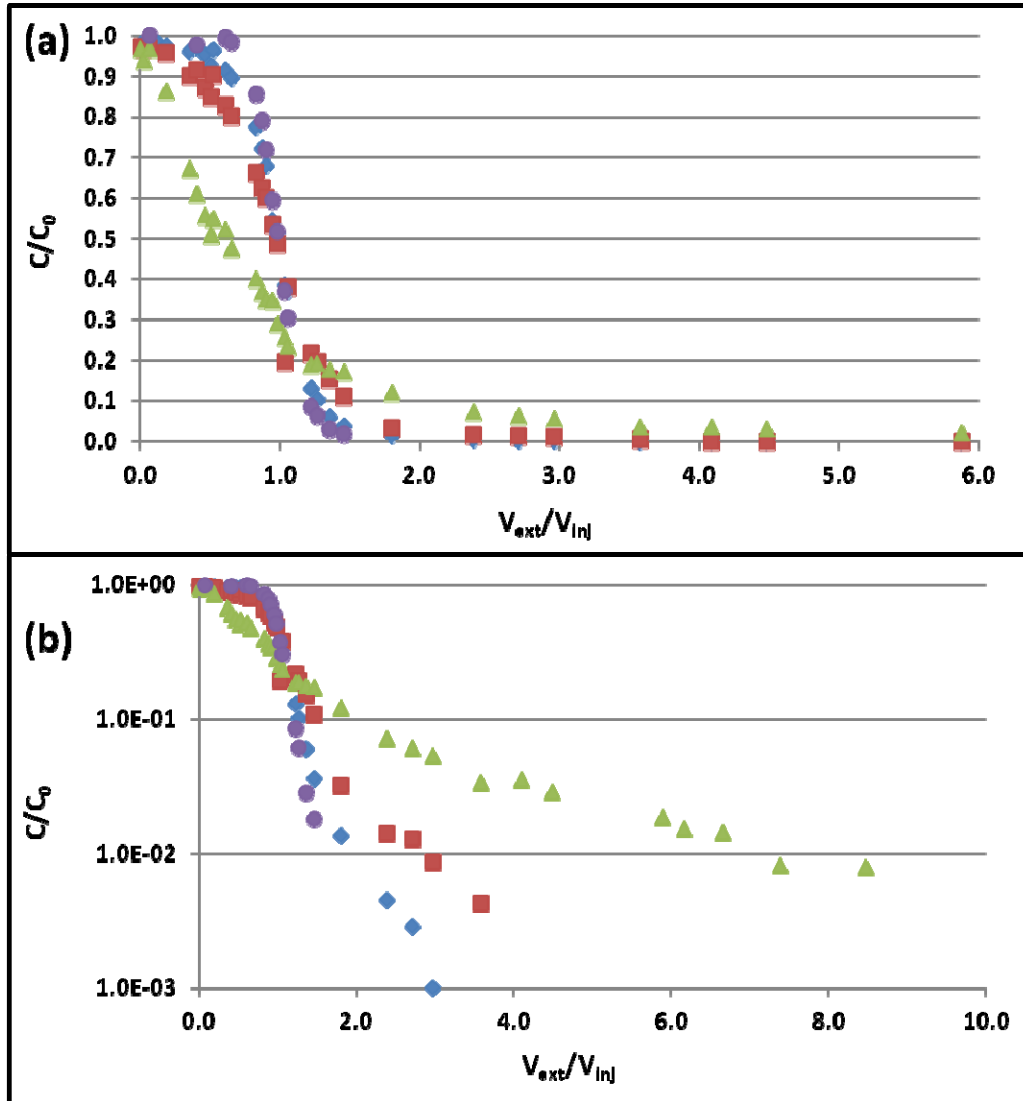


**Figure 7.19** High pool fraction fast-slow breakthrough curves: bromide (circles), 1-pentanol (diamonds), 1-hexanol (squares) and 2-octanol (triangles). Data is shown on a normal y-axis scale, and for a shorter extraction time (a) to display the differences in the front of the BTCs and then on a log scale axis, for a longer extraction time (b) to highlight tracer tailing.

Resulting BTCs from the three push-pull tests are shown in Figures 7.17 – 7.19. All three figures show the same general trends seen in the low and mid pool fraction boxes (increasing asymmetry and tailing with increasing partition coefficient). Here, a slight inflection point is again seen in the 2-octanol signal of the fast-fast test at a  $V_{\text{ext}}/V_{\text{inj}}$  of 0.9. As with the mid pool fraction box, this inflection point is not seen in the bromide signal, indicating that this feature of the 2-octanol signal is due more to tracer-NAPL interactions than to the flow field.

In Figures 7.20 and 7.21 the individual tracers are compared among the three experiments on both linear and log scales. In these experiments, the bromide, 1-pentanol and 1-hexanol curves are all almost indistinguishable. Even in the BTC tails, separation is slight and decreases with increasing partition coefficient, indicating that the separation may have been due mainly to slight differences in the flow field. The 2-octanol signals, which showed some differences among the three tests in the other boxes, lie almost directly on top of one another. In the high pool fraction box, the results indicate that tracer BTCs are not dependent on the differences in injection/extraction flow rate employed herein. It should also be noted, that unlike the low and mid pool fraction boxes, very little TCE-DNAPL (2.7 mL) was lost to dissolution and/or volatilization between the first and last push-pull test.

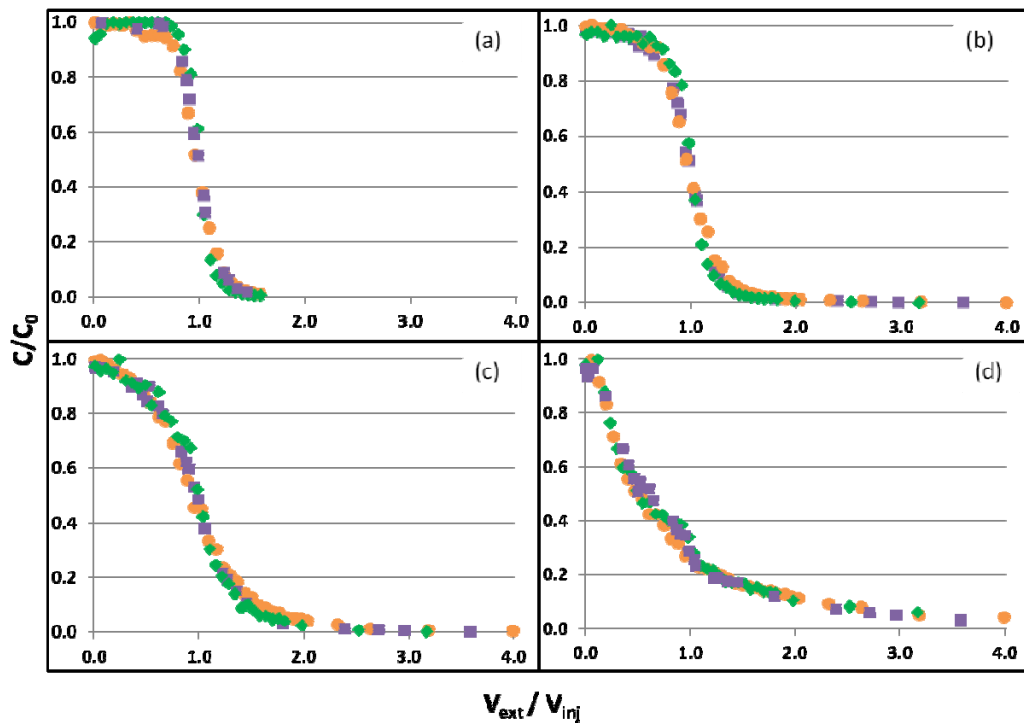


**Figure 7.20** Comparison of high pool fraction bromide (a), 1-pentanol (b), 1-hexanol (c) and 2-octanol (d) BTCs for each experiment. The fast-fast BTCs are shown in diamonds; the slow-fast in circles; the fast-slow in squares.

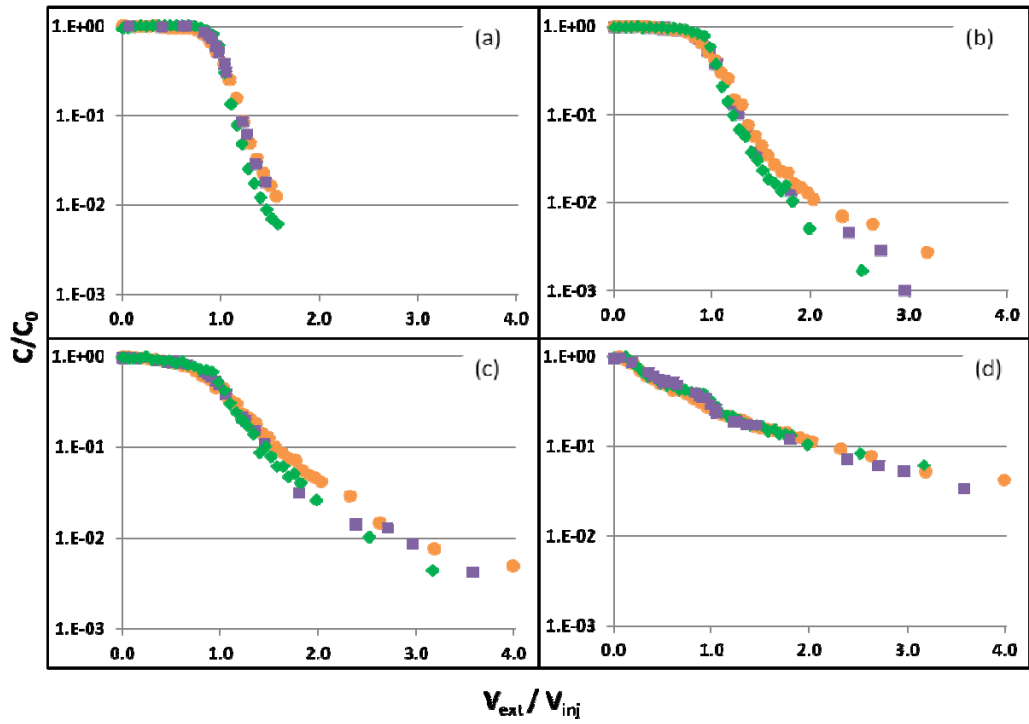


**Figure 7.21** Comparison of high pool fraction bromide (a), 1-pentanol (b), 1-hexanol (c) and 2-octanol (d) BTC tails for each experiment. The fast-fast BTCs are shown in diamonds; the slow-fast in circles; the fast-slow in squares. Note the y-axis is log scale.

## ***7.6 – Pool Fraction Comparison***

In Figures 7.22 – 7.27 the push-pull BTCs are plotted to show the effect of pool fraction for each injection/extraction flow rate combination. As can be seen in Figures 7.26 and 7.27, the fast-slow test produces almost the same BTC for each tracer, especially 2-octanol. Even the tails of these BTCs are similar, and do not distinguish between pool dominated and ganglia dominated source zones. The slow-fast test shows slight differences among the three tests. In the early part of the BTCs, the 2-octanol signals separate in order, low, mid, high pool fraction. However, the shapes are too similar to conclusively differentiate between pool fractions. The 2-octanol tails show no separation, indicating that tailing is not as dependent on pool fraction as was hypothesized before conducting these tests. The amount of TCE-DNAPL used to create these source zones (~30 mL) is relatively small; it maybe that the approximately 10 additional milliliters of pooled TCE in the high pool fraction box (compared to the low pool fraction box) does not appreciably increase tailing.

Interestingly, it appears that the fast-fast test (Figures 7.22 and 7.23) is as good as, or better, than the other push-pull tests at distinguishing between the three boxes. The fast-fast 2-octanol data sets are the only BTCs that show a difference between all three pool fractions. The low pool fraction 1-pentanol and 1-hexanol signals are strongly influenced by the flow field.

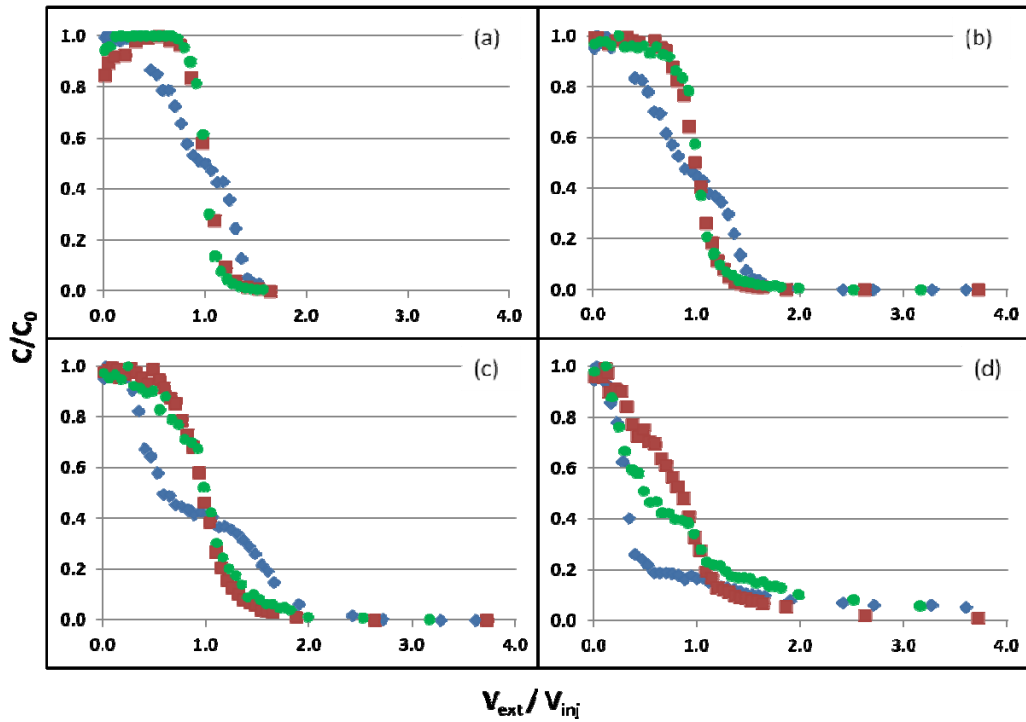


**Figure 7.22** Comparison of fast-fast experiments across all three pool fractions. Figure includes bromide (a), 1-pentanol (b), 1-hexanol (c) and 2-octanol (d) BTCs. The low pool fraction BTCs are shown in diamonds; the mid pool fraction in squares; the high pool fraction in circles.

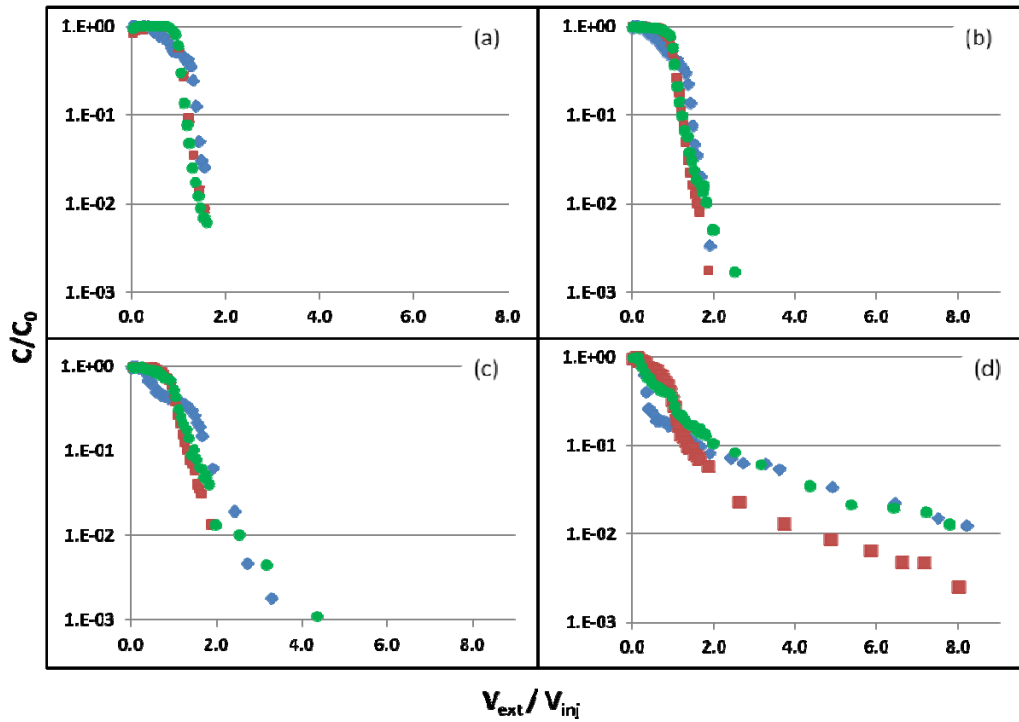


**Figure 7.23** Comparison of fast-fast experiment tails across all three pool fractions. Figure includes bromide (a), 1-pentanol (b), 1-hexanol (c) and 2-octanol (d) BTCs. The low pool fraction BTCs are shown in diamonds; the mid pool fraction in squares; the high pool fraction in circles.

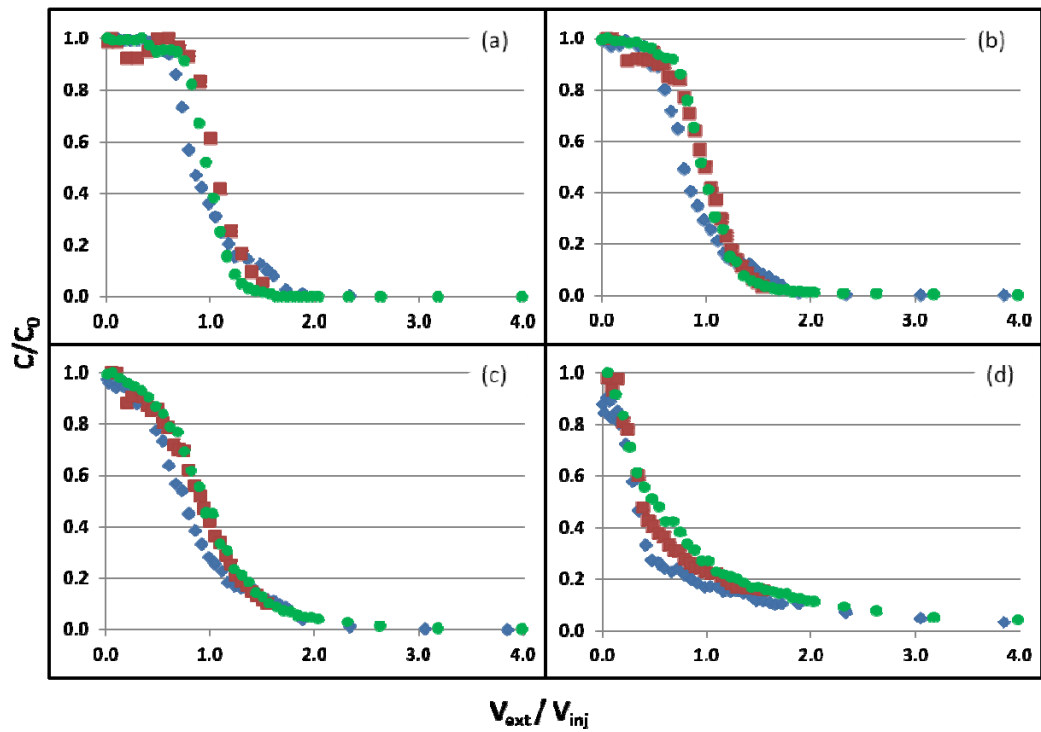


**Figure 7.24** Comparison of slow-fast experiments across all three pool fractions. Figure includes bromide (a), 1-pentanol (b), 1-hexanol (c) and 2-octanol (d) BTCs. The low pool fraction BTCs are shown in diamonds; the mid pool fraction in squares; the high pool fraction in circles.

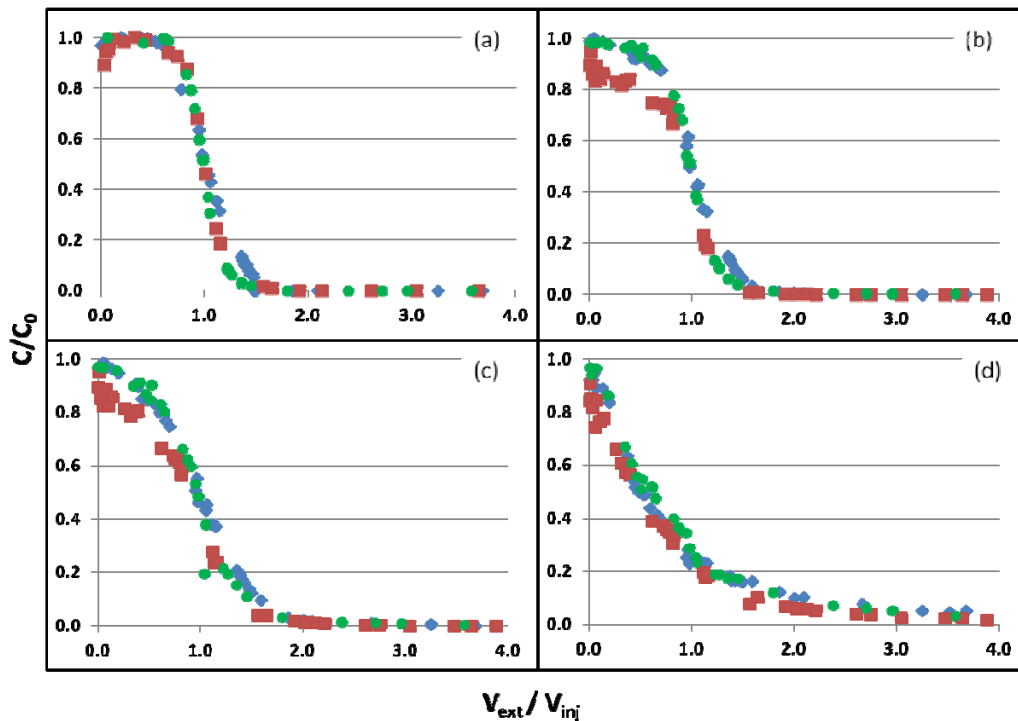


**Figure 7.25** Comparison of fast-slow experiments across all three pool fractions. Figure includes bromide (a), 1-pentanol (b), 1-hexanol (c) and 2-octanol (d) BTCs. The low pool fraction BTCs are shown in diamonds; the mid pool fraction in squares; the high pool fraction in circles.

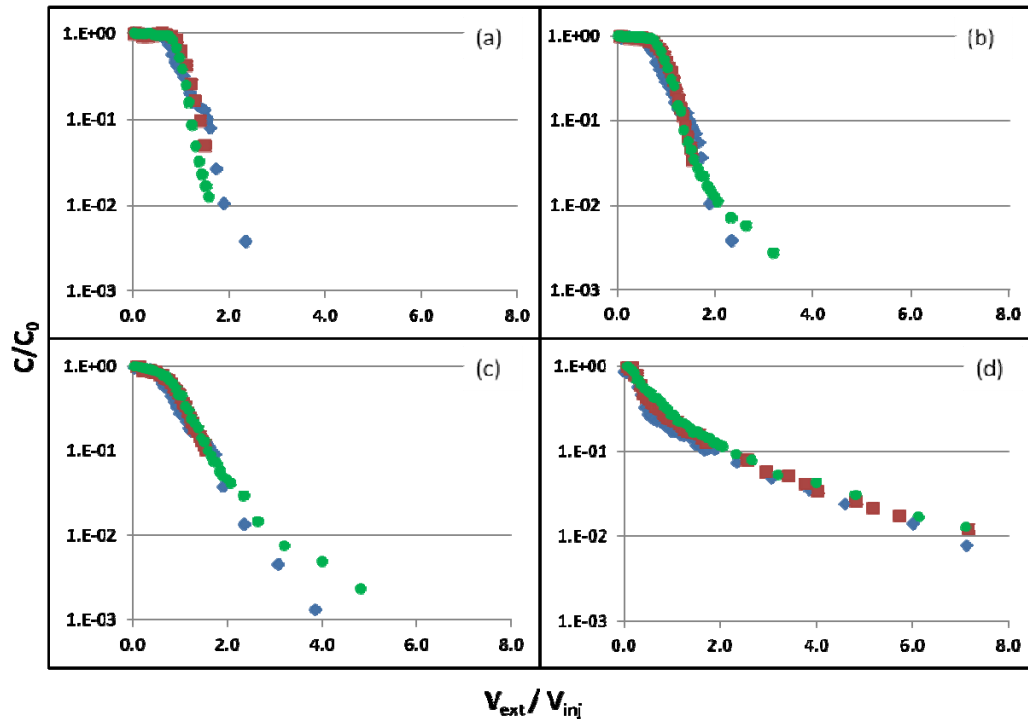


**Figure 7.26** Comparison of slow-fast experiment tails across all three pool fractions. Figure includes bromide (a), 1-pentanol (b), 1-hexanol (c) and 2-octanol (d) BTCs. The low pool fraction BTCs are shown in diamonds; the mid pool fraction in squares; the high pool fraction in circles.

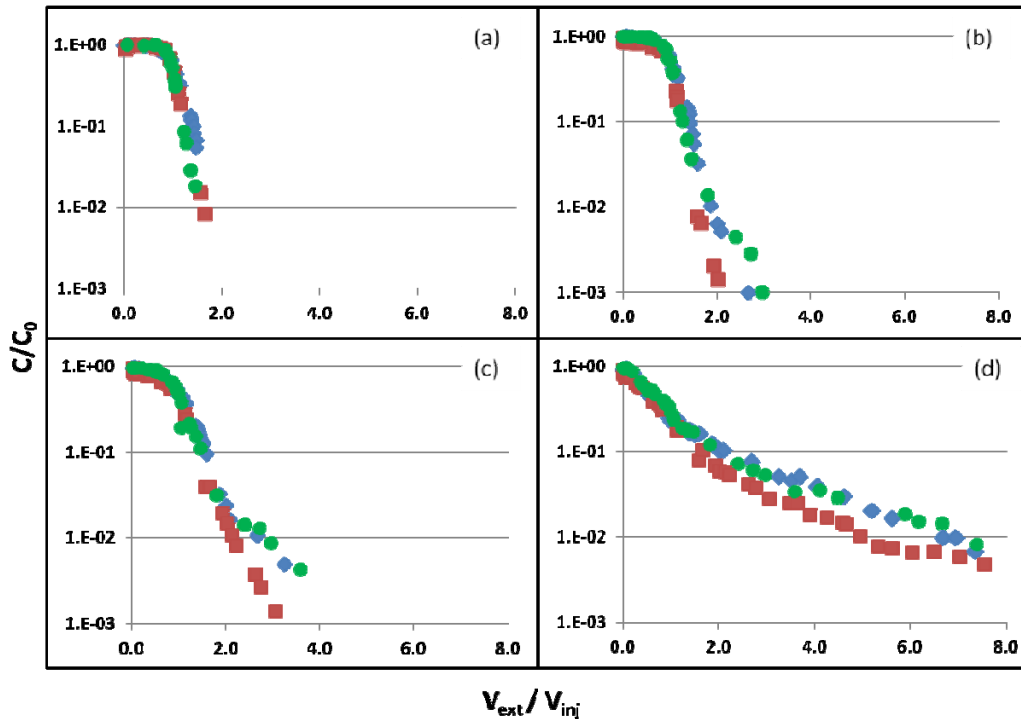


**Figure 7.27** Comparison of fast-slow experiment tails across all three pool fractions. Figure includes bromide (a), 1-pentanol (b), 1-hexanol (c) and 2-octanol (d) BTCs. The low pool fraction BTCs are shown in diamonds; the mid pool fraction in squares; the high pool fraction in circles.

It is therefore difficult to determine whether the 1-pentanol and 1-hexanol low pool fraction box curves differ from those of the mid and high pool fraction boxes solely due to the difference in flow field, or if tracer/DNAPL interactions are also causing these differences. The 2-octanol signal will also be affected by the flow field, but should be more strongly affected by interactions with the TCE-DNAPL than 1-pentanol and 1-hexanol.

Interestingly, for the fast-fast tests (Figures 7.22 and 7.23), the high pool fraction 2-octanol BTC falls between that of the low and mid pool fraction boxes. This, along with the fact that the other flow rate combinations are unable to distinguish between pool fractions, indicates that pool fraction may not be the metric that should be measured with these push-pull tests. As was discussed earlier in this chapter, the saturation distribution of the mid pool fraction box immediately preceding the fast-fast test is quite different than those of the other boxes (including the initial mid pool fraction source zone). The mid pool fraction source zone prior to the fast-fast test is characteristic of a late time source zone with the TCE-DNAPL grouped in five main locations without connection between the areas. The other source zones are more characteristic of early time source zones where the TCE-DNAPL high saturation areas are linked together with highly spread DNAPL ganglia. This difference in source zone connectivity, and not the differences in pool fraction, may be the reason for the differences seen among the fast-fast test results.

## 7.7 – Discussion

### 7.7.1 - Temporal Moments

In order for push-pull tests to be useful in quantifying source zone architecture metrics, it is important to be able to interpret the BTCs using modeling or another quantitative method. As described in Chapter 1 of this dissertation, the method of moments is one of the traditional methods used to analyze partitioning tracer tests. Davis et al. (2002) describe the use of normalized first moments of the partitioning and non-partitioning tracers are to estimate retardation coefficients from push-pull tests:

$$R = \frac{M_1^p}{M_1^{np}} \quad (7.1)$$

(Note the similarity to equation 1.4 for PITT tests. For the push-pull test is not necessary to correct for pulse width). As was done in Chapter 6, Section 6.3, saturation was estimated using the measured partition coefficient and the estimated retardation factor. Shown in tables 7.8 – 7.10 are the saturation and TCE-DNAPL volume estimates determined for each tracer, each test and each box using the method of moments.

Similar to the pooled box in Chapter 6, in all but one of the 27 estimates (3 boxes x 3 tests x 3 partitioning tracers) the source zone saturation was underestimated. This underestimation is common in heterogeneous source zones (e.g. Annable et al., 1998a; Brooks et al., 2002; Hartog et al., 2010) and is attributed to flow bypassing of high saturation zones. Here we can see that estimates of total TCE-DNAPL volume vary from 12 – 91% of the actual volume.

In this system, 1-pentanol and 1-hexanol (in five cases) provide less reliable estimates of saturation because they do not experience enough partitioning. Jin et al. (1997) recommend that retardation coefficients lie between 1.2 and 4.0 to obtain the best overall saturation estimates. This may explain why 1-pentanol frequently gives the least accurate estimate; the difference between the first normalized moment of 1-pentanol and that of bromide is so unsubstantial that noise in the data can have a large effect on the saturation estimation. For each experiment, the 2-octanol retardation coefficient lies within the recommended range, and therefore is taken to give the best estimate of saturation.

Applying the method of moments to the 2-octanol data results in estimations of 67 – 76% of the measured total volume for the low pool fraction box, 39 – 64 % for the mid pool fraction box and 60 – 61% for the high pool fraction box. Since the equilibrium assumption is incorporated into the method of moment analysis, it is unsurprising that it performs best for the low pool fraction box. The test on which the method of moments shows the poorest performance is the mid pool fraction fast-fast test. As discussed previously, this test was conducted after approximately half of the original DNAPL mass had dissolved from the source zone. If the results of the mid pool fraction fast-fast test are left out of the analysis, the method of moments appears to perform similarly on the mid and high pool fraction source zones. Though the method of moments does perform fairly well in a few of the cases examined herein, the overall performance does not give accurate estimations of source zone DNAPL volume.

**Table 7.8** Method of moment estimations of overall TCE-DNAPL saturation and volume for the low pool fraction box. Also included are the measured TCE-DNAPL source zone saturations and volumes.

<b>Low Pool Fraction</b>						
<b>Test</b>	<b>Tracer</b>	<b>Estimated R</b>	<b>Estimated DNAPL Sat.</b>	<b>Estimated DNAPL Vol. (mL)</b>	<b>Measured DNAPL Sat.*</b>	<b>Measured DNAPL Vol. (mL)*</b>
Fast-Fast	1-Pentanol	1.0	0.6%	10.9	1.8%	33.0
	1-Hexanol	1.3	1.4%	25.4	1.8%	33.0
	2-Octanol	3.0	1.3%	23.6	1.8%	33.0
Slow-Fast	1-Pentanol	0.9	NA	NA	1.6%	27.9
	1-Hexanol	1.1	0.6%	10.2	1.6%	27.9
	2-Octanol	2.6	1.1%	18.7	1.6%	27.9
Fast-Slow	1-Pentanol	1.0	0.7%	12.2	1.2%	20.5
	1-Hexanol	1.1	0.8%	13.9	1.2%	20.5
	2-Octanol	2.4	0.9%	15.5	1.2%	20.5

\* Measured DNAPL saturations and volumes vary between experiments due to both DNAPL dissolution between experiments and the swept volume (which is equal to the tracer pulse volume). After the first push-pull test, measured DNAPL volumes are calculated using light transmission.

**Table 7.9** Method of moment estimations of overall TCE-DNAPL saturation and volume for the mid pool fraction box. Also included are the measured TCE-DNAPL source zone saturations and volumes.

<b>Mid Pool Fraction</b>						
<b>Test</b>	<b>Tracer</b>	<b>Estimated R</b>	<b>Estimated DNAPL Sat.</b>	<b>Estimated DNAPL Vol. (mL)</b>	<b>Measured DNAPL Sat.*</b>	<b>Measured DNAPL Vol. (mL)*</b>
Fast-fast	1-Pentanol	1.0	NA	NA	0.8%	15.1
	1-Hexanol	1.0	0.1%	1.9	0.8%	15.1
	2-Octanol	1.5	0.3%	5.8	0.8%	15.1
Slow-Fast	1-Pentanol	0.9	NA	NA	1.4%	30.8
	1-Hexanol	1.1	0.7%	15.3	1.4%	30.8
	2-Octanol	2.4	0.9%	19.7	1.4%	30.8
Fast-Slow	1-Pentanol	1.0	NA	NA	1.2%	24.9
	1-Hexanol	1.1	0.5%	10.4	1.2%	24.9
	2-Octanol	1.9	0.6%	12.5	1.2%	24.9

\* Measured DNAPL saturations and volumes vary between experiments due to both DNAPL dissolution between experiments and the swept volume (which is equal to the tracer pulse volume). After the first push-pull test, measured DNAPL volumes are calculated using light transmission.

**Table 7.10** Method of moment estimations of overall TCE-DNAPL saturation and volume for the high pool fraction box. Also included are the measured TCE-DNAPL source zone saturations and volumes.

<b>High Pool Fraction</b>						
<b>Test</b>	<b>Tracer</b>	<b>Estimated R</b>	<b>Estimated DNAPL Sat.</b>	<b>Estimated DNAPL Vol. (mL)</b>	<b>Measured DNAPL Sat.*</b>	<b>Measured DNAPL Vol. (mL)*</b>
Fast-Fast	1-Pentanol	1.0	1.0%	17.8	1.8%	32.1
	1-Hexanol	1.2	1.0%	17.8	1.8%	32.1
	2-Octanol	2.7	1.1%	19.6	1.8%	32.1
Slow-Fast	1-Pentanol	1.1	2.3%	37.0	2.0%	31.9
	1-Hexanol	1.3	1.8%	29.0	2.0%	31.9
	2-Octanol	2.8	1.2%	19.3	2.0%	31.9
Fast-Slow	1-Pentanol	1.1	1.4%	24.4	1.8%	29.4
	1-Hexanol	1.2	1.1%	19.2	1.8%	29.4
	2-Octanol	2.5	1.0%	17.4	1.8%	29.4

\* Measured DNAPL saturations and volumes vary between experiments due to both DNAPL dissolution between experiments and the swept volume (which is equal to the tracer pulse volume). After the first push-pull test, measured DNAPL volumes are calculated using light transmission.

### 7.7.2 - Equilibrium Push-Pull Model

Another common method for analyzing push-pull tracer tests is to use an analytical solution to examine the data (Istok et al., 2002). It is important to note that the geometry in many push-pull studies (e.g. Schroth et al., 2001; Istok et al., 2002) has a radial flow field. Therefore, the analytical solutions found in these works were developed for radial or cylindrical coordinate systems. The experiments conducted for this work were completed in rectangular 2-D aquifer cells so that light transmission could be used to more accurately estimate pool fraction. Therefore an analytical push-pull model developed by Gelhar and Collins (1971) was employed to model the BTCs in this rectangular geometry. The analytical solution is as follows:

$$\frac{C}{C_0} = \frac{1}{2} \operatorname{erfc} \left[ \frac{\frac{V_{ext}}{V_{inj}} - 1}{\left( \frac{4\alpha}{x_{max}} \left( 2 - \left( 1 - \frac{V_{ext}}{V_{inj}} \right) \right) \right)^{1/2}} \right] \quad (7.2)$$

where  $\alpha$  is the dispersivity [L] and  $x_{max}$  is the maximum travel distance of each tracer [L]. For bromide, the  $x_{max}$  is taken to be  $V_{inj}$  divided by the aquifer cell cross sectional area and the porosity (Istok et al., 2002). For each of the partitioning tracers,  $x_{max}$  is the maximum travel distance of bromide, divided by the partitioning tracer retardation coefficient. Assumptions implicit in this analytical solution include equilibrium partitioning, uniform flow field, and a uniform distribution of DNAPL saturation.

The analytical solution is fit to the bromide data to determine dispersivity ( $\alpha$ ). This dispersivity is used in all subsequent fits of the partitioning tracer data to obtain the value of  $x_{\max}$  that corresponds to each tracer. All fits are carried out by minimizing the sum of squared error between the data and the BTC produced by the analytical model. Essentially, this model determines the apparent dispersion of each partitioning tracer compared to the dispersion observed in the breakthrough of the non-partitioning tracer (bromide). All of the excess spreading in the partitioning tracers is assumed to result from *equilibrium* interactions between the partitioning tracer and DNAPL. Under this assumption, the retardation coefficient for each tracer can be calculated as:

$$R = \frac{x_{\max}^{Br^-}}{x_{\max}^{part}} \quad (7.3)$$

where  $x_{\max}^{Br^-}$  is the bromide  $x_{\max}$  and  $x_{\max}^{part}$  is the  $x_{\max}$  of the partitioning tracer. The overall average saturation can be estimated:

$$S_n = \frac{R - 1}{K_p^{C_i} + R - 1} \quad (7.4)$$

Though tracer partitioning at the fast flow rate (and possibly 2-octanol at the slow flow rate) is occurring under nonequilibrium conditions, it is of interest to see how well the analytical solution is able to reproduce the BTCs since partitioning tracer tests are often assumed to occur at equilibrium. The results of this analysis are visually similar among the nine push-pull tests, therefore only the best predictions (mid pool fraction fast-fast test) and the worst predictions (low pool fraction fast-fast test) are shown, in Figures 7.28 and 7.29, respectively.

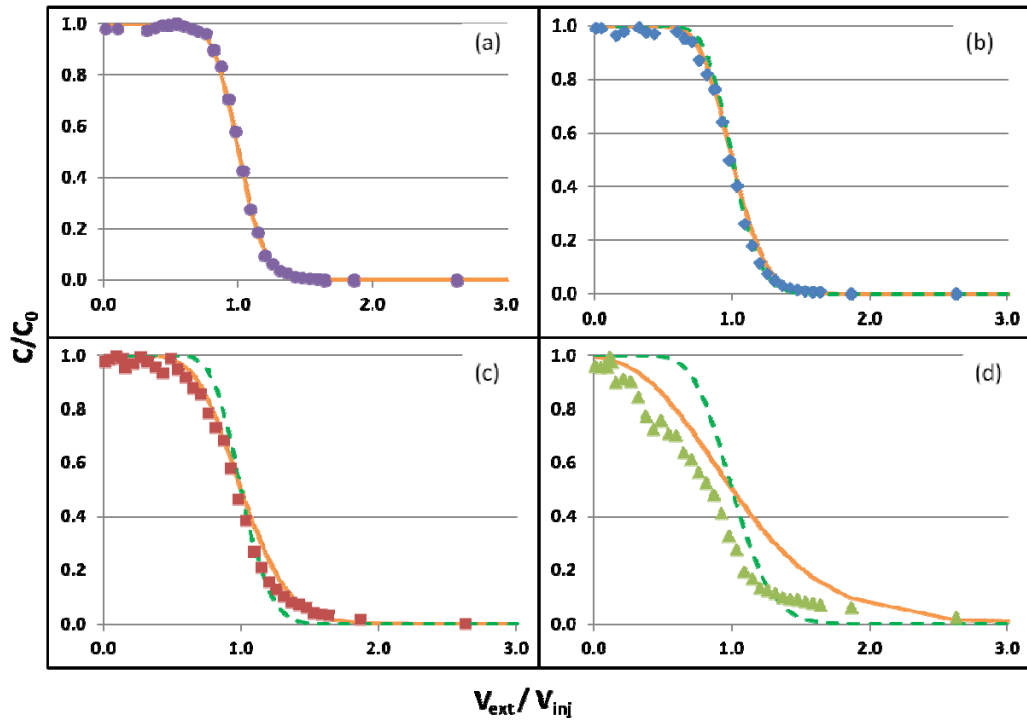


**Figure 7.28** Equilibrium modeling of mid pool fraction fast-fast experiment. Displayed are bromide (a), 1-pentanol (b), 1-hexanol (c) and 2-octanol (d) BTCs. Each panel includes a best fit BTC (solid line) and panels b-d include equilibrium predictions using the measured saturation (dashed).

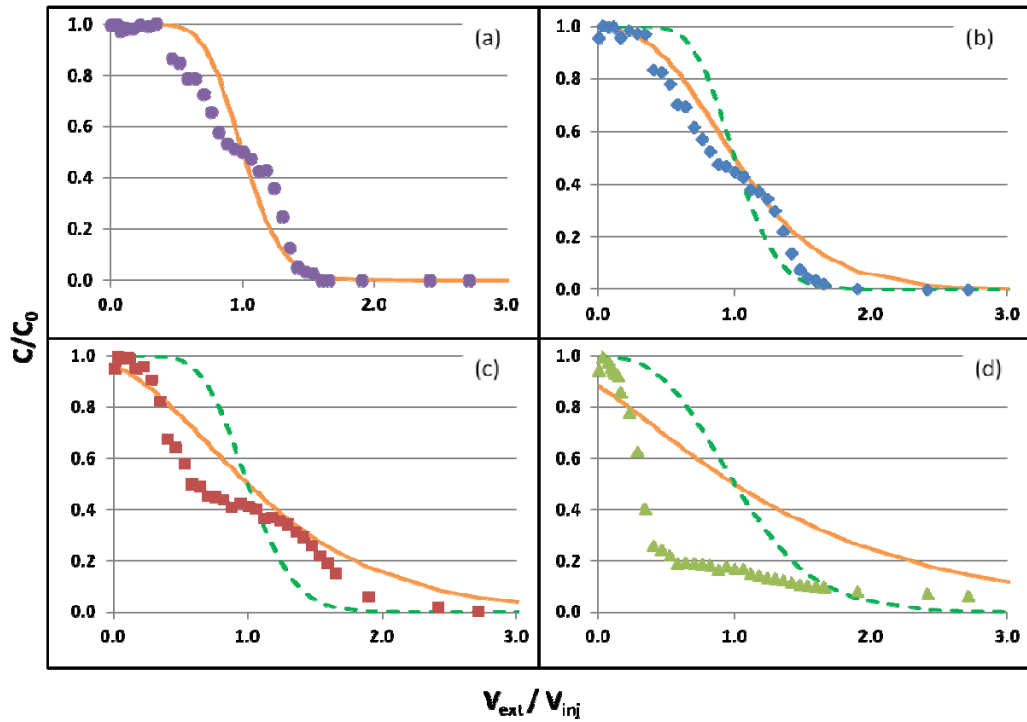


**Figure 7.29** Equilibrium modeling of low pool fraction fast-fast experiment. Displayed are bromide (a), 1-pentanol (b), 1-hexanol (c) and 2-octanol (d) BTCs. Each panel includes a best fit BTC (solid line) and panels b-d include equilibrium predictions using the measured saturation (dashed).

**Table 7.11** Analytical solution estimations of dispersivity, overall TCE-DNAPL saturation and volume for the low pool fraction box. Also included are the measured TCE-DNAPL source zone saturations and volumes.

<b>Low Pool Fraction</b>							
<b>Test</b>	<b>Tracer</b>	<b>Fit alpha (cm)</b>	<b>Sum of Squared Error<sup>1</sup></b>	<b>Estimated DNAPL Sat.</b>	<b>Estimated DNAPL Vol. (mL)</b>	<b>Measured DNAPL Sat.<sup>2</sup></b>	<b>Measured DNAPL Vol. (mL)<sup>2</sup></b>
Fast-Fast	Bromide	0.9	0.02	-	-	1.8%	32.5
	1-Pentanol	-	0.19	46.3%	841	1.8%	32.5
	1-Hexanol	-	0.38	37.5%	681	1.8%	32.5
	2-Octanol	-	2.98	14.0%	254	1.8%	32.5
Slow-Fast	Bromide	1.0	0.25	-	-	1.6%	27.9
	1-Pentanol	-	0.39	26.1%	443	1.6%	27.9
	1-Hexanol	-	0.50	18.2%	309	1.6%	27.9
	2-Octanol	-	2.29	15.6%	265	1.6%	27.9
Fast-Slow	Bromide	1.1	0.02	-	-	1.2%	20.5
	1-Pentanol	-	0.03	9.8%	170	1.2%	20.5
	1-Hexanol	-	0.05	11.5%	200	1.2%	20.5
	2-Octanol	-	1.26	9.5%	165	1.2%	20.5

<sup>1</sup>The sum of squared error for bromide corresponds to fitting alpha in equation 7.2 to the bromide data. For the partitioning tracers, sum of squared error corresponds to fitting  $x_{max}$  in equation 7.2 to each partitioning BTC.  $x_{max}$  is then used to calculate DNAPL saturation.

<sup>2</sup>Measured TCE-DNAPL saturations and volumes vary between experiments due to both TCE-DNAPL dissolution/volatilization between experiments and the swept volume (which is equal to the tracer pulse volume).

**Table 7.12** Analytical solution estimations of dispersivity, overall TCE-DNAPL saturation and volume for the mid pool fraction box. Also included are the measured TCE-DNAPL source zone saturations and volumes.

<b>Mid Pool Fraction</b>							
<b>Test</b>	<b>Tracer</b>	<b>Fit alpha (cm)</b>	<b>Sum of Squared Error<sup>1</sup></b>	<b>Estimated DNAPL Sat.</b>	<b>Estimated DNAPL Vol. (mL)</b>	<b>Measured DNAPL Sat.<sup>2</sup></b>	<b>Measured DNAPL Vol. (mL)<sup>2</sup></b>
Fast-Fast	Bromide	0.4	0.03	-	-	0.8%	15.1
	1-Pentanol	-	0.02	10.3%	200	0.8%	15.1
	1-Hexanol	-	0.07	10.2%	198	0.8%	15.1
	2-Octanol	-	0.63	7.4%	144	0.8%	15.1
Slow-Fast	Bromide	0.8	0.08	-	-	1.4%	30.8
	1-Pentanol	-	0.06	19.9%	436	1.4%	30.8
	1-Hexanol	-	0.17	19.5%	427	1.4%	30.8
	2-Octanol	-	1.87	17.2%	376	1.4%	30.8
Fast-Slow	Bromide	0.5	0.04	-	-	1.4%	30.8
	1-Pentanol	-	0.28	51.6%	1074	1.4%	30.8
	1-Hexanol	-	0.27	47.0%	978	1.4%	30.8
	2-Octanol	-	1.01	24.0%	500	1.4%	30.8

<sup>1</sup>The sum of squared error for bromide corresponds to fitting alpha in equation 7.2 to the bromide data. For the partitioning tracers, sum of squared error corresponds to fitting  $x_{max}$  in equation 7.2 to each partitioning BTC.  $x_{max}$  is then used to calculate DNAPL saturation.

<sup>2</sup>Measured TCE-DNAPL saturations and volumes vary between experiments due to both TCE-DNAPL dissolution/volatilization between experiments and the swept volume (which is equal to the tracer pulse volume).

**Table 7.13** Analytical solution estimations of dispersivity, overall TCE-DNAPL saturation and volume for the high pool fraction box. Also included are the measured TCE-DNAPL source zone saturations and volumes.

<b>High Pool Fraction</b>							
<b>Test</b>	<b>Tracer</b>	<b>Fit alpha (cm)</b>	<b>Sum of Squared Error<sup>1</sup></b>	<b>Estimated DNAPL Sat.</b>	<b>Estimated DNAPL Vol. (mL)</b>	<b>Measured DNAPL Sat.<sup>2</sup></b>	<b>Measured DNAPL Vol. (mL)<sup>2</sup></b>
Fast-Fast	Bromide	0.2	0.02	-	-	1.8%	32.1
	1-Pentanol	-	0.05	25.6%	334	1.8%	32.1
	1-Hexanol	-	0.09	38.2%	680	1.8%	32.1
	2-Octanol	-	0.92	37.4%	666	1.8%	32.1
Slow-Fast	Bromide	0.5	0.04	-	-	2.0%	31.9
	1-Pentanol	-	0.03	13.4%	216	2.0%	31.9
	1-Hexanol	-	0.06	19.2%	309	2.0%	31.9
	2-Octanol	-	0.98	12.9%	208	2.0%	31.9
Fast-Slow	Bromide	0.4	0.02	-	-	1.8%	29.4
	1-Pentanol	-	0.04	18.8%	328	1.8%	29.4
	1-Hexanol	-	0.13	23.8%	415	1.8%	29.4
	2-Octanol	-	0.73	22.2%	387	1.8%	29.4

<sup>1</sup>The sum of squared error for bromide corresponds to fitting alpha in equation 7.2 to the bromide data. For the partitioning tracers, sum of squared error corresponds to fitting  $x_{max}$  in equation 7.2 to each partitioning BTC.  $x_{max}$  is then used to calculate DNAPL saturation.

<sup>2</sup>Measured TCE-DNAPL saturations and volumes vary between experiments due to both TCE-DNAPL dissolution/volatilization between experiments and the swept volume (which is equal to the tracer pulse volume).

All results of this analysis are shown below in Tables 7.11 – 7.13. The complete set of analytical modeling results can be viewed in Appendix 1, Figures A1.1 – A1.9.

As demonstrated in Figures 7.28 and 7.29, the analytical solution can only produce symmetric BTCs. Generally, predictions of 1-pentanol BTCs using the fit dispersivity and measured source zone saturation capture the data. However, the model is unable to capture the degree of excess spreading present in the 1-hexanol BTCs using the measured saturation. In Tables 7.11 – 7.13 it is shown that fitting the analytical solution to the 1-hexanol BTCs results in DNAPL source zone saturation estimates that are 10-40 times larger than actual saturations. It appears in Figure 7.28 that the analytical solution provides a good prediction of the mid pool fraction fast-fast 1-hexanol BTC; however, the best fit saturation corresponds to a TCE-DNAPL source zone volume of 200 mL which is approximately 13 times the amount of TCE-DNAPL present in the actual source zone.

Though fitting the analytical solution to the 1-hexanol data provides gross over estimates of saturation, the model is capable of capturing the shape of the 1-hexanol data sets (note the low sum of squared errors in Tables 7.11-7.13). Model performance is worse for the 2-octanol BTCs. Here, the analytical solution is unable to capture the shape of the asymmetric 2-octanol BTCs, no matter how high a saturation value is used. The shape of the BTC in Figure 7.29, which is more representative of the other 7 BTCs (Appendix 1), is especially different from the BTCs produced by the analytical solution. The analytical solution

always produces curves that breakthrough at  $V_{\text{ext}}/V_{\text{inj}} = 1$ . Increasing saturation only increases the excess dispersion of the BTC, as shown in Figure 7.30. Because of this inability capture the shape of the 2-octanol BTC, the saturation predictions using the 2-octanol data shown in Tables 7.11 – 7.13 are relatively meaningless.

It should be noted that the model appears to perform better for the mid pool fraction fast-fast 2-octanol BTC (Figure 7.29) because only about half of the vertical source zone domain contains TCE-DNAPL. Therefore, most of the tracer mass by-passes the DNAPL, resulting in a more symmetrical BTC. Though fitting the saturation allows the analytical solution to produce a BTC that has a similar shape to the mid pool fraction fast-fast BTC, the fitted saturation is 9 times larger than the actual saturation.

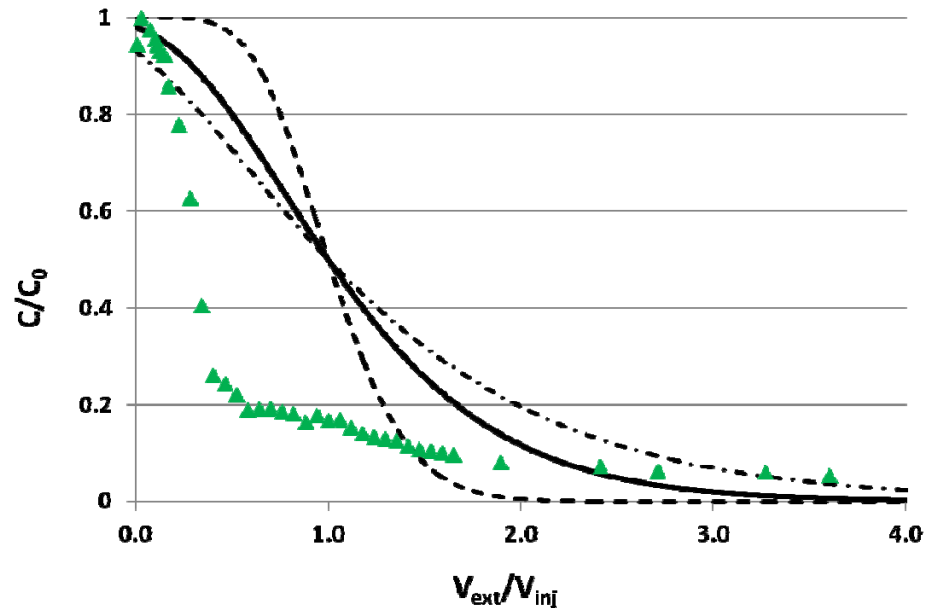


**Figure 7.30** Effect of increasing saturation on 2-octanol BTCs generated by the analytical solution. 2.0%, 10.0% and 20.0% saturations are shown in the dashed line, solid line and dot dashed line, respectively. Also included is the low pool fraction, fast-fast, 2-octanol data set (triangles).

Over estimation of NAPL saturations when using the analytical solution to interpret data from push-pull partitioning tracer tests has also been noted in other studies. Davis et al. (2002) found that the analytical solution resulted in average saturation estimations that were 3-4 times higher than the actual overall saturation, but did not offer an explanation of the overestimation. Istok et al. (2002) also found that applying the analytical solution to push-pull BTC resulted in an overestimation of average saturation, but did not report the magnitude of the overestimates. Istok et al. (2002) did, however, suggest that the overestimation is due to kinetic processes that are not accounted for in the analytical solution.

A closer examination of the analytical solution shows that estimates of saturation are very sensitive to the slope of the BTC. To demonstrate this sensitivity, the 1-pentanol and 1-hexanol BTCs from the high pool fraction, fast-slow test are shown below in Figure 7.31, as a representative data set. Note here that because the analytical solution was unable to capture the shape of the 2-octanol BTCs, the analysis the sensitivity of saturation estimates to the slope of the BTC focuses on 1-pentanol and 1-hexanol.

Three different fits are shown for each data set in Figure 7.31 (recall fits adjust the  $x_{\max}$  parameter in the analytical model): (i)  $x_{\max}$  fit to the entire BTC ( $0 \leq V_{\text{ext}}/V_{\text{inj}} \leq 3$ ); (ii)  $x_{\max}$  fit to the early portion of the BTC ( $0 \leq V_{\text{ext}}/V_{\text{inj}} \leq 1$ ); and (iii)  $x_{\max}$  fit to the late portion of the BTC ( $1 \leq V_{\text{ext}}/V_{\text{inj}} \leq 3$ ). Estimated saturations for these fits are shown in Table 7.14. Because the 1-pentanol BTC is slightly asymmetrical (Figure 7.31a) three different saturation estimates, 0.14, 0.29, and 0.02, are obtained when fitting using methods i, ii and iii, respectively.

**Table 7.14** Estimated average TCE-DNAPL saturation for the high pool fraction fast-slow test. Estimates are conducted by fitting the analytical solution to 3 sections of each 1-pentanol and 1-hexanol BTC.

	Estimates of Overall Saturation	
	1-pentanol BTC	1-hexanol BTC
Fitting from $0 \leq V_{\text{ext}}/V_{\text{inj}} \leq 3$	0.14	0.20
Fitting from $0 \leq V_{\text{ext}}/V_{\text{inj}} \leq 1$	0.29	0.28
Fitting from $1 \leq V_{\text{ext}}/V_{\text{inj}} \leq 3$	0.02	0.06

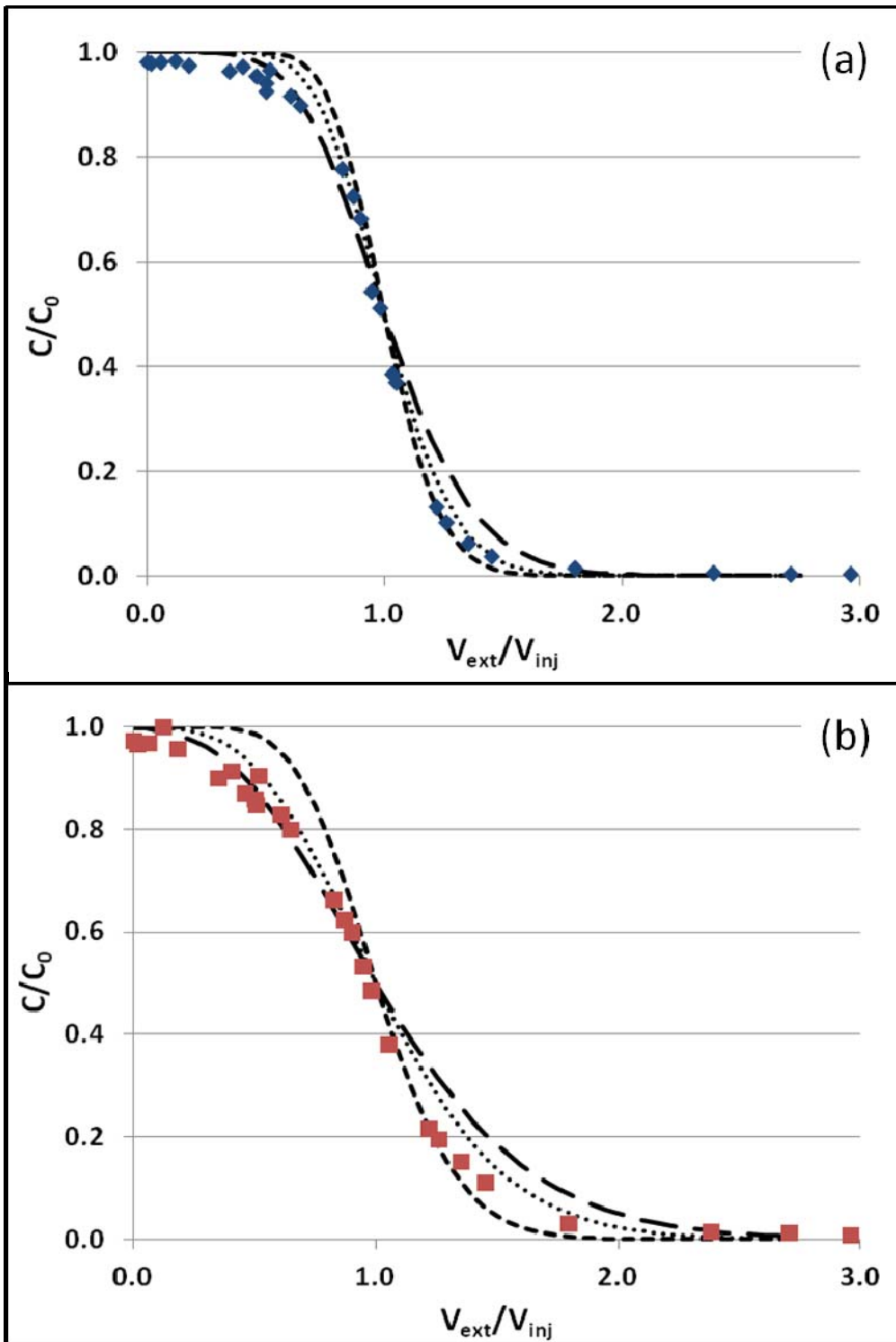


**Figure 7.31** 1-pentanol (panel a) and 1-hexanol (panel b) BTCs from the high pool fraction fast-slow test. Included in this figure are BTCs produced from the analytical solution when it is fit to the early portion of the BTC,  $0 \leq V_{\text{ext}}/V_{\text{inj}} \leq 1$ , (short dash) , late portion of the BTC,  $1 \leq V_{\text{ext}}/V_{\text{inj}} \leq 3$ , (long dash) and whole BTC,  $0 \leq V_{\text{ext}}/V_{\text{inj}} \leq 3$ , (dotted).

The actual overall saturation is 0.02. Visually, these three curves are quite similar, but only the fit to the later portion of the curve correctly estimates the overall saturation. Estimation using the early part of the BTC results in a saturation estimate that is 14.5 times greater than estimation using the later part of the BTC. The variability in saturation estimated using 1-pentanol is partially due to the relatively, weaker partitioning with TCE-DNAPL (partition coefficient is 4.2).

Because the analytical solution is incapable of describing the transport of 2-octanol, the tracer that offers the strongest partitioning, the influence of partition coefficient on the variability of the saturation estimates obtained from the analytical solution must be examined by comparing data and simulations for 1-hexanol to those of 1-pentanol. The influence of the partition coefficient can be observed in the form of greater separation between the three 1-hexanol fits (as compared to the separation between the three fits to the 1-pentanol data). Interestingly, the sensitivity of the model to the slope of the BTC is similar for 1-hexanol (partition coefficient of 17.4). Saturation estimates are 0.20, 0.28, and 0.06 using methods i, ii and iii, respectively (Table 7.14). Note that the 1-hexanol BTC has greater asymmetry than the 1-pentanol BTC, and that again, the fit to the later portion of the BTC provides a reasonable estimation of the overall saturation. Fits to the entire BTC and early portion of the BTC, however, result in very poor estimates of the overall saturation. The asymmetry and sensitivity of the model to the slope of the BTC seem to result in large over estimations of the average overall saturation. Asymmetry in the BTCs obtained in the experiments

described herein likely results from non-equilibrium mass transfer and non-uniform DNAPL saturation. These are explored further using a linear driving force expression within a numerical model (see Section 7.7.4 and Chapter 8).

### *7.7.3 – Comparison of Method of Moments and Analytical Solution for Interpretation of Push-pull Partitioning Tracer Tests*

In Section 7.7.1, the method of moments (Jin et al., 1995) was applied to each BTC to produce saturation estimates that underestimate the actual saturations. The contrast produced when comparing the saturations estimated via the moment analyses (underestimation) with those produced when using the analytical solution (overestimation) is particularly curious. Underestimation of saturations using the method of moments is commonly seen when PITTs are conducted in heterogeneous source zones (e.g. Annable et al., 1998a; Brooks et al., 2002; Hartog et al., 2010) and has also been seen when using the push-pull flow scheme (Davis et al., 2002). This underestimation is attributed to flow bypassing of high saturation areas.

Jin et al. (1995) describe the development of the method of moments. This method is derived from calculations of mean residence time of tracers flowing through a packed bed. A retardation coefficient can be calculated from the first moments of the partitioning and non-partitioning tracer BTCs. An average overall saturation is then calculated using Equation 7.4. Here, the simplifying assumptions are linear, equilibrium partitioning of the tracers between the aqueous and NAPL phases. Unlike the analytical solution, the assumption of

a uniform NAPL distribution is not implicit in the method of moments, though the technique is only capable of estimating an overall saturation. Additionally, the method of moments is less sensitive than the analytical solution to the slope of the BTCs. For example, the bromide curves with the steepest slope ( $\alpha = 0.2$  cm, high PF, fast-fast test) and the flattest slope ( $\alpha = 1.1$  cm, low PF, fast-slow test) are displayed in Figure 7.32. Note that the low PF fast-slow test has an alpha value that is 5.5 times that of the high PF, fast-fast test. However, the ratio of first moments for these bromide BTCs is approximately 1.1 (moments are 0.54 and 0.51 for the low PF fast-slow test and high PF, fast-fast test, respectively). This result should be expected because it is the second moment that considers the influence of dispersion, with a direct relationship readily attainable when the BTC is characteristic of normally distributed exit ages (Weber and DiGiano, 1996). Essentially the fact that the method of moments relies upon ratios of mean residence times, and not ratios of apparent dispersion, produces the superior performance in comparison to the analytical solution. Moreover, it is hypothesized that the reliance of the analytical solution on a uniform distribution of DNAPL saturation is a critical reason the analytical solution performs so poorly in comparison to the method of moments for these experiments. Non-uniformities in the DNAPL distribution serve to increase the asymmetry of the partitioning tracer breakthrough curve (see chapter 8), and thus, only exacerbate the inaccuracy of the estimating overall saturation based upon apparent dispersion. The method of moments, while superior to the analytical solution, still offers a poor prediction of DNAPL saturation for the experiments described

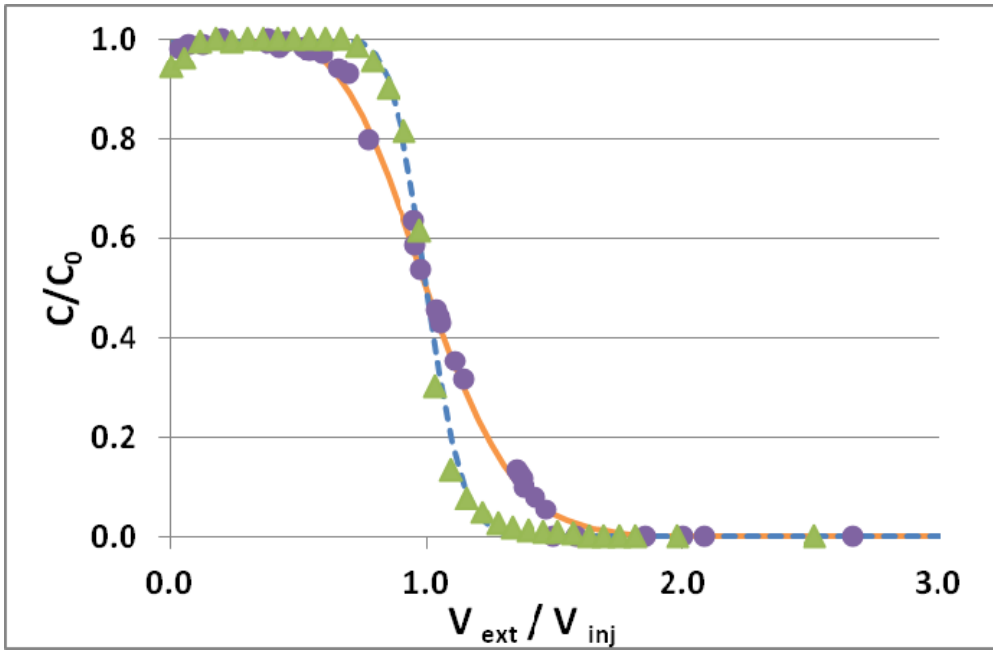


**Figure 7.32** Bromide BTCs for the low pool fraction, fast-slow test (circles) and the high pool fraction, fast-fast test (triangles). Also shown are the fits of the analytical solution to each BTC.

herein. The poor performance of the method of moments is thought to relate to the assumption of equilibrium partitioning, when mass transfer is kinetic in these experiments. Most field tests will be conducted using velocities similar to those employed here because it is impractical to use slow flow if multiple, small scale tests are to be conducted as part of a source zone characterization protocol. Therefore, it is recommended that the analytical model be avoided, and any use of the method of moments recognize that DNAPL saturation may be underestimated.

#### *7.7.4 - Linear Driving Force Model*

The numerical linear driving force model employed to examine the pooled box source zone in Chapter 6 was used to examine the push-pull BTCs generated in herein. To model these experiments, the model was modified to account for the push-pull flow field. Based upon the results of Chapter 6, the Nambi and Powers (2003) correlation was employed to estimate partitioning tracer mass transfer coefficients. For all nine push-pull tests, the model domain was constructed from light transmission results that measured the exact packing structure and TCE-DNAPL distribution. Dispersivity was fit (Table 7.15) to each bromide data set using a nonlinear least-squares curve fitting technique, the *lsqcurvefit* function, in Matlab 2010. Alcohol tracer BTCs were predicted based on these fitted dispersivity values and the measured partition coefficients (Chapter 4).

Linear driving force model predictions are shown in Figures 7.33 – 7.41 for all nine tracer tests on both linear and log scales. The sum of squared error of the model predictions are shown for each test in Table 7.16. Unlike the analytical

solution, the linear driving force model is able to predict the excess spreading of the 1-hexanol BTCs (Figures 7.33 – 7.41). Additionally, the simulations capture the nonsymmetrical shape of each 2-octanol BTC, including the mid pool fraction, fast-fast 2-octanol BTC (Figure 7.36), which has a different shape than all the other 2-octanol BTCs. The model is not only able to predict the general shape of the 2-octanol BTC; in most cases, simulations accurately capture the subtle inflection points seen in the data (most easily seen in Figures 7.36, 7.39, 7.41).

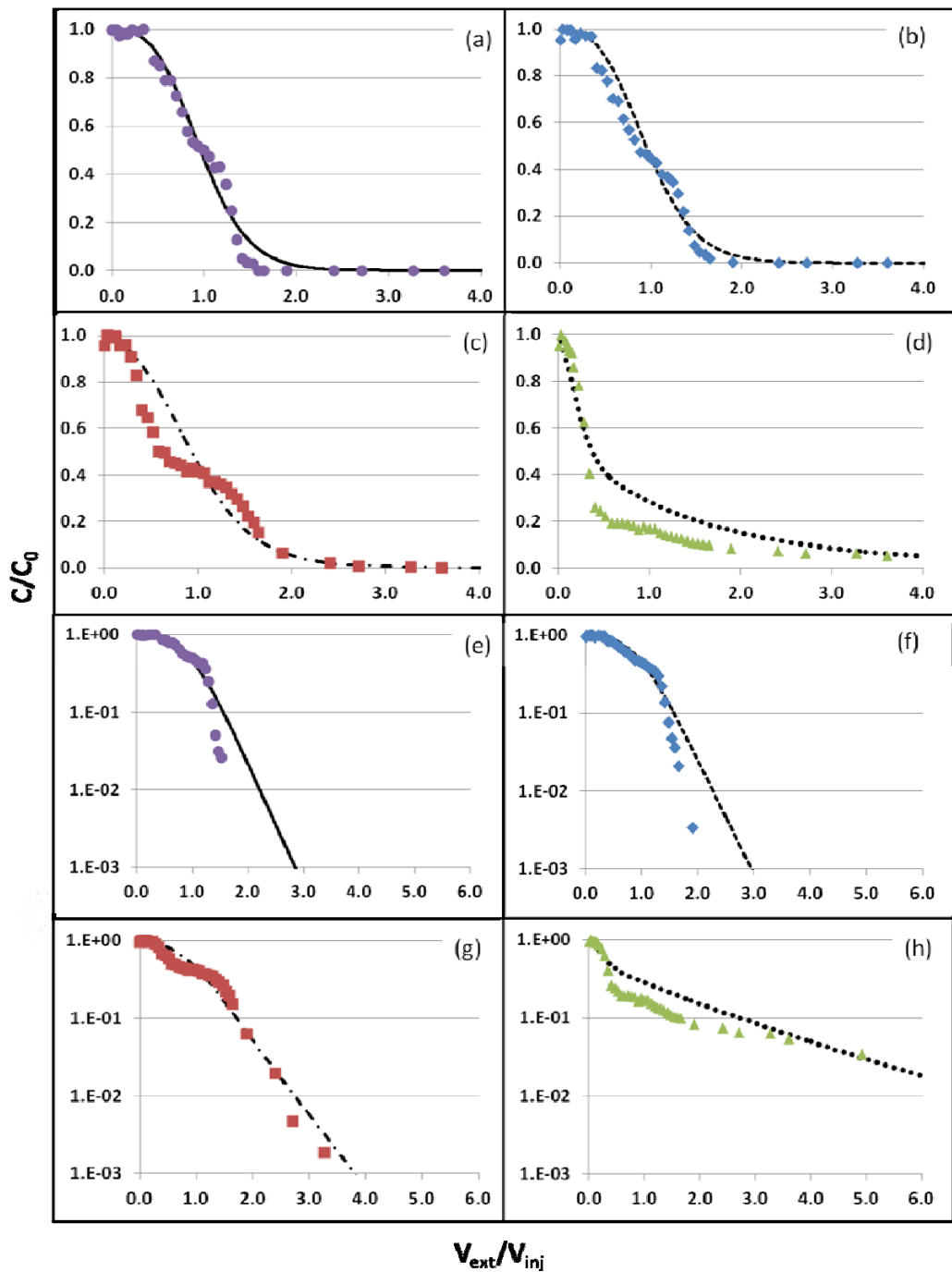


**Figure 7.33** Comparison of linear driving force push-pull simulations to experimental data for the fast-fast test in the low pool fraction box for bromide (a and e), 1-pentanol (b and f), 1-hexanol (c and g) and 2-octanol (d and h). Bromide simulation is fit to the data to obtain dispersivity, all partitioning simulations are predictive. Note the use of the extended x-axis and log-scale y-axis in panels e-h.

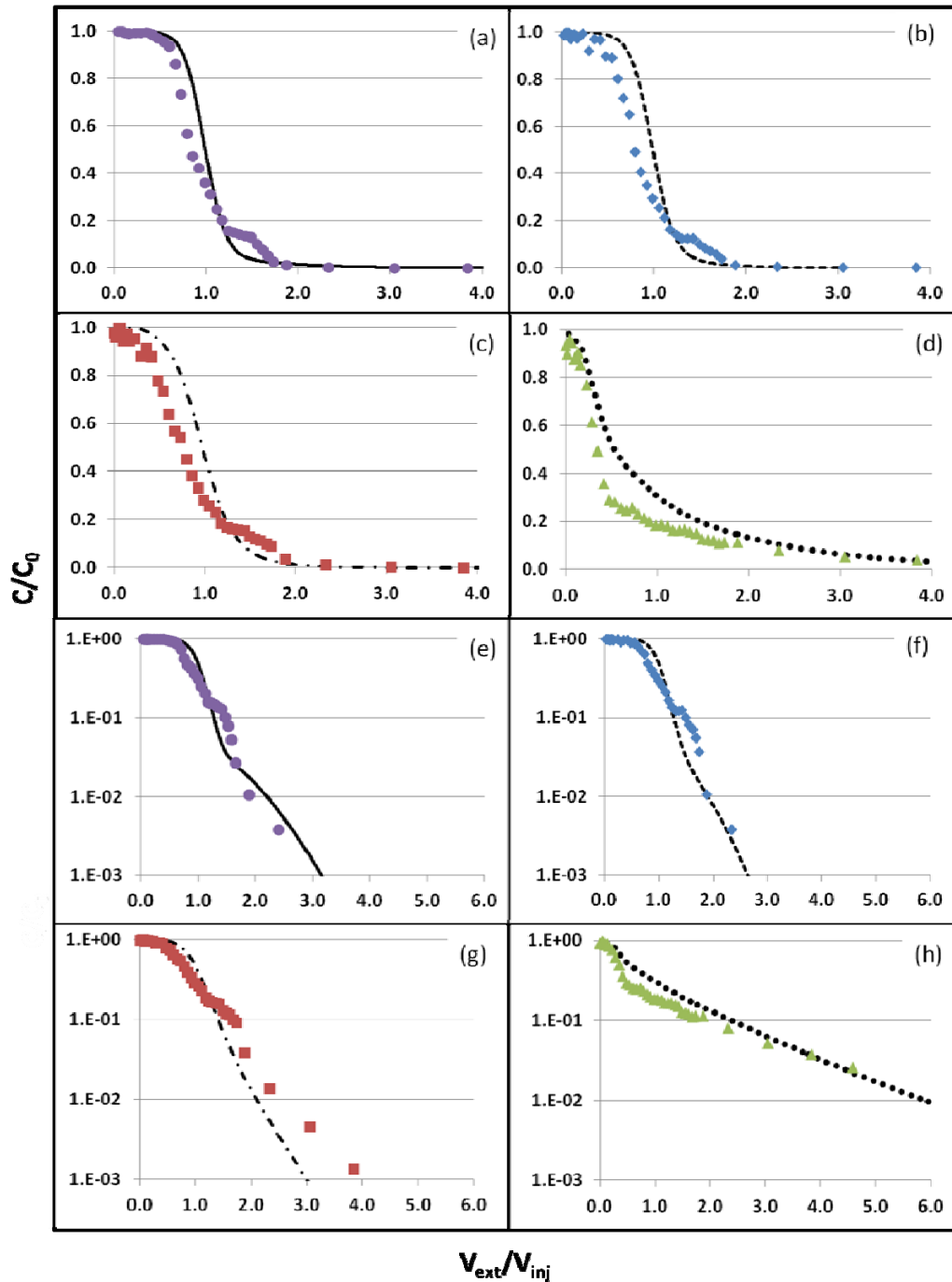


**Figure 7.34** Comparison of linear driving force push-pull simulations to experimental data for the slow-fast test in the low pool fraction box for bromide (a and e), 1-pentanol (b and f), 1-hexanol (c and g) and 2-octanol (d and h). Bromide simulation is fit to the data to obtain dispersivity, all partitioning simulations are predictive. Note the use of the extended x-axis and log-scale y-axis in panels e-h.

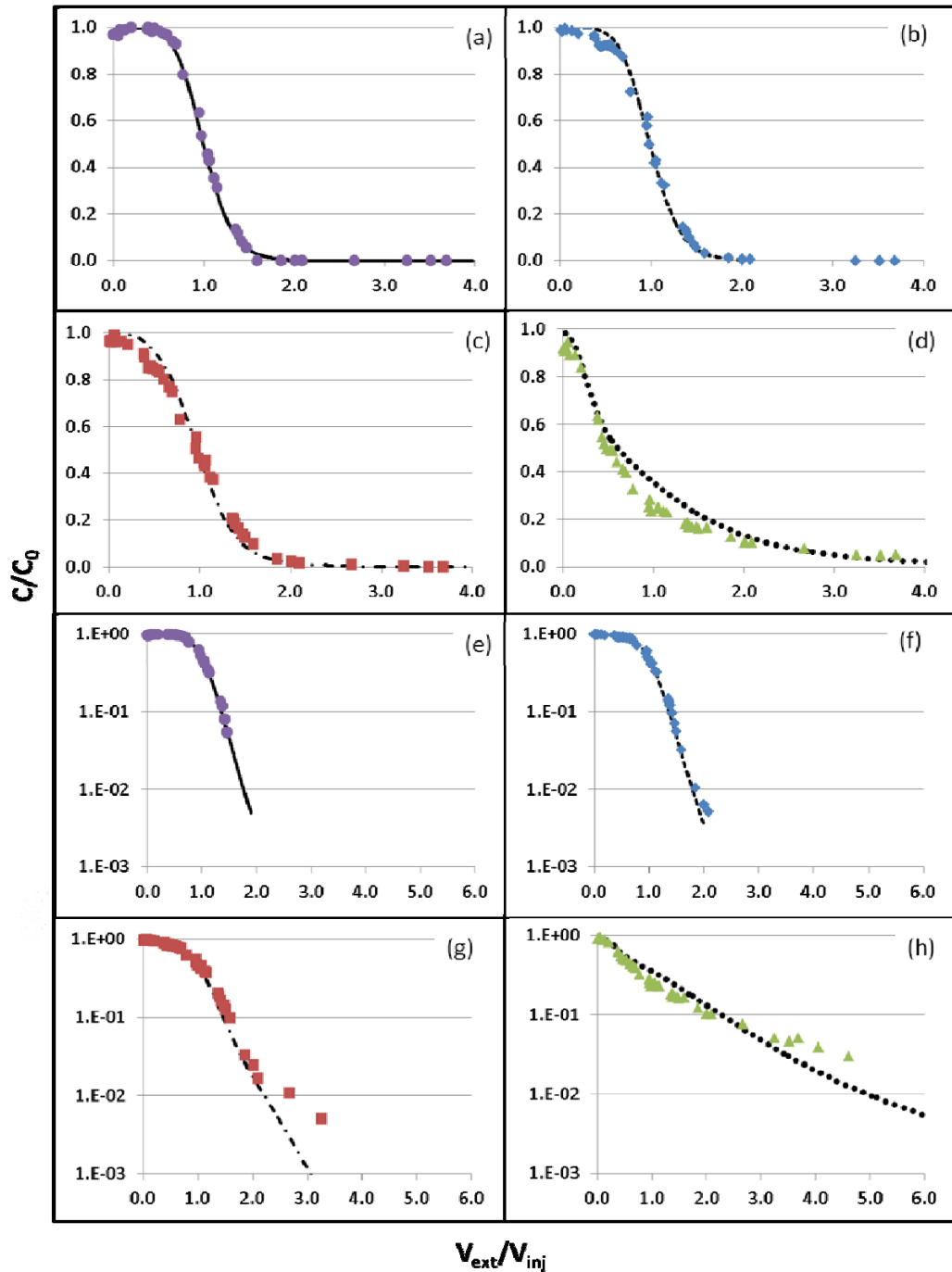


**Figure 7.35** Comparison of linear driving force push-pull simulations to experimental data for the fast-slow test in the low pool fraction box for bromide (a and e), 1-pentanol (b and f), 1-hexanol (c and g) and 2-octanol (d and h). Bromide simulation is fit to the data to obtain dispersivity, all partitioning simulations are predictive. Note the use of the extended x-axis and log-scale y-axis in panels e-h.

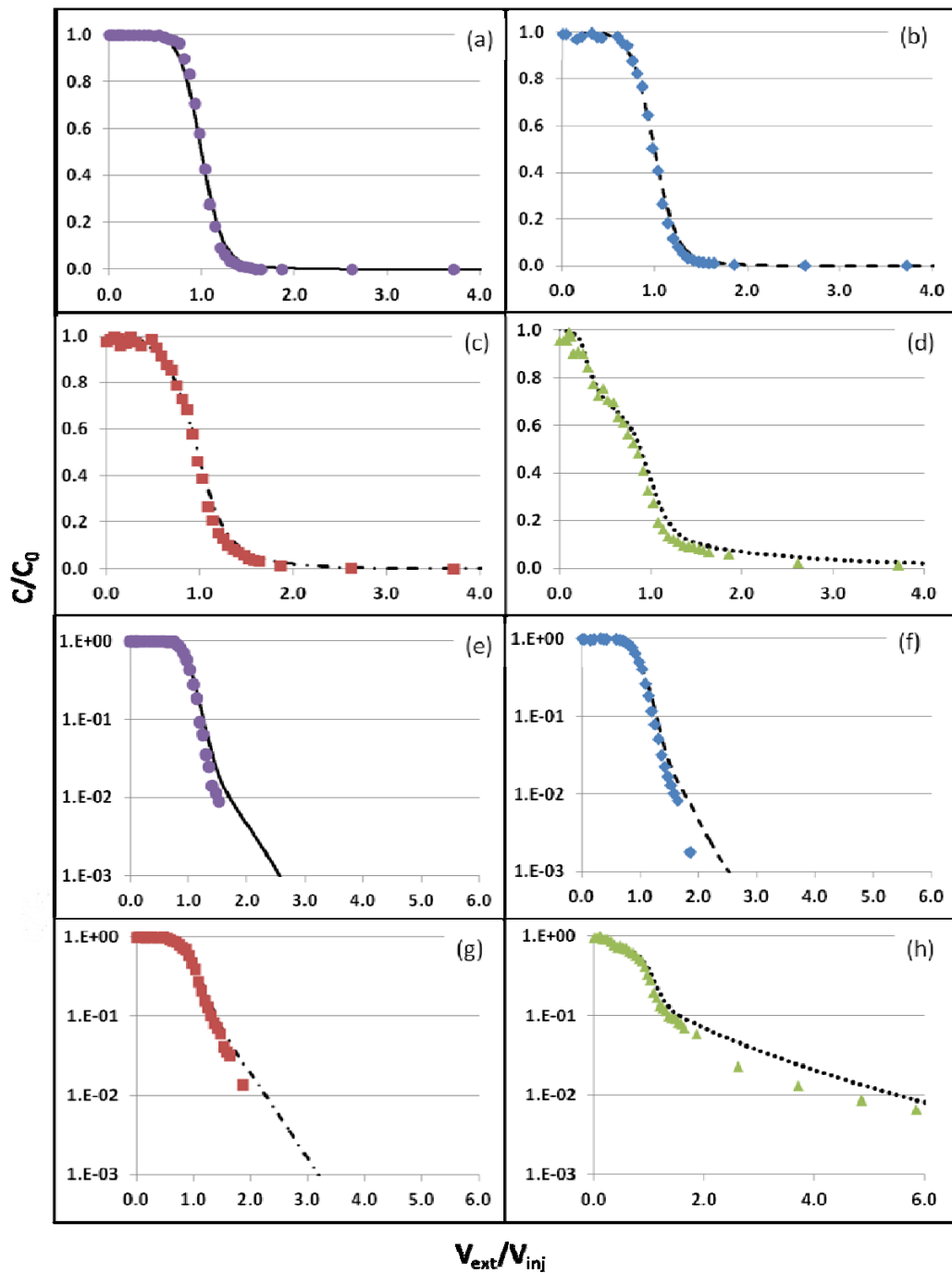


**Figure 7.36** Comparison of linear driving force push-pull simulations to experimental data for the fast-fast test in the mid pool fraction box for bromide (a and e), 1-pentanol (b and f), 1-hexanol (c and g) and 2-octanol (d and h). Bromide simulation is fit to the data to obtain dispersivity, all partitioning simulations are predictive. Note the use of the extended x-axis and log-scale y-axis in panels e-h.

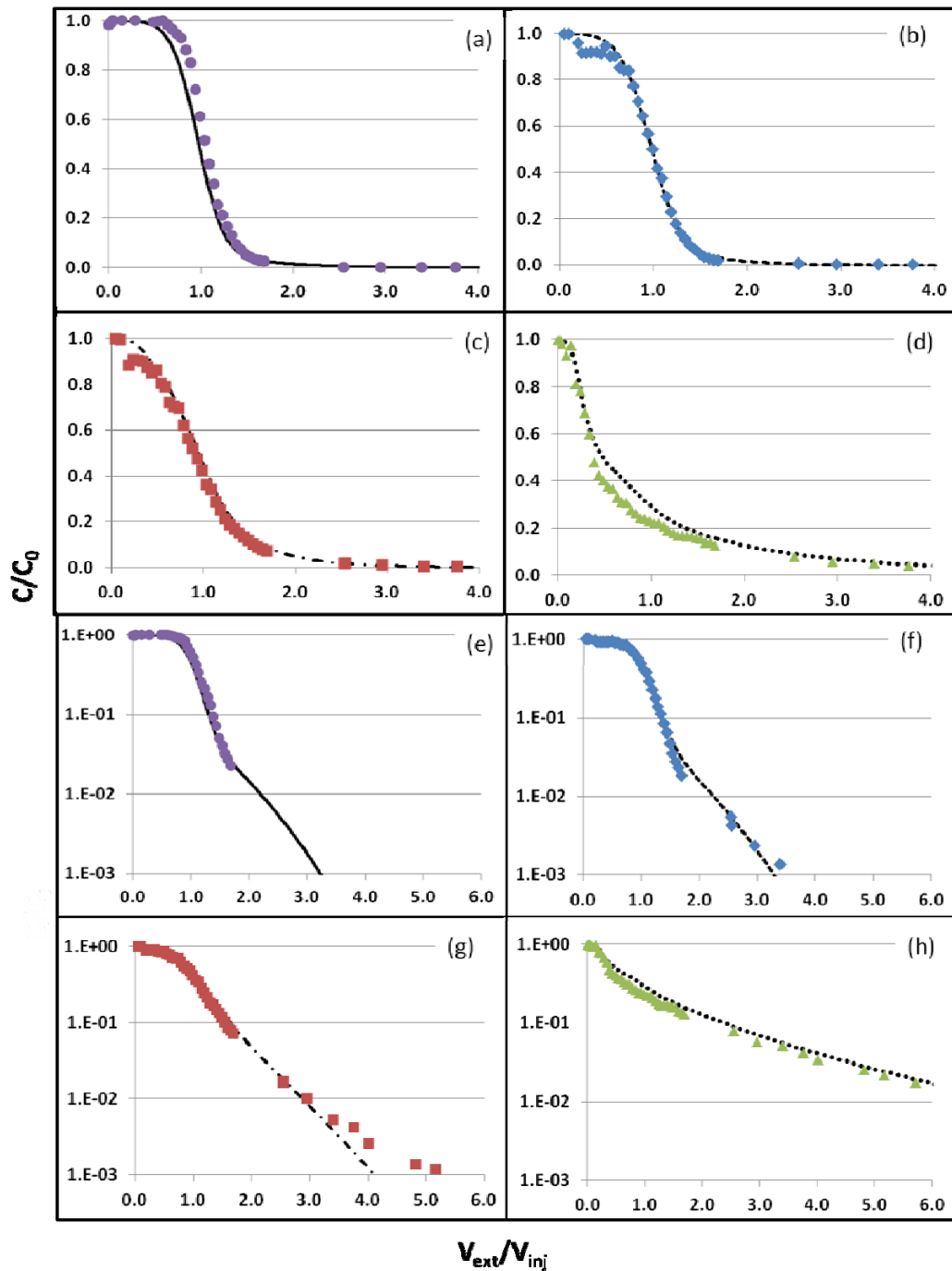


**Figure 7.37** Comparison of linear driving force push-pull simulations to experimental data for the slow-fast test in the mid pool fraction box for bromide (a and e), 1-pentanol (b and f), 1-hexanol (c and g) and 2-octanol (d and h). Bromide simulation is fit to the data to obtain dispersivity, all partitioning simulations are predictive. Note the use of the extended x-axis and log-scale y-axis in panels e-h.

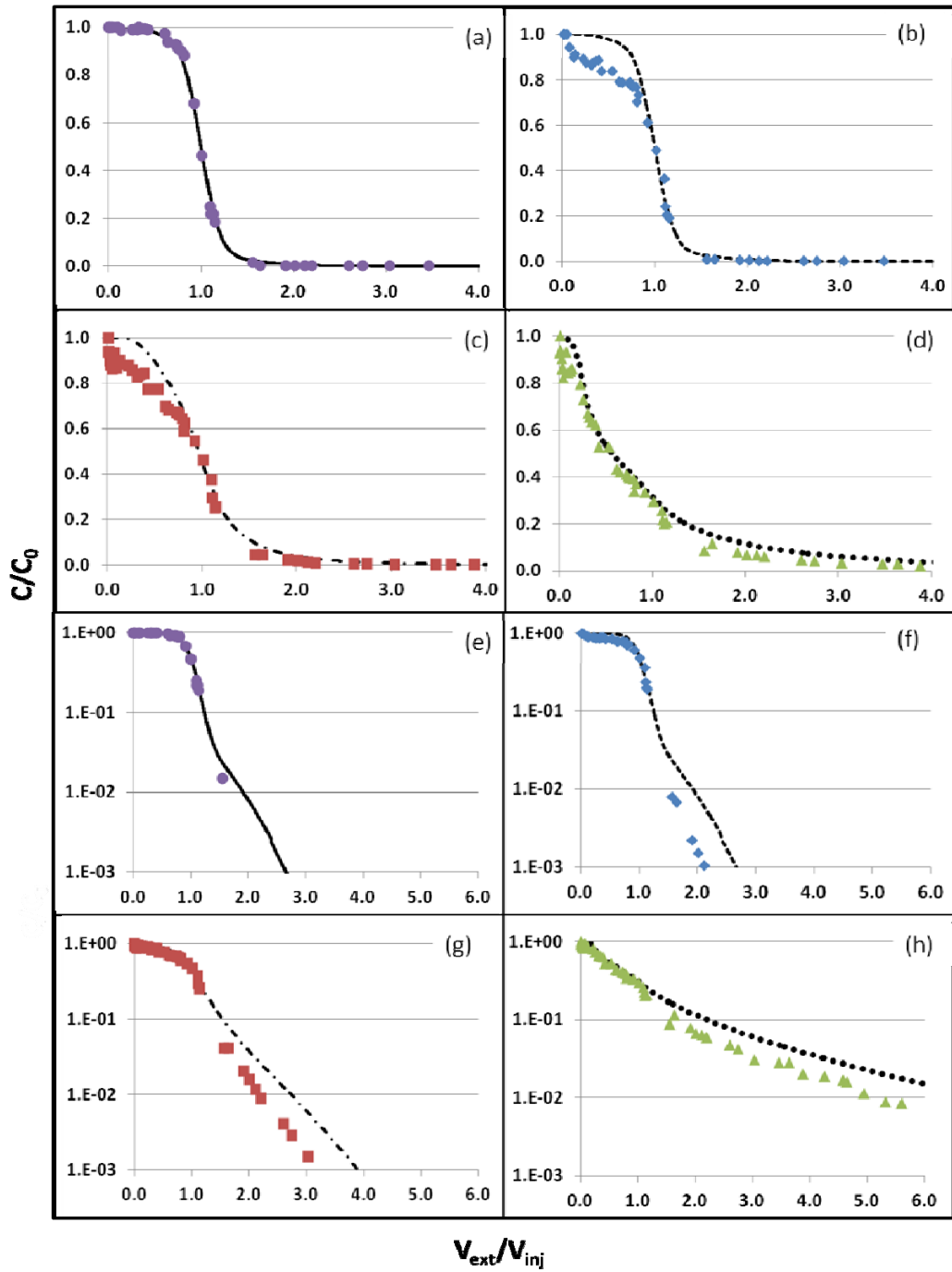


**Figure 7.38** Comparison of linear driving force push-pull simulations to experimental data for the fast-slow test in the mid pool fraction box for bromide (a and e), 1-pentanol (b and f), 1-hexanol (c and g) and 2-octanol (d and h). Bromide simulation is fit to the data to obtain dispersivity, all partitioning simulations are predictive. Note the use of the extended x-axis and log-scale y-axis in panels e-h.

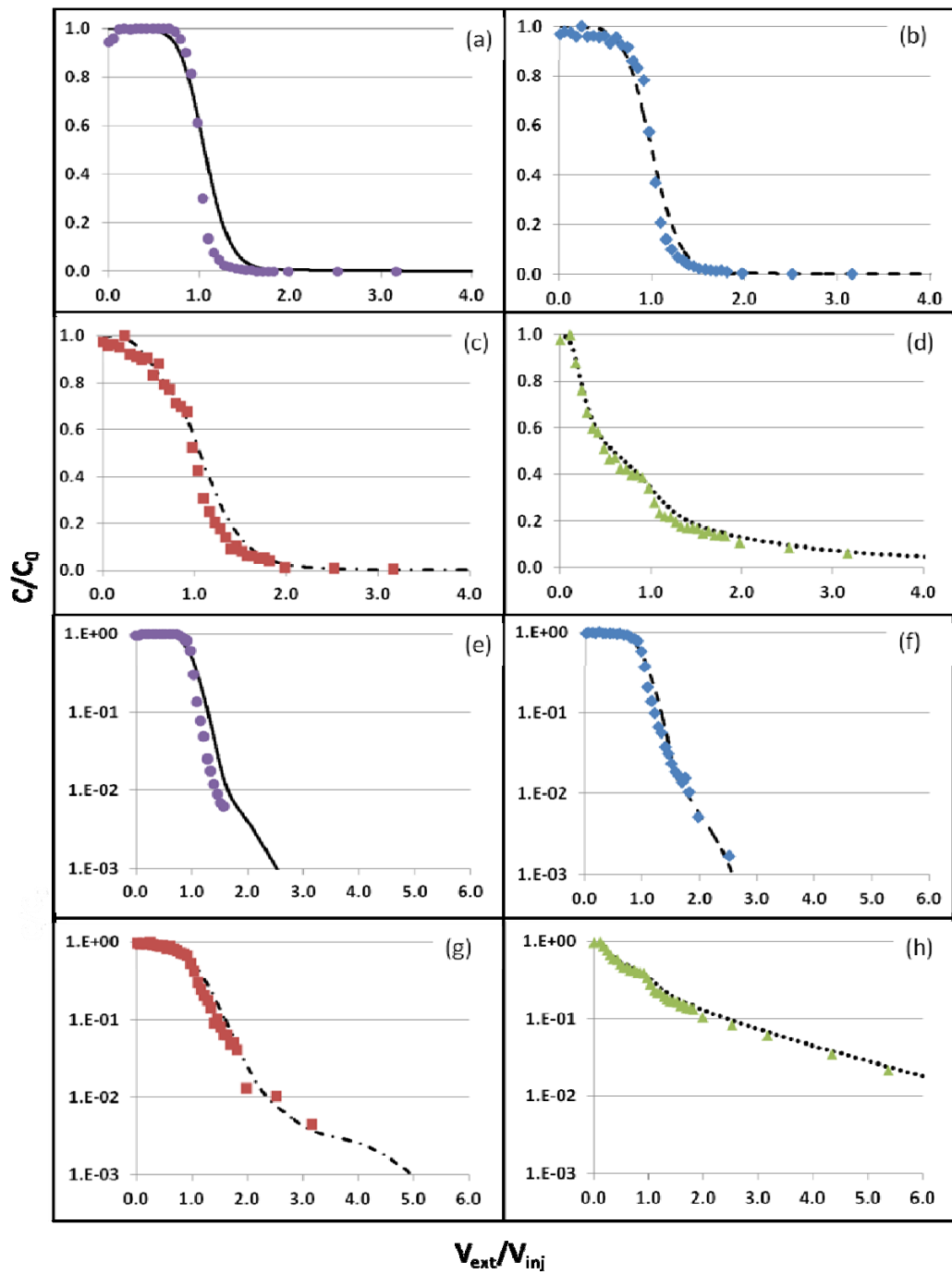


**Figure 7.39** Comparison of linear driving force push-pull simulations to experimental data for the fast-fast test in the high pool fraction box for bromide (a and e), 1-pentanol (b and f), 1-hexanol (c and g) and 2-octanol (d and h). Bromide simulation is fit to the data to obtain dispersivity, all partitioning simulations are predictive. Note the use of the extended x-axis and log-scale y-axis in panels e-h.

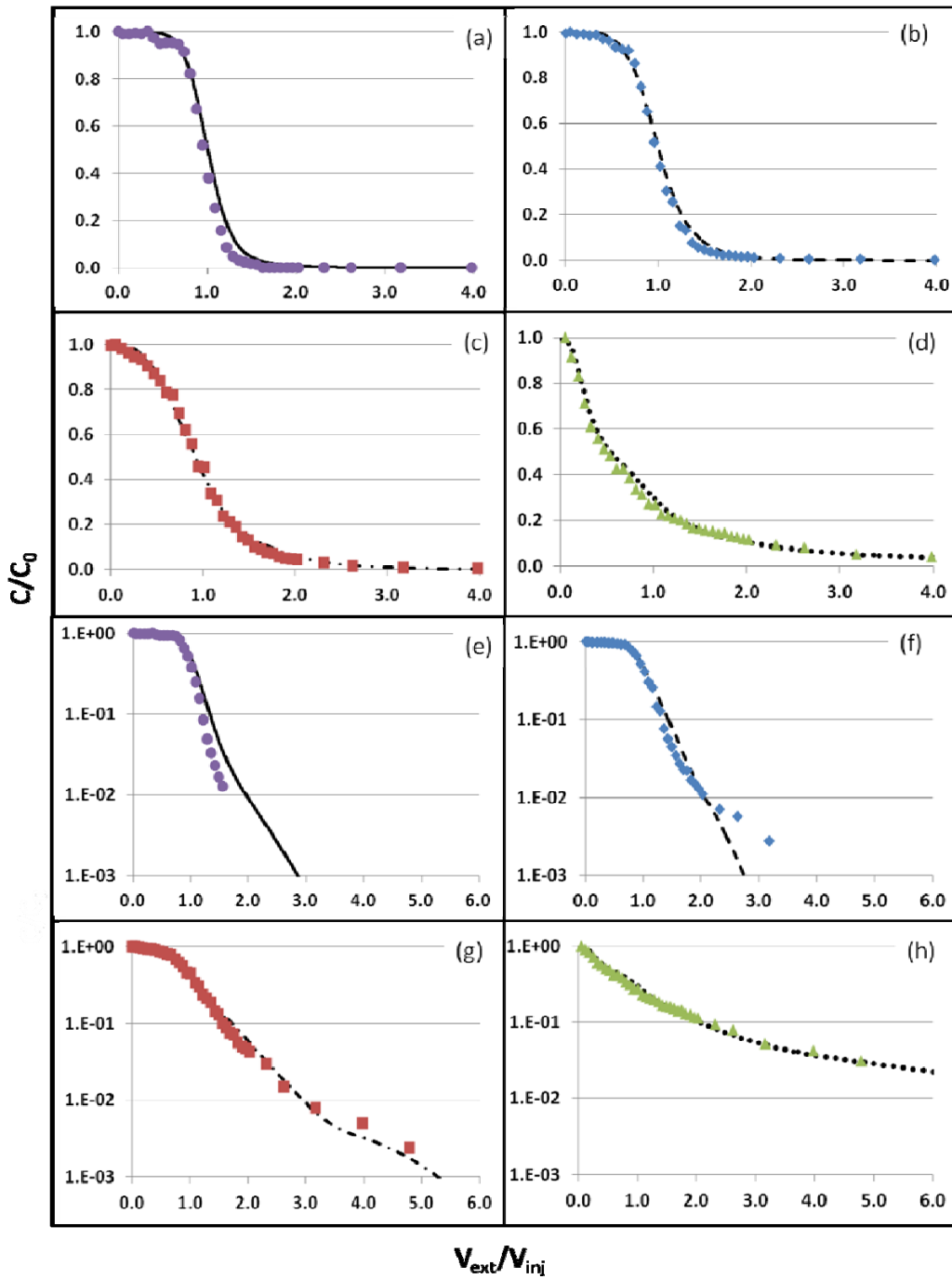


**Figure 7.40** Comparison of linear driving force push-pull simulations to experimental data for the slow-fast test in the high pool fraction box for bromide (a and e), 1-pentanol (b and f), 1-hexanol (c and g) and 2-octanol (d and h). Bromide simulation is fit to the data to obtain dispersivity, all partitioning simulations are predictive. Note the use of the extended x-axis and log-scale y-axis in panels e-h.

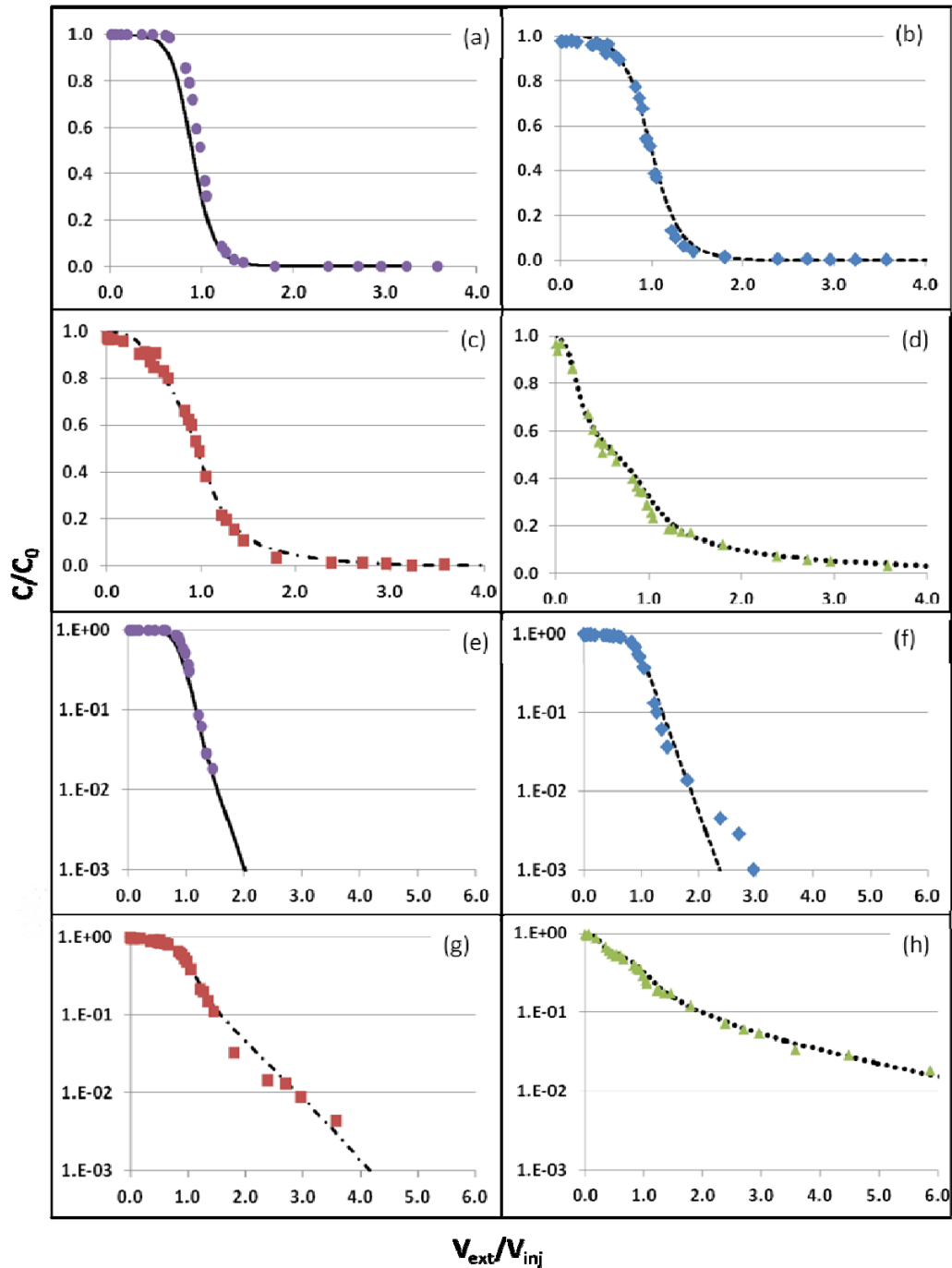


**Figure 7.41** Comparison of linear driving force push-pull simulations to experimental data for the fast-slow test in the high pool fraction box for bromide (a and e), 1-pentanol (b and f), 1-hexanol (c and g) and 2-octanol (d and h). Bromide simulation is fit to the data to obtain dispersivity, all partitioning simulations are predictive. Note the use of the extended x-axis and log-scale y-axis in panels e-h.

**Table 7.15** Fitted dispersivities and squared residual from the least squares fitting of all nine push-pull bromide data sets.

<b>Box</b>	<b>Test</b>	<b>Fitted Dispersivity (cm)</b>	<b>Squared Residual</b>
Low PF	Fast-Fast	3.20	0.086
	Slow-Fast	0.10	0.008
	Fast-Slow	0.73	0.031
Mid PF	Fast-Fast	0.10	0.027
	Slow-Fast	0.83	0.002
	Fast-Slow	0.10	0.021
High PF	Fast-Fast	0.21	0.049
	Slow-Fast	0.16	0.006
	Fast-Slow	0.12	0.027

**Table 7.16** Sum of squared error between laboratory BTCs and 2-D linear driving force model predictions for each partitioning tracer in all nine push-pull tests.

	Low Pool Fraction			Mid Pool Fraction			High Pool Fraction		
	Fast-Fast	Slow-Fast	Fast-Slow	Fast-Fast	Slow-Fast	Fast-Slow	Fast-Fast	Slow-Fast	Fast-Slow
<b>1-pentanol</b>	0.35	0.59	0.56	0.03	0.04	0.23	0.10	0.02	0.01
<b>1-hexanol</b>	0.50	0.60	0.48	0.03	0.07	0.19	0.13	0.01	0.02
<b>2-octanol</b>	0.73	0.50	0.28	0.16	0.12	0.28	0.03	0.02	0.02

The linear driving force model has the most difficulty predicting the low pool fraction fast-fast and the slow-fast tests (Table 7.16 and Figures 7.33 – 7.34). As discussed previously, these two tests have a slightly different flow fields resulting in a bromide BTCs that are not smooth like the other bromide curves, but have inflection points around  $V_{\text{ext}}/V_{\text{inj}} = 1$ . This inflection point is then accentuated in each of the partitioning tracer BTCs. Since the bromide curves in these two tests are not adequately captured, it is unsurprising that predictions of the corresponding partitioning tracer data have more error than the other tests. One possibility here is that the use of a confined flow model does not allow for any changes in flow field that may have produced the inflection in the bromide signal. The model is, however, able to capture the overall shape of each BTC.

The numerical modeling results show that the linear driving force model, employing the Nambi and Powers (2003) correlation, outperforms analytical solution. It is of interest to determine which of the simplifying assumptions in the analytical solution causes its poor performance relative to the linear driving force model. Again, these assumptions include: uniform packing distribution, uniform DNAPL distribution, equilibrium partitioning, and no permeability reduction due to the presence of the DNAPL. The influence of each assumption was examined individually, and in all combinations to determine which assumption(s) causes the poor performance of the analytical solution. The packing distribution can be changed from the exact distribution determined by light transmission analysis to a simple uniform distribution comprising the background 40-50 mesh sand. Similarly, the complex TCE-DNAPL architecture can be replaced with a

uniformly saturated domain having the same total mass as that measured in the heterogeneous saturation distribution. The model can be run with assuming equilibrium interactions between the partitioning tracers and the DNAPL, instead of the linear driving force kinetics employed above. Lastly the reduction in relative permeability calculated the correlation developed by Kaluarachichi and Parker (1992) can be replaced with  $k_{rw} = 1$ .

The parameters corresponding to two tests, the high pool fraction, fast-fast test and the mid pool fraction fast-fast test used for each simulation. The analysis was conducted for 2-octanol because the strong partitioning of 2-octanol can best illustrate the influence of each assumption. The high pool fraction fast-fast parameters were chosen because this test resulted in a 2-octanol BTC most like the other push-pull tests. Contrastingly, the mid pool fraction fast-fast test resulted in a 2-octanol BTC least like the other 2-octanol BTCs.

Results of this analysis, with the 2-octanol data included for reference, are shown in Figure 7.42 and 7.43. Simulations examining the effects of relative permeability reductions are not included in either because this parameter has no visual influence on results. Additionally, including the actual permeability distribution (as opposed to a uniform distribution) does not appreciably change the BTC; therefore, only one BTC produced using a uniform permeability distribution is shown.

The analytical solution (using the actual average saturation) is included in Figures 7.42 and 7.43 so that deviations from the analytical model can be easily seen. It is important to note here that the analytical solution is 1-D while the

numerical model is 2-D. For each test, a 2-D simulation that included the principal simplifying assumptions inherent in the analytical model (uniform permeability, uniform DNAPL distribution, equilibrium partitioning) was conducted. The results are very close to the analytical solution (Figures 7.42 and 7.43). The slight deviations between this 2-D simulation and the analytical solution are most likely due to the inclusion of vertical dispersivity in the 2-D model. Since the 2-D simulation that includes each simplifying assumption is almost identical to the analytical solution, the differences seen when simplifying assumptions are removed can be attributed to the assumptions themselves, and not to differences in dimensionality of the model.

As mentioned previously, including the actual permeability distribution has little effect on the BTC, as this can be seen by comparing the two BTCs generated using a uniform saturation distribution and equilibrium partitioning (Figures 7.42 and 7.43). Caution should be employed, however, when extrapolating this result to field sites where the geometry is likely to be more heterogeneous and more influential than in these aquifer cells. Interestingly, the simulation that includes the actual saturation distribution, but assumes equilibrium partitioning produces a BTC that can capture the general shape and asymmetric nature characteristic of both 2-octanol curves. In contrast, the simulation that includes kinetic partitioning, but assumes a uniform DNAPL distribution is able to capture the general shape of the high pool fraction fast-fast BTC, but not the BTC from the mid pool fraction fast-fast test. These results suggest that these BTCs are strongly linked to source zone DNAPL distribution. The source zone

corresponding to the high pool fraction fast-fast test (Figure 7.16 I) has much more spreading of TCE-DNAPL in the source zone than that of the mid pool fraction fast-fast test (Figure 7.9 III). The uniform saturation distribution also has a lot of spreading, which may explain the better performance of the uniform saturation assumption in describing the high pool 2-octanol data. The best results occur when both the actual saturation distribution and kinetic transport are included in the model. As discussed above, this allows the model to capture even the slight perturbations seen in the data.

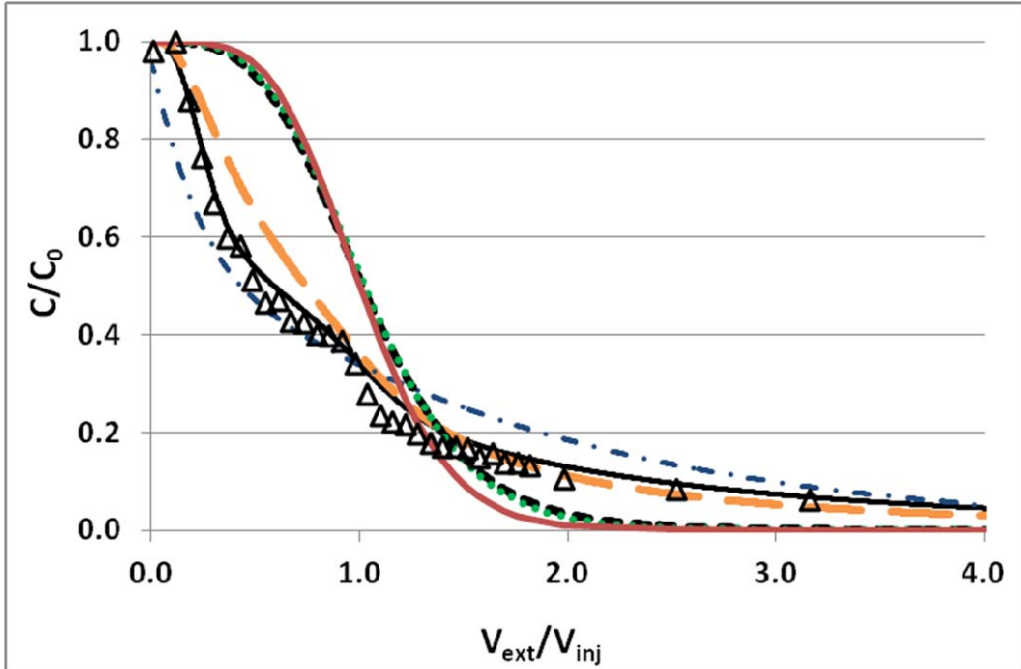


**Figure 7.42** Influence of simplifying assumptions inherent in the push-pull analytical solution. 2-octanol data from the high pool fraction fast-fast test are shown in open triangles as a representative data set. The analytical solution is shown as a solid red line. Five numerical simulation results are shown: uniform permeability, uniform saturation, equilibrium (dotted, green); actual permeability, uniform saturation, equilibrium (short-dash, black); actual permeability, uniform saturation, kinetic (dot-dash, blue); actual permeability, actual saturation, equilibrium (long-dash, orange); actual permeability, actual saturation, kinetic (solid, black).

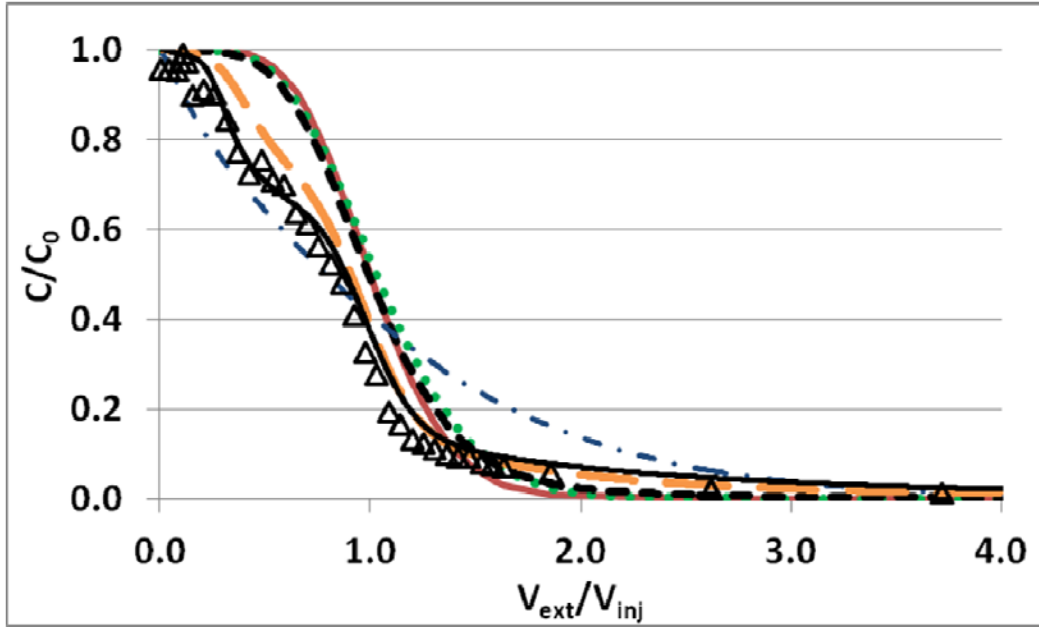


**Figure 7.43** Influence of simplifying assumptions inherent in the push-pull analytical solution. 2-octanol data from the mid pool fraction fast-fast test are shown in open triangles as a representative data set. The analytical solution is shown as a solid red line. Five numerical simulation results are shown: uniform permeability, uniform saturation, equilibrium (dotted, green); actual permeability, uniform saturation, equilibrium (short-dash, black); actual permeability, uniform saturation, kinetic (dot-dash, blue); actual permeability, actual saturation, equilibrium (long-dash, orange); actual permeability, actual saturation, kinetic (solid, black).

## 7.8 – *Conclusions*

Focus in this chapter is placed on quantifying tracer transport in source zones of heterogeneous saturation distribution. Push-pull tests were conducted in three source zones of low, mid and high pool fraction. Three combinations of fast and slow flow rates were employed to determine if the difference in transport time scales between ganglia and pools can be manipulated to differentiate pool dominated source zones from ganglia dominated source zones. Results indicate that all three flow rate combinations (fast injection, fast extraction; slow injection, fast extraction; fast injection, slow extraction) provide similar BTCs. As slow flow rates are costly (in both time and money) to run in the field, it is beneficial that the fast push, fast pull test provides the same results as the other two flow rate combinations.

Results also showed that the push-pull tracer tests do not appear to be sensitive to pool fraction. However, the resulting BTCs are influenced by source architecture. This is most easily seen in the 2-octanol signal from the mid pool fraction fast-fast test, which is quite different from the other 2-octanol BTCs. The source zone corresponding to the mid pool fraction fast-fast test is also the most visually different source zone.

Two techniques commonly employed to estimate overall saturation from partitioning tracer tests (method of temporal moments and the analytical solution to the transport equation) were shown to have large errors in saturation estimation. The method of temporal moments underestimates total source zone volume by 9 – 88%. This is similar to what has been seen when temporal

moments is employed in other heterogeneous source zones (e.g. Annable et al., 1998a; Brooks et al., 2002; Hartog et al., 2010) and is attributed to flow bypassing of high saturation zones. On the other hand, to capture the excess spreading seen in the 1-hexanol signals, the analytical model estimates overall saturations that 10-40 times larger than the actual saturation. Additionally, the analytical solution is completely unable to capture the early breakthrough and asymmetrical shapes characteristic of all 2-octanol BTCs.

BTCs resulting from the nine push-pull tests were used to show that a 2-D numerical linear driving force model employing the Nambi and Powers (2003) mass transfer correlation, developed from NAPL pool dissolution studies, is able to accurately reproduce partitioning tracer BTCs in these systems. This model was used to show that the assumptions of equilibrium partitioning and uniform saturation distribution are the two assumptions that prevent the analytical solution from being able to capture the behavior of the higher partitioning tracers. Here it was shown that a model assuming equilibrium partitioning, but including the precise distribution of TCE-DNAPL was able to produce good predictions of 2-octanol BTCs, again highlighting the relationship between push-pull BTCs and source zone architecture. In the following chapter, focus is placed on identifying the specific aspects of source zone architecture to which these BTCs are most sensitive.

## **CHAPTER 8 – 2-D MODELING ASSESSMENT OF PUSH-PULL CAPABILITIES**

### **8.1 - Introduction**

Results presented in Chapter 7 suggest that push-pull partitioning tracer test BTCs are not particularly sensitive to pool fraction. These tests, however, may be able to determine source zone characteristics in addition to overall saturation. Therefore, Chapter 8 focuses on employing the numerical model used to make accurate predictions of the experiments in Chapter 7 to determine what information may be obtained from localized push pull partitioning tracer tests.

### **8.2 - Simulation Design**

Forty simple source zones (Figure 8.1) were created to produce domains with TCE-DNAPL source zones that vary in vertical and horizontal distribution, distance of DNAPL to the injection/extraction well, total DNAPL mass, and local TCE-DNAPL saturation. The model domain for the source zone is the same as the aquifer cells used in Chapter 7 (44 cm x 100 cm). A dispersivity of 0.5 cm was selected for use in all simulations as this value is representative of the dispersivities fit to conservative tracer data in Chapter 7. The permeability distribution was comprised of 40-50 mesh sand. The source zones were artificially generated (as opposed to simulating the DNAPL spill) so that comparisons between very specific source zone features can be made. Also shown in Figure 8.1 are realization numbers (1 through 40) and the saturation values of all grid cells that contain TCE-DNAPL. In each realization (except for

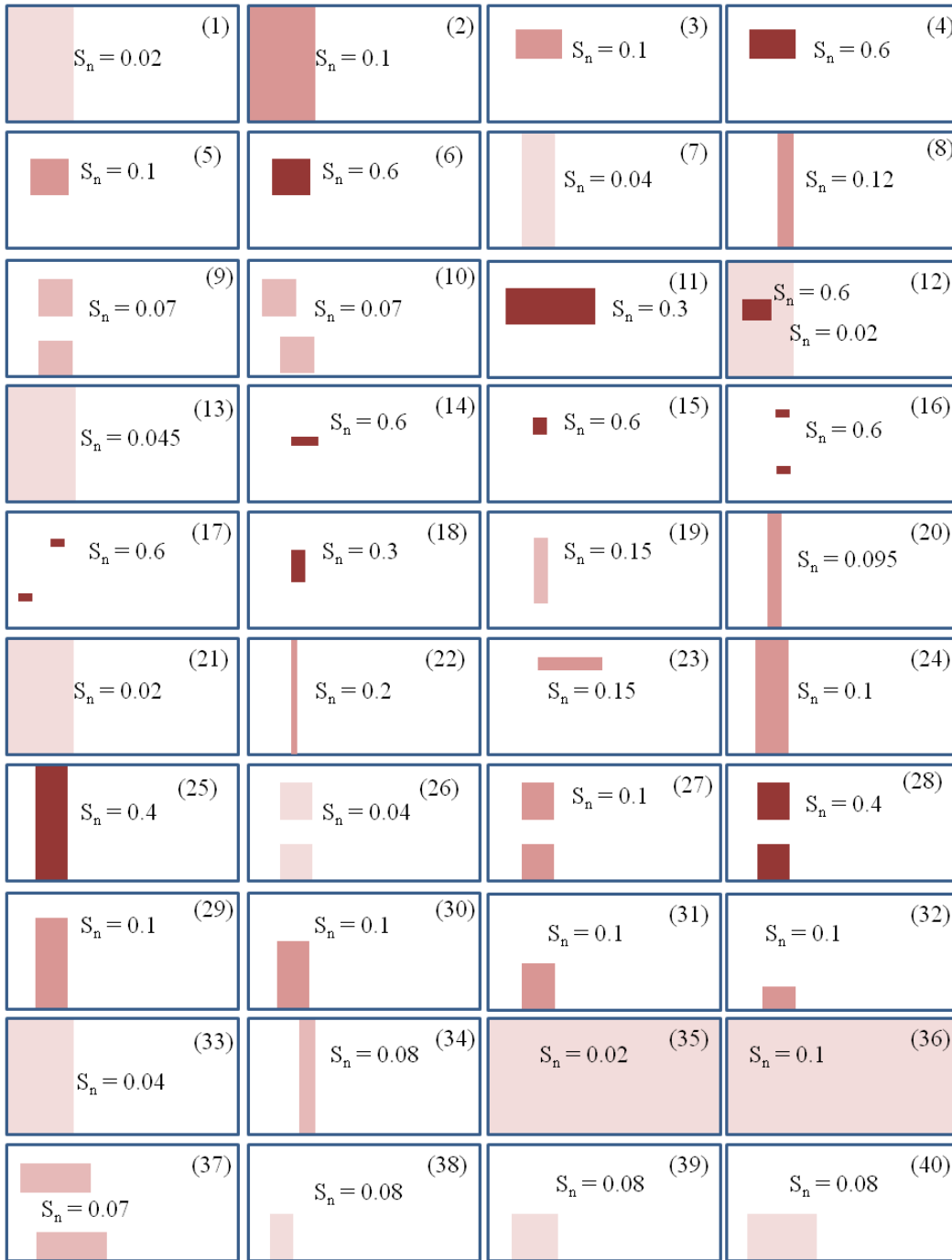


**Figure 8.1** Representations of the 40 source zones examined with the 2-D push-pull model.

realization 12) all cells in the domain containing DNAPL have the same saturation value. This saturation value varies from realization to realization, but is consistent within each realization. Realization 12 has an area of high saturation within a region of low saturation, and therefore has two saturation values as depicted in Figure 8.1. Based upon results described in Chapter 7, simulations using these artificial DNAPL architectures focused on 2-octanol using a fast-fast flow condition.

### **8.3 - Results**

#### *8.3.1 – Effect of Vertical Distribution on Push-Pull BTCs*

The source zones presented in Figure 8.1 were first examined to determine if push-pull tests are capable of distinguishing vertical differences in DNAPL source zone architecture. Shown below, in Figure 8.2, are five BTCs resulting from tests conducted in domains with 20%, 40%, 60%, 80% and 100% of the vertical distribution containing TCE-DNAPL saturation (realizations 24 and 29-32). These five source zones produce five distinct curves, suggesting the shape of the BTC depends on the vertical distribution of DNAPL. There are a few important characteristics of these curves. First, there is an inflection point early in each BTC where the slope of the concentration signal levels out. The  $C/C_0$  value of this inflection point appears to decrease as more of the vertical domain is occupied with DNAPL. Also, on some of the curves, there is a second inflection point (around  $V_{ext}/V_{inj} = 1.5$ ) where concentrations level out and start to tail.

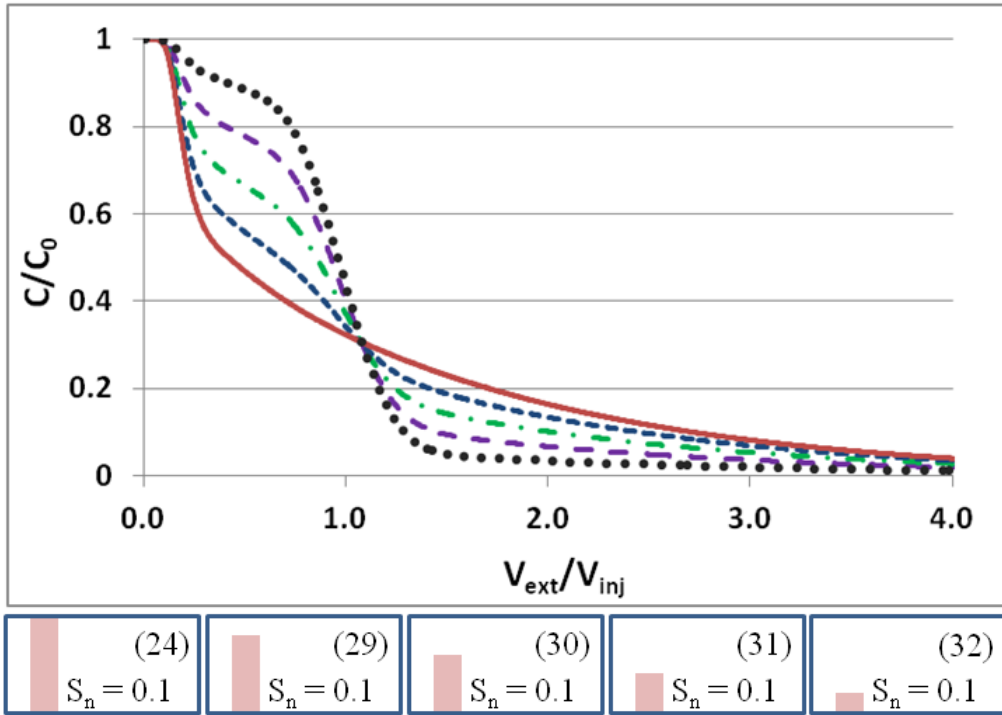


**Figure 8.2** 2-octanol BTCs resulting from push-pull tests conducted in realizations 24 (solid), 29 (short dash), 30 (dot dash), 31 (short dash) and 32 (dotted). Also included are the diagrams of the corresponding source zones.

This inflection point is most obvious in domains where less of the vertical dimension contains DNAPL, and is not present in domains where the vertical dimension is completely filled with DNAPL. The BTCs shown in Figure 8.2 suggest that for the same horizontal distribution and distance from the injection/extraction well, these push-pull tests respond to variations in the percent of the vertical domain containing DNAPL saturation (%Z).

To further explore the concept of the vertical extent of DNAPL saturation, %Z was examined in simulations when other aspects of the distribution, such as variation in the horizontal distribution or DNAPL saturation are included. 2-octanol BTCs resulting from push-pull tests in realizations 9, 10, 27 and 28 are shown in Figure 8.3. The purpose of this figure is twofold: (i) to show the influence of saturation on the BTCs (by comparing realizations 9, 27 and 28); and (ii) to determine if a difference in horizontal distribution affects the initial interpretations regarding %Z (by comparing realizations 9 and 10). When viewed using a linear scale (panel a) there are no apparent differences in the realizations produced with the same vertical and horizontal distribution, but different DNAPL saturations (realizations 8, 27, 28). On a log-scale (panel b) separation within the tails can be seen for simulations conducted with source zones having higher local saturations. Overall however, it is difficult to distinguish between source zones with the same vertical and horizontal distribution.

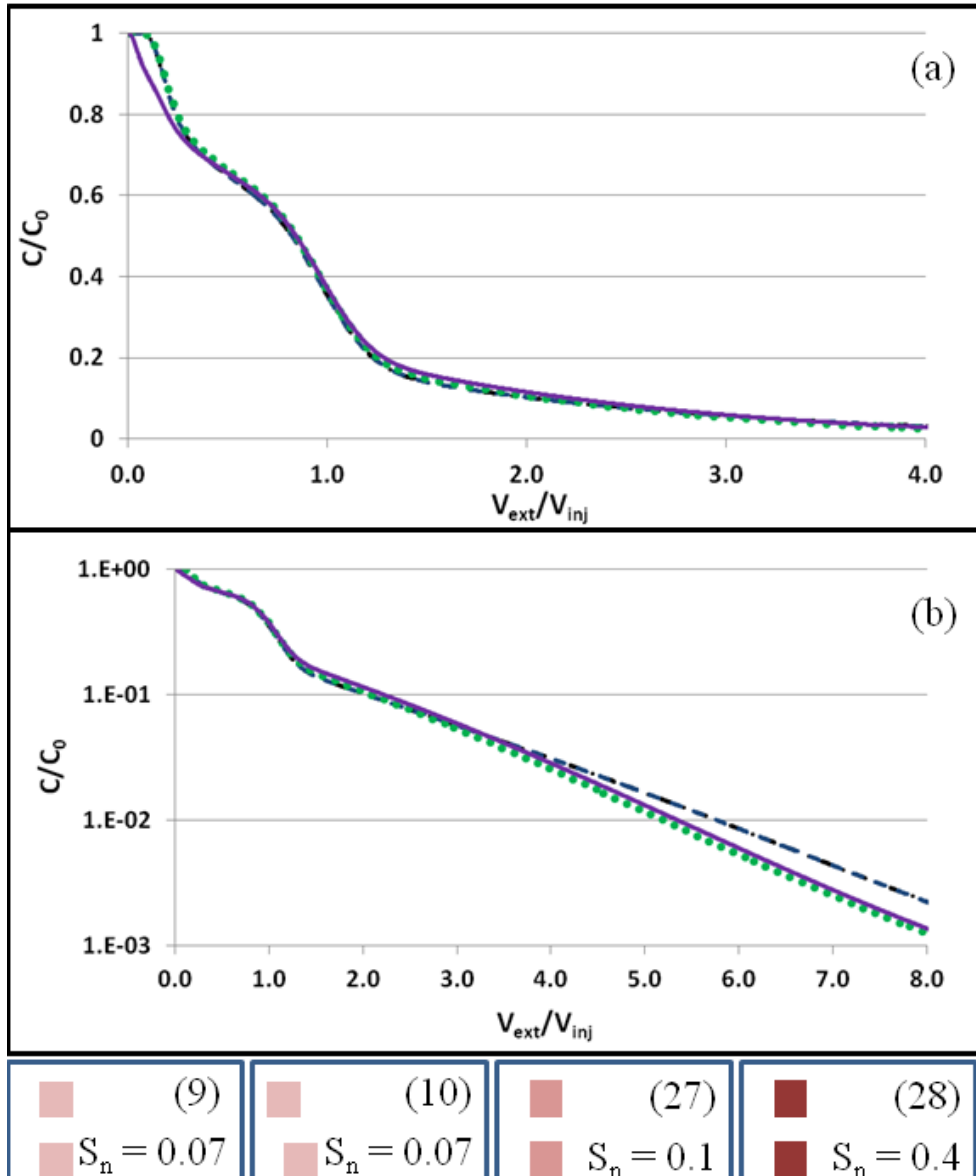


**Figure 8.3** 2-octanol BTCs resulting from push-pull tests conducted in realizations 9 (dotted), 10 (solid), 27 (long dash), and 28 (dot dash). Note that BTCs for realization 27 and 28 are coincident and that panel b uses a larger x-axis and a log-scale y-axis to show BTC tails. Also included are the diagrams of the corresponding source zones.

The BTC resulting from realization 10 is distinct from the other three at the initial part of the BTC. Interestingly, this BTC meets the other curves right at the first inflection point and all curves are very similar from that point on. Additionally, each of these realizations has a %Z of 57; the resulting BTC shapes are similar to realization 30 (Figure 8.2) where %Z=60, providing further evidence of %Z on BTC shape.

In Figure 8.4 the effects of both slight changes in %Z and larger changes in saturation are shown using the BTCs resulting from realizations 3-6. Realizations 3 and 5 have the same saturation and overall TCE-DNAPL mass, but differ slightly in shape. The same is true for realizations 4 and 6. Realizations 3 and 4 have the same rectangular shape, while realizations 5 and 6 have a square shape that occupies an additional 9% of the vertical distribution. In Figure 8.4a it can be seen that realizations with the same shape result in BTCs with similarities in early time (around the first inflection point) and BTCs with the same saturation are similar later in the BTC (around the second inflection point). The separation due to differences in saturation is more prominent in the log-scale (Figure 8.4b) in both the second inflection point and the strong tailing in the BTCs corresponding to the higher saturation realizations. Again, here it is seen that even slight differences in %Z influence the BTCs, most visibly in the initial part of the BTC. It should be noted here that the separation between the BTCs from realizations with different vertical distributions shown in Figure 8.4 is likely too small to be distinguished in a field test; however, the larger separations seen in Figure 8.2 could be detected in a field test.

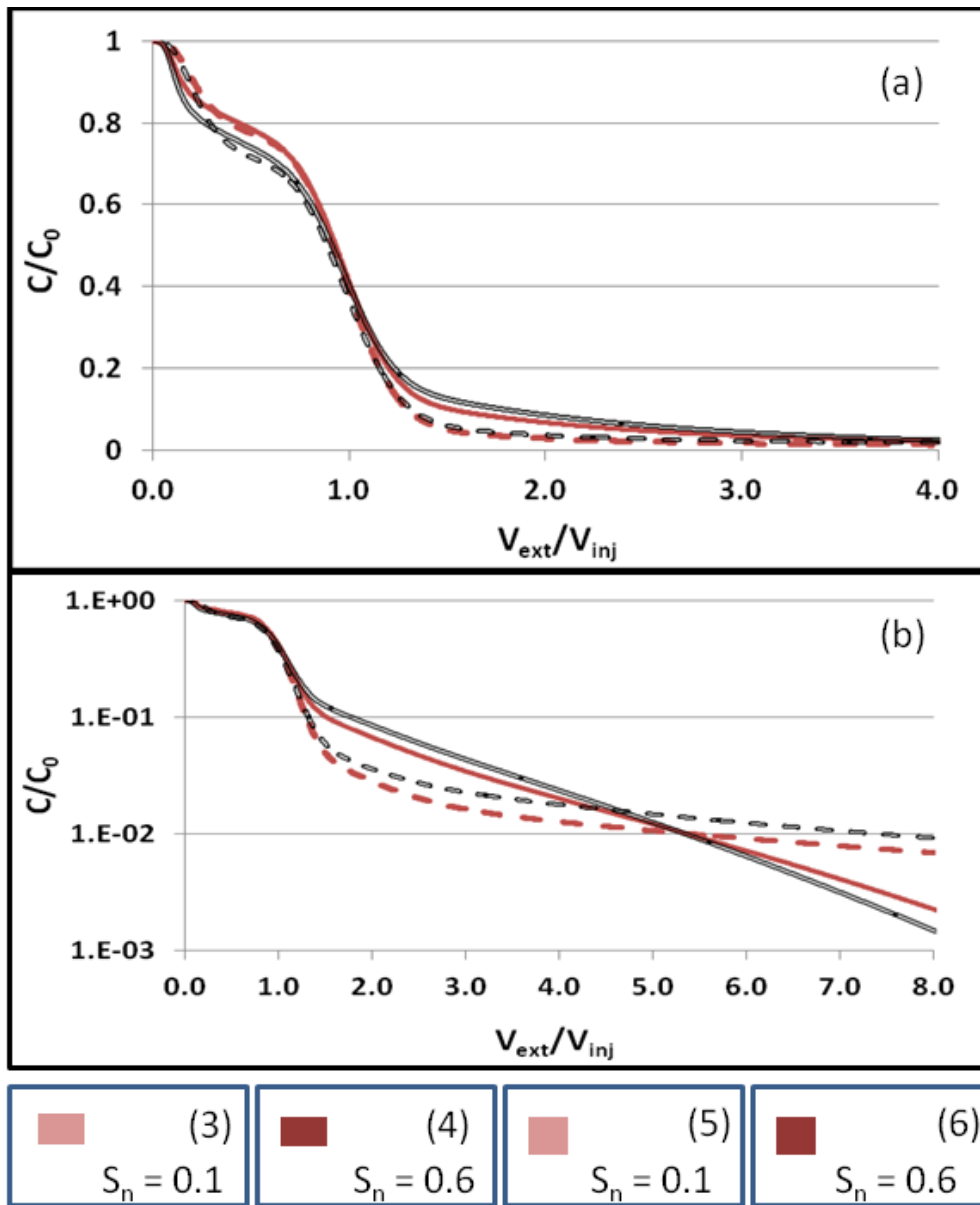


**Figure 8.4** 2-octanol BTCs resulting from push-pull tests conducted in realizations 3 (solid), 4 (dashed), 5 (double solid), and 6 (double dash). Note that panel b uses a larger x-axis and a log-scale y-axis to show BTC tails. Also included are the diagrams of the corresponding source zones.

### 8.3.2 – *Effect of Horizontal Distribution on Push-Pull BTCs*

Results from section 8.3.1 show that variations in vertical extent of the TCE-DNAPL distribution may be detected in the BTCs from the push pull tests. Moreover, results are shown in Figure 8.3 in which realization 10 has a different horizontal distribution than the other three realizations suggests there is potential for BTCs to elucidate the horizontal extent of DNAPL. To further examine the influence of horizontal distribution, a series of simulations were conducted using realizations 7, 8, and 21 (Figure 8.5). These realizations all cover the entire vertical domain (%Z =100), have the same TCE-DNAPL mass, have the same distance from the injection/extraction well to the back edge of the DNAPL mass, but differ in distance between the injection/extraction well and the front edge of the DNAPL mass. These three realizations result in separated curves in the early portion of the BTC, that all come together to form the same BTC at  $V_{ext}/V_{inj} = 0.6$ . These results show that the closer the DNAPL front to the injection/extraction well, the earlier  $C/C_0$  concentrations drop from 1. Here it has been established that push-pull tests can distinguish variations in horizontal distribution when the location of the source zone front (relative to the injection/extraction well) changes, but the location of the back of the source zone remains constant. This leads to the next question: can the push-pull test detect differences in horizontal distribution when the distance between the injection/extraction well remains constant?

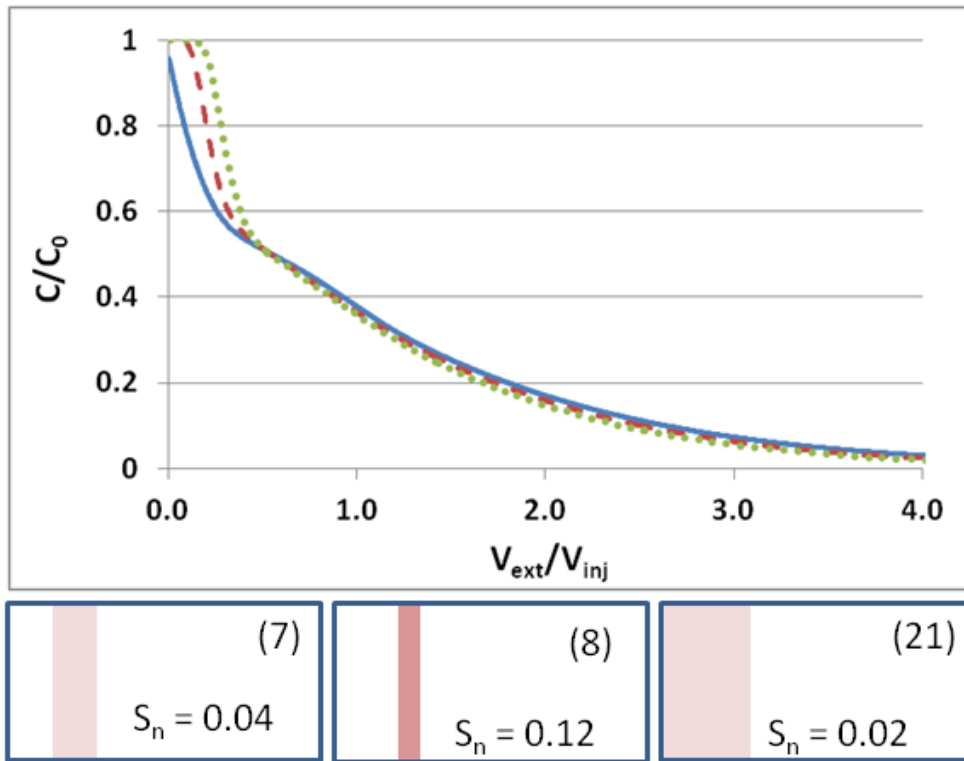


**Figure 8.5** 2-octanol BTCs resulting from push-pull tests conducted in realizations 7 (dashed), 8 (dotted), and 21 (solid). Also included are the diagrams of the corresponding source zones.

Shown in Figure 8.6 are push-pull BTCs resulting from realizations 38-40. These distributions all have the same vertical distribution ( $\%Z=40$ ), and distance between the injection/extraction well and DNAPL front. They differ in location of the back end of the source zone and total TCE-DNAPL mass in the source zone. In contrast to Figure 8.5, there is no visual difference among the three BTCs. These results indicate that the distinct BTC fronts seen in Figure 8.5 are only due to distance from the DNAPL front to the injection/extraction well and not due to differences in horizontal distribution. The same results are seen in Figure 8.7, where BTCs result from realizations with different vertical distributions than those used to create BTCs in Figure 8.6. Again in Figure 8.7, it can be seen that if the distance between the injection/extraction well remains constant, the push-pull test cannot distinguish between different horizontal distributions.

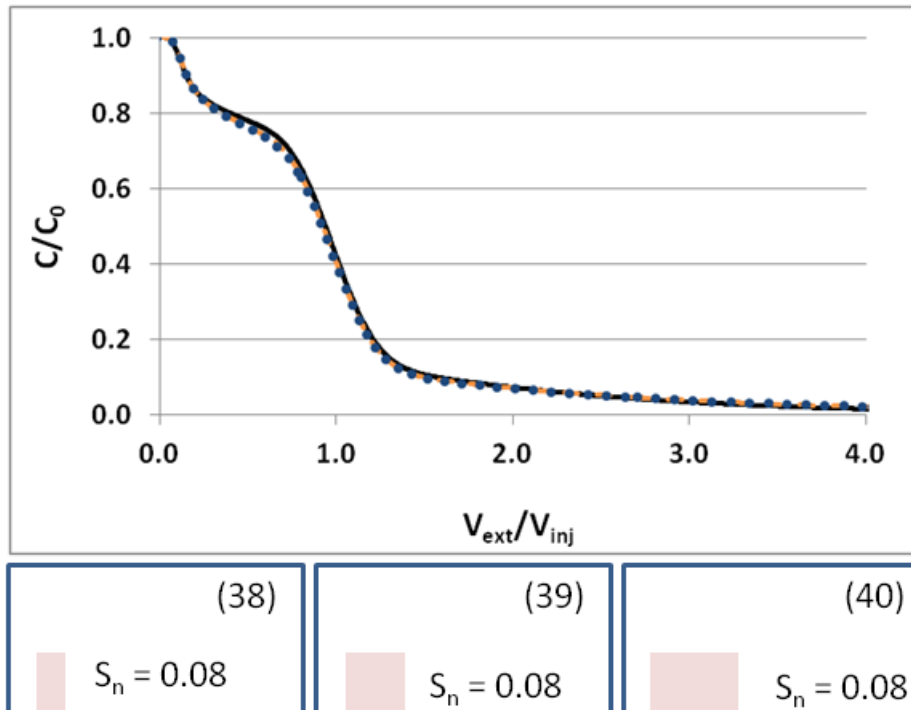


**Figure 8.6** 2-octanol BTCs resulting from push-pull tests conducted in realizations 38 (solid), 39 (dashed), and 40 (dotted). Also included are the diagrams of the corresponding source zones.

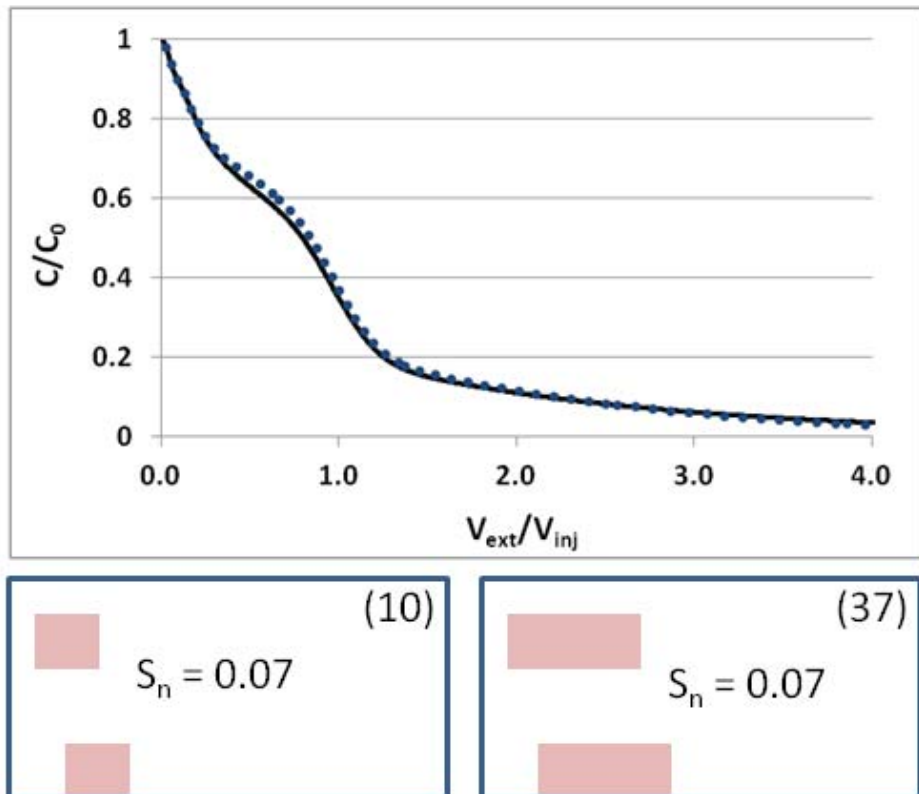


**Figure 8.7** 2-octanol BTCs resulting from push-pull tests conducted in realizations 10 (dotted) and 39 (solid). Also included are the diagrams of the corresponding source zones.

## 8.4 - Discussion

### 8.4.1- Development of Simplified Regressions

Analysis of the results presented above, as well as BTCs produced by the other 20 realizations not shown, indicates that three key aspects of the BTCs may provide information on source zone architecture: i) the point at which  $C/C_0$  concentrations fall from a nominal value of 1.0; ii) the  $C/C_0$  value corresponding to the first inflection point; iii) the  $C/C_0$  value corresponding to the second inflection point. The following discussion attempts to pin point what information on source zone architecture distribution can be gained from each of these aspects of the BTC.

While exploring the ability of the push-pull test to distinguish variations in horizontal distribution, it was observed that the closer the DNAPL front to the injection/extraction well, the earlier in the BTC concentrations drop from a  $C/C_0$  of 1.0. 2-octanol should behave like a conservative tracer in the area between the well and the DNAPL front (assuming no tracer/porous media interaction). The reason for the  $C/C_0$  value to drop below 1.0 is either because enough tracer mass has been pumped out of the system or because tracer interactions with the TCE-DNAPL are causing retardation. The bromide signals of each of these curves (not shown) drop from 1.0 much later than the 2-octanol curves; therefore, the early drop in the 2-octanol must be related to tracer partitioning.

It may therefore be possible to estimate the distance from the injection/extraction well to the TCE-DNAPL front using the  $V_{\text{ext}}/V_{\text{inj}}$  value at

which normalized concentration drops from 1. In this system the distance to the DNAPL front would be calculated as:

$$D_{front} = \frac{\left[ (V_{ext} / V_{inj})^* \right] * V_{inj}}{An} \quad (8.1)$$

where  $D_{front}$  is the distance between the injection/extraction well and the DNAPL front [L],  $(V_{ext}/V_{inj})^*$  is the  $V_{ext}/V_{inj}$  value at which normalized concentration drops from 1.0 [-], and  $A$  is the cross sectional area of the 2-D system [L<sup>2</sup>].

This calculation was completed for all 40 realizations, using  $C/C_0 = 0.980$  to define the point at which normalized concentrations drop from 1.0. The relationship between  $D_{front}$  and  $(V_{ext}/V_{inj})^*$  is shown in Figure 8.8. A linear regression of the data results in an  $R^2$  value of 0.88. However, the vertical lines of data at distances of 15.0 and 18.5 cm indicate that  $(V_{ext}/V_{inj})^*$  may also be dependent on another variable.

Analysis of the 40 simulations indicated that saturation also has some influence the drop from a normalized concentration of 1.0. Therefore a nonlinear regression was performed to see if both saturation and  $D_{front}$  can be used to better describe the drop in normalized concentration. Predictions of  $(V_{ext}/V_{inj})^*$  using this nonlinear regression are shown in Figure 8.9. Here it can be seen that including saturation improves the overall regression and removes the vertical pattern in the data seen in Figure 8.8. The resulting regression equation ( $R^2 = 0.94$ ) is:

$$\left( V_{ext} / V_{inj} \right)^* = (0.015 \pm 0.003) (D_{front})^{(0.922 \pm 0.06)} (S_n)^{(0.174 \pm 0.04)} \quad (8.2)$$

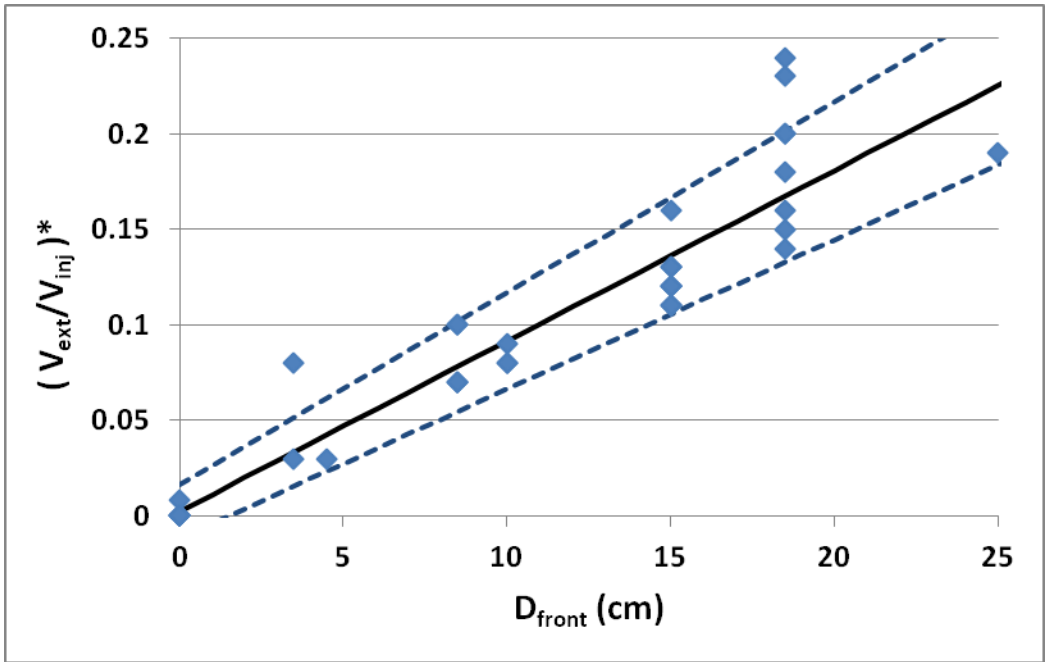


**Figure 8.8** Relationship between the  $(V_{\text{ext}}/V_{\text{inj}})^*$  and  $D_{\text{front}}$ . The data (diamonds), regression line (solid) and 95% confidence intervals (dashed) are all displayed.

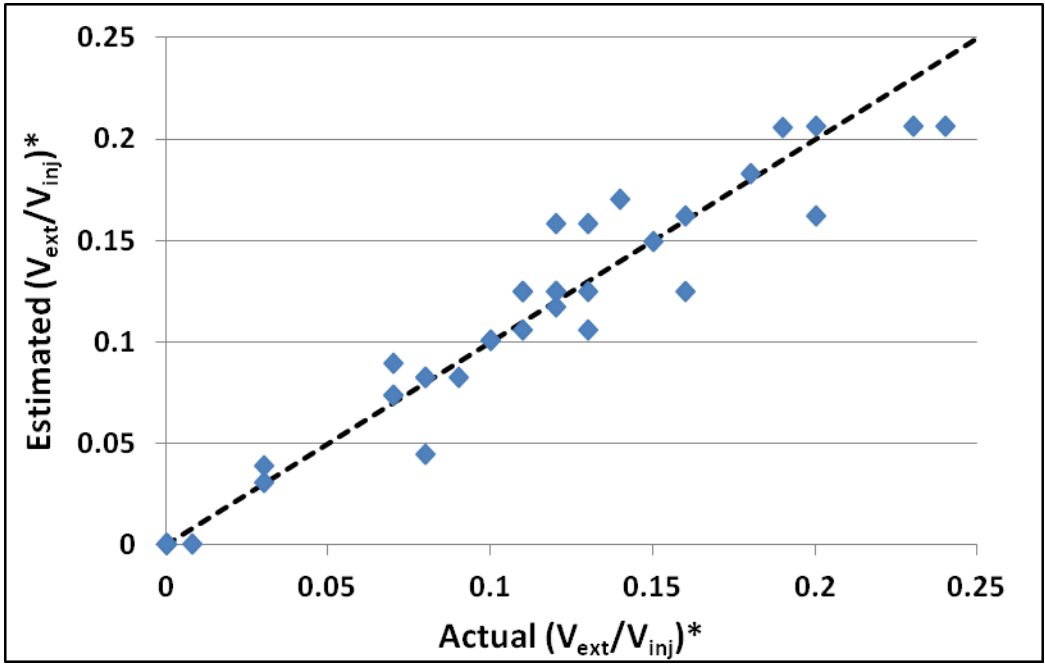


**Figure 8.9** Estimated vs. actual  $(V_{ext}/V_{inj})^*$ . The predicted  $(V_{ext}/V_{inj})^*$  was calculated using the nonlinear regression employing both saturation and  $D_{front}$  (Eq 8.2). Shown in the solid line is the 1:1 slope, indicating where estimated values equal actual values.

where regressed values are shown as (value  $\pm$  standard deviation). Results of this regression indicate that the drop in normalized concentration is related to both saturation and distance between the injection/extraction well and the DNAPL source zone. It must be remembered that these regression results are only strictly valid for the simplified systems used to develop the regression. Extrapolation of results to field test BTC may be difficult due to increased heterogeneity, analytical error in tracer analysis and less sharply defined DNAPL fronts.

The next feature which may hold information on the DNAPL architecture is the inflection point that occurs in early time on all of the BTCs. Analysis of each BTC suggested that the  $C/C_0$  value of the inflection point may depend on %Z. This is most clearly demonstrated in Figure 8.2, where increasing %Z results in decreased  $C/C_0$  value of the inflection point. In Figure 8.10, the relationship between %Z and the  $C/C_0$  value of the inflection point is shown. A linear fit to these data results in an  $R^2$  value of 0.95, showing that there is a relationship between the amount of vertical space occupied by DNAPL and the location of the inflection point. In Figure 8.10, it can be seen that a range of inflection point  $C/C_0$  values (0.51 – 0.60) occurs when the entire vertical saturation is filled with DNAPL. The realizations where %Z=100 were examined more closely to see if the variation in inflection point was caused by either local saturation or total DNAPL volume. Results of these regressions indicated that no relationship existed for either predictor. However, it appears that in these systems the  $C/C_0$  value of the inflection point allows for the estimation of the percent of the vertical domain containing TCE-DNAPL.

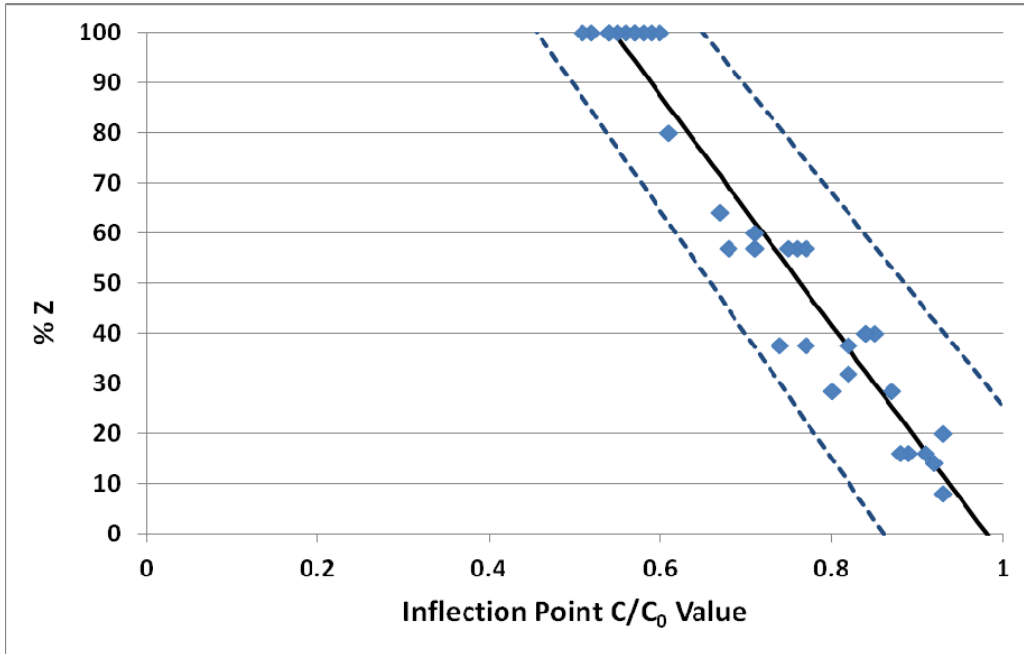


**Figure 8.10** Relationship between %Z and the  $C/C_0$  value of the first inflection point. The data (diamonds), regression line (solid) and 95% confidence intervals (dashed) are all displayed.

The final distinct feature in these BTC that may provide information on source zone architecture is the inflection point that occurs further along the x-axis, generally around a  $V_{\text{ext}}/V_{\text{inj}}$  value of 1.3. The  $C/C_0$  value of this inflection point appears to be dependent on both local saturation and %Z. In Figure 8.2, it can be seen that as %Z increases, the  $C/C_0$  value of the inflection point increases and the inflection point becomes less distinct until it is no longer visible in curves derived from source zones where %Z = 100. Also, the inflection point  $C/C_0$  value tends to be lower when the BTC is generated from a higher saturation source zone, as demonstrated in Figure 8.4. Three regressions are used to determine the dependence of the  $C/C_0$  value of the second inflection point on saturation and %Z. The first two are single variable regressions to determine how strongly saturation and %Z individually relate to the inflection point. The third regression is a nonlinear regression that includes both saturation and %Z as independent variables. The resulting regression equations and squared correlation coefficients are displayed in Table 8.1. Predictions of inflection point  $C/C_0$  value from each regression are shown in Figure 8.11. It should be noted here that since all realizations with DNAPL in the entire vertical domain do not have a second inflection point, these three regressions were completed only on the BTCs from the 24 realizations that have a second inflection point.

**Table 8.1** Regression equations and corresponding  $R^2$  values representing the dependence of the  $C/C_0$  value of the second inflection point on saturation and %Z.

<b>Independent Regression Variables</b>	<b>Regression Equation</b>	<b><math>R^2</math></b>
Saturation	$Y = (-0.17 \pm 0.03)(S_n) + (0.16 \pm 0.01)$	0.63
%Z	$Y = (0.23 \pm 0.03)(Z) + (0.03 \pm 0.01)$	0.78
Saturation and %Z	$Y = (0.09 \pm 0.02)(S_n^{(-0.28 \pm 0.05)})(Z^{(0.39 \pm 0.08)})$	0.87

\* Here "Y" is used to represent the  $C/C_0$  value of the second inflection point and  $Z = \%Z/100$ .

\*\* All regressed values are shown as (value  $\pm$  standard deviation)

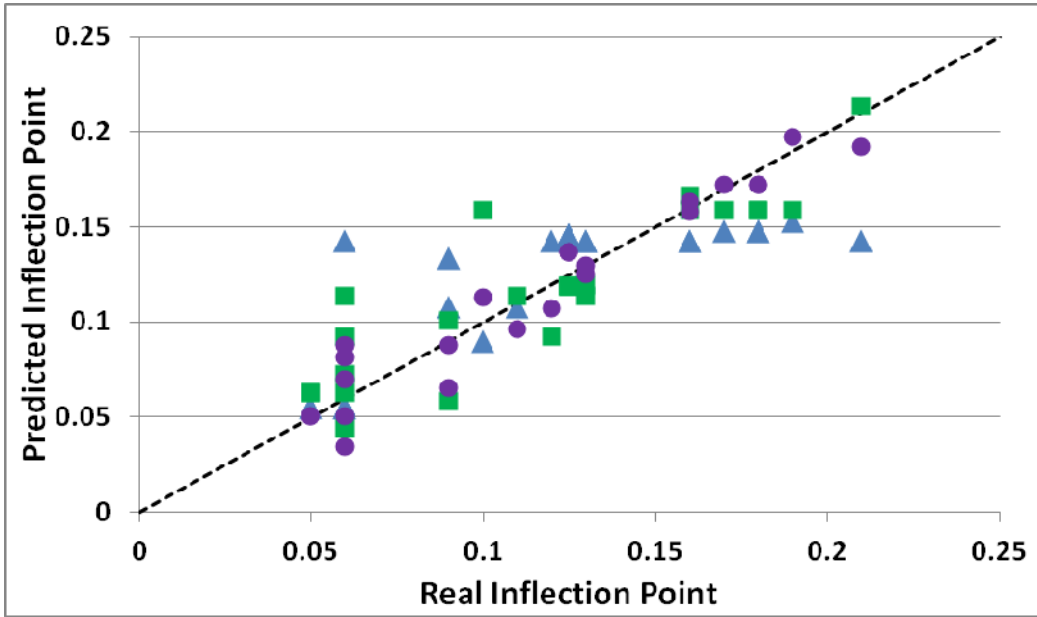


**Figure 8.11** Predicted vs. actual  $C/C_0$  value of second inflection point. Results of three regressions are shown: linear regression depending on saturation (triangles); linear regression depending on %Z (square); nonlinear regression depending on both saturation and %Z (circles). Shown in the solid line is the 1:1 slope, indicating where estimated values equal actual values

As can be seen in both Table 8.1 and Figure 8.11, the  $C/C_0$  value of the second inflection point seems to have some dependence on both saturation and %Z. The  $R^2$  values derived from regressing the inflection point against either saturation or %Z are only 0.63 and 0.78, respectively. However, when combined in the multivariate regression, the squared correlation coefficient is 0.93. This shows that there is a strong relationship between this inflection point and both saturation and %Z.

There are many significant caveats to this analysis, the most important of which is that these results are only strictly valid for the system in which they were developed. A field push-pull test will be complicated by radial flow and the potential for DNAPL to be localized within one sector of the well circumference. Also, heterogeneous geology may necessitate the use of the bromide curve to determine what features of the partitioning BTC are due to flow field and what are due to interactions with the DNAPL; as was seen with the low pool fraction, fast-fast test (Chapter 7) this distinction is difficult to make. Heterogeneities in the DNAPL saturation will also make distinctions between regions with and without DNAPL less sharp (i.e. how high does the local DNAPL saturation need to be for the results of these tests to apply). Additionally with a field test, the BTC will not be as smooth as a simulation and may be data limited, causing inflection point locations to be miscalculated or missed completely.

#### 8.4.2 – Application of Simplified Regressions

Some of the caveats mentioned above can be examined in greater detail using the data and simulations from the experimental source zones presented in Chapter 7. As discussed previously, these source zones were created by injecting TCE-DNAPL into sandy porous media. Though the media is relatively homogeneous (compared to geologies at many field sites), it allows for the creation of three, distinct, heterogeneous DNAPL architectures. The simulated BTCs from these source zones are used to assess the effect of heterogeneous DNAPL saturation on the analysis techniques described above. The experimental data from these source zones may add more error to the analysis due to both noise in the data and data gaps. Applying the analysis techniques to the laboratory data will shed light on the added complications of using experimentally measured data.

Shown in Figures 8.12, 8.13, and 8.14 are the estimated locations of the TCE-DNAPL front for the each test in the low, mid and high pool fraction source zones, respectively. Each panel in Figures 8.12 – 8.13 has two estimated front locations, one from analysis of the simulated BTC (line a) and the other from a similar analysis of the analytical effluent data (line b). Though the multivariate regression (equation 8.2) provides a better prediction of  $D_{\text{front}}$ , it requires knowledge of local saturation; therefore, estimations of DNAPL front were completed as using equation 8.1. When simulated BTCs are analyzed, it is possible to use  $C/C_0 = 0.980$  to represent the point at which normalized concentrations fall from 1.0. However, with the lab data, the choice of the  $C/C_0$  value that indicates a drop from 1 is more subjective because of scatter in the

analytical data and small data gaps. The curves were visually examined to discern the  $V_{\text{ext}}/V_{\text{inj}}$  value at which concentrations appeared to drop due to interactions with the TCE-DNAPL. For the mid pool fraction fast-slow test the drop off from normalized concentrations could not be determined because early BTC data are too noisy. Results for the low pool fraction source zone (Figure 8.12) show that the simulated data estimates the DNAPL front to coincide with the pooled TCE-DNAPL at the bottom of the box. Estimates using the measured data determine a DNAPL front that is 3 - 6 cm further from the injection/extraction well. This difference in estimation seems to be primarily due to incomplete information in the BTC, making it difficult to find the exact point at which normalized concentrations drop from 1.0. For the mid pool fraction source zone (Figure 8.13) DNAPL front estimations for the first two tests are closer to the injection/extraction well than those corresponding to the last test. This may be due to the visible loss of TCE-DNAPL mass in the pool along the bottom low permeability layer (Figure 9.13 III). Estimations of DNAPL front in the high pool fraction box (Figure 8.14) occur closer to the bulk of the DNAPL front and appear to be less effected by the TCE-DNAPL pool on the bottom low permeability layer.

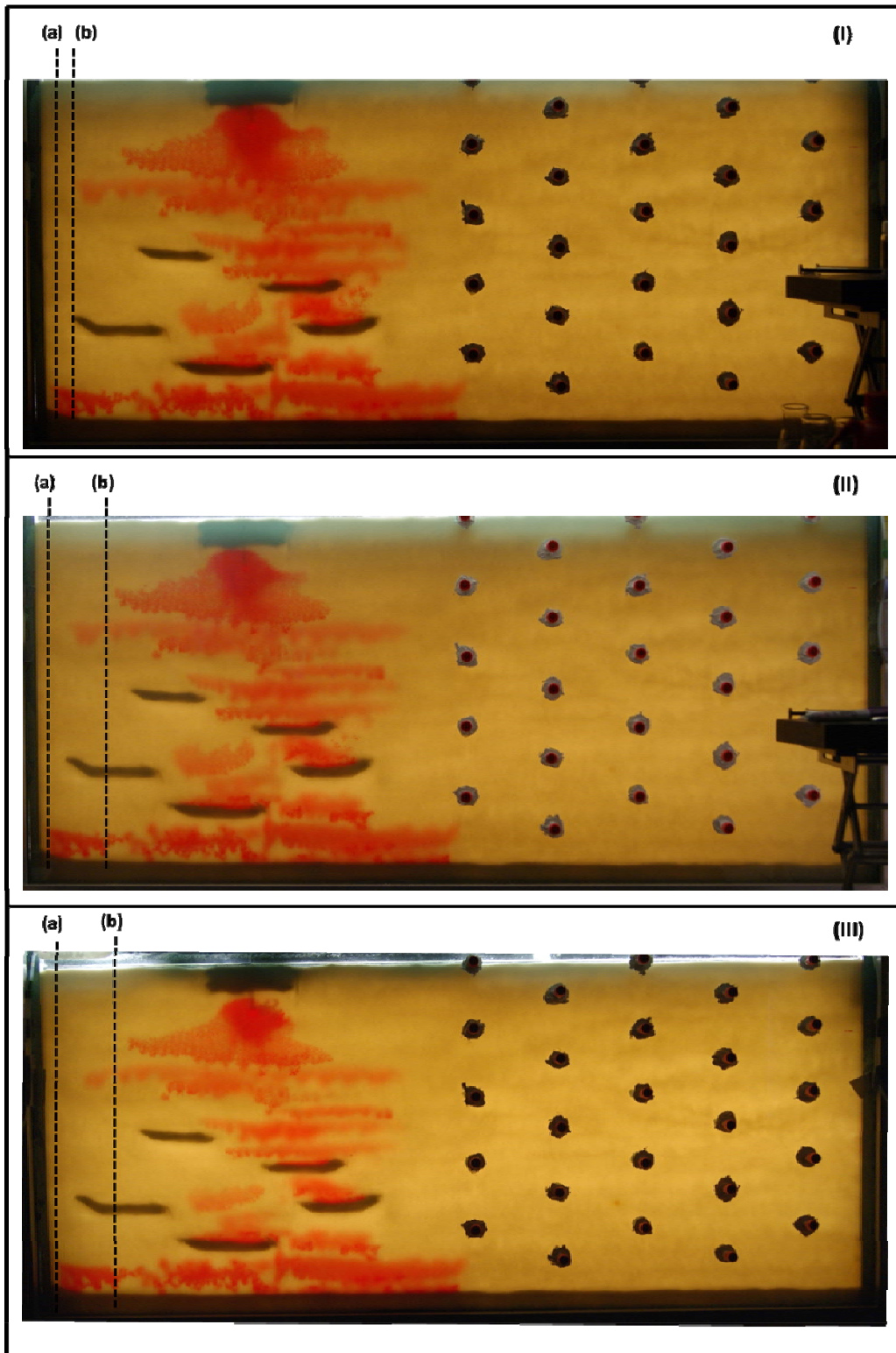


**Figure 8.12** Estimations of TCE-DNAPL front using simulated (a) and measured (b) 2-octanol BTCs in the low pool fraction box. Results from the fast-fast test are shown in panel I, the slow-fast test in panel II and the fast-slow test in panel III.

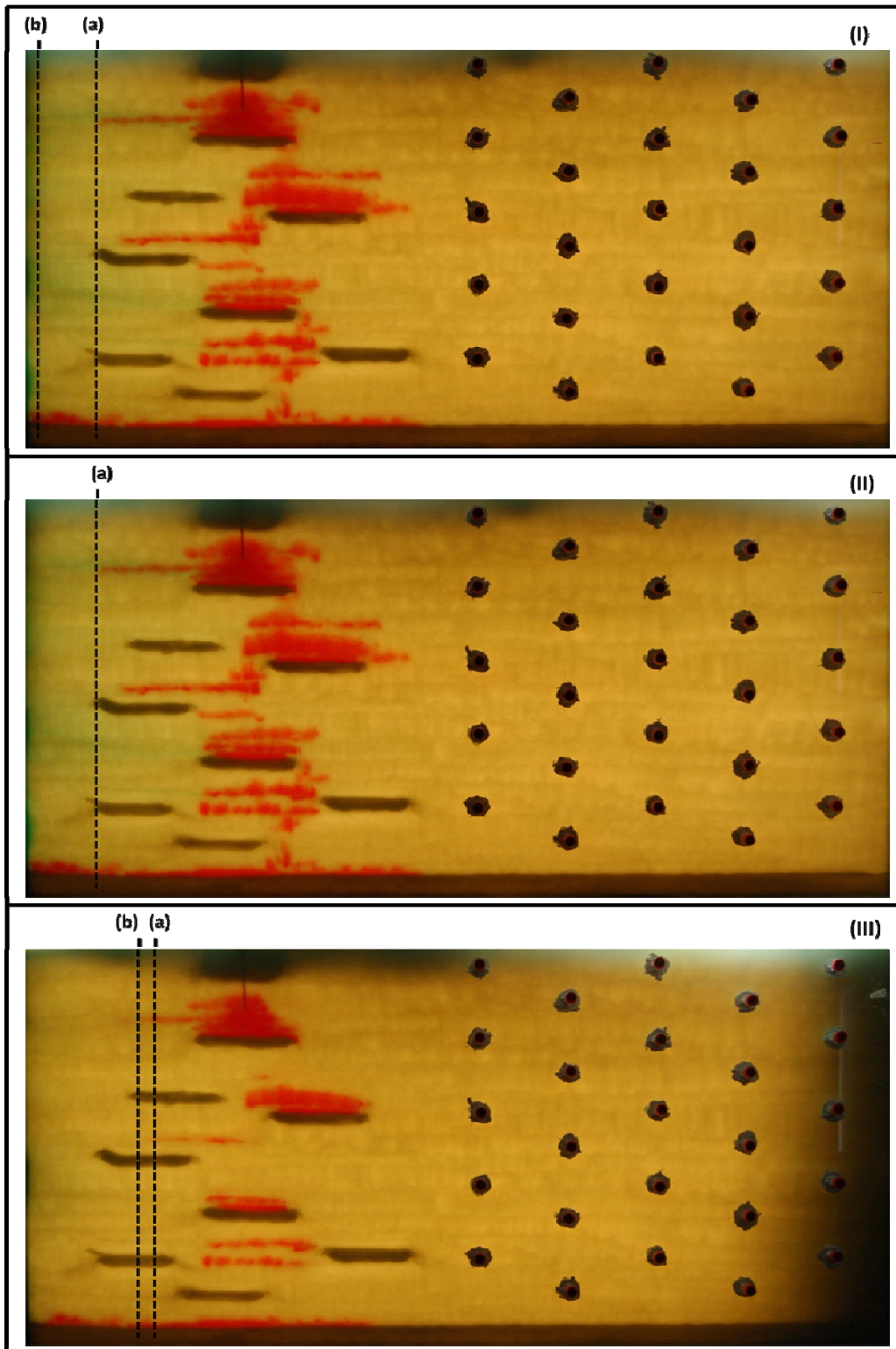


**Figure 8.13** Estimations of TCE-DNAPL front using simulated (a) and measured (b) 2-octanol BTCs in the mid pool fraction box. Results from the slow-fast test are shown in panel I, the fast-slow test in panel II and the fast-fast test in panel III. Note that there is no estimation using the fast-slow test effluent data.

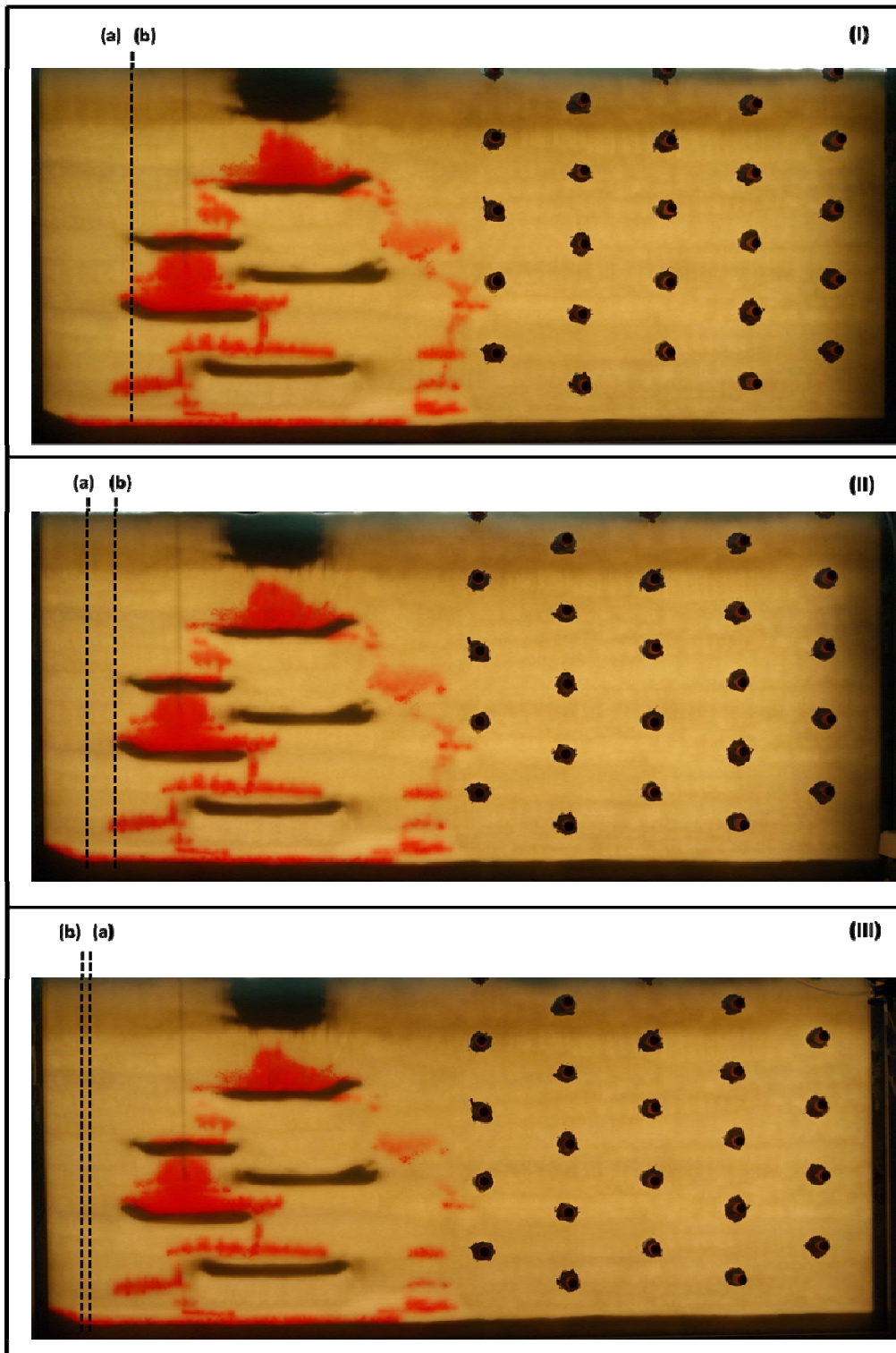


**Figure 8.14** Estimations of TCE-DNAPL front using simulated (a) and measured (b) 2-octanol BTCs in the high pool fraction box. Results from the fast-fast test are shown in panel I, the slow-fast test in panel II and the fast-slow test in panel III. Note, in panel II, the simulated and analytical BTCs provide the same estimate of  $D_{front}$ .

These examples demonstrate that equation 8.1 provides reasonable estimates of the distance between the DNAPL front and the injection/extraction well in heterogeneous source zones. The use of laboratory effluent data does complicate the analysis because of incomplete and slightly scattered data sets, but overall still provides good estimates of  $D_{\text{front}}$ . Additionally, the close proximity of the TCE-DNAPL source zone to the injection/extraction well in these experimental systems complicates analysis because the concentration drop often occurs within the first few data points, making it the drop difficult to identify.

The percent of the vertical domain containing TCE-DNAPL was also estimated for each of the push-pull tests (Table 8.2). Again, estimations were completed using both simulated and measured BTCs. The 1<sup>st</sup> inflection point on each curve was used as the independent variable in the linear regression shown in Figure 8.10 to calculate %Z. This regression equation estimates values over 100% for most of the tests (Table 8.2); since %Z cannot physically be higher than 100%, anything calculated to be over 100% is assumed to be equal to 100%. The actual %Z of each source zone was determined from the saturation input files used in the 2-D model. Recall that these saturation files were generated using the light transmission data. The cell size in this domain is 5 mm x 5 mm (similar to the scale used for averaging the light transmission data). Any cell that had a local TCE-DNAPL saturation greater than 1% was determined to contain TCE-DNAPL. The %Z was then calculated as the number of rows in the domain containing any DNAPL normalized by the total number of rows in the domain (e.g. 88 rows for the 44 cm tall low pool fraction box).

**Table 8.2** Estimated percent of the vertical domain containing TCE-DNAPL. Actual values are compared to those estimated using both simulated and measured 2-octanol BTCs.

Box	Actual %Z	Estimations using Simulated BTC		Estimations using Measured BTC	
		1st Inflection Point C/C <sub>0</sub> Value	Estimated %Z	1st Inflection Point C/C <sub>0</sub> Value	Estimated %Z
Low PF					
Fast-Fast	86.4	0.46	121	0.26	167
Slow-Fast	86.4	0.48	116	0.29	160
Fast-Slow	86.2	0.54	103	0.55	100
Mid PF					
Fast-Fast	50.0	0.73	58	0.72	60
Slow-Fast	82.6	0.57	95	0.41	132
Fast-Slow	82.6	0.41	132	NA <sup>1</sup>	NA <sup>1</sup>
High PF					
Fast-Fast	77.0	0.47	118	0.47	118
Slow-Fast	76.1	0.55	98	0.43	127
Fast-Slow	69.3	0.62	84	0.51	109

<sup>1</sup>No inflection point was seen in the experimental data for the mid pool fraction fast-slow test. This appears to be due to data gaps in the BTC.

It is difficult to determine the performance of this analysis for these source zones since all but two have  $\%Z > 75$ . Both the simulated and effluent data provide  $\%Z$  estimates that are close to 100 for all but the mid pool fraction fast-fast test. This may suggest that the analysis has difficulty distinguishing  $\%Z$  in heterogeneous source zones with high  $\%Z$  values. However, the analysis gives a good estimate of  $\%Z$  for the mid pool fraction box, and is able to distinguish it from the other two boxes. As mentioned above, predictions using simulated and measured BTCs are close, suggesting that the additional complications using measured data may not strongly affect this analysis.

Analysis of the second inflection point is more complicated for these heterogeneous source zones. Of the nine push-pull tests conducted in the aquifer cells, only the mid pool fraction fast-fast test has an obvious second inflection point. Therefore, analysis will be performed on this data set to illustrate how the second inflection point holds information on source zone architecture. Recall, this second inflection point appears to be related to both  $\%Z$  and local saturation (Table 8.1). As demonstrated above,  $\%Z$  can be estimated using the first inflection point. The local saturation can then be estimated from  $\%Z$  and the  $C/C_0$  value of the second inflection point. Applying this process to both the simulated and measured BTCs results in local saturation estimations of  $S_n = 0.18$  and  $S_n = 0.19$ , respectively. Two steps were necessary to calculate the actual saturation value to which these estimates correspond. First, an average saturation ( $S_{n1}$ ,  $S_{n2}$ ,  $S_{n3}$ ,  $S_{n4}$  and  $S_{n5}$ ) was calculated for each of the 5 TCE-DNAPL regions

highlighted below in Figure 8.15. Then, these 5 averages were weighted by the corresponding %Z and averaged together as:

$$(S_{n1} * \%Z_1) + (S_{n2} * \%Z_2) + (S_{n3} * \%Z_3) + (S_{n4} * \%Z_4) + (S_{n5} * \%Z_5) \quad (8.3)$$

The result of equation 8.3 is an average local saturation of 0.14, which is slightly lower than the estimations obtained using the second inflection point.

The above illustrations using 2-octanol BTCs generated from the heterogeneous source zones, demonstrate how push-pull BTCs might be useful for estimating DNAPL source zone features. If a BTC has both inflection points discussed in this analysis, it may be able to provide three pieces of information: i) the distance between the injection/extraction well and the DNAPL front; ii) the percent of the vertical domain that contains DNAPL; iii) the average local saturation of the DNAPL. This analysis cannot determine the vertical location of the DNAPL. For example, if it is determined that %Z=60, this analysis cannot indicate whether the DNAPL is in the bottom 60% percent of the domain, the top 60% of the domain or spaced throughout the vertical domain. Additionally, the analysis does not give information on the horizontal extent of the domain. However, it appears that these curves can be used to estimate more than just the overall average saturation of a source zone.

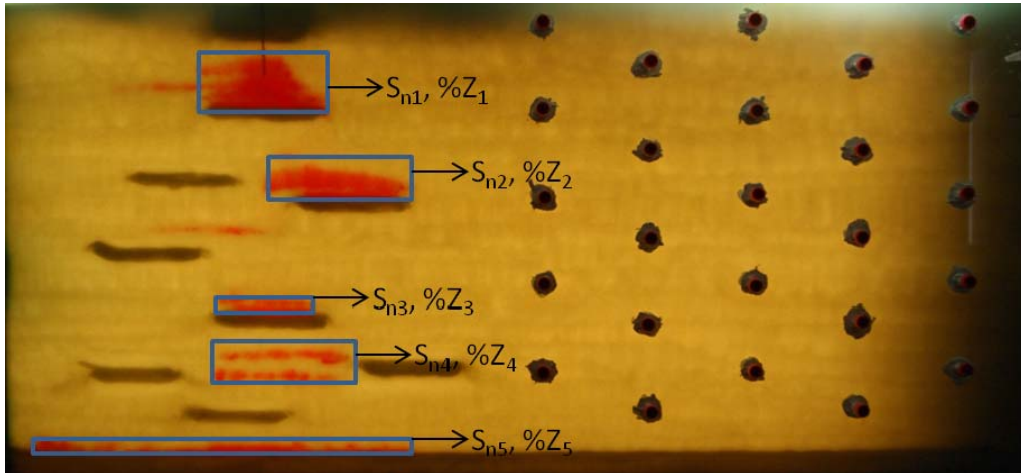


**Figure 8.15** Source zone corresponding to the mid pool fraction fast-fast test. The five boxes highlight the regions used to estimate local saturation of the source zone.

#### 8.4.3 – Estimation of Average Saturation

As shown in Chapter 7, Section 7.7.4, when detailed knowledge of the saturation distribution is available, a linear driving force model using the Nambi and Powers (2003) mass transfer coefficient correlation is able to describe partitioning tracer transport. Thus, incorporating partitioning kinetics into current analytical models may greatly improve predictions of DNAPL saturation. The problem with this approach is that detailed saturation distributions are not known a priori when push-pull tests are conducted in the field. Interestingly for most of the experiments conducted herein (eight of the nine), the kinetic model performs well when the DNAPL distribution is assumed to be uniform throughout the domain (see Figure 7.42). This observation has an important implication for analytical modeling tools which rely upon assumptions of uniform saturation – replacing the equilibrium assumption with linear driving force partitioning kinetics may greatly increase the ability of these tools to estimate overall saturation from push-pull test BTCs.

The exception to the general trend was the BTC produced in the mid pool fraction, fast-fast test (Figure 7.43). Here the DNAPL distribution was appreciably different than in the other eight experiments. The principal difference is that only about 50% of the vertical extent of the domain contains DNAPL, where as the other eight experiments had DNAPL that extended throughout greater than 70% of the vertical dimension. The BTC from this one experiment does not exhibit the early breakthrough and concavity seen in the other eight BTCs; instead it is characterized by an inflection in the slope early in the BTC

that is similar in character to the type of curves examined in Chapter 8, Section 8.3.1. Thus, the predictive power of the kinetic model employed with uniform saturations is less for this experiment (solid line and versus dotted line in Figure 8.16). However, if both linear driving force kinetics and %Z are incorporated into the modeling, the prediction of the mid pool fraction fast-fast curve is greatly improved (dashed line in Figure 8.16). The simulation noted by the dashed line in Figure 8.16 includes the linear driving force kinetics, and assumes that the DNAPL saturation is uniform but only within 60% of the vertical extent of the domain. The other 40% of the vertical dimension contains no DNAPL. In the simulation, the uniform saturation distribution was assumed to occupy 60% of the vertical domain because this is the %Z value estimated from the BTC following the procedure described in Chapter 8, Section 8.4 (Table 8.2). This demonstrates that incorporating both linear driving force kinetics and %Z into solution modeling approach results in an ability to capture the shape of the data. This is an important result because it suggests that BTCs can be interrogated by first estimating %Z from the data and then fitting the overall saturation.

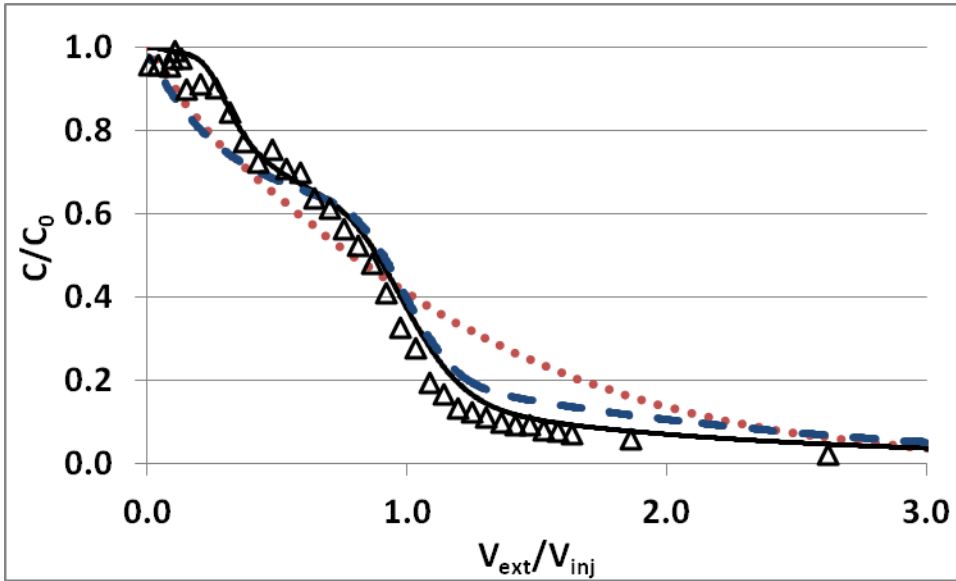


**Figure 8.16** 2-octanol BTC (triangles) from the mid pool fraction, fast-fast test. The plot includes a simulation using the linear driving force model and actual saturation distribution (solid), a simulation including linear driving force kinetics and a uniform saturation distribution (dotted) and a simulation including linear driving force kinetics and a uniform saturation distribution in 60% of the vertical domain (dashed).

## 8.5 Conclusions

The purpose of this chapter was to determine what features of the DNAPL architecture are discernible from push-pull partitioning tracer tests conducted in localized regions within the source zone. Push-pull tests were simulated in 40 artificial source zones to explore the extent of saturation in the vertical and horizontal directions. Results indicate that the test does distinguish differences in vertical DNAPL distribution. Additionally, the test appears to be able to distinguish differences in the distance between the injection/extraction well and the front of the DNAPL source zone.

BTC data generated by the 40 push-pull simulations suggest three locations on the BTC may hold information pertaining to features of the DNAPL architecture. The point at which normalized concentrations drop below a nominal value of 1.0 holds information on the distance between the injection/extraction well and the front of the DNAPL source zone. Additionally, an inflection point located in early time on the BTC appears to be correlated to the amount of the vertical domain containing DNAPL. Lastly, a second inflection point occurring further along the BTC can be correlated to both the percent of the vertical domain containing DNAPL and the local saturation of this DNAPL.

To expand the scope of these analyses, the observed relationships were tested using the laboratory and simulated push-pull tests conducted in Chapter 7. The intent here was to examine the influence of both more realistic saturation distributions and error inherent in real measurements on the features seen in BTCs generated from the contrived source zones. Results here showed that the drop in

normalized concentrations provides a reasonable estimate of distance between the injection/extraction well and DNAPL front. The analysis did not seem to be dependent on the use of simulated or real data, indicating that as long as the sampling density is high, the use of measured data may not strongly impact estimations. It is difficult to differentiate distributions where over 70% of the vertical domain contained DNAPL. However analysis using this first inflection point was able to distinguish the mid pool fraction source zone, with a %Z closer to 50. It may be that the strength of this analysis is differentiating between source zones characterized by greater vertical spreading (characteristic of younger source zones) from source zones with more localized hot spots (characteristic of aged source zones). The ability of these BTC features to predict aspects of the DNAPL source zone needs to be examined in much greater depth for more realistic source zones. However, the preliminary analysis conducted herein indicates that because of these features, push-pull tests may be useful for estimating more than just overall DNAPL saturation.

## CHAPTER 9 – CONCLUSIONS AND RECOMMENDATIONS

### *9.1 - Conclusions*

The current state of DNAPL source zone characterization focuses on quantifying dissolved concentrations (or perhaps mass flux) emanating from a source zone and on estimating an overall DNAPL saturation if necessary for remediation design. Given the established linkage between DNAPL architecture and mass discharge, it may be advantage to develop tools to estimate metrics that more specifically describe DNAPL architecture. Partitioning interwell tracer tests are one method that can be used to estimate architecture metrics; however, the high density of sampling points required to obtain estimates of architecture is economically prohibitive. The use of partitioning tracers in a push-pull flow scheme in localized settings may provide such a tool. To date the push-pull test has been used to estimate overall DNAPL saturation, but has not been used to estimate source zone architecture metrics. Therefore, the overall objective of this work was to determine if alcohol tracer push-pull tests can be used to characterize local-scale source zone architecture metrics. The work in this dissertation primarily focused on quantifying pool fraction, defined as the amount of pooled source zone mass normalized by the total source zone mass. This overall investigation was carried out by considering the influence of nonlinear partitioning, non-equilibrium mass exchange and non-uniformity in DNAPL distribution on resulting tracer breakthrough curves.

Equilibrium partitioning of the tracer between the DNAPL and aqueous phase defines the thermodynamic driving force for tracer transport. Hence,

Chapter 4 of this dissertation focused on complete characterization of the equilibrium phase behavior for three representative alcohol tracers (1-pentanol, 1-hexanol and 2-octanol) in a TCE-DNAPL/water system. Findings show that though linear partitioning is often assumed for these tracers, partitioning is non-linear for each tracer. However, each tracer does have a dilute concentration range in which linear partitioning can be safely assumed. This concentration range is now well-defined for each of the selected tracers, along with the corresponding linear partition coefficient, determined by a linear regression of the partitioning data in the dilute range. The UNIFAC model, a thermodynamic equilibrium model commonly employed to estimate equilibrium phase behavior, provides good estimations of overall phase behavior, but was found to over predict partition coefficients in the linear range. Overall, Chapter 4 demonstrates the importance of careful laboratory measurements to characterize the exact partition coefficient as well as the concentration range in which linear partitioning can be safely assumed.

Once thorough characterization of the equilibrium behavior of each tracer was complete, focus shifted to studying the processes influencing partitioning tracer transport. Chapter 5 examined the importance of surface capacity, and diffusional resistances in both the aqueous and DNAPL phases in a 1-D column system comprised of TCE-DNAPL ganglia. Application of a 1-D numerical model to the column tracer BTCs shows that neither diffusion in the TCE-DNAPL nor tracer accumulation at the DNAPL/water interface are important transport processes in these column systems. A linear driving force model, using

the Powers et al. (1992) mass transfer coefficient (derived from NAPL dissolution experiments) is able to adequately capture partitioning tracer BTCs. This suggests that diffusion through an aqueous boundary layer surrounding the TCE-DNAPL droplets is the controlling mechanism in partitioning tracer transport in these column systems. Additionally, it was demonstrated that equilibrium partitioning, another common assumption in partitioning tracer tests, is not a safe assumption at flow rates often employed in field tracer tests.

Upon characterizing transport at one end member of pool fraction (a region comprising TCE-DNAPL ganglia), Chapter 6 examined partitioning tracer transport at the other end member of pool fraction (a region comprising one large TCE-DNAPL pool). Here, it was hypothesized that diffusional resistance in the DNAPL phase is more important because of the longer diffusion path length, relative to that of TCE-DNAPL ganglia. Three tracer tests were conducted in a 2-D box system containing a source zone comprised of a single, large, TCE-DNAPL pool. The tests employed different flow rates and the use of flow interruptions to examine their influence on both overall and local-scale tracer transport. Modeling of BTCs resulting from the no flow interruption test demonstrate that partitioning tracer transport through a pooled source zone can be described with a linear driving force model employing the Nambi and Powers (2003) mass transfer correlation (developed from NAPL pool dissolution experiments). This model is able to describe local BTCs as well as overall effluent BTCs. A sensitivity analysis to available mass transfer coefficient correlations indicates that the Powers et al. (1992, 1994) correlations (developed

from NAPL ganglia dissolution) are also able to describe partitioning tracer transport in pool dominated systems.

Once flow was characterized at the two end members of pool fraction, tracer transport in heterogeneous source zones was examined (Chapter 7). Specifically, three source zones, one of each low, mid and high pool fraction, were created in three 2-D aquifer cells. The focus here was to examine the influence of push-pull injection and extraction flow rates on resulting BTCs for each pool fraction. It was hypothesized that a slow injection flow rate followed by a fast extraction flow rate would take advantage of the differences in diffusion path length between ganglia and pools, enabling the differentiation of high and low pool fraction source zones. Results indicate that all three flow rate combinations (fast injection, fast extraction; slow injection, fast extraction; fast injection, fast extraction) result in similar BTCs. This suggests that the mass transfer limitation between the ganglia and pools are not distinct enough to be interrogated with the selected flow rate. The implications of these results are that information is not lost when using a fast-fast test, which is advantageous in the field where faster flows on the push and pull phase may reduce costs and increase practicability (i.e., ability to interrogate more locations in a fixed amount of time). Additionally, results of the push-pull tests indicate that though different source zones can result in distinct BTCs, pool fraction does not seem to be the metric to which these differences are related.

Modeling of the push-pull BTCs show that the commonly employed analytical solution, which assumes a uniform geology, uniform saturation

distribution and equilibrium partitioning, cannot capture the partitioning behavior of the higher partitioning tracers. Since it is these higher partitioning tracers that contain most of the information on DNAPL saturation, the analytical solution does not provide good estimates of overall DNAPL saturation. However, when the flow field is well understood, a linear driving force model, using the Nambi and Powers (2003) mass transfer correlation, can adequately describe partitioning BTCs. Use of the linear driving force model to examine the importance of assumptions implicit in the analytical solution indicates that assuming equilibrium partitioning and/or a uniform saturation distribution lead to the poor performance of the analytical solution. A model that incorporates either kinetic transport or the actual saturation distribution is able to capture the general shape of higher partitioning tracers. Best results occur when models include both kinetic mass transfer and the actual saturation distribution.

The linear driving force model validated in Chapter 7 was used to conduct 2-octanol push-pull experiments in 40 artificial source zones to examine the ability of the test to differentiate between source zones of different vertical and horizontal distributions. Results demonstrate that three different features of the 2-octanol BTC may provide information on DNAPL architecture. First, an inflection point occurring early in the BTC may be useful for estimating the amount of the vertical test domain containing DNAPL. Second, the point at which the normalized tracer concentration drops from 1.0, may help estimate the distance between the injection/extraction well and the front of the DNAPL source zone. Third, a second inflection point in the BTC appears to be related to both the

percent of the vertical domain containing DNAPL and the saturation of the DNAPL in the source zone. However, the information held in this second inflection point may be difficult to obtain in real source zones with heterogeneous DNAPL saturations. The simplified nature of the source zones from which these results are derived necessitates further study to validate the relationships discussed here.

### *9.2 –Scientific and Engineering Contributions*

- Rigorous liquid-liquid-equilibrium characterization of each 1-pentanol, 1-hexanol and 2-octanol in a ternary system comprised of the alcohol, water and trichloroethene. Characterization includes thermodynamic modeling using UNIFAC and establishment of dilute regions for which partitioning may be approximated as linear.
- Identification that tracer transport in a system of residual DNAPL saturation can be well approximated using a linear driving force model and a mass transfer coefficient derived from DNAPL dissolution experiments (i.e., diffusion and surface partitioning do not appreciably influence partitioning in ganglia dominated systems).
- Assessment that partitioning tracer transport in heterogeneous DNAPL source zones can be well predicted using a linear driving force model and a mass transfer coefficient derived from DNAPL pool dissolution experiments.
- Quantitative assessment of mass transfer correlations available for domains containing pooled DNAPL.

- Elucidation that push-pull partitioning tracer tests provide information on three characteristics of simplified DNAPL source zones: i) the distance between the injection/extraction well and the front of the DNAPL source zone; ii) the amount of the vertical domain containing DNAPL; iii) the average local saturation of the source zone.

### *9.3 – Recommendations*

The findings of this dissertation result in the following recommendations related to the use of push-pull tests to estimate overall DNAPL saturation. Quantification of the partition coefficient for each tracer at multiple concentrations is critical. Where possible, the partitioning should be characterized using DNAPL and groundwater collected from the site. This quantification will aid in selecting applied concentrations from within the range of concentrations where the partitioning can be reasonably approximated as linear, thereby increasing the accuracy when interpreting partitioning tracer test results. Results of this work, and of others (e.g. Davis et al., 2002; Istok et al., 2002), suggest caution should be exercised when considering use of current analytical solutions to interpret push-pull test BTCs. The assumptions underlying these solutions are rarely met in the field, where it is difficult to ensure there is equilibrium partitioning within a zone of uniform DNAPL saturation. Where these assumptions are violated, use of the analytical solution will result over-estimation, possibly extreme over-estimation, of the overall DNAPL saturation.

Presently the main alternative to the analytical solution is to analyze breakthrough data using the method of moments. This type of analysis is superior

to existing analytical solutions, but the method tends to underestimate DNAPL saturations, especially when the retardation factors are not between 1.2 and 4.0 as suggested by Jin et al. (1997) and Annable et al. (1998a). Thus, great care should be taken when basing remedial action decisions on mass estimates obtained using the methods of moments. The method may be better suited to differentiating zones of high and low saturation within a given source zone.

Future research should consider that the current analytical solutions can be enhanced or reworked to include rate-limited partitioning and some degree of nonuniformity in the DNAPL saturation. The research described in this dissertation suggests existing mass transfer correlations - those developed for dissolution - hold promise for application. While these correlations are often a function of spatially-dependent DNAPL saturation, the research herein illustrates the benefits of using these correlations even when the DNAPL distribution is assumed to be uniform. The result suggests inclusion of the kinetics may be the most important next step in the evolution of analytical models employed to interpret push-pull tests. One example of work in this area is that of Huang et al. (2010).

Research in this dissertation shows how asymmetric breakthrough curves obtained within localized regions of a source zone may be interpreted using the inflection points of the BTC (Chapter 8). While the correlations for %Z and saturation developed therein are currently restricted to 2-D rectangular domains, there approach developed here holds substantial promise for increasing the utility of analytical solutions that incorporate mass transfer kinetics. The approach of

using the BTC characteristics (location of inflection points) to characterize the %Z should enable models that include kinetic mass transfer to estimate the overall saturation within the vertical portion of the domain containing DNAPL, even when the saturation is assumed to be uniform within the vertical portion of the domain containing DNAPL. The observation that kinetics and vertical extent of DNAPL are the two most important parameters controlling the shape of the push-pull BTC also establishes a foundation for future research aimed at upscaling the kinetics for use in simplified modeling tools.

It should be noted that the aforementioned recommendations focus on interpreting partitioning BTCs in cases where the non-partitioning BTC is smooth and well behaved. If the non-partitioning BTC has inflections in slope, similar to those seen in the low pool fraction fast-fast and slow-fast tests (Figures 7.3 and 7.4), there is likely a large degree of non-uniformity in the flow field that cannot be captured by existing tools. Thus it is recommended that tests in which the bromide BTC contains multiple inflection points be re-run or excluded, as there is not currently a robust way of analyzing the partitioning data associated with the test.

Additional recommendations for future work on this research focus on the 2-D box experiments, both pooled source zone and heterogeneous source zone. It would be beneficial to develop an unconfined model to examine tracer transport in these systems, as this would be more realistic to the experimental systems in which these tests were conducted. This modification may enable the model to better capture the local port data from experiments 2 and 3 in Chapter 6. It is

hypothesized that the flow field generated near the TCE-DNAPL pool upon restarting flow (after the flow interruption) cannot be fully captured with an unconfined model. Additionally, it is hypothesized that the unusual flow field seen in the low pool fraction fast-fast test may be better captured using an unconfined model. Therefore, an unconfined model could be useful for interpreting tests conducted in both Chapters 6 and 7.

Results from the push-pull tests conducted in the 40 simplified source zones discussed in Chapter 8 indicate that these tests may be able to provide information on source zone DNAPL distribution. However, work in more complicated 2-D source zones is necessary for the relationships developed in Chapter 8 to prove useful for interpreting field partitioning tracer push-pull tests. First, push-pull tests should be conducted in heterogeneous source zones where the actual DNAPL spill is simulated, resulting in more realistic source zones than those used herein. Three more realistic source zones were examined using light transmission data from the low, mid and high pool fraction boxes in Chapter 7. However, two of these source zones have very similar source zones in terms of horizontal distribution, vertical distribution and overall DNAPL mass. Push-pull tests should be simulated in heterogeneous source zones that vary in the same aspects as the contrived source zones (i.e. vertical distribution, horizontal distribution, distance between the front of the source zone and the injection/extraction well and total DNAPL mass). If results of these simulations indicate similar relationships to those found in Chapter 8, two or three of the simulated heterogeneous source zones should be examined experimentally.

If additional 2-D simulations and experiments in heterogeneous source zones also indicate that push-pull BTCs do provide information on DNAPL source zone distribution, push-pull tests should be conducted in 3-D push-pull model. This would allow for the examination of the influence of radial flow around the well and the added complication of DNAPL contamination on multiple sides of the well. Here the best design for use in the field could be further refined. For example, the injection/extraction well screen could be packed to confine flow to one side of the well. Results from that packing could be compared to results generated by allowing flow through the entire circumference of the well. Results may indicate if the test can be used to estimate architecture all around the well, or if performance is greatly improved by localizing the test to one side of the well. Additionally, the use of a 3-D model can be used to up-scaling results, which is necessary before applying them to field push-pull tests. The qualitative relationships seen in Chapter 8 may still hold in field tests, but differences in vertical and horizontal correlation lengths will likely necessitate different quantitative correlations between source zone architecture and the key BTC features identified in Chapter 8.

## APPENDIX I

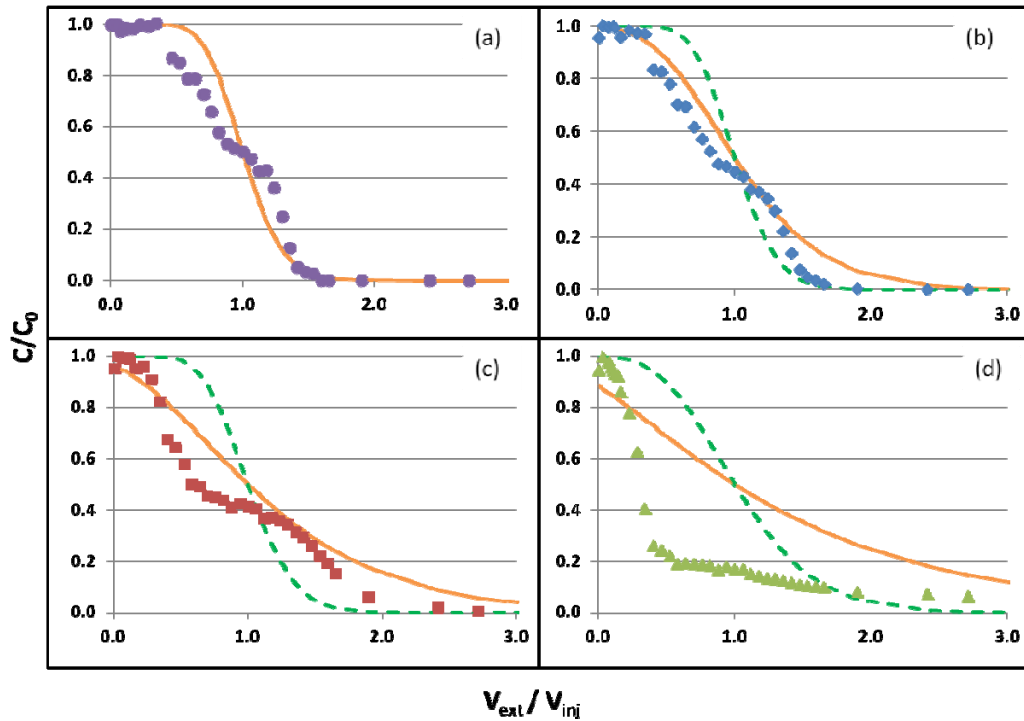


**Figure A1.1** Equilibrium modeling of low pool fraction fast-fast experiment. Displayed are bromide (a), 1-pentanol (b), 1-hexanol (c) and 2-octanol (d) BTCs. Each panel includes a best fit BTC (solid line) and panels b-d include equilibrium predictions using the measured saturation.

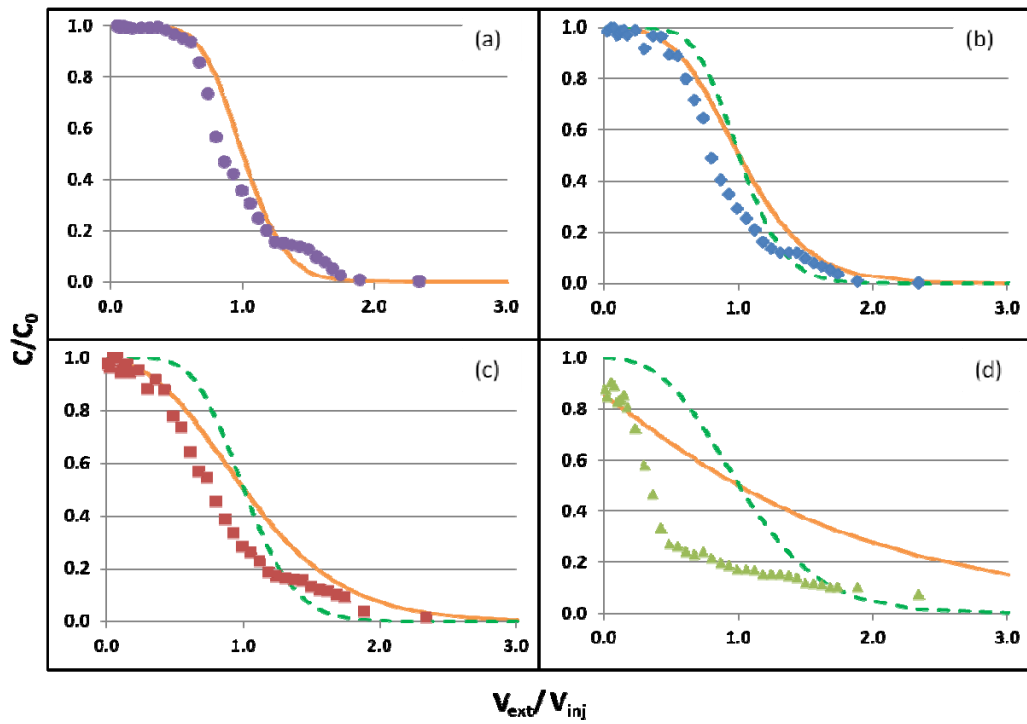


**Figure A1.2** Equilibrium modeling of low pool fraction slow-fast experiment. Displayed are bromide (a), 1-pentanol (b), 1-hexanol (c) and 2-octanol (d) BTCs. Each panel includes a best fit BTC (solid line) and panels b-d include equilibrium predictions using the measured saturation.

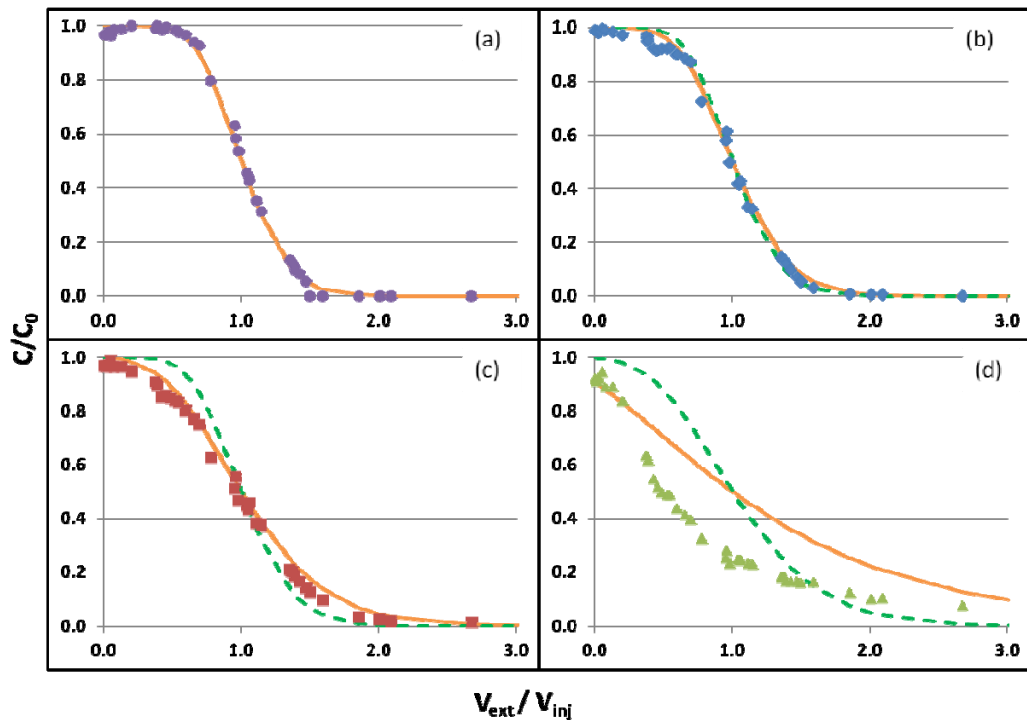


**Figure A1.3** Equilibrium modeling of low pool fraction fast-slow experiment. Displayed are bromide (a), 1-pentanol (b), 1-hexanol (c) and 2-octanol (d) BTCs. Each panel includes a best fit BTC (solid line) and panels b-d include equilibrium predictions using the measured saturation.

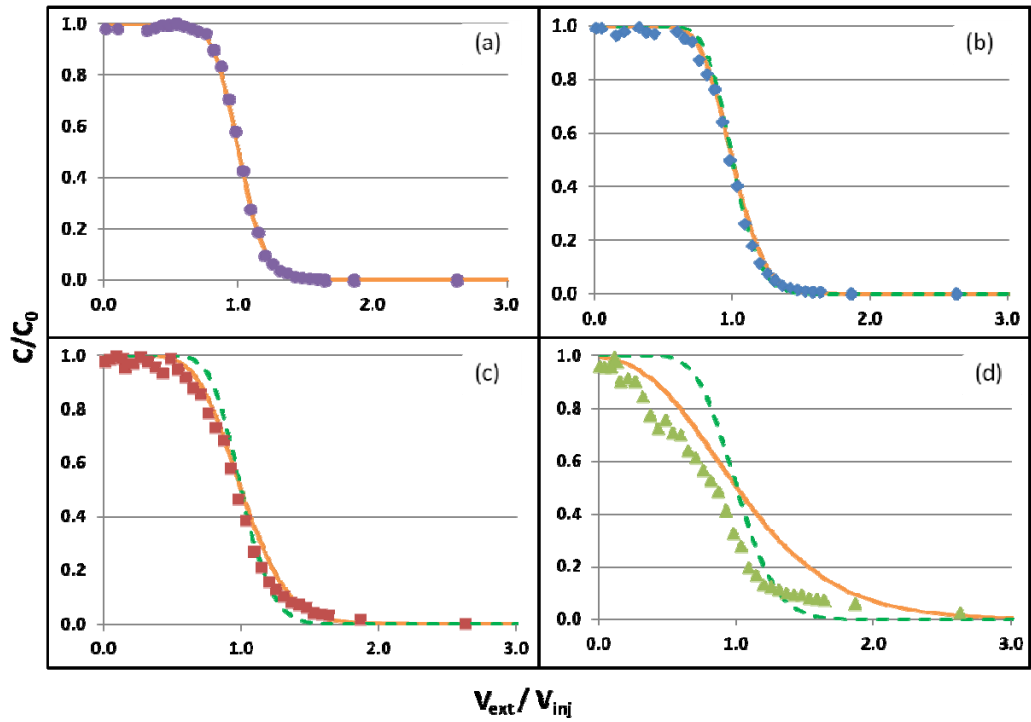


**Figure A1.4** Equilibrium modeling of mid pool fraction fast-fast experiment. Displayed are bromide (a), 1-pentanol (b), 1-hexanol (c) and 2-octanol (d) BTCs. Each panel includes a best fit BTC (solid line) and panels b-d include equilibrium predictions using the measured saturation.

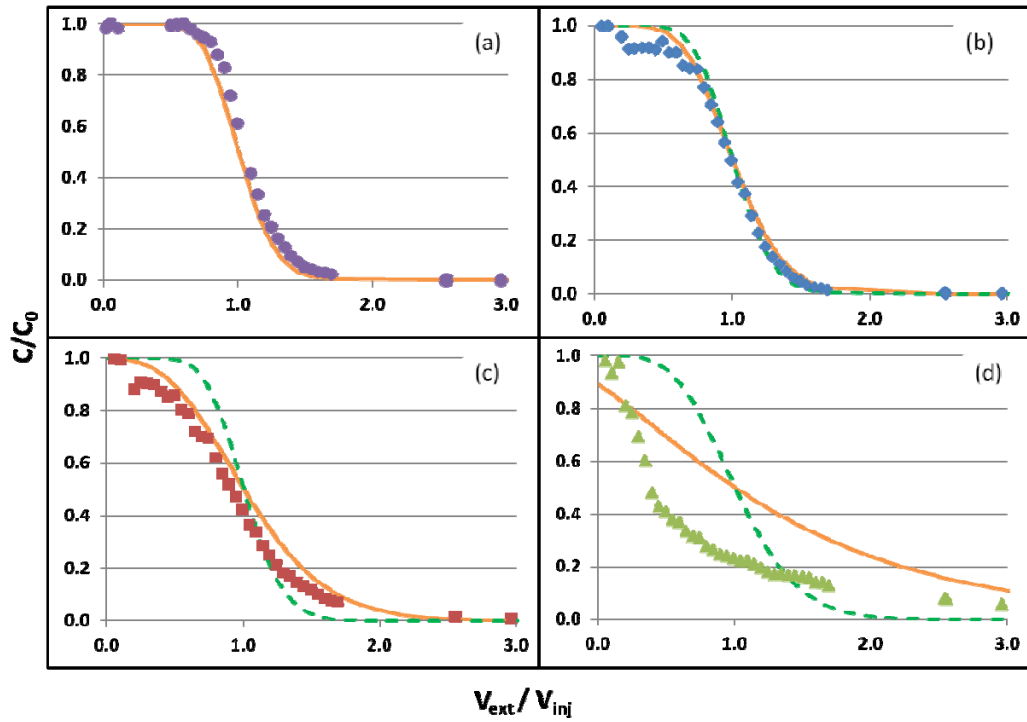


**Figure A1.5** Equilibrium modeling of mid pool fraction slow-fast experiment. Displayed are bromide (a), 1-pentanol (b), 1-hexanol (c) and 2-octanol (d) BTCs. Each panel includes a best fit BTC (solid line) and panels b-d include equilibrium predictions using the measured saturation.

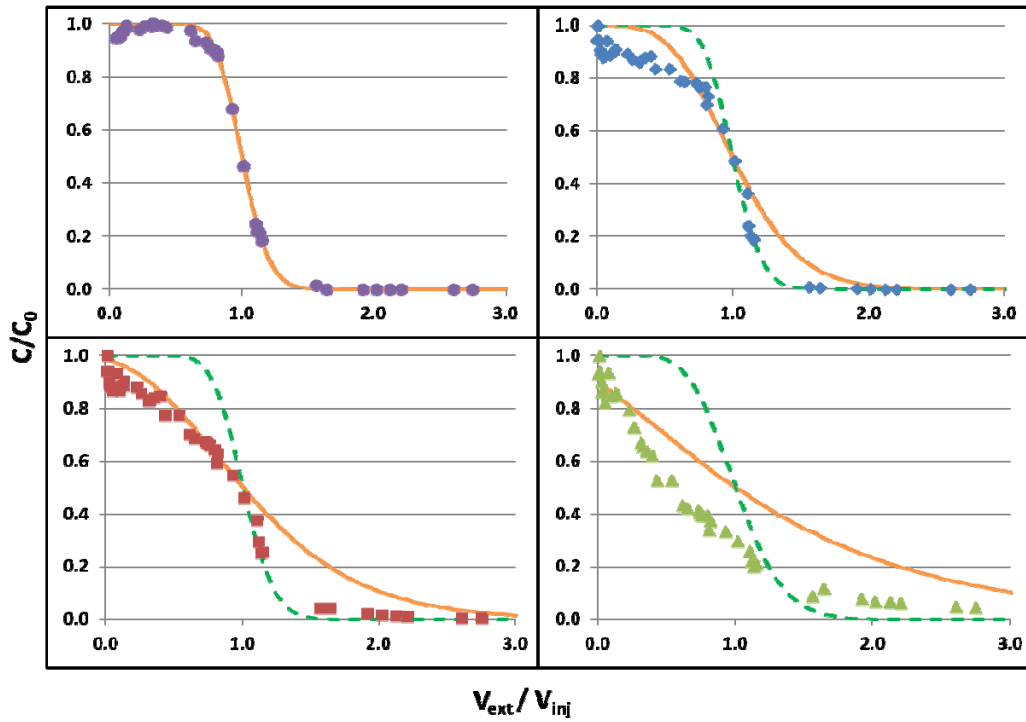


**Figure A1.6** Equilibrium modeling of mid pool fraction fast-slow experiment. Displayed are bromide (a), 1-pentanol (b), 1-hexanol (c) and 2-octanol (d) BTCs. Each panel includes a best fit BTC (solid line) and panels b-d include equilibrium predictions using the measured saturation.

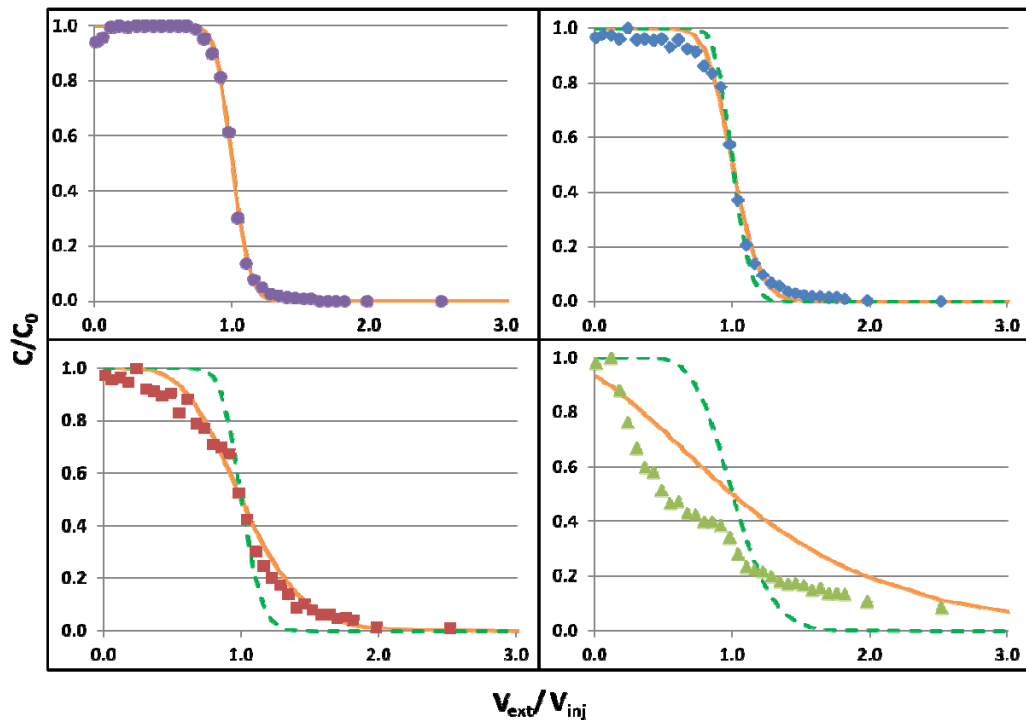


**Figure A1.7** Equilibrium modeling of high pool fraction fast-fast experiment. Displayed are bromide (a), 1-pentanol (b), 1-hexanol (c) and 2-octanol (d) BTCs. Each panel includes a best fit BTC (solid line) and panels b-d include equilibrium predictions using the measured saturation.

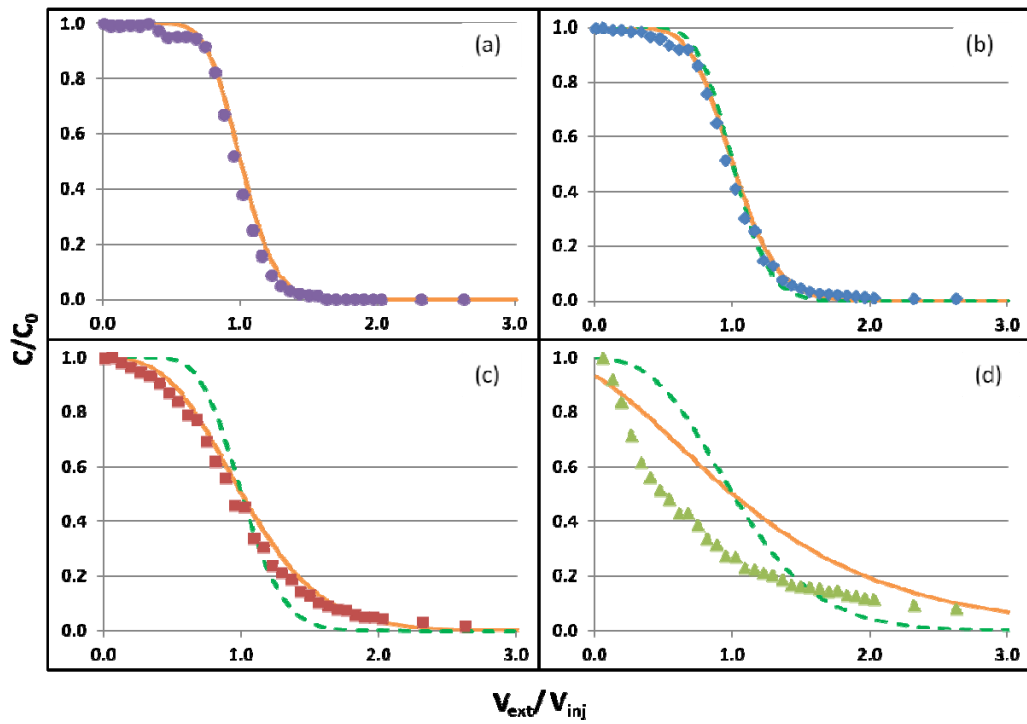


**Figure A1.8** Equilibrium modeling of high pool fraction slow-fast experiment. Displayed are bromide (a), 1-pentanol (b), 1-hexanol (c) and 2-octanol (d) BTCs. Each panel includes a best fit BTC (solid line) and panels b-d include equilibrium predictions using the measured saturation.

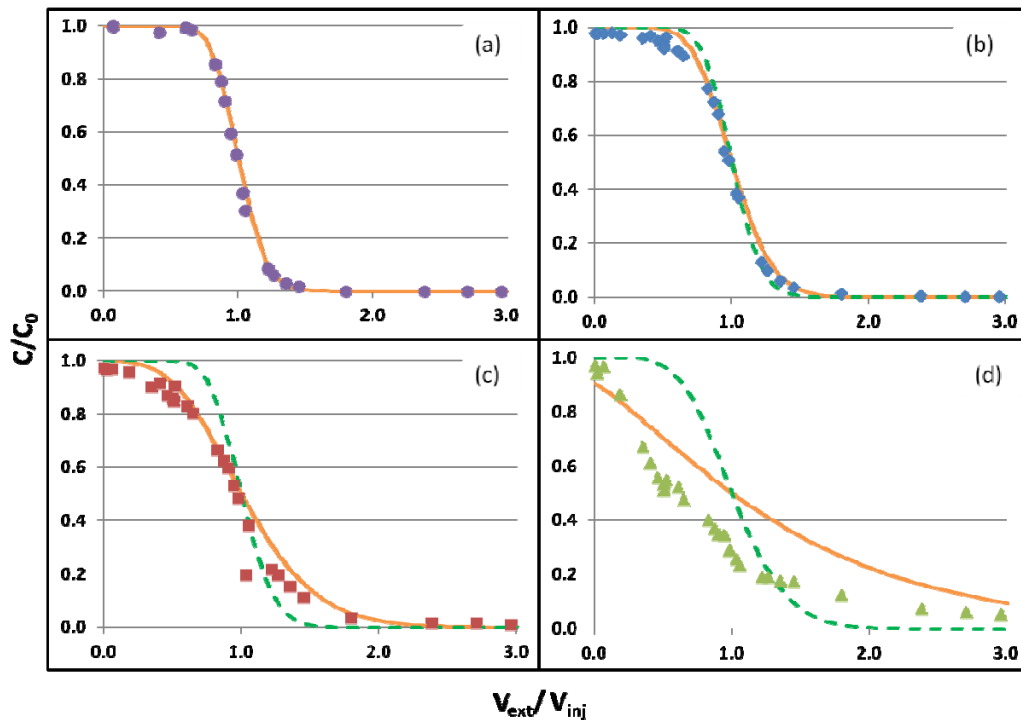


**Figure A1.9** Equilibrium modeling of high pool fraction fast-slow experiment. Displayed are bromide (a), 1-pentanol (b), 1-hexanol (c) and 2-octanol (d) BTCs. Each panel includes a best fit BTC (solid line) and panels b-d include equilibrium predictions using the measured saturation.

**Table A1.1** Analytical solution estimations of dispersivity, overall TCE-DNAPL saturation and volume for the low pool fraction box. Also included are the measured TCE-DNAPL source zone saturations and volumes.

Low Pool Fraction							
Test	Tracer	Fit alpha (cm)	Sum of Squared Error <sup>1</sup>	Estimated DNAPL Sat.	Estimated DNAPL Vol. (mL)	Measured DNAPL Sat. <sup>2</sup>	Measured DNAPL Vol. (mL) <sup>2</sup>
Fast-Fast	Bromide	0.9	0.02	-	-	1.8%	32.5
	1-Pentanol	-	0.19	46.3%	841	1.8%	32.5
	1-Hexanol	-	0.38	37.5%	681	1.8%	32.5
	2-Octanol	-	2.98	14.0%	254	1.8%	32.5
Slow-Fast	Bromide	1.0	0.25	-	-	1.6%	27.9
	1-Pentanol	-	0.39	26.1%	443	1.6%	27.9
	1-Hexanol	-	0.50	18.2%	309	1.6%	27.9
	2-Octanol	-	2.29	15.6%	265	1.6%	27.9
Fast-Slow	Bromide	1.1	0.02	-	-	1.2%	20.5
	1-Pentanol	-	0.03	9.8%	170	1.2%	20.5
	1-Hexanol	-	0.05	11.5%	200	1.2%	20.5
	2-Octanol	-	1.26	9.5%	165	1.2%	20.5

<sup>1</sup>The sum of squared error for bromide corresponds to fitting alpha in equation 7.2 to the bromide data. For the partitioning tracers, sum of squared error corresponds to fitting  $x_{max}$  in equation 7.2 to each partitioning BTC.  $x_{max}$  is then used to calculate DNAPL saturation.

<sup>2</sup>Measured TCE-DNAPL saturations and volumes vary between experiments due to both TCE-DNAPL dissolution/volatilization between experiments and the swept volume (which is equal to the tracer pulse volume).

**Table A1.2** Analytical solution estimations of dispersivity, overall TCE-DNAPL saturation and volume for the mid pool fraction box. Also included are the measured TCE-DNAPL source zone saturations and volumes.

<b>Mid Pool Fraction</b>							
<b>Test</b>	<b>Tracer</b>	<b>Fit alpha (cm)</b>	<b>Sum of Squared Error<sup>1</sup></b>	<b>Estimated DNAPL Sat.</b>	<b>Estimated DNAPL Vol. (mL)</b>	<b>Measured DNAPL Sat.<sup>2</sup></b>	<b>Measured DNAPL Vol. (mL)<sup>2</sup></b>
Fast-Fast	Bromide	0.4	0.03	-	-	0.8%	15.1
	1-Pentanol	-	0.02	10.3%	200	0.8%	15.1
	1-Hexanol	-	0.07	10.2%	198	0.8%	15.1
	2-Octanol	-	0.63	7.4%	144	0.8%	15.1
Slow-Fast	Bromide	0.8	0.08	-	-	1.4%	30.8
	1-Pentanol	-	0.06	19.9%	436	1.4%	30.8
	1-Hexanol	-	0.17	19.5%	427	1.4%	30.8
	2-Octanol	-	1.87	17.2%	376	1.4%	30.8
Fast-Slow	Bromide	0.5	0.04	-	-	1.4%	30.8
	1-Pentanol	-	0.28	51.6%	1074	1.4%	30.8
	1-Hexanol	-	0.27	47.0%	978	1.4%	30.8
	2-Octanol	-	1.01	24.0%	500	1.4%	30.8

<sup>1</sup>The sum of squared error for bromide corresponds to fitting alpha in equation 7.2 to the bromide data. For the partitioning tracers, sum of squared error corresponds to fitting  $x_{max}$  in equation 7.2 to each partitioning BTC.  $x_{max}$  is then used to calculate DNAPL saturation.

<sup>2</sup>Measured TCE-DNAPL saturations and volumes vary between experiments due to both TCE-DNAPL dissolution/volatilization between experiments and the swept volume (which is equal to the tracer pulse volume).

**Table A1.3** Analytical solution estimations of dispersivity, overall TCE-DNAPL saturation and volume for the high pool fraction box. Also included are the measured TCE-DNAPL source zone saturations and volumes.

<b>High Pool Fraction</b>							
Test	Tracer	Fit alpha (cm)	Sum of Squared Error <sup>1</sup>	Estimated DNAPL Sat.	Estimated DNAPL Vol. (mL)	Measured DNAPL Sat. <sup>2</sup>	Measured DNAPL Vol. (mL) <sup>2</sup>
Fast-Fast	Bromide	0.20	0.02	-	-	1.8%	32.1
	1-Pentanol	-	0.05	25.6%	334	1.8%	32.1
	1-Hexanol	-	0.09	38.2%	680	1.8%	32.1
	2-Octanol	-	0.92	37.4%	666	1.8%	32.1
Slow-Fast	Bromide	0.5	0.04	-	-	2.0%	31.9
	1-Pentanol	-	0.03	13.4%	216	2.0%	31.9
	1-Hexanol	-	0.06	19.2%	309	2.0%	31.9
	2-Octanol	-	0.98	12.9%	208	2.0%	31.9
Fast-Slow	Bromide	0.4	0.02	-	-	1.8%	29.4
	1-Pentanol	-	0.04	18.8%	328	1.8%	29.4
	1-Hexanol	-	0.13	23.8%	415	1.8%	29.4
	2-Octanol	-	0.73	22.2%	387	1.8%	29.4

<sup>1</sup>The sum of squared error for bromide corresponds to fitting alpha in equation 7.2 to the bromide data. For the partitioning tracers, sum of squared error corresponds to fitting  $x_{max}$  in equation 7.2 to each partitioning BTC.  $x_{max}$  is then used to calculate DNAPL saturation.

<sup>2</sup>Measured TCE-DNAPL saturations and volumes vary between experiments due to both TCE-DNAPL dissolution/volatilization between experiments and the swept volume (which is equal to the tracer pulse volume).

## REFERENCES

- Abrams, D.S. and J.M. Prausnitz. 1975. Statistical thermodynamics of liquid-mixtures – new expression for excess Gibbs energy of partially or completely miscible systems. *AIChE J.*, 21:116-128.
- Abriola, L.M., Christ, J.A., Pennell, K.D., Ramsburg, C.A., in review. Chapter 10: Source zone remediation challenges, in: Kitanidis, P.K., McCarty, P.L., (Eds.), *Delivery and mixing in the subsurface: Processes and design principles for in situ remediation*. In press.
- Abriola, L.M. 2005. Contaminant source zones: remediation or perpetual stewardship? *Environmental Health Perspectives*, 113(7):438-439.
- Annable, M.D., P.S.C. Rao, K. Hatfield, W.D. Graham, and C.G. Enfield. 1998a. Partitioning tracers for measuring residual NAPL: Field-scale test results. *Journal of Environmental Engineering*, June, 498-503.
- Annable, M.D., Jawitz, J.W., P.S.C. Rao, D.P. Dai, H. Kim, and A.L. Wood. 1998b. Field evaluation of interfacial and partitioning tracers for characterization of effective NAPL-water contact areas. *Ground Water* 36(3): 495-502.
- Annable, M.D., Hatfield, K., Cho, J. Klammler, H. Parker, B., Cherry, J.A., and Rao, P.S.C. 2005. Field-scale evaluation of the passive flux meter for simultaneous measurement of groundwater and contaminant fluxes. *Environ. Sci. Technol.*, 39(18): 7194-7201
- Bauer, S., Bayer-Raich, M., Holder, T., Kolesar, C., Müller, D., and Ptak, T. 2004. Quantification of groundwater contamination in an urban area using integral pumping tests. *J.Contam. Hydrol.*, 75:183-213.
- Bayer-Raich, M. Baumann, R. and Ptak, T. 2003a. Application of pumping tests to estimate contaminant mass fluxes in a multi-layered aquifer: a numerically simulated field-scale experiment at the SAFIRA-Bitterfeld site. In: *Groundwater Quality: Natural and Enhanced Restoration of Groundwater Pollution*, Thornton, S.F., Oswald S.E. (Eds.), IAHS Publication 275, IAHS Press, Wallingford, Oxfordshire, UK pp. 257-263.
- Bayer-Raich, M. Jarsjö, J. Holder, T., and Ptak, T. 2003b. Numerical estimations of contaminant mass flow based upon concentration measurements in pumping wells. *ModelCare 2002: A Few Steps Closer to Reality*, IAHS Publication 277, IAHS Press, Wallingford, Oxfordshire, UK pp. 10-16.

- Bayer-Raich, M. Jarsjö, J.Liedl, R., Prak, T., and Teutsch, G. 2004. Average contaminant concentration and mass flow in aquifers from time-dependent pumping well data: Analytical framework. *Water Resour. Res.*, 40: W08303.
- Beyke, G. and D. Flemming. 2005. In Situ Thermal Remediation of DNAPL and LNAPL Using Electrical Resistance Heating. *Remediation*, Summer 2005: 5-22
- Bockelmann, A., Ptak, T., and G. Teutsch. 2001. An analytical quantification of mass fluxes and natural attenuation rate constants at former gasworks site. *Journal of Contaminant Hydrology*. 53:429-453.
- Borden, R.C., Daniel, R.A., LeBrun L.E., and Davis, C.W. 1997. Intrinsic biodegradation of MTBE and BTEX in a gasoline-contaminated aquifer. *Water Resour. Res.*, 33:1105-1115.
- Brooks, M.C., M.D. Annable, P.S.C. Rao, K. Hatfield, J.W. Jawitz, W.R. Wise, A. L. Wood, C. G. Enfield. 2002. Controlled release, blind tests of DNAPL characterization using partitioning tracers. *Journal of Contaminant Hydrology*, 59: 187-210.
- Brooks, M.C., A.L. Wood, M.D. Annable, K Hatfield, J. Cho, C. Holbert, P.S.C. Rao, C.G. Enfield, K. Lynch, R.E. Smith. 2008. Changes in contaminant mass discharge from DNAPL source mass depletion: Evaluation at two field sites. *Journal of Contaminant Hydrology*. 102:140-153
- Brusseau, M.L., Rao, P.S.C., 1989. Sorption nonideality during organic contaminant transport in porous-media. *Critical Reviews in Environmental Control* 19 (1), 33-99.
- Brusseau, M.L., 1992. Rate-limited mass transfer and transport of organic solutes in porous media that contain immobile immiscible organic liquid. *Water Resour. Res.* 28, 33–45.
- Cain, R.B., Johnson, G.R., McCray, J.E., Blanford, W.J., Brusseau, M. L. 2000. Partitioning tracer tests for evaluating remediation performance. *Ground Water* 38, 752-761.
- California Environmental Protection Agency. Air Resources Board. 2007. Amended Dry Cleaning ATCM Requirements. Sacramento, CA.
- Chang, C.H., Franes, E.I., 1994. Dynamic tension behavior of aqueous octanol solutions under constant-area and pulsating-area conditions. *Chemical Engineering Science* 49 (3), 313-325.
- Christ, J.A., C.A. Ramsburg, L.M. Abriola, K.D. Pennell and F.E. Löffler. 2005. Coupling aggressive mass removal with microbial reductive dechlorination for

remediation of DNAPL source zones: A review and assessment. *Environmental Health Perspectives*, 113(4): 465-477.

Christ, J.A., C.A. Ramsburg, K.D. Pennell, and L.M. Abriola. 2006. Estimating mass discharge from DNAPL source zones using upscaled mass transfer coefficients: An evaluation using multiphase numerical simulations. *Water Resources Research*, 42, W11420, doi:10.1029/2006WR004886

Christ, J.A., K.D. Pennell and L.M. Abriola. 2012. Quantification of Experimental Subsurface Fluid Saturation from High-resolution Source Zone Images. *Water Resources Research*, 48, W01517, doi: 10.1029/2011WR010400

Chrysikopoulos, C.V. 1995. Three-Dimensional analytical models of contaminant transport from nonaqueous phase liquid pool dissolution in saturated subsurface formations. *WRR* 31(4):1137-1145.

Chrysikopoulos, C.V. and T.J. Kim. 2000. Local mass transfer correlations for nonaqueous phase liquid pool dissolution in saturated porous media. *Transport in Porous Media* 38:167-187.

Cooling, M.R., Khalfoui, B. Newsham, D.M.T., 1992. Phase-equilibria in very dilute mixtures of water and unsaturated chlorinated hydrocarbons and of water and benzene. *Fluid Phase Equilibria*, 88 (1-2), 217-229.

Conant, B., Cherry, J.A., and R.W. Gillham. 2004. A PCE groundwater plume discharging to a river: influence of the streambed and near-river zone on contaminant distributions. *JCH*, 73(1-4):249-279.

Costanza, J., Davis, W.M., 2000. Rapid detection of volatile organic compounds in the subsurface by membrane introduction into a direct sampling ion trap mass spectrometer. *Field Analytical Chemistry and Technology* 4 (5), 246-254.

Cussler, E.L., 1984. *Diffusion: Mass Transfer in Fluid Systems*, Cambridge University Press, New York, NY.

Dai, D., Barranco Jr., F.T., Illangasekare, T.H., 2001. Partitioning and interfacial tracers for differing NAPL entrapment configuration: column-scale investigation. *Environmental Science and Technology* 35, 4894-4899.

Darnault C.J.G., J.A. Throop, D.A. DiCarlo, A. Rimmer, T.S. Steenhuis, J.Y. Parlange. 1998. Visualization by light transmission of oil and water contents in transient two-phase flow fields. *J. Contam. Hydrol.*, 31(3-4), 337-348.

Davis, B.M., J.D. Istok, and L. Semprini. 2005. Numerical simulations of radon as an in situ partitioning tracer for quantifying NAPL contamination using push-pull tests. *Journal of Contaminant Hydrology*, 78: 87-103.

Davis BM; Istok JD and L. Semprini. 2002. Push-pull partitioning tracer tests using radon-222 to quantify non-aqueous phase liquid contamination. *Journal of Contaminant Hydrology*, 58(1-2): 129-146.

DeGroot, D.J. 1996. Analyzing spatial variability of insitu soil properties. *Uncertainty in the Geologic Environment: From Theory to Practice*, GSP No. 58, ASCE, Vol.1, pp. 210-238.

Dekker, T.J. and L.M. Abriola. 2000. The influence of field-scale heterogeneity on the infiltration entrapment of dense nonaqueous phase liquids in saturated formation. *Journal of Contaminant Hydrology*, 42:187-218.

Dwarakanath, V. 1997. Characterization and remediation of aquifers contaminated by non-aqueous phase liquids using partitioning tracers and surfactants. Doctoral dissertation. University of Texas at Austin, Department of Petroleum Engineering.

Dwarakanath, V., Pope, G.A., 1998. New approach for estimating alcohol partition coefficients between nonaqueous phase liquids and water. *Environmental Science and Technology* 32, 1662-1666.

Einarson, M. D. and Mackay, D.M. 2001. Predicting impacts of groundwater contamination. *Environ. Sci. Technol*, 35: 66A-73A.

Ervin, R.E., Boroumand, A.B., Abriola, L.M. and C.A. Ramsburg. 2011. Kinetic limitation on tracer partitioning in ganglia dominated source zones. *Journal of Contaminant Hydrology*, 126:195-207.

Essad, H.I., and K.M. Hess. 1993. Monte carlo simulations of multiphase flow incorporating spatial variability of hydraulic properties. *Ground Water*, 31:123-134.

Falta, R.W., Rao, P.S.C. and Basu, N. 2005. Assessing the impacts of partial mass depletion in DNAPL source zones I. Analytical modeling of source strength functions and plume response, *J. Contam. Hydrol.*, 78, 259-280.

Ferrari, M., Liggieri, L., Ravera, F., Amodio, C., Miller, R., 1997. Adsorption kinetics of alkylphosphine oxides at water/hexane interface 1. Pendant drop experiments. *Journal of Colloid and Interface Science* 186, 40-45.

Fredenslund, A., Jones, R.L., Prausnitz, J.M. 1975. Group-contribution estimation of activity coefficients in nonideal liquid-mixtures, *AIChE Journal* 21 (6), 1086-1099.

Gelhar, L.W. and M.A. Collins. 1971. General analysis of longitudinal dispersion in nonuniform flow. *Water Resources Research*, 7(6) DOI: 10.1029/WR007i006p01511

Gmehling, J., U. Onken and W. Arlt (1977-1990). Vapor-Liquid Equilibrium Data Collection. Chemistry Data Series, Vol. I, Parts 1-8, DECHEMA, Frankfurt/Main, Germany.

Gmehling, J., Rasmussen, P., Fredenslund A., 1982. Vapor-liquid-equilibria by UNIFAC group contribution – revision and extension 2. *Industrial and Engineering Chemistry Process Design and Development* 21, 118-127.

Goltz, M.N., Kim, S., Yoon, H. and Park, J. 2007. Review of groundwater contaminant mass flux measurement, *Environ. Eng. Res.*, 12: 176-193.

Gossett, J.M. 1987. Measurement of Henry's Law Constants for C1 and C2 chlorinated hydrocarbons. *ES&T*, 21(2):202-208.

Gracia, A., Lachaise, J., Cucuphat, C., Bourrel, M., Salager, J.L., 1993. Improving solubilization in microemulsions with additives 2. Long chain alcohol as lipophilic linkers. *Langmuir*, 9: 3371-3374.

Guilbeault, M.A., B.L. Parker, and J.A. Cherry. 2005. Mass and flux distributions from DNAPL zones in Sandy Aquifers. *Ground Water*, 43(1): 70-86.

Hansen, H.K., Rasmussen, P., Fredenslund, A., Schiller, M., Gmehling, J., 1991. Vapor-liquid equilibria by UNIFAC group contribution. 5. Revision and extension. *Industrial and Engineering Chemistry Research* 30 (10), 2352-2355.

Hartog, N., Cho, J., Parker, B., Annable, M.D., 2010. Characterization of a heterogeneous DNAPL source zone in the Borden aquifer using partitioning and interfacial tracers: Residual morphologies and background sorption. *Journal of Contaminant Hydrology* 115, 79-89.

Hatfield, K., Ziegler, J., Burris, D.R., 1993. Transport in porous media containing residual hydrocarbon. II. Experiments. *J. Environ. Eng* 199, 559–575.

Hatfield, K. Annable, M.D., Kuhn, S., Rao, P.S.C. and Campbell, T. 2002. A new method for quantifying contaminant flux at hazardous waste sites. *Groundwater Quality: Natural and Enhanced Restoration of Groundwater Pollution*. IAHS publication 275, pp. 25-31.

Hatfield, K. Annable, M.D., Cho, J., Rao, P.S.C. and Klammler, H. 2004. A direct passive method for measuring water and contaminant fluxes in porous media. *J. Contam. Hydrol.*, 75:155-181.

Hayduk, W., Laudie, H., 1974. Prediction of diffusion coefficients for nonelectrolytes in dilute aqueous solutions. *AIChE Journal* 20 (3), 611-615.

Hoffmann, B. 1969. Über die Ausbreitung gelöster Kohlenwassertoffe im Grundwasserleiter. Mitteilungen des Institutes für Wasserwirtschaft und Landwirtschaftlichen. Wasserbau-Heft. Teche. univ. Hannover, Germany, 197.

Holzmer, F.J., Pope, G.A. and Yeh, L. 2000. Surfactant-enhanced aquifer remediation of PCE DNAPL in low-permeability sand. In: Wickramanayake, G.B., Gavaskar, A.R., Gupta, N., (Eds.), *Treating Dense Nonaqueous-Phase Liquids (DNAPLs): Remediation of Chlorinated and Recalcitrant Compounds*, Battelle Press, Columbus, OH, pp. 211-218.

Hovarth, A.L, F.W Getzen, and Z. Maczynska. 1999. IUPAC-NIST Solubility Data Series 67. Halogenated Ethanes and Ethenes with Water. *Journal of Physical and Chemical Reference Data*, 28(2):395-627.

Huang, J., J.A. Christ and M.N. Goltz. 2010. Analytical solutions for efficient interpretation of single-well push-pull tracer tests. *Water Resources Research*, 46, W08538, doi:10.1029/2008WR007647.

Illangasakare, T.H., Ramsey, J.L., Jensen, K.H., and M. Butts. 1995. Experimental study of movement and distribution of dense organic contaminants in heterogeneous aquifers. *Journal of Contaminant Hydrology*, 20(1-2):1-25.

Imhoff, P.T., Jaffé, P.R., Pinder G.F., 1994. An experimental study of complete dissolution of a nonaqueous phase liquid in saturated porous media, *Water Resources Research* 30 (2), 307-320.

Imhoff, P.T., Pirestani, K., 2004. Influence of mass transfer resistance on detection of nonaqueous phase liquids with partitioning tracer tests. *Advances in Water Resources* 27, 429-444.

Istok, J.D., J.A. Field, M.H. Schroth, B.M. Davis, and V. Dwarakanath. 2002. Single-well “push-pull” partitioning tracer test for NAPL detection in the subsurface. *Environmental Science and Technology*, 36(12): 2708-2716.

Jalbert, M., Dane, J.H., Bahaminyakamwe, L., 2003. Influence of porous medium and NAPL distribution heterogeneities on partitioning inter-well tracer tests: a laboratory investigation. *Journal of Hydrology* 272, 79-94.

James, A.I., W.D. Graham, K. Hatfield, P.S.C. Rao, and M.D. Annable. 1997. Optimal estimation of residual non-aqueous phase liquid saturations using partitioning tracer concentration data. *Water Resources Research*, 33(12): 2621-2636.

- Jarsjö, J., Bayer-Raich, M. and Ptak, T. 2005. Monitoring groundwater contamination and delineating source zones at industrial sites: Uncertainty analyses using integral pumping tests. *J.Contam. Hydrol.*, 79: 107-134.
- Jawitz, J.W., M.D. Annable, P.S.C. Rao, and R.D. Rhue. 1998. Field implementation of a Winsor type I surfactant/alcohol mixture for in situ solubilization of a complex LNAPL as a single-phase microemulsion. *Environmental Science and Technology*, 32: 523-530.
- Jawitz, J.W., Sillan, R.K., Annable, M.D., Rao, P.S.C. and Warner, K., 2000. In-situ alcohol flushing of a DNAPL source zone at a dry cleaner site. *Environ. Sci. Technol.* 34 (17), 3722-3729
- Jawitz, J.W., Annable, M.D., Demmy, G.G., Rao, P.S.C., 2003. Estimating nonaqueous phase liquid spatial variability using partitioning tracer higher temporal moments. *Water Resources Research* 39 (7), 1192-1212.
- Jawitz, J. W., A. D. Fure, G. G. Demmy, S. Berglund, and P. S. C. Rao. 2005. Groundwater contaminant flux reduction resulting from nonaqueous phase liquid mass reduction. *Water Resources Research*, 41, W10408, doi:10.1029/2004WR003825.
- Jin, M., M. Delshad, V. Dwarakanath, D.C. McKinney, G.A. Pope, K. Sepehrnoori, C.E. Tilburg, and R.E. Jackson. 1995. Partitioning tracer test for detection, estimation and remediation performance assessment of subsurface nonaqueous phase liquids. *Water Resources Research*, 31(5): 1201-1211.
- Jin M., G.W. Butler, R.E. Jackson, P.E. Mariner, J.F. Pickens, G.A. Pope, C.L. Brown, D.C. McKinney. 1997. Sensitivity models and design protocol for partitioning tracer tests in alluvial aquifers. *Ground Water*, 35(6):964-972.
- Johnson, R.L., and J.F. Pankow. 1992. Dissolution of dense chlorinated solvents into groundwater. 2. Source functions for pools of solvent. *Environmental Science and Technology*, 26:896-901.
- Johnston, J.E. and J.M. Gibson. 2011. Probabilistic Approach to Estimating Indoor Air Concentrations of Chlorinated Volatile Organic Compounds from Contaminated Groundwater: A Case Study in San Antonio, Texas. *ES&T* 45:1007-1013.
- Kaluarachchi, J.J., and J.C. Parker. 1992. Multiphase flow in porous media with a simplified model for oil entrapment. *Transport in Porous Media*, 7:1-14.
- Kao, C. M., and Y. S. Wang. 2001. Field investigation of the natural attenuation and intrinsic biodegradation rates at an underground storage tank site. *Environ. Geol.*, 40, 622-631.

Kavanaugh, M.C. and P.S.C. Rao. 2003. The DNAPL remediation challenge: is there a case for source depletion? *EPA-600-R-03-143*

Kavanaugh, M., Deeb, R. and E. Hawley. 2011. Final Report-Fort Lewis: Diagnostic Tools for Performance Evaluation of Innovative In-Situ Remediation Technologies at Chlorinated Solvent-Contaminated Sites. Malcolm Pirnie, Inc. Funded by ESTCP.

Kim, J.K., Jung, J.Y., Kang, Y.T., 2007. Absorption performance enhancement by nano-particles and chemical surfactants in binary nanofluids. *International Journal of Refrigeration* 30, 50-57.

Kim, T.J. and C.V. Chrysikopoulos. 1999. Mass transfer correlations for nonaqueous phase liquid pool dissolution in saturated porous media. *WRR* 35(2):449-459.

King, M.W.G., Barker, J.F., Devlin, J.F. and Butler, B.J. 1999. Migration and natural fate of a coal tar creosote plume: 2. Mass balance and biodegradation indicators. *J.Contam. Hydrol.*, 39(3-4): 281-307.

Kram, M.L., Keller, A.A., Rossabi, J., Everett, L.G., 2001. DNAPL characterization methods and approaches, Part 1: Performance comparisons. *Ground Water Monitoring and Remediation* 21 (4), 109-123.

Kueper, B.H. and E.O. Frind. 1991. Two phase flow in heterogeneous porous media: 2. Model application. *Water Resources Research*, 27:1059-1070.

Kueper, B.H., Redman, D., Starr, R.C., Reitsma, S. and M. Mah. 1993. A field experiment to study the behavior of tetrachloroethylene below the water table: Spatial distribution of residual and pooled DNAPL. *Ground Water*, 31(5): 756-766.

Lee, K.Y., C.V. Chrysikopoulos and T.C. Harmon. 1998. Measuring and modeling DNAPL pool dissolution in three-dimensional porous media, 1, Ideal pool geometry, in Proceedings of the 1998 Symposium on Environmental Models and Experiments Envisioning Tomorrow (EnviroMEET'98), edited by C.V. Chrysikopoulos, T.C. Harmon and J. Bear. pp 151-159. Univ. of Calif., Irvine, 1998.

Lee, K.Y. and C.V. Chrysikopoulos. 2002. Dissolution of a well-defined trichloroethylene pool in saturated porous media: experimental results and model simulations. *Water Research* 36:3911-3918.

Lemke L.D., Abriola, L.M. and Goovaerts, P. 2004a. DNAPL source zone characterization: Influence of hydraulic property correlation on predictions of

DNAPL infiltration and entrapment, *Water Resour. Res.*, 40, W01511, doi: 10.1029/2003WR001980.

Lemke, L.D., Abriola, L.M. and Lang, J.R. 2004b. DNAPL source zone remediation: Influence of source zone architecture on predictions of DNAPL recovery and contaminant flux. *Water Resour. Res.*, 40, W12417, doi:10.1029/2004WR003061.

Lemke, L.D. and Abriola, L.M. 2006. Modeling DNAPL mass removal in nonuniform formations: Linking source zone architecture and system response, *Geosphere*, 2, 74-82.

Li, K.B., P. Goovaerts, and L.M. Abriola. 2007. A geostatistical approach for quantification of contaminant mass discharge uncertainty using multilevel sampler measurements. *Water Resources Research*, 43, W06436, doi:10.1029/2006WR005427.

Li, K.B. and L.M. Abriola. 2009. A multistage multicriteria spatial sampling strategy for estimating contaminant mass discharge and its uncertainty. *Water Resources Research*, 45: Art. No. W06407

Liggieri, L., Ravera, F., Ferrari, M., Passrone, A., Miller, R., 1997. Adsorption kinetics of alkylphosphine oxides at water/hexane interface 2. Theory of the adsorption with transport across the interface in finite systems. *Journal of Colloid and Interface Science* 186, 46-52.

Little, J. C., Daisey, J.M., and W.W. Nazaroff. 1992. Transport of Subsurface Contaminants into Buildings. *ES&T* 26:2058-2066.

Londergan, J.T., H.W. Meinardus, P.E. Mariner, R.E. Jackson, C.L. Brown, V. Dwarakanath, G.A. Pope, J.S. Ginn, and S. Taffinder. 2001. DNAPL removal from a heterogeneous alluvial aquifer by surfactant-enhanced aquifer remediation. *Ground Water Monitor Remediation*, 21:57-67.

Lorah, M.M. and L.D. Olsen. 1999. Natural attenuation of chlorinated volatile organic compounds in a freshwater tidal wetland: Field evidence of anaerobic biodegradation. *WRR*, 35(12):3811-3827.

Lyman, W. J., Reehl, W. F., Rosenblatt, D. H., 1990. *Handbook of Chemical Property Estimation Methods*; American Chemical Society, Washington, DC.

Mackay, D.M. and J.A. Cherry 1989. Groundwater contamination: Pump and Treat remediation. *ES&T*, 23:630-636.

Magnussen, T., Rasmussen, P., Fredenslund, A., 1981. UNIFAC parameter table for prediction of liquid-liquid equilibria. *Industrial and Engineering Chemistry Process Design and Development* 20 (2), 331-339.

Mayer, A.S. and S.M. Hassanizadeh. 2005. *Soil and Groundwater Contamination: Nonaqueous Phase Liquids*. American Geophysical Union. Washington, D.C.

Meinardus, H.W., V. Dwarakanath, J. Ewing, G.J. Hirasaki, R.E. Jackson, M. Jin, J.S. Ginn, J.T., Londergan, C.A. Miller, and G.A. Pope. 2002. Performance assessment of NAPL remediation in heterogeneous alluvium. *Journal of Contaminant Hydrology*, 54, 173-193.

McGuire, T.M., McDade, J.M. and C.J. Newell. 2006. Performance of DNAPL source depletion technologies at 59 chlorinated solvent-impacted sites. *Ground Water Monitoring and Remediation*, 26(1):73-84.

Mendoza-Sanchez, I., Cunningham, J., 2007. Efficient algorithm for modeling transport in porous media with mass exchange between mobile fluid and reactive stationary media. *Transport in Porous Media* 68 (3), 285-300.

Moreno-Barbero, E. and T.H. Illangasekare. 2005. Simulation and performance assessment of partitioning tracer tests in heterogeneous aquifers. *Environmental and Engineering Geoscience*, 11(4):395-404.

Moreno-Barbero, E. and T.H. Illangasekare. 2006. Influence of dense nonaqueous phase liquid pool morphology on the performance of partitioning tracer tests: Evaluation of the equilibrium assumption. *Water Resources Research*, 42(4): Art. No. W04408

Moreno-Barbero, E., Kim, Y., Seaton, S., Illangasekare, T.H., 2007. Intermediate scale investigation of nonaqueous phase liquid architecture on partitioning tracer test performance. *Vadose Zone Journal* 6 (4), 725-734.

Morrison, R.D. 2007. *Introduction to Environmental Forensics*, Second Edition. Elsevier Inc. Burlington, MA

Nambi, I.M. 1999. Dissolution of non-aqueous phase liquids in heterogeneous subsurface systems, Ph.D. dissertation, Department of Civil and Environmental Engineering, Clarkson University, Potsdam, NY.

Nambi, I.M. and S.E. Powers. 2003. Mass transfer correlations for nonaqueous phase liquid dissolution from regions with high initial saturations. *Water Resources Research*, 39(2) doi:10.1029/2001WR000667

National Oceanic and Atmospheric Administration. 2012. Database of Hazardous Materials. <http://cameochemicals.noaa.gov/chris/DEL.pdf>

National Research Council. 2005. *Contaminants in the Subsurface: Source Zone Assessment and Remediation*. Washington, D.C: National Academic Press

Nelson, N.T., Brusseau, M.L., 1996. Field study of the partitioning tracer method for detection of dense nonaqueous phase liquid in a trichloroethene-contaminated aquifer. *Environmental Science and Technology* 30 (9), 2859-2863.

Nkeddi-Kizza, P., Biggar, J.W., Selim, H.M., van Genuchten, M.Th., Wierenga, P.J., Davidson, J.M., Nielsen, D.R., 1984. On the equivalence of two conceptual models for describing ion exchange during transport through an aggregated Oxisol. *Water Resour. Res.* 20, 1123–1130.

Pankow, J.F. and J.A. Cherry. 1996. *Dense Chlorinated Solvents and Other DNAPLs in Groundwater*. Portland: Waterloo Press

Parker, J.C. and Lenhard, R.J. 1987. A model for hysteretic constitutive relations governing multiphase flow, 1. Saturation-pressure relations, *Water Resour. Res.*, 23, 2187-2196.

Pfannkuch, H.O. 1984. Determination of the contaminant source strength from mass exchange processes at the petroleum-ground-water interface in shallow aquifer systems. In: Proceedings of the NWWA/API conference on Petroleum Hydrocarbons and Organic Chemicals in Ground Water-Prevention, Detection and Restoration. Houston, TX. Natl. Water Well Assoc., Worthington, OH, Nov. 1984. 111-129.

Pennell, K.D., L.M. Abriola and W.J. Weber, Jr. 1993. Surfactant-enhanced solubilization of residual dodecane in soil columns. 1. Experimental investigation. *Environmental Science and Technology*, 27: 2332-2340.

Pope, G.A., Sepehrnoori, K., Shiles, G. 1994. Numerical simulation of interwell tracers. *In Situ* 18, 107-121.

Poulsen, M.M. and B.H. Kueper. 1992. A Field Experiment To Study The Behavior Of Tetrachloroethylene In Unsaturated Porous-media. *Environmental Science and Technology*, 26(5):889-985.

Powers, S.E., L.M. Abriola, and W.J. Weber, Jr. 1992. An Experimental Investigation Of Nonaqueous Phase Liquid Dissolution In Saturated Subsurface Systems - Steady-State Mass-Transfer Rates. *Water Resources Research*, 30(2): 321-332.

Powers, S.E., L.M. Abriola, and W.J. Weber, Jr. 1994. An Experimental Investigation Of Nonaqueous Phase Liquid Dissolution In Saturated Subsurface Systems - Transient Mass-Transfer Rates. *Water Resources Research*, 28(10): 2691-2705.

Ramachandran, B.R., Allen, J.M., Halpern, A.M., 1996. The importance of weighted regression analysis in the determination of Henry's Law constants by static headspace gas chromatography. *Analytical Chemistry* 68, 281-286.

Ramsburg, C.A. and K.D. Pennell. 2002. Density-modified displacement for DNAPL source zone remediation: density conversion and recovery in heterogeneous aquifer cells. *Environmental Science and Technology*, 36:3176-3187.

Ramsburg, C.A., K.D. Pennell, L.M. Abriola, G. Daniels, C.D. Drummond, M. Gamache, H-L Hsu, E.A. Petrovskis, K.M. Rathfelder, J.L. Ryder, and T. P. Yavaraski. 2005. Pilot-scale demonstration of surfactant-enhanced PCE solubilization at the Bachman Road site. 2. System operation and evaluation. *Environmental Science and Technology*, 39: 1791-1801.

Ramsburg, C.A., Thornton, C.E., Christ, J.A., 2010. Degradation product partitioning in source zones containing chlorinated ethene DNAPL. *Environmental Science and Technology*. Available Online doi:10.1021/es102536f.

Ramsburg, C.A., J.A. Christ, S.R. Douglas, and A. Boroumand. 2011. Analytical modeling of degradation product partitioning kinetics in source zones containing entrapped DNAPL. *Water Resources Research*, 47. DOI:10.1029/2010WR009958. Article Number: W03507.

Rao, P.S.C., Annable, M.D., Sillan, R.K., Dai, D.P., Hatfield, K., Graham, W.D., Wood A.L., Enfield, C.G., 1997. Field scale evaluation of in situ cosolvent flushing for enhanced aquifer remediation. *Water Resources Research* 33 (12), 2621-2636.

Rao, P.S.C., M.D. Annable, and H. Kim. 2000. NAPL source zone characterization and remediation technology performance assessment: recent developments and applications of tracer techniques. *Journal of Contaminant Hydrology*, 45: 63-78.

Rao, P.S.C., Jawitz, J.W., Enfield, C.G., Falta Jr., R.W., Annable, M.D. and A.L. Wood. 2001. Technology integration for contaminated site remediation: clean-up goals and performance criteria. *Proceedings of the Groundwater Quality, 2001*, Sheffield, U.K.

- Rao, P.S.C., Jawitz, J.W., Enfield, C.G., Falta, R.W., Annable, M.D. and Wood, A.L. 2002. Technology integration for contaminated site remediation: clean-up goals and performance criteria. *Groundwater Quality: Natural and Enhanced Restoration of Groundwater Pollution*. IAHS Publication 275, 571-578.
- Rao, P.S.C., J.W. Jawitz. 2003. Comment on, “Steady-state mass transfer from single component dense non-aqueous phase liquids in uniform flow fields” by T.C. Sale and D.B. McWhorter. *Water Resources Research*, 33(12):2673-2686.
- Rasmuson, A., Neretnieks, I., 1980. Exact solution of a model for diffusion in particle and longitudinal dispersion in packed-beds. *AIChE Journal* 26 (4), 686-690.
- Rathfelder, K. and L.M. Abriola. 1994. Mass conservative numerical-solutions of the head-based Richards Equation. *Water Resources Research*, 30(9):2579-2586.
- Rathfelder, K. and L.M. Abriola. 1996. Mass conservative numerical-solutions of the head-based Richards Equation – Reply. *Water Resources Research*, 32(3):761.
- Ravera, F., Ferrari, M., Liffieri, L., Miller, R., 1997. Adsorption kinetics of alkyl phosphine oxides in water/alkane systems with transfer across the interface. *Progress in Colloid and Polymer Science* 105, 346-350.
- Ravera, F., Ferrari, M., Liggieri, L., 2000. Adsorption and partitioning of surfactants in liquid-liquid systems. *Advances in Colloid and Interface Science* 88, 129-177.
- Riddick J.A. and W.B. Bunger, Techniques of Chemistry, Vol. II, 3rd edn., Wiley Interscience, New York, 1970.
- Saenton, S. and Illangasekare, T. 2007. Upscaling of mass transfer rate coefficient for the numerical simulation of dense nonaqueous phase liquid dissolution in heterogeneous aquifers. *Water Resour. Res.*, 43(2):WR004274
- Sale, T.C. and McWhorter, D.B. 2001. Steady state mass transfer from single-component dense nonaqueous phase liquids in uniform flow fields, *Water Resour. Res.*, 37, 393-404.
- Sandler, S.I. 2006. Chemical, Biochemical, and Engineering Thermodynamics, 4<sup>th</sup> Ed. John Wiley & Sons, Inc. Hoboken, NJ.
- Sardin, M., Schweich, D., Leij, F.J., van Genuchten, M.Th., 1991. Modeling the sorption of linearly interacting solutes in porous media: a review. *Water Resour. Res.* 27, 2287–2307.

- Saripalli, K.P., Annable, M.D., Rao, P.S.C., 1997. Estimation of nonaqueous phase liquid-water interfacial areas in porous media following mobilization by chemical flooding. *Environmental Science and Technology* 31, 3384-3388.
- Schmidt, Robin. R. DeZeeuw, L. Henning, D. Trippler. 1999. State Programs to Clean Up Drycleaners. State Coalition for Remediation of Drycleaners.
- Schnaar, G., Brusseau, M.L., 2005. Pore-Scale characterization of organic immiscible-liquid morphology in natural porous media using synchrotron x-ray microtomography. *Environmental Science and Technology* 39, 8403-8410.
- Schroth, M.H., J.D. Istok, R. Haggerty. 2001. In situ evaluation of solute retardation using single-well push-pull tests, *Advances in Water Resources*, 24: 105-117
- Schwartz, R., Ptak, T., Holder, T.H. and Teutsch, G. 1998. Groundwater risk assessment at contaminated sites: a new investigation approach. *Groundwater Quality: Remediation and Protection*. IAHS publication 250. pp. 68-71.
- Schwille, F., *Dense Chlorinated Solvents in Porous and Fractured Media*, translated from German by J. F. Pankow, Lewis, Chelsea, Mich., 1988.
- Seagren, E.A., B.E. Rittmann, and A.J. Valocchi. 1999a. A critical evaluation of the local-equilibrium assumption in modeling NAPL-pool dissolution. *JCH* 39:109-135.
- Seagren, E.A., B.E. Rittman, A.J. Valocchi. 1999b. An experimental investigation of NAPL-pool dissolution enhancement by flushing. *JCH* 37:111-137
- Seagren, E.A. and T.O. Moore. 2003. Nonaqueous phase liquid pool dissolution as a function of average pore water velocity. *J. Environmental Engineering* 9:786-799.
- Selim, H.M., Davidson, J.M., Mansell, R.S., 1976. Evaluation of a two-site adsorption-desorption model for describing solute transport in soil. *Proc. Comp. Simul. Conf., Am. Inst. Chem. Eng, New York*, 444-448.
- Semprini, L., P. K. Kitanidis, D. H. Kampbell, and J. T. Wilson. 1995. Anaerobic transformation of chlorinated aliphatic hydrocarbons in a sand aquifer based on spatial chemical distributions. *Water Resour. Res.*, **31**, 1051-1062.
- Skopp, J. 1984. Estimation of true moments from truncated data. *AIChE J.* 30, 151-155.

- Smith, J.M., Van Ness, H.C., 1987. *Introduction to Chemical Engineering Thermodynamics*, 4<sup>th</sup> ed., McGraw-Hill, Inc., New York, NY.
- Soga, K., J.W.E. Page, and T.H. Illangasekare. 2004. A review of NAPL source zone remediation efficiency and the mass flux approach. *Journal of Hazardous Materials*, 110:13-27.
- Sorensen, J.M., Magnussen, T., Rasmussen, P., Fredenslund, A., 1979. Liquid-liquid equilibrium data: their retrieval, correlation and prediction. Part I: Retrieval. *Fluid Phase Equilibria* 2, 297-309.
- SCRD, Drycleaner Remediation Programs. August 2001. An Overview and Case Studies, Prepared by Kate Cardamone National Network of Environmental Management Studies (NNEMS) Fellow.
- Stroo, H.F., Unger, M., Ward, C.H., Kavanaugh, M.C., Vogel, C., Leeson, A., Marqusee, J.A., and B.P. Smith. 2003. Remediating chlorinated solvent source zones. *Environmental Science and Technology*, 37(11): 224A-230A.
- Suchomel, E.J. and K.D. Pennell. 2006. Reductions in contaminant mass discharge following partial mass removal from DNAPL source zones. *Environmental Science and Technology*, 40(19):6110-6116.
- Taylor, T.P., Pennell, K.D., Abriola, L.M., Dane, J.H., 2001. Surfactant enhanced recovery of tetrachloroethylene from a porous medium containing low permeability lenses. 1. Experimental studies. *Journal of Contaminant Hydrology* 48, 325-350.
- Thal Jr., A.E., Knox, R.K., Sabatini, D.A., 2007. Estimating Partition Coefficients of Tracers. *Groundwater Monitoring and Remediation* 27 (4), 135-142.
- Toxics Use Reduction Institute. 2010. <http://www.turi.org/>
- United States Environmental Protection Agency, Office of Research and Development. 1991. Understanding Bioremediation: A Guidebook for Citizens; EPA/540/2-90/013; Washington, D.C.
- United States Environmental Protection Agency. 2002. OSWER Guidance for Evaluating the Vapor Intrusion to Indoor Air Pathway from Groundwater and Soils (Subsurface Vapor Intrusion Guidance). Washington, D.C.
- United States Environmental Protection Agency (USEPA) 2003. *The DNAPL remediation challenge: Is there a case for source depletion?*, Rep. EPA/600/R-03-143, Washinton, D.C.

- United States Environmental Protection Agency, Office of Solid Waste and Emergency Response. 2004. DNAPL Remediation: Selected Projects Approaching Regulatory Closure. EPA 542R-04-016, Washington, D.C.
- United States Environmental Protection Agency, Integrated Risk Information System. 2011. Trichloroethylene (CASRN 79-01-6). Washington, D.C.
- United States Environmental Protection Agency, Technology Innovation and Field Services Division. 2012. Clu-in.org. Washington, D.C.
- U.S. Silica Company. 2012. Product Data Sheets. Frederick, MD.  
<http://www.ussilica.com/why-us-silica/sales-support/product-data-sheets>
- Valocchi, A.J. 1985. Validity of the Local Equilibrium Assumption for Modeling Sorbing Solute Transport through Homogeneous Soils. *Water Resour. Res.*, 21(6), 808-820.
- Vangenuchten, M.T. and R.J. Wagenet. 1989. 2-Site 2-Region Models for Pesticide Transport and Degradation - Theoretical Development and Analytical Solutions. *Soil Science Society of America Journal* 53(5):1303-1310.
- Wang, P., Dwarakanath, V., Rouse, B.E., Pope, G.A., Sepehrnoori, K. 1998. Partition coefficients for alcohol tracers between nonaqueous-phase liquids and water from UNIFAC solubility method. *Advances in Water Resources* 21 (2), 171-181.
- Weber, W.J. Jr., and F.A. DiGianno. 1996. Process Dynamics In Environmental Systems. *Wiley-Interscience, John Wiley & Sons, Inc*, ISBN 0-471-01711-6
- Willson, C.S., O. Pau, J.A. Pedit, and C.T. Miller. 2000. Mass transfer limitation effects on partitioning tracer tests. *Journal of Contaminant Hydrology*, 45: 79-97.
- Wilson, R.D. and D.M. Mackay. 1995. Direct Detection of Residual Nonaqueous Phase Liquid in the Saturated Zone using SF<sub>6</sub> as a Partitioning Tracer. *ES&T*, 29(5):1255-1258.
- Wise, W.R. 1999. NAPL characterization via partitioning tracer tests: Quantifying effects of partitioning nonlinearities. *Journal of Contaminant Hydrology*, 36: 167-183.
- Wise, W.R., D. Dai, D., E.A. Fitzpatrick, L.W. Evans, P.S.C. Rao, and M.D. Annable. 1999. Nonaqueous phase liquid characterization via partitioning tracer tests: A modified Langmuir relation to describe partitioning nonlinearities. *Journal of Contaminant Hydrology*, 36: 153-165.

Young, C.M., Jackson, R.E., Jin, M., Londergan, J.T., Mariner, P.E., Pope, G.A., Anderson, F.J., Houk, T., 1999. Characterization of a TCE DNAPL zone in alluvium by partitioning tracers. *Groundwater Monitoring and Remediation* 19 (1), 84-94.

Zhu, W., Xu, L., Ma, J., Yang, R., Chen, Y., 2009. Effect of the thermodynamic properties of W/O microemulsions on samarium oxide nanoparticle size. *Journal of Colloid and Interface Science* 340, 119-125.